Forschungszentrum Jülich

Institut für Nuklearchemie

Activation Cross Sections and Isomeric Cross Section Ratios in Neutron Induced Reactions on Cr-, Fe-, and Ni-Isotopes in the Energy Range 9 to 21 MeV

Andreas Fessler

Jül-3502

Activation Cross Sections and Isomeric Cross Section Ratios in Neutron Induced Reactions on Cr-, Fe-, and Ni-Isotopes in the Energy Range 9 to 21 MeV

Andreas Fessler

Berichte des Forschungszentrums Jülich ; 3502
ISSN 0944-2952
Institut für Nuklearchemie Jül-3502
D 38 (Diss. Universität Köln)

Zu beziehen durch: Forschungszentrum Jülich GmbH · Zentralbibliothek
D-52425 Jülich · Bundesrepublik Deutschland
☎ 02461/61-6102 · Telefax: 02461/61-6103 · e-mail: zb-publikation@fz-juelich.de

Abstract

A knowledge of cross sections of neutron induced reactions on the structural materials Cr, Fe and Ni is important for practical applications in fusion reactor technology as well as for testing nuclear models. In the present study excitation functions were measured for the $^{50}Cr(n,pn+np+d)^{49}V$, $^{52}Cr(n,2n)^{51}Cr$, $^{52}Cr(n,p)^{52}V$, $^{53}Cr(n,p)^{53}V$ $^{53}Cr(n,pn+np+d)^{52}V$, $^{54}Cr(n,p)^{54}V$ $^{54}Cr(n,pn+np+d)^{53}V$, $^{54}Cr(n,\alpha)^{51}Ti$, $^{54}Fe(n,2n)^{53}Fe$, $^{54}Fe(n,t)^{52}Mn$, $^{58}Ni(n,\alpha)^{55}Fe$, $^{58}Ni(n,p\alpha+\alpha p)^{54}Mn$ and $^{62}Ni(n,\alpha)^{59}Fe$ reactions from 9 to 21 MeV. In addition, isomeric cross section ratios were also measured for the isomeric pairs formed in $^{54}Fe(n,2n)^{53m,g}Fe$ and $^{54}Fe(n,t+dn)^{52m,g}Mn$ processes.

Use was made of the activation technique. The radioactivity was measured via high-resolution gamma-ray and X-ray spectrometry, the latter in combination with radiochemical separation and preparation of thin samples. Monoenergetic neutrons produced via the $^{2}H(d,n)^{3}He$ reaction at the FZ Jülich and the $^{3}H(d,n)^{4}He$ reaction at the IRMM at Geel, Belgium, were used to irradiate samples of metallic natural chromium, iron and nickel as well as samples of enriched $^{53}Cr_2O_3$, $^{54}Cr_2O_3$ and $^{54}Fe_2O_3$. The neutron flux density was determined via the $^{27}Al(n,p)^{27}Mg$, $^{27}Al(n,\alpha)^{24}Na$, $^{56}Fe(n,p)^{56}Mn$ and $^{93}Nb(n,2n)^{92m}Nb$ monitor reactions. A pneumatic sample transport system was installed at Geel to enable measurements of short-lived reaction products. This system was successfully applied to the determination of reaction products with half-lives $\geq$ 10 seconds.

For all the studied reactions substantial new information was obtained and the present data should contribute appreciably to solving large discrepancies in the major evaluations for most of the reactions. For the (n,p) and (n,np) reactions on the four stable Cr-isotopes, viz. ^{50}Cr, ^{52}Cr, ^{53}Cr and ^{54}Cr, a systematic trend in the excitation functions could be observed which is ascribed to the Q-values of the reactions. The isomeric cross section ratio for the $^{54}Fe(n,2n)^{53m,g}Fe$ reaction increases with the increasing neutron energy whereas the ratio for the $^{54}Fe(n,t+dn)^{52m,g}Mn$ reaction decreases with the increasing neutron energy. These trends are explained in terms of the involved spins of the respective nuclides.

The experimentally determined cross sections and isomeric cross section ratios were compared with the results of nuclear model calculations carried out using the code STAPRE-H. The aim was to test the underlying models. STAPRE-H uses the Hauser-Feshbach formula for the equilibrium and the Exciton or Geometry Dependent Hybrid (GDH) Model for the pre-equilibrium (PE) contribution. Neutron, proton and alpha emission were taken into account. The influence of the PE contribution on the cross section was investigated with the two PE models and by varying the FM parameter in the Exciton Model. Most of the reactions could be described by the model calculation with deviations of $\pm$ 10 % to the experiment. This shows that the underlying models can reproduce the excitation functions satisfactorily, provided the input parameters are well chosen.

Table of Contents

Preface

The discovery of the neutron by Chadwick in 1932 [Cha 32a, Cha 32b] gave a great impetus to the study of nuclear reactions. The absence of charge enables the neutron to interact with a nucleus at close distances and at all neutron energies. Therefore it was the first projectile to be used in the study of nuclear structure and nuclear reaction mechanisms. Even today, many decades after the first experiments, the need to understand the fundamental nuclear processes has remained unchanged. Accurate experimental data are required upon which theories and computational techniques can be based.

Along with these interests in the basic physics, precise nuclear data became important for applications in many disciplines, such as nuclear energy (fission and fusion systems), medicine and biology (radiotherapy for cancer treatment, diagnostics, radio-biological studies), materials science and industry (production of radioisotopes, neutron radiography, materials analysis). Since many of the requests for data cannot be met by experimental measurements alone, the quantification of neutron interaction parameters must also be approached by a better quantitative understanding of the nuclear processes. Establishing systematic trends from high quality measurements and good fundamental understanding of the subject would allow the calculation of unmeasured data.

Thus neutron activation cross sections over a wide energy range are of fundamental significance for testing nuclear models. However, extensive data exist only around 14 MeV. In the energy range from 15 to 20 MeV only a few measurements have been done and the results are often inconsistent. Different cross section evaluations, mostly based on calculations, differ frequently by a factor of two to three. In this energy region many reaction channels are open (e. g. elastic scattering, inelastic scattering, radiative capture, (n,2n), (n,p), (n,α), (n,np), (n,d), (n,nα) etc.) and different reaction mechanisms need to be considered (compound, precompound and direct interactions). For nuclear reaction model calculations several computer codes are available but the parameterization is often uncertain. Therefore more experimental data are needed to test the model parameterizations. Apart from this fundamental interest, the activation data are important for practical applications in fusion reactor technology, e.g. estimation of activity level, hydrogen and helium gas production, nuclear heating or radiation damage. With the D-T fusion reaction the neutron energy of primary interest is 14 MeV. However , cross sections at lower neutron energies are also needed since neutrons are degraded in the reactor blanket. Neutron cross sections above 14 MeV are of interest mainly in radiation damage studies. The testing of fusion materials is often done with broad spectrum neutron sources with neutron energies up to 50 MeV. In order to predict the behaviour at and below 14 MeV on the basis of measurements with such sources, the dependence of the relevant cross section on neutron energy needs to be known.

The investigation of isomeric cross section ratios is another interesting subject. Since the discovery of the first isomer by Hahn [Hah 21], the ^{234m}Pa with a half-life of 70 seconds, many isomers have been identified. However, the quantitative formation of those states in different nuclear reactions is still not exactly understood. The lack of data is due to many reasons, namely, very short or very long half-lives of the isomers, low cross sections for the population of the individual levels, close level spacings or low transition energies make experiments difficult. Thus more experimental and theoretical studies are needed to shed some more light on the reaction mechanisms involved.

Radiochemical methods accompanied the study of nuclear reactions right from the beginning. The production of suitable targets, the separation of the reaction products and the preparation of appropriate samples for activity measurement are essential aspects of accurate cross section measurements.

This thesis describes neutron activation cross section measurements on Cr, Fe and Ni-isotopes in the energy ranges 9 to 12 MeV and 14 to 20 MeV. In addition isomeric cross section ratios have been measured in two reactions on ^{54}Fe.

In *chapter 1* the basic properties and concepts of nuclear reactions are given, followed by a discussion of the status and some systematic trends of (n,charged particle) and (n,xn) cross sections. Also some systematics of isomeric cross section ratios are discussed. The techniques of cross section measurements including radiochemical methods are outlined and the available neutron sources for the production of monoenergetic neutrons are reviewed.

Chapter 2 is devoted to a more detailed description of the motivation of the present investigation. The needs of precise nuclear data for the selected reactions on structural materials are explained.

Chapter 3 describes the experimental techniques, dealing with the sample irradiation at different facilities and the gamma- and X-ray spectrometry in detail. The radiochemical separations and the sample preparation for the X-ray spectrometry are also considered in this chapter. Finally, the determination of the experimental cross sections and isomeric cross section ratios from the analysed gamma- and X-ray spectra are explained.

In *chapter 4* the principle of nuclear model calculation is presented together with a detailed description of the calculations performed using the code STAPRE-H [Avr 87]. The selection of the input parameters is discussed in detail.

Chapter 5 compares the experimental results with the model calculations and some major evaluations. Some observed systematic trends are discussed.

Finally, in *chapter 6* a short summary of the work performed is given together with some conclusions.

1. Introduction

1.1 Nuclear Reactions - Basic Properties and Concepts

- **Cross Sections**

We speak of a nuclear reaction **X(n,x)Y** when an incident particle **n** hits a target nucleus **X**, a particle **x** is emitted, leaving a residual nucleus **Y**. The probability for this type of reaction to occur is called the cross section $\sigma_{n,x}$. It is defined as the number of reactions **(n,x)** on a target nucleus per unit time and unit incident particle flux. The cross section is given in barns ($1b = 10^{-28}\ m^2$); integrated over all angles it is called *integral cross section.* It is a function of the energy of the incident particle and the plot of $\sigma(E)$ versus **E** is called the *excitation function.* Taking into account the angular distribution of the emitted particle in the solid angle $d\Omega$ one obtains the *differential cross section* $d\sigma/d\Omega$. The *double-differential cross section* $d^2\sigma/d\Omega dE$ is a function of the kinetic energy **E** of the emitted particle and of the angle of emission Θ.

In a nuclear reaction the energy is conserved. The remaining kinetic energy of the reaction products is described by the *Q-value.* It can be derived from the difference in the nuclidic masses and serves as an indication whether a reaction is energetically possible or not. The minimum incident energy which is required to initiate a reaction is called the *threshold energy.* It takes also into account the energy which is needed to conserve the momentum in the reaction and can be described as

$$E_{thres} = -Q \cdot \left(1 + \frac{M_n}{M_X}\right) \qquad (1.1)$$

where M_n and M_X are the mass of the projectile and the target nucleus, respectively. Other quantities which are also conserved are the charge, the angular momentum, the parity, the isospin and the number of nucleons.

- **Isomeric Cross Section Ratios (ICSR)**

Nuclides with the same mass and proton number (i. e. the same chemical properties) but different decay properties (different half-lives, different decay modes and energies) are considered as *isomers.* They occur when an excited energy state has a measurable half-life ($T_{1/2}$ ~0.1 s to several years). The *isomeric state* decays either by gamma-ray emission to the ground state or by EC, beta- or alpha-particle emission to another nuclide. The "half-life" of the isomeric state is explained in terms of the difference in the spins of the isomers [Wei 36]. Furthermore, the momentum and the energy of the projectile influence the

population of isomeric states. With increasing energy of the projectile the isomer with the higher spin is preferably populated. Therefore, the determination of ICSR's provides useful information on the influence of energy and spin of the isomeric state as well as of the energy and momentum of the projectile on nuclear reactions. Generally the ICSR is given as $\sigma_m / \sigma_m + \sigma_g$ (**m** denotes the metastable state, **g** the ground state) or as σ_m / σ_g.

- **Reaction Channels**

If different reactions are energetically possible for a defined incident particle energy we speak of different *reaction channels*. For example, at incident neutron energies between 10 and 20 MeV, the energy range of this work, generally the following reactions are energetically possible: elastic scattering, inelastic scattering, radiative capture, (n,2n), (n,p), (n,α), (n,np), (n,d), (n,t), (n,^{3}He), and (n,nα). The sum of the cross sections of all these reaction channels is called the *total cross section*, σ_T. It can be easily determined by transmission measurements. The typical shapes of some threshold reactions, e. g. the (n,p), (n,α) or (n,2n) reactions, can be explained by the coexistence of these different reaction channels. Above the threshold the excitation function increases steadily, reaching a small plateau, and then decreases above energies where other reactions are also energetically possible.

- **Reaction Mechanisms**

In general, one can distinguish between three types of reaction mechanisms: direct, compound nucleus and preequilibrium or precompound. For a given reaction all three mechanisms contribute to the cross section, depending on the type of reaction (projectile and emitted particle), the incident energy and the excitation energy of the residual nucleus.

Direct reactions occur mainly as binary processes and are characterized by a direct transition from the entrance to the exit channel in a very short time (~10^{-23} - 10^{-22} s). No intermediate state is formed. Typical examples of direct reactions are elastic and inelastic scattering, charge-transfer (p,n), stripping (d,p) or pick-up (n,d).

Compound nucleus reactions occur mainly at low energies and proceed via an intermediate state. The energy of the projectile is distributed over all nucleons. The deexcitation of the nucleus is finally reached by evaporation of nucleons with a Maxwellian energy distribution. The time-scale for this type of reaction is much longer than that for the direct reaction (10^{-16} s).

The *precompound or preequilibrium reactions* are somehow intermediate processes between the two other ones. They occur when an incident particle has still enough energy, after the first collision, to leave the nucleus via direct emission or to collide with another nucleus. This process can be continued until the typical energy distribution over many degrees of freedom of the nucleus is reached. We speak of pre-equilibrium emission when a particle is emitted in between this relaxation period. A more detailed description of the different reaction mechanisms is given in **chapter 4** together with the nuclear model calculations.

1.2 Some Systematics of (n,charged particle) and (n,xn) Reactions

1.2.1 Integral Cross Sections

Several reports have been published on the systematic trends in cross sections for (n,2n), (n,p), (n,α), (n,np+pn+d), (n,^{3}He) and (n,t) reactions at 14 MeV. In most of those works the experimentally determined cross sections were plotted as a function of the asymmetry parameter (S = (N-Z)/A). Some systematics are based purely on cross section calculations using the statistical model, but considering the effective Coulomb barrier for the emitted particle (e. g. [Gul 95]). Extensive reviews about cross section systematics were given by Qaim [Qai 86b], Forrest [For 86] and others (for example [Ede 72], [Lev 73], [Byc 80], [Ait 87], [Bad 91] and [Kas 96]). Recently, Dóczi et al. [Dóc 97a] and Majdeddin et al. [Maj 97] presented new empirical formulas for the (n,p) and (n,α) reactions, respectively, and compared their results with the available systematics. Some of the conclusions from the systematics are briefly summarized below.

The cross sections of (n,charged particle) reactions decrease with the increasing asymmetry parameter whereas the emission of neutrons increases [Mol 77]. This fact is explained by the increasing Coulomb barrier for charged particles. Possible effects of proton and neutron shell closures on the three major nuclear reactions - (n,p), (n,α) and (n,2n) - have been stated to be negligible [Qai 72]. Mostly the systematics are based on the first order asymmetry term in the exponential. Forrest also included the second order asymmetry term and a term which involves the mass number A [For 86]. Dóczi et al. [Dóc 97b] stated that both for (n,p) and (n,α) cross sections the simple expression

$$\sigma\ (A,Z) = a\ \left(A^{1/3}+1\right)^2 \cdot e^{-b\left(S+S^2\right)} \qquad \textbf{(1.2)}$$

gives a substantial improvement in fitting the experimental data. Nevertheless, they recommend for the fitting of the (n,p) cross sections formulas containing additional terms in the exponential depending either on A, Z or N (as done by Forrest [For 86]).

For (n,p) and (n,α) reactions an *isotope effect* was demonstrated: it means that the cross section for a particular reaction on two adjacent isotopes of the same element may vary by about a factor of two [Gar 62, Gar 64]. This observation is understood to be essentially a Q-value effect. With higher incident neutron energies this effect should decrease and increase with lower values. The isotopic dependence of the (n,p) and (n,α) cross sections can be well approximated by the following expression [Dóc 97a]

$$\sigma\ (A) = a\ e^{-bS-cS^2} \qquad \textbf{(1.3)}$$

Also for the (n,t) reaction a similar trend was found [Qai 76]. Here the systematic trend for the cross section behaviour could be split into two parts, one for odd mass nuclei

(higher σ) and the other for even mass nuclei (lower σ). For (n,np+pn+d) reactions a dependence of the cross section on the separation energies for neutrons $\mathbf{S_n}$ and protons $\mathbf{S_p}$ was found. The values for reactions on nuclei with $S_n>S_p$ are somewhat larger than those for nuclei with $S_n<S_p$. This is explained as follows. Generally the (n,np) reaction channel is very weak, since the excited levels of the (n,n') reaction product tend to emit a second neutron rather than a proton. However, in cases where $S_n>S_p$, after the emission of the first neutron, a large number of levels of the excited nucleus have no neutron decay width and the only open channels are gamma or proton emission. Due to the rather high excitation energy of the (n,n') reaction product, it is expected that a considerable number of protons will be emitted at the second stage [Qai 82].

Some systematics are also devoted to the complete excitation functions of (n,p), (n,α), (n,t), (n,2n) and (n,3n) reactions [Zha 86a, Zha 86b]. They all rely on some simplified analytical expressions on the bases of the evaporation model, considering the pre-equilibrium part, which are fitted to the experimental data. Nevertheless, the prediction of unknown excitation functions out of these systematics is quite unsatisfactory. Better predictions can be drawn from simple nuclear model codes containing one parameter set for all mass numbers and projectile energies like the code EXIFON [Kal 90, Kal 91].

1.2.2 Isomeric Cross Section Ratios (ICSR)

In contrast to the systematics of the integral cross sections for neutron induced reactions, those predicting the isomeric cross section ratio are rather incomplete. The empirical formula for the cross section prediction is usually simply a least squares fit of experimentally determined cross section values versus the asymmetry parameter (one parameter fit, see above). To predict the isomer ratios with certainty more parameters are needed, in particular those related to the distribution and population of competing levels. Therefore, the level density parameters and the nuclear structure become important (see also **chapter 4**).

The first studies of ICSR's were reported by Uray et al. [Ura 78] who plotted the ratio σ_m / σ_g versus the spin of the isomeric state $\mathbf{J_m}$. Data on (n,2n), (n,p) and (n,α) reactions gave a parabolic curve with the peak maximum at $J_m \sim 5$, based on a purely visual treatment. Later Qaim [Qai 85] suggested a similar parabolic dependence for the (n,t) reaction plotting the isomeric ratio σ_m / $\sigma_m + \sigma_g$ versus J_m. He found a maximum at $J_m \sim 2 - 3$. However, this study suffered from the facts that limited experimental data was available and that some of the σ_g values had to be estimated from the cross section systematics. In addition to these experimentally based systematics Kopecky and Gruppelar [Kop 87] calculated the isomeric ratio as a function of the two spins J_m and J_g with the code GNASH [You 77]. Their calculation confirmed the parabolic dependence (maximum at $J_m \sim 3 - 5$). The ICSR's are almost similar for the (n,p), (n,α), (n,2n) and (n,t) reactions (height and maximum of the parabolic curve). Only the (n,2n) reaction shows a slower decrease of isomer ratios for $J_m>J_g$. The reason for this effect is probably the emission of

two successive neutrons, leading to a residual nucleus with rather low excitation energy, and thus the number of subsequent gamma-rays is restricted. Consequently, the possibility to populate the ground state (with a low spin) from high-spin states is smaller compared to one step reactions for which the excitation energy is much larger. The calculated values from Kopecky et al. are plotted in **Fig.1.1** as a function of the spin of the isomeric state J_m.

A different approach was used by Huang and Cai [Hua 97] in a most recent study. They fitted all the available data from different databases [Qai 81, For 86, Kop 87, Gru 88, Ike 88, Lu 89] with a parametrized formula based on the Hauser-Feshbach theory (see also **chapter 4**), including two adjustable parameters. Their results confirm the former results and lead to the conclusion that the isomeric ratio may be taken from the systematics with an uncertainty of 30 %.

Some of the interesting areas of work relevant to the isomeric cross sections were recently reviewed [Qai 94]. No systematics are available for the influence of the projectile energy on the ICSR. A few works investigated the ICSR in different nuclear reactions leading to the same nucleus [Man 88, Maj 90, Qai 88, Qai 90, Sud 93, Cse 94, Bir 95, Sud 96]. Nevertheless, up to now very few reactions have been studied in a systematic way to derive some conclusion about the behavior of the ICSR with different incident projectiles.

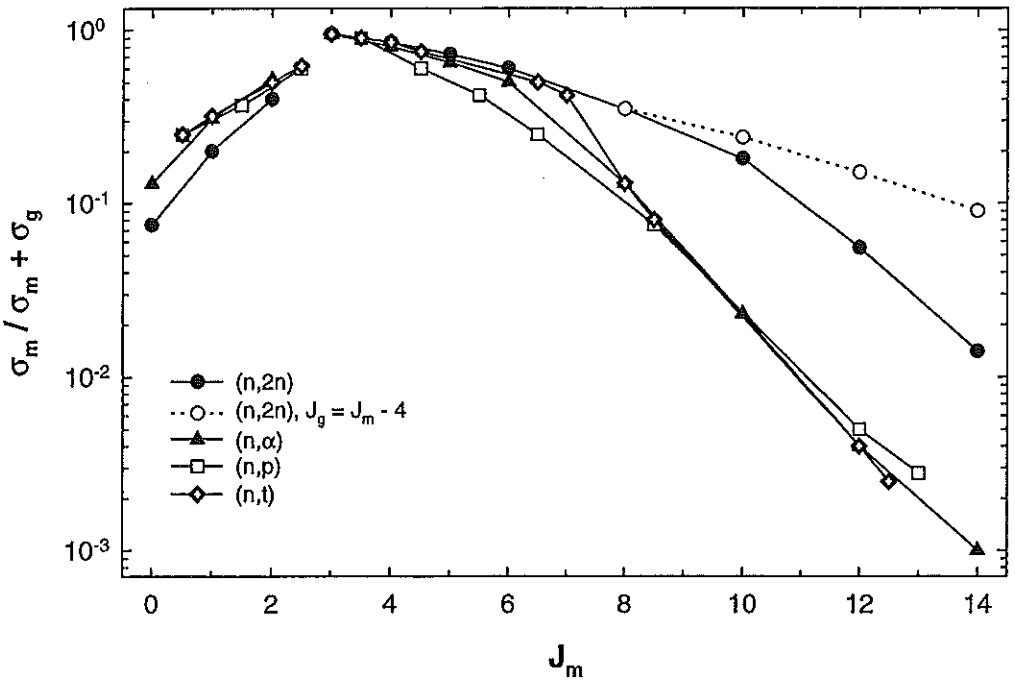

Fig. 1.1 Calculated isomeric cross section ratio $\sigma_m / \sigma_m + \sigma_g$ as a function of the spin of the isomeric state. For low-spin isomers (J_m<3) the ground state spin was set as $J_g = J_m + 4$, while for high-spin isomers (J_m>3) the values $J_g = 0$ or ½ were used. Dotted lines represent the isomer ratio calculated for $J_g = J_m - 4$ values. For single step reactions only one curve is plotted, because the calculations do not differ substantially among each other (taken from [Kop 87]).

1.3 Techniques for (n,charged particle) and (n,xn) Cross Section Measurements

Cross sections of (n,charged particle) or (n,xn) reactions can be determined either via the detection of the emitted particle or through the measurement of the induced activity or mass of the reaction product. A short overview of some characteristics of the two methods is given in **Tab. 1.1**. In the next sections the charged particle and neutron detection is briefly described followed by a more detailed description of the activation method which constituted the main technique in this work. Finally some radiochemical separation methods are outlined which are needed in activation measurements.

Tab. 1.1 Comparison of some characteristics of the spectral and activation methods.

Spectroscopy of the emitted particle	Activation method
on-line	off-line
double differential data (DDX)	integral data
particle selective ((n,p) and (n,np) not easy to distinguish, same particles from different reactions)	product selective ((n,d) not to distinguish from(n,np), several production routes possible) e.g $^{52}Cr(n,p)^{52}V$, $^{53}Cr(n,np)^{52}V$
sample must be thin	sample can be thick
product may be stable or radioactive	product has to be radioactive
special cases: (n,t) reaction - accumulation and beta-counting after chemical separation (n,α) or (n,^{3}He) reactions - mass spectrometry of the accumulated gas	

1.3.1 Detection of Emitted Particle

On-line detection of the emitted particle in an (n,x) reaction (x = H, D, T, ^{3}He, α, ^{6}Li, ^{7}Be etc.) involves measurement of the energy and angular distribution of the emitted particle (⇒ double-differential cross sections, DDX). In general, the sample must be very thin since the ranges of the emitted particles are rather short. The emitted particles are detected with different types of detector systems. Frequently used are reaction chambers in combination with multi-telescope systems. Protons or α-particles are detected at several angles with counter telescopes, each consisting of one or two energy loss detectors (dE/dx-detector) and one total energy detector (E-detector) in a double or triple coincidence arrangement. The dE/dx detector (proportional counter) gives the specific energy loss in

the detector and thus leads to an identification of the emitted particle, whereas the E-detector (surface barrier detector) defines the total energy of the registered particle [Bre 70, Mil 70, Alv 72, Bre 72, Per 74, Pau 81, Wat 83, Wat 91, Tsa 94, Tsa 97].

Quadrupole spectrometer systems used in some laboratories transport the emitted particle 2 - 3 m away from the neutron field. The background with such an arrangement is drastically reduced since neutrons and gamma-rays are not focussed by the magnetic field [Gri 77, Gri 78, Gri 79, Hai 81]. However, their use is generally limited to 14 MeV neutrons due to intensity problems in other neutron fields.

Recently, precise measurements for (n,xα) cross sections have been performed with gridded ionization chambers (GIC) employing high-Z structural elements to suppress charged particle background [Gov 94, Bab 94a, Bab 94b, Ito 94]. Other advantages of the GIC are the good energy resolution (50 - 70 keV) for measuring cross sections for separate α-groups and the high counting efficiency due to the large solid angle (~ 4π) which permits the use of very thin targets (~ 300 $\mu g/cm^2$).

For investigating the neutron emission in (n,n') and (n,xn) reactions, time of flight (TOF) techniques are used in combination with large liquid scintillation detectors [Fre 80]. The relative contributions of the emitted first and second chance neutrons can be resolved by the angular correlations between the various outgoing neutrons [Sal 71, Han 73]. For the measurement of (n,2n) cross sections also a method has been employed which uses a watertank to thermalise the emitted neutrons prior to identification [Här 71].

1.3.2 Activation Method

This technique involves an *off-line* identification and quantitative determination of a radioactive reaction product. The principle of the method is illustrated in **Fig. 1.2.** Considering a nuclear reaction of the type

$$X(n,x)Y \xrightarrow{\beta^-,\beta^+ or\ EC} Z$$

the cross section can be determined by measuring the induced activity of the product Y. Normally this is done by measuring the gamma-ray emission, which follows the beta decay (here γ_3, γ_4 or γ_5), with HPGe or NaI detectors. In cases where there is no gamma-ray emission the activity has to be determined by beta-counting or X-ray spectroscopy. If a metastable state is populated, the isomeric cross section ratio (ICSR) can be determined either by measuring the gamma-ray of the internal transition (IT) leading to the ground state or the γ_1 or γ_2 which follow the beta decay from the metastable state.

Let us consider now the basic underlying equations. The production rate of a radioactive nuclide can be described as a function of the irradiation time by the following first order linear differential equation:

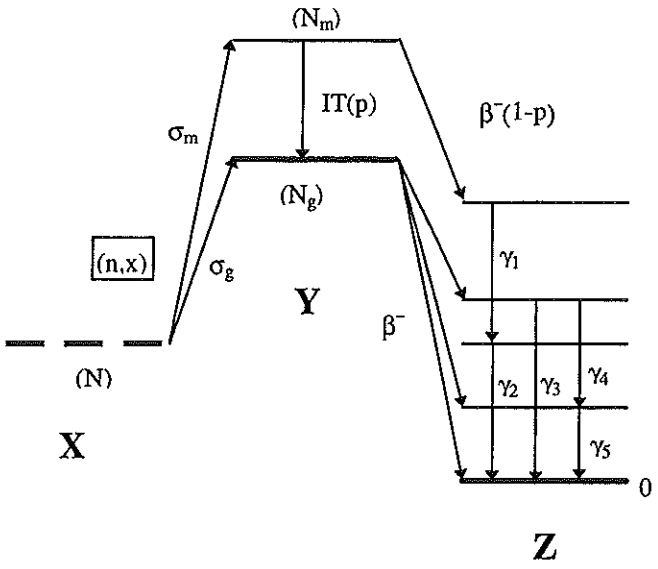

Fig. 1.2 Production and decay of the metastable and the ground state in a neutron activation process (n,x). The figure is taken from [Vän 81].

$$\frac{dN_i}{dt} = N\sigma_i\Phi(t) - \lambda_i N_i(t) \tag{1.4}$$

where N_i is the number of produced atoms, N the number of target atoms, σ_i the reaction cross section, λ_i the decay constant and $\Phi(t)$ the time dependent particle flux. The first term on the right-hand side gives the increase in N_i because of the activation process, while the second term gives the decrease owing to decay. Solving **(1.4)** leads to

$$N_i(t) = N\sigma_i e^{-\lambda_i t}\int_0^t \Phi(t)e^{\lambda_i t}dt \tag{1.5}$$

for the instantaneous number of reaction products. Restricting the solution to a constant flux $\Phi=\Phi_0$ and assuming the initial condition $N_i=0$ for $t=0$ yields

$$N_i(t_i) = \frac{N\sigma_i\Phi_0}{\lambda_i}\left(1-e^{-\lambda_i t_i}\right)\ , \tag{1.6}$$

where t_i is the activation time. At the time t_c ("cooling time") elapsed from the end of the activation, the induced activity is given by

$$A_i = \lambda_i N_i(t_i, t_c) = N\sigma_i\Phi_0\left(1 - e^{-\lambda_i t_i}\right)\ e^{-\lambda_i t_c}\ . \qquad \textbf{(1.7)}$$

the so-called *activation formula*. By determining the activity the cross section can be calculated if **N** and Φ are known. As can be seen from **(1.7)** the activation method is also useful for the determination of **N** or Φ if σ is known. Similar to the measurement of radioactivity, an analogous method involves the determination of the mass of the reaction product, if a stable nuclide is formed. This can be done by mass spectrometry (MS) [Kne 86, Hai 96] or accelerator mass spectrometry (AMS) [Mul 77, Elm 87, Dit 90, Sut 90, Sch 95]. The determination of cross sections of (n,t) and (n,^{7}Be) reactions constitutes two special cases. Here not the activity of the reaction product is measured but the activity of the emitted particle ^{3}H [Qai 73, Qai 74c, Bir 75, Qai 78, Sud 79, Wöl 84, Wöl 85, Lis 88, Suh 88a, Suh 88b, Wöl 90, Wöl 93] or ^{7}Be [Sch 93].

Let us come back to **Fig. 1.2** and consider a case where also a metastable state of the final nucleus is populated. For the formation of the metastable state one can use similar expressions as outlined above (**eq. 1.4 - 1.7**). For example, if there is only isomeric feeding from one single metastable state, the formation of the metastable (m) and the ground state (g) can be described by

$$\frac{dN_m}{dt} = N\sigma_m\Phi(t) - \lambda_m N_m(t) \qquad \textbf{(1.8)}$$

and

$$\frac{dN_g}{dt} = N\sigma_g\Phi(t) + p\lambda_m N_m(t) - \lambda_g N_g(t) \qquad \textbf{(1.9)}$$

where **p** denotes the probability for the isomeric transition (IT). Assuming again a constant flux $\Phi=\Phi_0$ and initial conditions $N_m=N_g=0$ for t=0, the solutions for **(1.8)** and **(1.9)** will be

$$N_m(t_i) = \frac{N\sigma_m\Phi_0}{\lambda_m}\left(1 - e^{-\lambda_m t_i}\right) \qquad \textbf{(1.10)}$$

and

$$N_g(t_i) = N\Phi\left[\frac{\sigma_g + p\sigma_m}{\lambda_g}\left(1 - e^{-\lambda_g t_i}\right) - \frac{p\sigma_m}{\lambda_g - \lambda_m}\left(e^{-\lambda_m t_i} - e^{-\lambda_g t_i}\right)\right] \qquad \textbf{(1.11)}$$

The activity at the time $\mathbf{t_c}$ will be

$$A_m = \lambda_m N_m(t_i, t_c) = N\sigma_m\Phi_0\left(1 - e^{-\lambda_m t_i}\right)\ e^{-\lambda_m t_c} \qquad \textbf{(1.12)}$$

and

$$A_g = \lambda_g N_g(t_i, t_c) = N\Phi_0 \left[p\sigma_m \frac{\lambda_g}{\lambda_g - \lambda_m} \left(1 - e^{-\lambda_m t_i}\right) e^{-\lambda_m t_c} + \left(\sigma_g - p\sigma_m \frac{\lambda_m}{\lambda_g - \lambda_m} \right) \left(1 - e^{-\lambda_g t_i}\right) e^{-\lambda_g t_c} \right] . \quad \textbf{(1.13)}$$

If the metastable state decays directly via beta emission, i. e. there is no IT (p=0), then **(1.13)** becomes similar to **(1.7)** and **(1.12)**; the ICSR can be determined by two separate cross section measurements for both states, especially when the half-lives of the metastable and ground states are very different. In the case where p≠0, the ICSR can be derived by a straightforward calculation from **(1.12)** and **(1.13)** combined. We obtain

$$\frac{\sigma_m}{\sigma_g} = \left[\frac{\lambda_g \left(1 - e^{-\lambda_m t_i}\right) e^{-\lambda_m t_c}}{\lambda_m \left(1 - e^{-\lambda_g t_i}\right) e^{-\lambda_g t_c}} \left(\frac{A_g}{A_m} - p \frac{\lambda_g}{\lambda_g - \lambda_m} \right) + p \frac{\lambda_m}{\lambda_g - \lambda_m} \right]^{-1} . \quad \textbf{(1.14)}$$

Here the sample mass and the neutron flux do not have to be known. It is more common to give the ratio $\sigma_m / \sigma_m + \sigma_g$

1.3.3 Role of Radiochemistry in Activation Measurements

Radiochemical separations of the reaction products from the irradiated samples are used frequently in nuclear data measurements via the activation method. They are mandatory when

- ◊ low yield reactions are studied [Hus 68, Qai 73, Qai 74a, Qai 74b, Qai 74c],
- ◊ large samples are irradiated (⇒ bad counting geometry),
- ◊ short-lived isotopes have to be separated from strong long-lived matrix activities (⇒ overlapping gamma-rays, high detector dead time) [Fes 94a, Fes 96],
- ◊ thin samples of the reaction products have to be prepared for beta- or X-ray counting (⇒ self-absorption) [Yaf 62, Bos 94, Qai 96, Klo 97].

The criteria for a good radiochemical separation are

- ◊ high decontamination from radioactive impurities
- ◊ high chemical separation yield
- ◊ simplicity, fastness and easy reproduction (mandatory in case of short-lived isotopes) [Her 82].

The radiochemical methods commonly used involve

- ◊ Precipitation and crystallization [Oki 92, Bos 94, Qai 96]
- ◊ Co-precipitation by adsorption [Hay 51, Fes 94a, Fes 94b]
- ◊ Electroplating [Hah 45, Qai 84, Zwe 88, Fes 94a, Fes 94b]
- ◊ Solvent extraction [Fre 59, De 67, Oki 92]
- ◊ Ion exchange (anion- or cation-exchange) [Kra 57, Nel 64, Qai 84, Kor 89, Oki 92, Fes 94a, Fes 94b, Qai 96, Klo 97]
- ◊ HPLC (high performance liquid chromatography) [Qai 79, Sch 82a, Wei 91, Fas 96]
- ◊ Thermochromatography [Fas 94, Neu 94, Den 95]

Some of the techniques used in this work are briefly described below.

- **Co-precipitation by adsorption**

The principle is based on the adsorption of the radionuclide on gelatinous or colloidal precipitates (e. g. $Fe(OH)_3$, $Al(OH)_3$, MnO(OH), AgBr, AgI, As_2S_3, $BaSO_4$ or aluminium silicates) which offer a large surface. Adsorption of metal cations is also possible if the precipitate is negatively charged. After the precipitation the precipitate is dissolved and the radionuclide is separated from the carrier with one of the numerous methods listed above. Co-precipitation is used when no carrier added (n.c.a.) radionuclides have to be separated from the targets. If very low radionuclide concentrations have to be separated from strong matrix solutions (high concentrations of metal ions) and the concentration of the radionuclide is too low to allow precipitation, or when no isotopic carrier can be added (e. g. when very thin samples for X-ray counting have to be prepared), co-precipitation with non-isotopic carrier sometimes offers the only possibility of a quantitative separation.

- **Electroplating**

Metal cations are plated out from an electrolytic solution on a metal cathode if a potential is put between the two electrodes. In principle it is possible to separate two or more cations because of their different standard potentials, or by masking one component by a complexing agent. Nevertheless, the method is normally used to prepare thin samples for beta- or X-ray counting rather than for separating radioactive products from matrix activities.

- **Solvent extraction (liquid-liquid extraction)**

Solvent extraction involves the interchange of ions between an aqueous solution and a liquid organic solvent. Let us consider the reaction

$$M_{aq}^{+n} + n\ HL_{org} \Leftrightarrow ML_{n,org} + n\ H_{org}^{+} \qquad \textbf{(1.15)}$$

in which the reagent **HL**, initially dissolved in an organic phase reacts with a metal ion $\mathbf{M^{+n}}$ in the aqueous solution to form a product $\mathbf{ML_n}$ which is more soluble in the organic

phase than in water. The extraction equilibrium constant for this reaction may be written as (nomenclature used in the solvent extraction process see [Ric 81])

$$K_{eq} = \frac{\left[ML_n\right]_{org}\left[H^+\right]^n_{aq}}{\left[M^{+n}\right]_{aq}\left[HL\right]^n_{org}} \quad . \tag{1.16}$$

The whole process can be divided into three steps:

- ◊ *extraction* - initial transfer step in which the main solute, often together with some of the impurities is transferred from the aqueous solution to the solvent.
- ◊ *scrubbing* - process of selectively removing the coextracted solutes (impurities) from the loaded solvent by treatment with a new immiscible (aqueous) phase.
- ◊ *stripping* - process of recovering the main solute(s) from the solvent or for extracting back into an aqueous phase.

- **Ion exchange**

Ion exchange separation involves the interchange of ions between an aqueous solution and a solid resin. The ion exchange resins are insoluble, porous, resinous structures to which active groups such as $(-SO_3)^-$ or $(COO)^-$ or $(-NR_3)^+$ are attached. These active groups, depending on their own charge, selectively pick up cations (e. g. simple metal ions M^+, M^{++}, ⇛ *cation exchanger*) or anions (e. g. negatively charged metal complexes, ⇛ *anion exchanger*) from aqueous solutions. A typical cation exchange equilibrium reaction can be represented as

$$n\ R\left(SO_3\right)H + M^{n+} \Leftrightarrow n\ H^+ + R\left(SO_3\right)_n M \tag{1.17}$$

where **R** is the designation for the ion exchange resin, **M** is the metal which has to be separated and recovered, and **H** is hydrogen. This equation represents a chemical equilibrium and is amenable to shifting in either direction by a suitable choice of the conditions. The equilibrium constant is given by:

$$K_{eq} = \frac{\left[R(SO_3)_n M\ \right]\left[H^+\right]^n}{\left[R(SO_3)H\ \right]^n\left[M^{n+}\right]} \quad . \tag{1.18}$$

Ion exchange essentially involves a three step operation in columns filled with resin. These are

- ◊ *loading (adsorption)* - transfer of the desired metal ion from the solution to the ion exchange resin.
- ◊ *washing* - physical separation of the depleted solution from the resin.

◊ *elution (desorption)* - transfer of the metal ion from the resin into a fresh aqueous solution.

1.4 Monoenergetic Neutron Sources

Neutron beams with well-defined energies can be provided either by the source itself or neutrons of a particular energy can be selected from a continuum by a TOF measurement over a fixed flight path. In the first case we speak of *monoenergetic* or *quasi-monoenergetic* neutron sources. In the latter case we call them *continuum* or *white neutron* sources. Since this work deals with the activation measurements which yield integrated results over the time of the irradiation, no information can be immediately derived about the effective energy of the neutron as it is possible in combination with TOF measurements. Therefore, pointwise measurements of energy-dependent cross sections require the usage of monoenergetic neutron sources. Some of such sources, mainly accelerator based monoenergetic neutron sources, are given below. For more details, the reader is referred to some review articles [e. g. Oka 80, Oka 87, Cie 83, Böd 87].

1.4.1 Neutron Source Reactions and Experimental Details

Most of the activation cross section measurements to date have employed the reactions $T(p,n)^3He$, $T(d,n)^4He$, $D(d,n)^3He$ and $^7Li(p,n)^7Be$ using electrostatic accelerators (Van de Graaff accelerators) or cyclotrons to produce incident charged particle beams of proper energies. The limitations for their usage are given by their intensity and spectral distribution. To achieve a high specific yield, it is necessary to have a high neutron production cross section and a small energy loss of the projectile in the target. All of these source reactions, when used over a wide energy range, not necessarily produce only monoenergetic neutrons. The primary neutron group is contaminated by secondary neutron groups due to breakup of the projectile or the target nucleus (see **Tab. 1.2**). Other background neutrons are produced by reactions of the incident charged particles with the beam stop and other components of the target construction. In some cases these neutrons can be measured, e. g. with *gas-in / gas-out* measurements in the case of a gas target (see below).

The different energy regions in which the sources can be used are compared in **Fig. 1.3**. The yields for many reactions are given by Drosg [Dro 90]. A difficult region for neutron activation is from 8 to 12 MeV. Here none of the sources behaves as monoenergetic. But with the precise measurement of the cross section of the breakup reaction D(d,np)D by Cabral et al. [Cab 90], the $D(d,n)^3He$ source reaction was made available for adequate measurements in this energy region [e. g. Bir 94b, Bos 94, Mia 94, Man 94, Klo 97,

Tab. 1.2 Thresholds and neutron energy ranges of commonly used monoenergetic neutron sources. For comparison also the less common $^{1}H(t,n)^{3}He$ and $^{2}H(t,n)^{4}He$ reactions are given.

primary reaction	threshold [MeV]	breakup reaction	threshold [MeV]	E_n (max) (no breakup) [MeV]	used neutron energy range [MeV]
$^{7}Li(p,n_0)^{7}Be$ $^{7}Li(p,n_1)^{7}Be^{*}$	1.881 2.372	$^{7}Li(p,n^{3}He)^{4}He$	3.697	0.65	< 5
$^{3}H(p,n)^{3}He$	1.019† 1.148‡	$^{3}H(p,np)^{2}H$ $^{3}H(p,2n)2^{1}H$	8.35 11.34	7.58	0.3 - 8
$^{2}H(d,n)^{3}He$		$^{2}H(d,np)^{2}H$ $^{2}H(d,2n)2^{1}H$	4.45 8.90	7.74	3 - 14
$^{3}H(d,n)^{4}He$		$^{3}H(d,np)^{3}H$ $^{3}H(d,2n)^{3}He$	3.71 4.92	20.46	12.5 - 21
$^{1}H(t,n)^{3}He$	3.05†	$^{1}H(t,np)^{2}H$	24.99	17.6	5 - 25
$^{2}H(t,n)^{4}He$		$^{2}H(t,np)^{3}H$	5.56	23.01	14 - 28

† forward directed ‡ backward directed

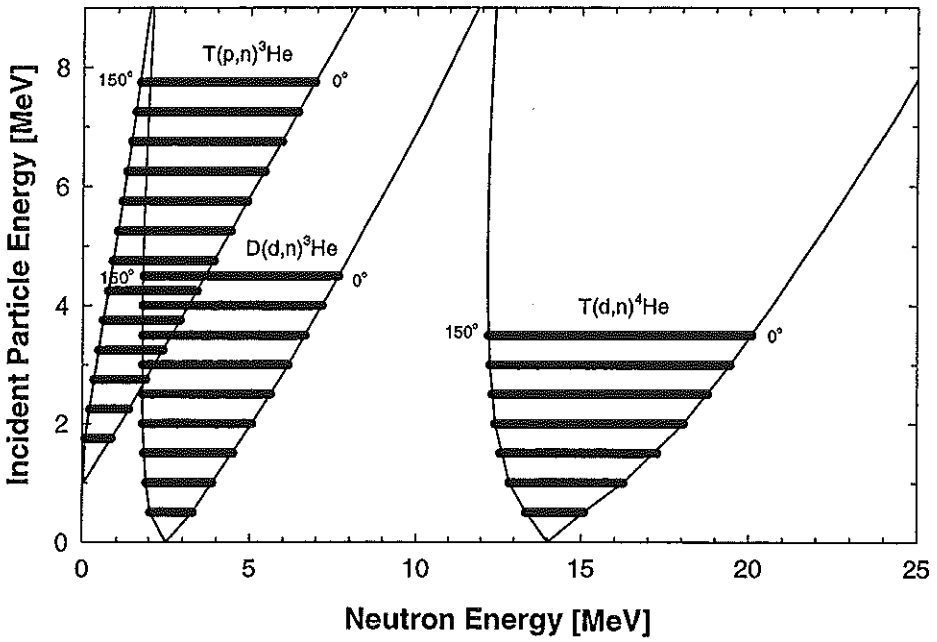

Fig. 1.3 Average neutron energies and angular dependence of the reactions $T(p,n)^{3}He$, $D(d,n)^{3}He$ and $T(d,n)^{4}He$ on bombardments of solid targets (areal density of 2.04 mg / cm^2) with varying incident proton or deuteron energies (taken from [Lis 75]). The reaction $^{7}Li(p,n)^{7}Be$, not shown in the figure, covers the same region as the $T(p,n)^{3}He$ reaction. The sources behave as monoenergetic in the areas of the bold lines.

Man 97]. Recently, the $^{14}N(d,n)^{15}O$, $^{15}N(d,n)^{16}O$ and $^{1}H(^{11}B,n)^{11}C$ reactions were successfully used to produce quasi-monoenergetic neutrons with energies between 7 and 12 MeV [Chi 89, Ike 92, Mat 94].

The spallation neutron source at Los Alamos (LAMPF[1]/WNR[2]/LANSCE[3]) [Lis 90b] provides data over the continous neutron energy range from threshold to 50 MeV [Gri 96, Hai 97a, Hai 97b]. The neutrons are identified with TOF techniques. Quasi-monoenergetic neutron fields used for neutron energies up to 40 MeV are the $^{9}Be(p,n)^{9}B$ reaction [Uwa 88, Uwa 92, Uwa 94] or the $^{7}Li(p,n)^{7}Be$ reaction [Uno 96, Uwa 97]. For these type of neutron fields accelerators are needed which can provide 40 MeV proton beams.

As the last point should be mentioned the kinematically collimated sources, e. g. $^{2}H(t,n)^{4}He$, $^{1}H(t,n)^{3}He$, $^{1}H(^{7}Li,n)^{7}Be$, $^{1}H(^{11}B,n)^{11}C$, $^{1}H(^{13}C,n)^{13}N$ and $^{1}H(^{15}N,n)^{15}O$. These sources emit neutrons only in the forward direction which gives a minimum room background and simplifies shielding [Dro 90]. They might be also usable in the gap region, i. e. at ~10 MeV, but surprisingly they are not commonly used for cross section measurements. Even the outstanding feature of the $^{1}H(t,n)^{3}He$ reaction [Hai 89, Hai 90], the specific yield over most of the energy range (1000 times more than the $T(d,n)^{4}He$ reaction at 14 MeV with a Ti/T target), does not overcome the main disadvantage of the source, i. e. the handling of the radioactive triton beam. Nevertheless, some measurements were done for neutron energies up to 13 MeV [Dra 77, Hai 90, Hai 96].

Different types of targets are commonly used [Dro 90]. Gas targets consist of a small thin-walled cell of stainless steel with a thin entrance window (made of Havar, Ni or Mo; 5 - 10 μm thick) towards the accelerator vacuum. On the other end a solid disk (made of Au, Pt, Ta or W) serves as a beam stop. Because of much lower neutron background tungsten has been proven to be a more advantageous material for the beam stop [Gra 93, Gra 94] than brass and molybdenum, as used earlier. Usually the gas pressure is around 2 bar (2×10^{5} Pa) and beam currents of 4 - 5 μA are used. With special target arrangements, e. g. beam diffusion [Mea 80] or rotating cells [Hai 90], currents up to 20 μA can be used.

Solid hydrogen targets usually consist of deuterium or tritium impregnated titanium or zirconium foils (1 to 1.5 deuterium or tritium atoms per titanium atom). Lithium is used either as metal or fluoride.

Solid targets are more easy to handle (no leakage problems) and have a better geometry than gas targets (point source instead of line source). Their disadvantage is the strongly reduced yield (by about one order of magnitude) and neutron energy width and that the target nuclide is not uniformly distributed over the target area (beamspot position becomes very important). There is also no easy way to produce a dummy target for the simulation of the target background. With gas targets the background can be estimated using gas-out runs, i. e. via irradiations with an empty gas cell.

[1] Los Alamos Meson Physics Facility
[2] Weapons Nuclear Research Facility
[3] Los Alamos Neutron Science Centre

For the determination of the neutron energy spectrum several methods are applied [Csi 87]. The scattering of neutrons on hydrogen is used in the proton recoil method. The recoil spectrum of protons is determined using proportional counters, scintillation or semiconductor detectors. The relationship between proton and neutron energy is given by

$$E_p = E_n \cos^2 \Theta \,. \qquad \textbf{(1.19)}$$

High energy resolution spectra can be obtained in combination with theTOF method (see chapter 3.2.2). Another popular method is the multiple foil activation technique in combination with computer codes such as SAND II [McE 67, Ost 73], CRYSTAL BALL [Kam 74] or RFSP [Fis 72] for the spectrum unfolding. Several metal foils are activated and by measuring the activity of different threshold reactions the spectrum can be unfolded [Qai 84, Wöl 84, Wöl 85, Man 90, Uwa 92, Wöl 93]. The requirements of the method are a good knowledge of the excitation functions and decay characteristics of the reaction products. The programs obtain their solution by introducing an input spectrum and making an iterative refinement of this input spectrum. The problem of this procedure is that the solution depends more or less on the quality of the input spectrum. Sudár solved this problem by developing the code SULSA [Sud 89] which is based on the iterative solution of the generalized least squares method. Here only the individual reaction rates have to be known but no input spectrum is needed.

1.4.2 Neutron Fluence Determination and the Use of Cross Section Standards

The measurement of activation cross sections requires a knowledge of the neutron fluence $\Phi(E)$ according to **(1.4)**. Absolute fluence measurements are possible with the *associated-particle method*. The emitted ^{3}He or ^{4}He particle of the D(d,n)^{3}He, T(p,n)^{3}He or T(d,n)^{4}He neutron source reaction can be counted with high accuracy (~1 %) with a surface barrier detector [Bar 52, Few 68, Lis 69, Pau 71, Fow 80, Win 91]. Nevertheless, the method is difficult to use since the geometry has to be measured with the same accuracy.

Therefore, most nuclear cross section measurements are done relative to a cross section "standard" [Böd 87, Con 92]. The cross section in question is then derived from the ratio of the measured reaction rates in the investigated sample material to the reference material. Besides a good knowledge of the cross section the reference reaction should have

- a low sensitivity to contaminant low energy neutrons (high reaction threshold),
- an excitation function which does not vary too rapidly with the energy (the response of the reference is less sensitive to the correct energy scale),
- a half-life of the reaction product which is long compared to the irradiation time in order to enable integration over a time-dependent neutron flux.

The detection techniques for the reference reaction should fulfil the same accuracy

requirements to which the standard is known. As an example, the accuracy of the very well-known elastic scattering cross section of hydrogen [Ran 92, Hal 92] is somehow affected by the uncertainty of the proton recoil detection efficiency of the employed telescope counter incorporating the hydrogen-containing substance (i. e. polyethylene) and the uncertainty in the arial density of the hydrogen atoms.

The fission reaction ^{238}U(n,f) has also been very reliably evaluated over the whole energy range up to 20 MeV [Kan 92]. The method is based on the prompt detection of fission fragments by means of a low-mass ionization chamber [Win 80, Wag 88a, Wag 88b, Win 91, Man 97]. The accuracy depends on the precise knowledge of the properties of the thin uranium deposit (mass, thickness, areal density, isotopic purity) and the fission fragment detection efficiency (corrections have to be applied for attenuation and total absorption of some fission fragments) [Win 89, Dra 89].

If the fluence value determined by the monitor has to be adjusted to the sample position, the accuracy of the fluence determination will be influenced by a knowledge of the relative positions of sample and monitor. Also the fluence gradient will affect the results.

Several source reactions produce a radioactive product which can be measured via gamma-ray spectrometry and therefore used as a fluence monitor. For example, the ^{7}Li(p,n)^{7}Be reaction has the property that the number of ^{7}Be atoms produced in the ^{7}Li target is equal to the number of the monoenergetic peak neutrons released in the 4π direction [Tak 96].

As a conclusion, the simplest way to monitor the neutron fluence is to use metal monitor foils which are chemically pure and stable and where the induced radioactivity can easily be measured. Generally these foils are used in "sandwich" arrangements (almost same geometry of sample and reference). An even better way is the use of two independent methods (i. e. activation of metal foils and proton recoil telescope, see [Wöl 88, Lis 89a, Lis 89b, Lis 90a, Mol 91]). In any case the influence of possible contaminant neutrons has to be estimated or measured both for the sample and the reference.

In this work the absolute flux determination was done using metal foils of Al, Fe and Nb in sandwich geometry and the relative fluence during the irradiations was continuously monitored with a Bonner sphere [God 95] or a long counter [Ler 70]. The cross sections of the respective reference reactions are shown in **Fig. 1.4**. They have been extracted from the "International Reactor Dosimetry File" (IRDF) [Kor 93], an evaluated data file which gives recommended values for the cross sections of nuclear reactions used in neutron dosimetry. Generally, evaluations are based on model calculations, cross section systematics (see **section 2.2**) and experimental data, including a detailed error analysis with error correlations. Many different evaluations exist for all types of nuclear reactions with a more or less good accuracy (e. g. ENDF/B-VI[4], JENDL-3.2[5], JEF-2.2[6],...).

[4] Evaluated Nuclear Data File, U.S.A.
[5] Japanese Evaluated Nuclear Data Library, Japan.
[6] Joint Europeen File, Europe.

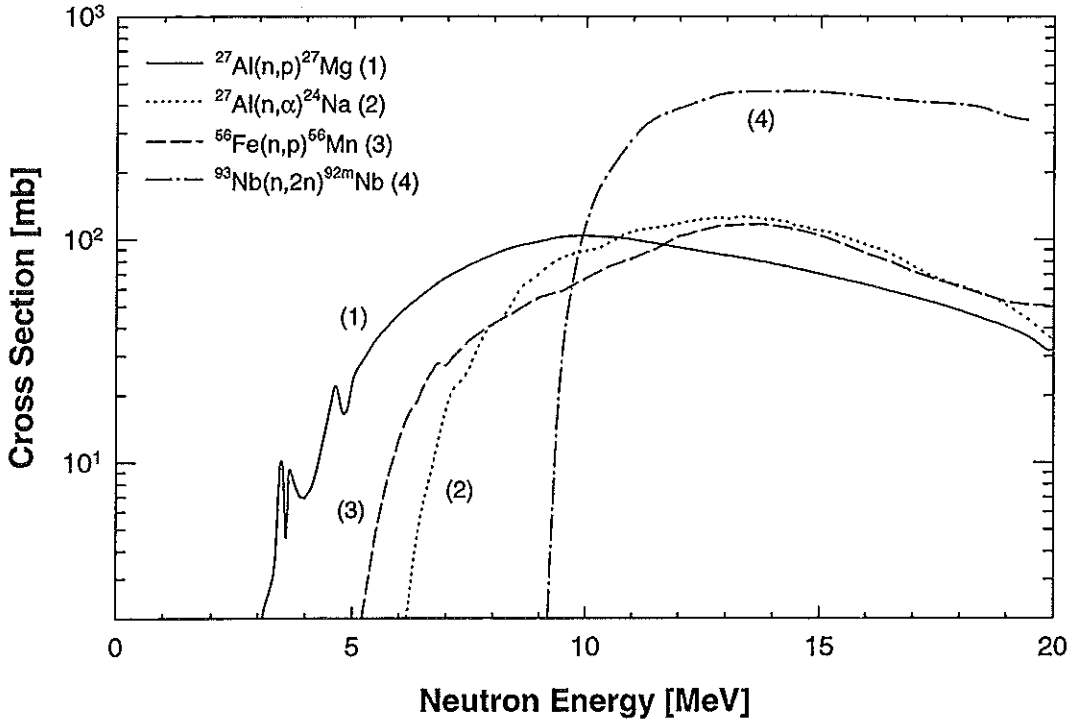

Fig. 1.4 Evaluated cross sections for the reference reactions used in this work. The data are taken from IRDF-90, Version 2 [Koc 93].

1.5 Status of Available Neutron Activation Cross Section Data for Cr, Fe and Ni

The elements Cr, Fe and Ni consist of several stable isotopes (see **Tab. 1.3**). They are important constituents of structural materials for fission or fusion reactors. Extensive studies of activation cross sections at neutron energies around 14 MeV have been done on (n,p), (n,α) and (n,2n) reactions. At neutron energies below and above 14 MeV, mainly reactions on the high abundant isotopes ^{52}Cr, ^{56}Fe and ^{58,60}Ni have been investigated. Complete excitation functions from threshold to 20 MeV with good accuracy (< 5%) have been measured for the ^{56}Fe(n,p)^{56}Mn and ^{58}Ni(n,p)^{58}Co reactions which are now frequently used as reference cross sections in activation cross section measurements.

Activation cross sections on Cr have been measured for ^{50}Cr(n,np)^{49}V, ^{52}Cr(n,p)^{52}V, ^{52}Cr(n,2n)^{51}Cr, ^{53}Cr(n,p)^{53}V, ^{53}Cr(n,np)^{52}V, ^{54}Cr(n,p)^{54}V, ^{54}Cr(n,np)^{53}V and ^{54}Cr(n,α)^{51}Ti reactions around 14 MeV. The ^{52}Cr(n,2n)^{51}Cr reaction has been investigated from threshold to 20 MeV. The data below 16 MeV agree within 15 % whereas beyond that energy the three available data sets bifurcate into two groups (see **Fig. 1.5**): the data of Liskien et al. [Lis 89b] rise up to a value of 650 mb at 20 MeV whereas the two other data sets [Bor 68, Gho 87] give a lower value (σ_{max} ~ 500 mb at 18 MeV). The different

evaluations for the $^{52}Cr(n,p)^{52}V$ reaction at 14 MeV agree fairly well (within about 10 %). In addition, Smith and Meadows [Smi 80] reported one precise measurement from threshold to 9 MeV. Two other reported data sets between 14 and 18 MeV are contradictory: one is ~ 35% higher than the average value at 14 MeV [Ker 59] and the other 20 % lower [Gho 87] (see **Fig. 1.6**). The cross sections of reactions on the less abundant Cr-isotopes ^{50}Cr, ^{53}Cr and ^{54}Cr at 14 MeV scatter within 30 and 100 % (for references see **chapter 5**). Here only for the $^{53}Cr(n,p)^{53}V$ reaction one data set has been measured from threshold to 9 MeV (relative to the $^{52}Cr(n,p)^{52}V$ reaction) [Smi 81]. As an example of huge existing discrepancies in different evaluations the excitation function of the $^{53}Cr(n,p)^{53}V$ reaction is plotted in **Fig. 1.7**.

The calculated Q-values and reaction thresholds of all reactions on Cr, Fe and Ni which will be of relevance for this work are listed in **Tab. 1.4**. The mass numbers were taken from the mass evaluation of Audi and Wapstra [Aud 95].

Tab. 1.3 Natural abundances of the stable isotopes of Cr, Fe and Ni.

Element	Isotope and natural abundance (%)
Cr	^{50}Cr (4.35), ^{52}Cr (83.79), ^{53}Cr (9.5), ^{54}Cr (2.36)
Fe	^{54}Fe (5.8), ^{56}Fe (91.7), ^{57}Fe (2.2), ^{58}Fe (0.3)
Ni	^{58}Ni (68.27), ^{60}Ni (26.10), ^{61}Ni (1.13), ^{62}Ni (3.59), ^{64}Ni (0.91)

Tab. 1.4 Q-values and reacion thresholds of some neutron induced reactions on Cr, Fe and Ni.

Nuclear reaction	Q-value [MeV]	Threshold [MeV]	Nuclear reaction	Q-value [MeV]	Threshold [MeV]
$^{50}Cr(n,d)^{49}V$	-7.3627	7.5114	$^{54}Cr(n,d)^{53}V$	-10.1482	10.3380
$^{50}Cr(n,pn)^{49}V$	-9.5873	9.7809	$^{54}Cr(n,pn)^{53}V$	-12.3728	12.6042
$^{52}Cr(n,p)^{52}V$	-3.1931	3.2551	$^{54}Cr(n,\alpha)^{51}Ti$	-1.5551	1.5842
$^{52}Cr(n,2n)^{51}Cr$	-12.0395	12.2733	$^{54}Fe(n,2n)^{53}Fe$	-13.3786	13.6287
$^{53}Cr(n,p)^{53}V$	-2.6537	2.7043	$^{54}Fe(n,t)^{52}Mn$	-12.4258	12.6582
$^{53}Cr(n,d)^{52}V$	-8.9077	9.0774	$^{58}Ni(n,\alpha)^{55}Fe$	2.8984	0
$^{53}Cr(n,pn)^{52}V$	-11.1323	11.3444	$^{58}Ni(n,\alpha p)^{54}Mn$	-6.3144	6.4243
$^{54}Cr(n,p)^{54}V$	-6.2593	6.3763	$^{62}Ni(n,\alpha)^{59}Fe$	-0.4379	0.4450

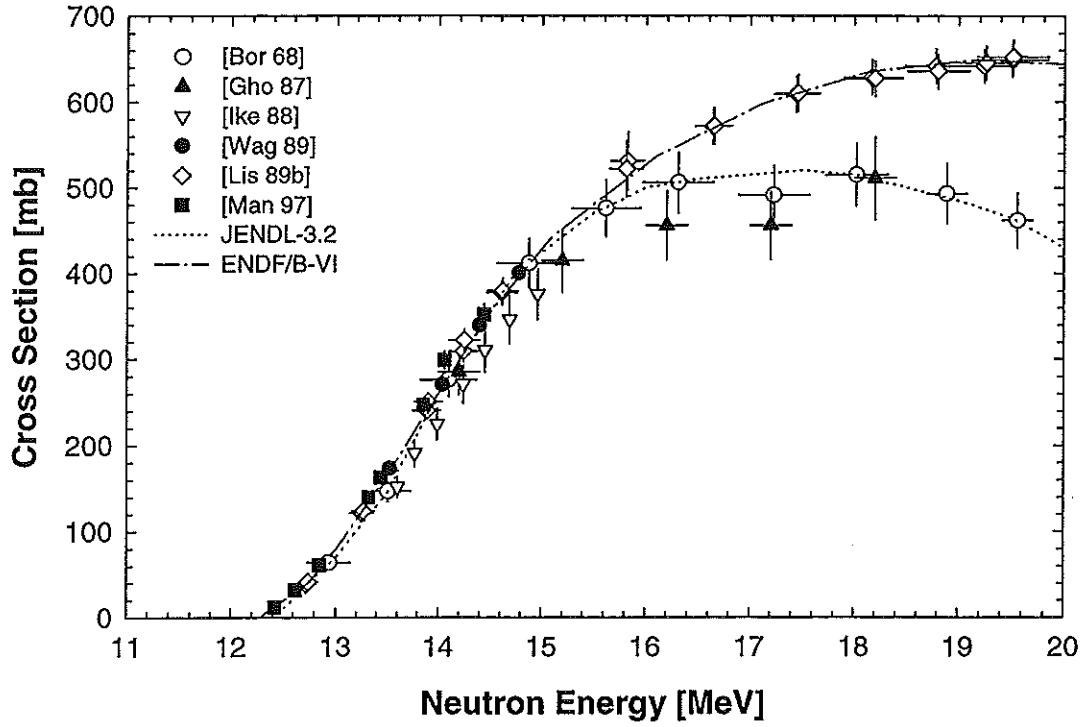

Fig. 1.5 Measured and evaluated cross sections for the $^{52}Cr(n,2n)^{51}Cr$ reaction. Some more data of single measurements around 14 MeV are not given [Wen 62, Mas 72, Qai 72, Ara 73, Sai 77, Mol 83, Maj 84, Bah 84, Rib 85].

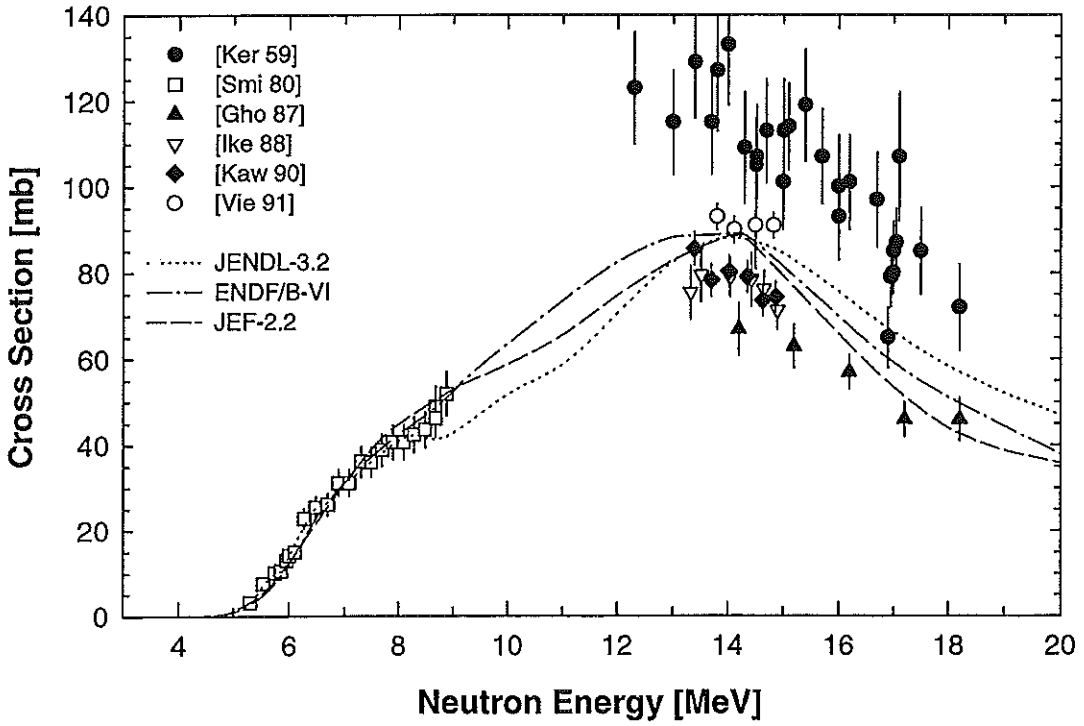

Fig. 1.6 Measured and evaluated cross sections for the $^{52}Cr(n,p)^{52}V$ reaction. Some more data of single measurements around 14 MeV are not given [All 61, Mit 66, Hus 67, Pra 71, Hol 74, Mol 77, Bah 85].

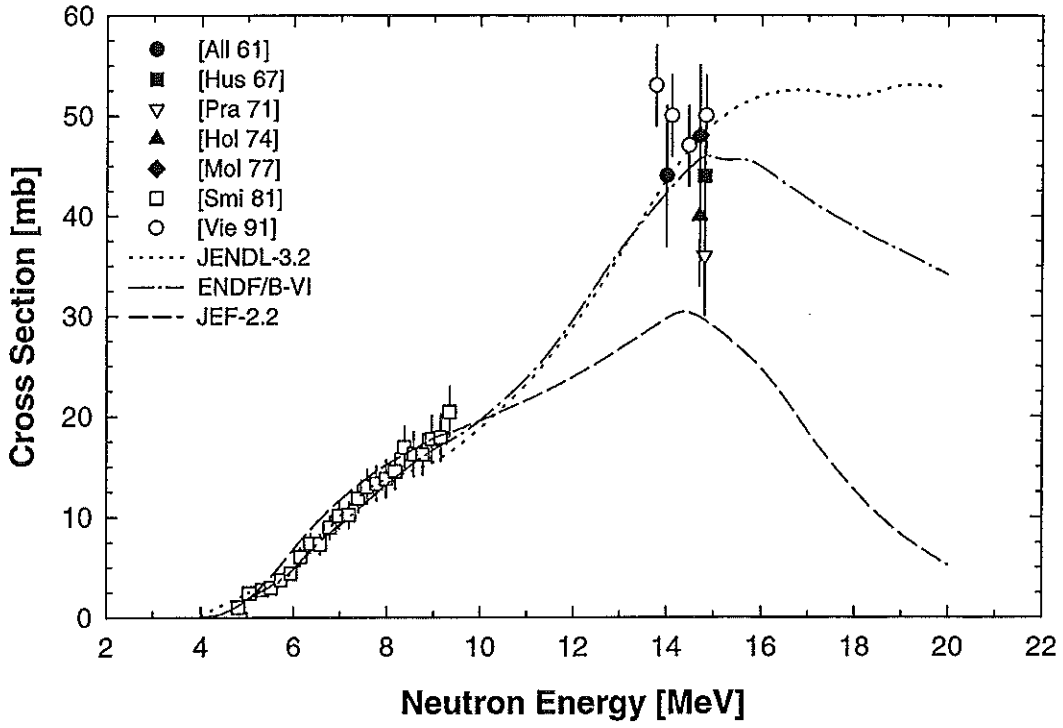

Fig. 1.7 Measured and evaluated cross sections for the $^{53}Cr(n,p)^{53}V$ reaction.

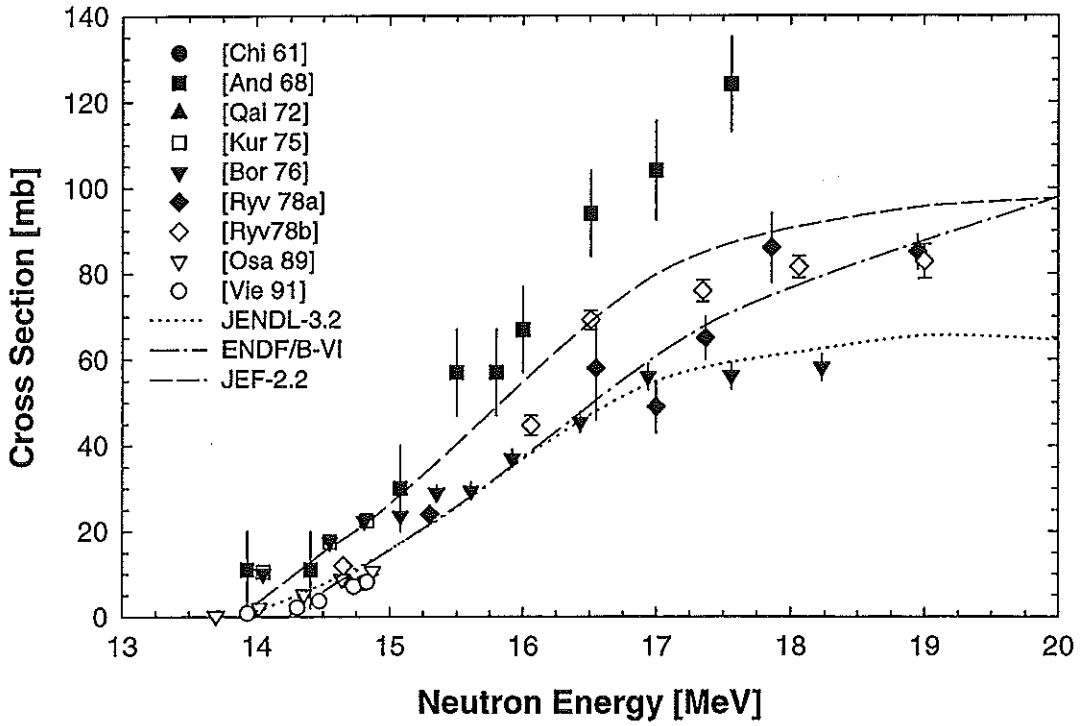

Fig. 1.8 Measured and evaluated cross sections for the $^{54}Fe(n,2n)^{53m+g}Fe$ process.

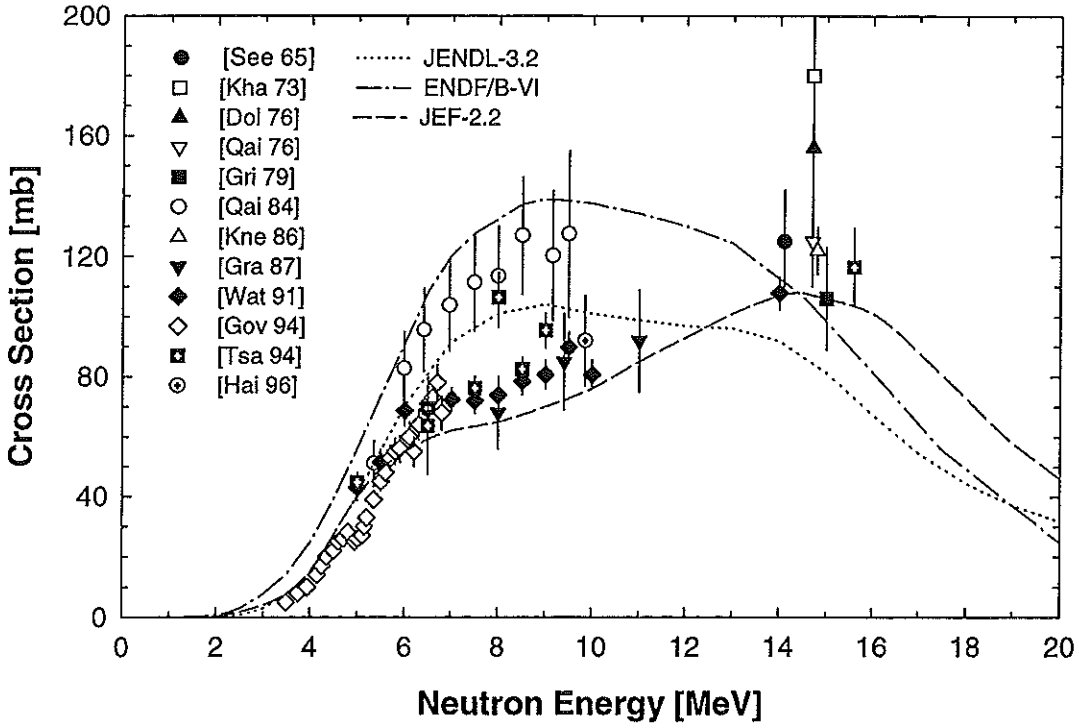

Fig. 1.9 Measured and evaluated cross sections for the $^{58}Ni(n,\alpha)^{55}Fe$ ([Qai 77], [Qai 84], JENDL-3.2, ENDF/B-VI and JEF-2.2) and $^{58}Ni(n,x\alpha)$ reactions (all others).

Complete excitation functions with good accuracy are known for the $^{54}Fe(n,p)^{54}Mn$, $^{54}Fe(n,\alpha)^{51}Cr$ and $^{56}Fe(n,p)^{56}Mn$ reactions. The $^{54}Fe(n,2n)^{53m+g}Fe$ process has been investigated by several groups up to 19 MeV. The cross sections determined agree fairly well in the threshold region whereas at higher energies the values differ by a factor of two (see **Fig. 1.8**). Some data at 14 MeV have been measured for the $^{57}Fe(n,p)^{57}Mn$ and $^{58}Fe(n,p)^{58}Mn$ reactions, however, with large scatters (factor 2 to 3) in the cross section values (see [McL 88] and references therein). For the $^{56}Fe(n,2n)^{55}Fe$ reaction a few data points have been determined between 12 and 19 MeV [Wen 62, Qai 77, Koz 78, Cor 78, Fre 80].

Excitation functions for the reactions $^{58}Ni(n,p)^{58}Co$, $^{58}Ni(n,np)^{57}Co$, $^{58}Ni(n,2n)^{57}Ni$ and $^{60}Ni(n,p)^{60}Co$ are fairly well known (see [McL 88] and references therein). **Fig. 1.9** shows the situation for the $^{58}Ni(n,x\alpha)$ process. Most of the data were determined by measuring the total helium emission. Only the data of Qaim et al. [Qai 77, Qai 84] were determined by the activation method, that means they represent the cross sections for the $^{58}Ni(n,\alpha)^{55}Fe$ reaction. The 14 MeV data show a scatter of about 30 %; below 10 MeV most of the data sets are quite consistent, except those of Qaim et al. [Qai 84] which are about 20 to 40 % higher. Some work on the Ni(n,xα) process was done with natural nickel as target (for example [Pau 81, Bab 94a, Bab 94b]). Wattecamps [Wat 91] measured the ratio $^{58}Ni(n,x\alpha)$ to $^{60}Ni(n,x\alpha)$ so that these data can be compared with the ones with enriched targets ^{58}Ni and ^{60}Ni. All other reactions have been only poorly investigated.

In summary, for the three elements under consideration, a few reactions have been investigated in detail whereas for several others either there are gaps or only scanty information is available. Furthermore, in a few cases of key importance, considerable discrepancies exist, so that a new attention is necessary.

2. Aim and Scope of this Work

As mentioned in the Introduction, the elements chromium, iron and nickel are all important constituents of structural materials for fission or fusion reactors. The main aim of this work was to study the excitation functions of (n,p), (n,np), (n,α), (n,αp), (n,2n) and (n,t) reactions which lead to radioactive products and are therefore measurable via the activation method. Special emphasis was on those energy regions where no data existed.

For the measurement of short-lived activities involved in this work, a special pneumatic transport system should be developed to transport the irradiated samples from the neutron source area to the counting area. This system would allow the first activity measurements ~10 s after the end of irradiation.

The reactions ^{52}Cr(n,p)^{52}V, ^{53}Cr(n,p)^{53}V and ^{54}Cr(n,p)^{54}V all lead to short-lived radioactive products. The reaction on the main isotope ^{52}Cr is the only one which is fairly well investigated. The high abundance and the substantial cross section (~ 100 mb between 14 and 15 MeV) make this reaction of practical interest. Nevertheless, no data are available between 10 and 14 MeV (a region rather difficult to investigate) and beyond 15 MeV there is considerable scatter in the two existing data sets. The reactions on the two less abundant isotopes ^{53}Cr and ^{54}Cr have been poorly characterized. It was therefore thought worthwhile to investigate those reactions. Since very few (n,np) reactions have been studied in any detail, the ^{50}Cr(n,np)^{49}V reaction is of considerable interest. It poses a great challenge since the product ^{49}V emits only soft X-rays with energies of 4 and 4.5 keV which cannot be studied by routine gamma-ray spectrometry. An additional problem is the non-availability of standard extended sources for those soft X-rays. The use of a radiochemical separation and preparation of a thin sample for X-ray counting appears very promising. In addition a standard source of ^{49}V for the calibration of the Si(Li) detector also needs to be prepared. From a fundamental point of view, the measured reaction cross sections on the different stable isotopes of chromium should shed some light on the effect of varying neutron and proton binding energy on the reaction cross section.

The reactions ^{54}Fe(n,2n)^{53m,g}Fe and ^{54}Fe(n,t)^{52m,g}Mn are of appreciable fundamental interest. Both of them lead to high spin isomeric states. Their formation was recently investigated in charged particle induced reactions like (^{3}He,2n) and (^{3}He,t+dn+p2n), respectively. A comparison of the isomeric cross section ratios in neutron and charged particle induced reactions should lead to some information about the effect of mass and charge of the projectile on the population of the isomeric state.

The ^{nat}Ni(n,xα) process is of practical importance for the estimation of helium production in structural materials. Although extensive measurements have been performed recently to determine the total helium production in ^{nat}Ni and ^{58,60}Ni below 15 MeV, the individual contributions of the reactions like ^{58}Ni(n,α)^{55}Fe, ^{62}Ni(n,α)^{59}Fe or ^{58}Ni(n,αp)^{54}Mn to the total production cross section have hitherto not been investigated

beyond 15 MeV. These individual reaction cross sections are important for the improvement of the calculation of excitation functions with nuclear model codes. The reasons for this lack of experimental data are the low abundance of ^{62}Ni and the fact that the reaction product ^{55}Fe decays only via soft X-ray emission. In this work the ^{58}Ni(n,α)^{55}Fe reaction should be investigated for the first time between 13 and 20 MeV with the activation method after a radiochemical separation and thin sample preparation by electrolysis. The reaction ^{62}Ni(n,α)^{59}Fe should also be investigated for the first time beyond 14 MeV.

For most of the experimentally determined excitation functions nuclear model calculations using the code STAPRE-H should be done in order to test the quality of the underlying models and to help develop input parameters for reactions on adjacent isotopes which are difficult to measure or which are not measurable at all.

3. Experimental Methods

3.1 Irradiations

Three series of irradiations (in the following called *Jülich*, *Geel 1* and *Geel 2*) were carried out using different experimental facilities with different neutron sources. In the neutron energy range of 9.3 to 12.3 MeV irradiations were performed at the variable energy Compact Cyclotron CV 28 at the Forschungszentrum Jülich GmbH using the $^{2}H(d,n)^{3}He$ reaction (Q-value = 3.269 MeV) on a deuterium gas target. In the energy range from 13.3 to 21.0 MeV irradiations were conducted at the 7 MV Van de Graaff accelerator at the CEC-JRC, IRMM at Geel using the $^{3}H(d,n)^{4}He$ reaction (Q-value = 17.59 MeV) on a solid-state Ti/T target. Here two different irradiation geometries were used. One allowed the irradiation of several samples simultaneously under several angles (*Geel 1*), useful for long irradiations; the other used a pneumatic sample transport system (*Geel 2*), especially designed for measurements on short-lived isotopes. The details are given below.

3.1.1 Setup -*Jülich*-

A sketch of the irradiation geometry is shown in **Fig. 3.1**. A more detailed description of the gas target is given by Qaim et al. [Qai 84]. The collimated deuteron beam from the cyclotron enters the deuterium gas cell (3.7 cm long, 4.0 cm in diameter, 1.8 x 10^5 Pa pressure of deuterium gas) via the 5.3 μm niobium window, loses some energy in the window and the gas and is stopped in the tungsten "beam stop" which is cooled by a jet of air. The samples irradiated in the 0° direction relative to the incident beam were placed at a distance of 1 cm from the back of the beam stop. The target is insulated against the beam tube and the integrated charge is recorded for each individual irradiation. The deuteron energies were measured by a time-of-flight technique [Kor 94].

For each chosen deuteron energy one irradiation was done with a filled cell (gas-in) and one with an empty cell (gas-out), both of them in an identical geometry. The gas-out irradiations are needed to allow a correction of the corresponding background neutrons stemming from interactions of the deuterons with structural materials (entrance window, beam stop, cell wall, ...). At the highest incident deuteron energy of 9.7 MeV the contribution of these background neutrons to the total activation was 5 to 10 % for the investigated reactions, depending on the reaction threshold involved.

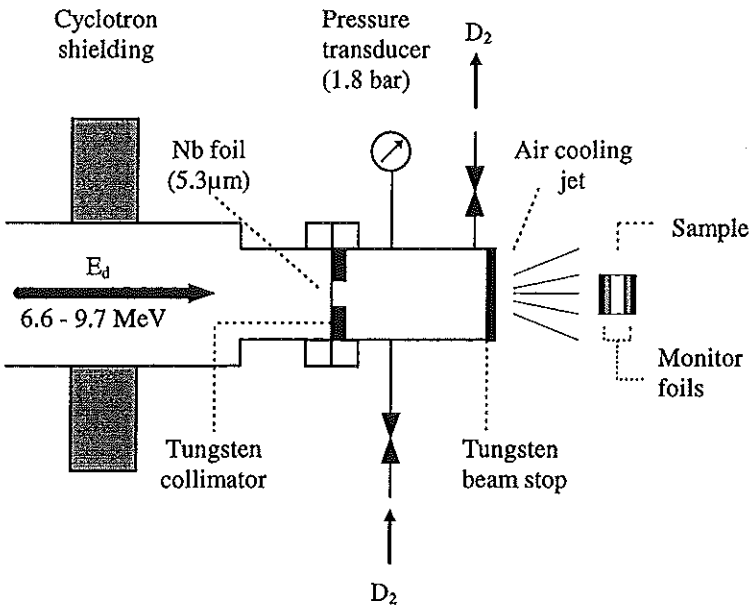

Fig. 3.1 Sketch of the D_2 gas target at the compact cyclotron in Jülich for irradiations with quasi-monoenergetic neutrons produced via the $^2H(d,n)^3He$ reaction.

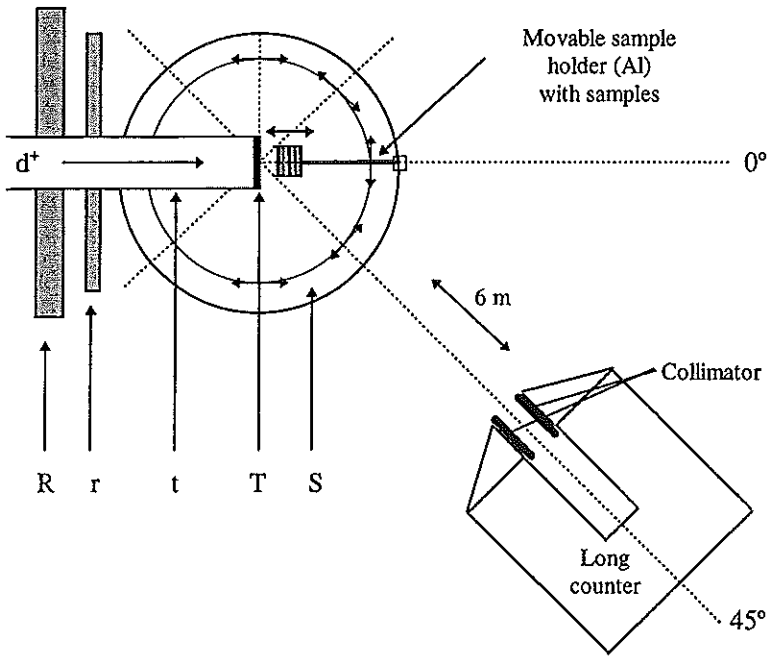

Fig. 3.2 Sketch of the *Geel 1* setup at the Van de Graaff accelerator. Irradiations can be carried out simultaneously under several angles. **R** → Target support structure (Cu and SS, r(in) = 10 cm, r(out) = 25 cm, l = 4 cm), **r** → target tube ring (Al and Cu, r(in) = 5 cm, r(out) = 10 cm, l = 3 cm), t → target tube (Al, r(in) = 4 cm, r(out) = 4.2 cm, l = 15 cm), **T** → Ti/T target (2.042 mg/cm^2 , 0.4 mm Ag backing), **S** → sample support ring (Al, 18 cm diameter, 300 g total weight, 1 - 3 cm distance sample/target).

3.1.2 Setup -*Geel 1*-

This irradiation facility (**Fig. 3.2**) uses the beamline L3 at the 7 MV Van de Graaff accelerator in Geel. The deuteron beam impinges on a solid Ti/T target (2.042 mg/cm^2 thickness, backed by a 0.4 mm silver foil) where the neutrons are generated. The energy scale of this accelerator is calibrated via a nuclear magnetic resonance system relative to well-known reaction thresholds and resonances with an accuracy of ± 5 keV. The target tube is wobbled and air cooled. The samples were fixed in an aluminium sample holder ring of 18 cm diameter, as described by Pavlik et al. [Pav 82]. This sample holder ring was then adjusted with its centre above the nominal source position. The whole target assembly was designed for the purpose of cross section measurements to keep the amount of structural material around the target small and as light as possible and to allow measurements under different angles with respect to the incident d^+ beam direction. Either only one or several samples under different angles were mounted. During all irradiations, the source intensity was continuously monitored by counting the neutrons in a long counter using the Multi-Channel-Scaling (MCS) method. The beam current was recorded in a charge integrator.

3.1.3 Setup -*Geel 2*-

A pneumatic sample transport system ("rabbit system") was especially designed for activation measurements of activities with short half-lives. A sketch of the target assembly is shown in **Fig. 3.3**. The same Ti/T target is used as for the *Geel 1* setup (same neutron field). The samples are placed in a small container ("rabbit"), shown in **Fig. 3.4**, which is pushed with compressed air through a plastic tube (20 m long, 4 cm in diameter) to the target and sucked back with a commercial vacuum cleaner. The front part of the tube is made of transparent lucite to allow a check of the positioning of the rabbit during the irradiations from the counting room (hot lab) with a video camera. The pushed rabbit is stopped at 1 cm distance to the target through two steel wires (see **Fig. 3.5**). Since the samples are irradiated very close to the target, a careful check of the beam position is mandatory. This was done by irradiating four aluminium foils which were glued on the front side of the lucite tube, one on the top, one on the bottom, one on the left side and one on the right side. The measured activity of all the four foils agreed within 3 %, the order of the uncertainty of the count rates, implying that the beam was well centered. A HPGe detector is placed outside the target hall in the counting room behind a thick concrete wall. The time for retrieving, unpacking and placing the sample on the detector was on the average 12 to 15 seconds. A Bonner sphere was placed at 2.5 m distance and at 45° to the direction of the deuteron beam. It was operated in MCS mode and served as a relative fluence monitor for each irradiation (same as Long Counter in *Geel 1*).

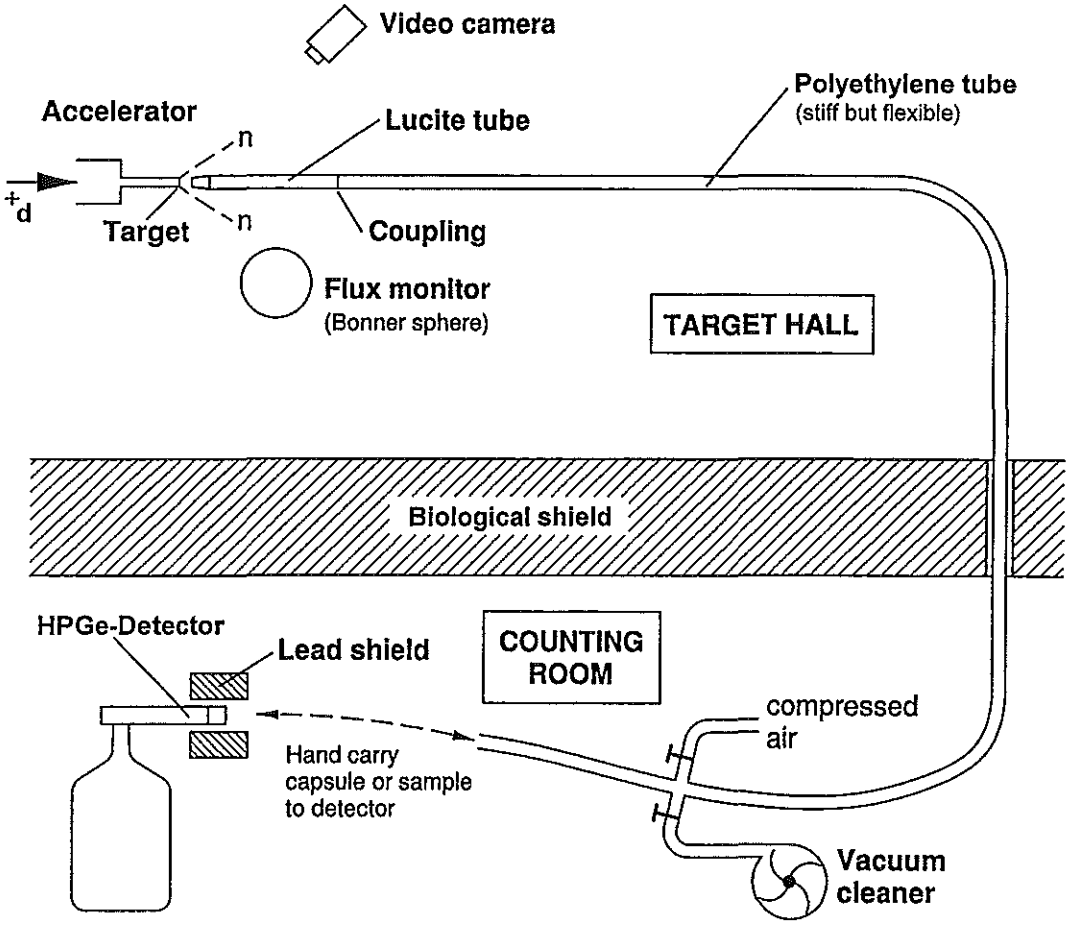

Fig. 3.3 Sketch of the pneumatic sample transport system at beamline R3 of the 7 MV Van de Graaff accelerator (*Geel 2*).

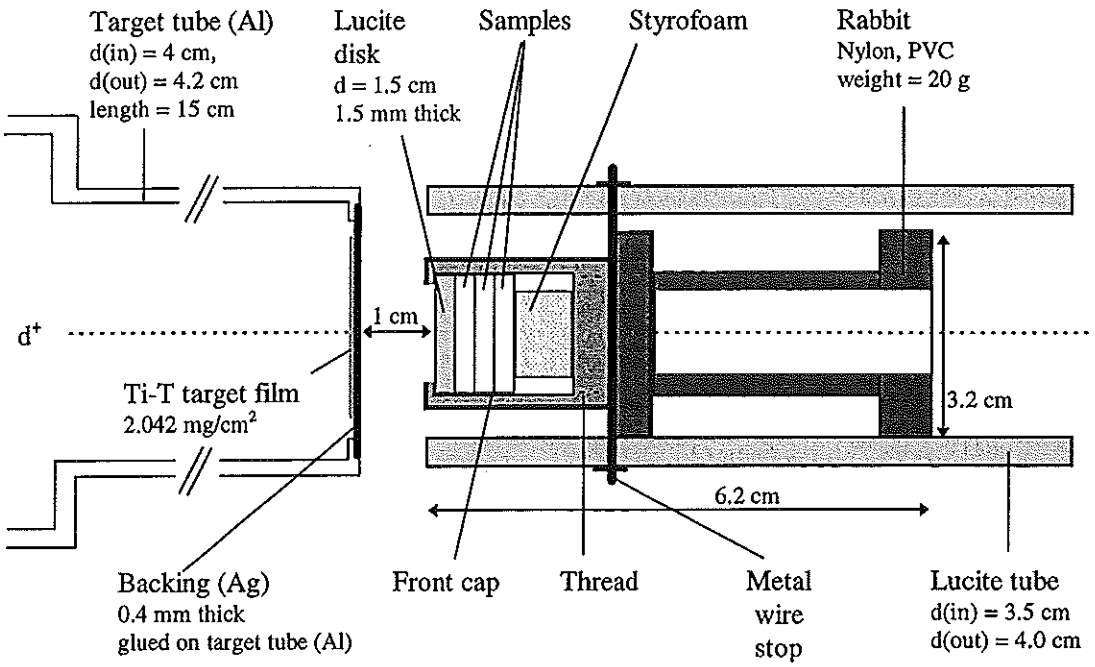

Fig. 3.4 Sample holder and "rabbit" in front of the target at the *Geel 2* setup (not on scale). The front cap can be unscrewed to load the rabbit with the samples.

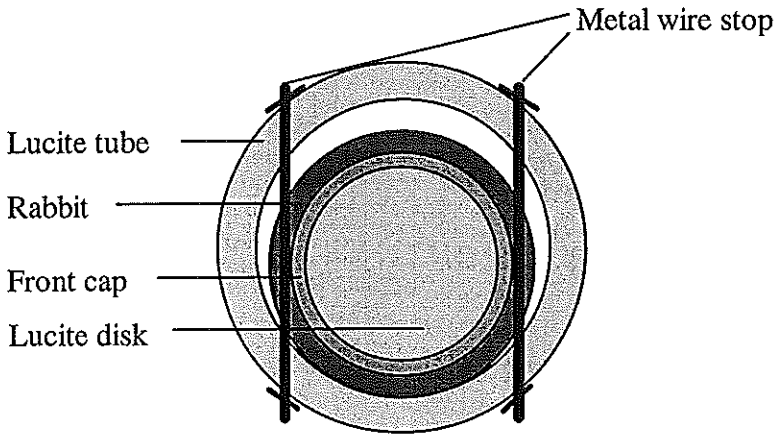

Fig. 3.5 Front view of the rabbit as seen from the target (not on scale).

3.1.4 Samples

Several types of sample materials of chromium, iron and nickel were used. The samples were prepared by using different methods (e. g. rolling, punching, pressing, laser cutting). The chromium samples were metallic disk-shaped foils, 13 mm in diameter and 1 mm thick. Due to the mechanical brittleness of chromium, they were fabricated with a laser cutting technique. For the measurements at Geel also samples of enriched chromium oxide ($^{52}Cr_2O_3$, $^{53}Cr_2O_3$ and $^{54}Cr_2O_3$), natural iron, enriched iron oxide ($^{54}Fe_2O_3$) and natural nickel were irradiated. The enriched isotopes were supplied by Chemotrade[7] or were borrowed from JAERI[8]-Tokai-mura (originally supplied by Oak Ridge[9]). A spectrographic analysis has stated some impurities only in ppm amounts. All powders were pressed into stable pellets. Only the $^{52}Cr_2O_3$ and some $^{54}Fe_2O_3$ samples were not pressed but just wrapped in a small cartridge paper (10 x 10 mm). As reference samples, thin metallic foils of aluminium, iron or niobium were used. They were fastend in front and at the back of the above mentioned materials (sandwich geometry). For example, a stack of a chromium foil and reference foils of aluminium and iron was made in the sequence Al-Fe-Cr-Fe-Al. **Tab. 3.1** gives an overview of all the samples used and their characteristics.

3.1.5 Summary of Irradiations Performed

In **Tab. 3.2** all the irradiations performed using different facilities are listed. Some features of the individual irradiations are given below.

For the irradiations at *Jülich* four different deuteron energies between 6.7 and 9.7 MeV were chosen, leading to corresponding neutron energies between 9.3 and 12.3 MeV. The deuteron beam currents were ~ 4 μA (limited by the mechanical stability of the thin niobium entrance window of the gas cell). Only natural chromium foils sandwiched between aluminium and iron foils were irradiated. In total 24 irradiations, each lasting 10 min, were done (three gas-in and three gas-out for each deuteron energy).

At *Geel I* the same chromium sample stacks as used in *Jülich* were irradiated with 7 different neutron energies between 13.7 and 21.1 MeV (deuteron energies between 1 and 5 MeV, sample at angles of 0°, 60° and 110°). The deuteron beam current was between 5 and 20 μA. In total 21 irradiations were done. Similar irradiations were performed with natural iron samples. But here no reference samples were used (reaction $^{56}Fe(n,p)^{56}Mn$ as internal standard) and only two irradiation angles were chosen (0° and 60°). 25 irradiations at 9 different energy points in the neutron energy range from 15.0 to 21.1 MeV were done. In addition, 15 irradiations were carried out with a stack of 7 iron pellets at 0°: 10 at 3 different neutron energies between 18.8 and 20.9 MeV, each lasting for 5 min during the

[7] CHEMOTRADE, Chemiehandelsgesellschaft mbH, 40239 Düsseldorf, Germany
[8] Japanese Atomic Energy Research Institute, Tokai-mura, Japan
[9] Oak Ridge National Laboratory, Oak Ridge, Tennessee 37830, U.S.A.

investigation of the isomeric pair ^{53m,g}Fe, and 5 longer runs (8 to 10 h) for the determination of the (n,t) reaction on ^{54}Fe (five energy points between 16 and 20.4 MeV). In a very long irradiation of ~100 hours a total of 9 sample stacks were irradiated under 0°, 30°, 60°, 105°, 130°, 230°, 255°, 300° and 330°, with neutrons between 13.0 and 19.7 MeV, depending on the irradiation angle. The stacks were made of natural chromium foils and natural nickel pellets with niobium reference foils in between. The stacks at 130° and 230° consisted only of nickel pellets sandwiched between niobium.

Geel 2 was used mainly for irradiations of the enriched isotopes. Using five different deuteron energies, neutrons between 16.0 and 20.2 MeV were generated. Samples of ^{nat}Cr, $^{52}Cr_2O_3$, $^{53}Cr_2O_3$, $^{54}Cr_2O_3$ and $^{54}Fe_2O_3$, each sandwiched between aluminium, were irradiated for 3 to 10 min, each sample 2 to 4 times at each energy point. The latter ones were also used in 3 longer irradiations (each 1 h) for the investigation of the population of the isomeric state in the reaction ^{54}Fe(n,t)^{52m}Mn. Additionally, some irradiations were carried out without aluminium. Here only the ICSR of the ^{54}Fe(n,2n)^{53m,g}Fe reaction was determined, and no individual cross sections, were measured.

Tab. 3.1 Size and composition of sample materials

Material	Type	Isotopic composition [%]	Dimension [mm]	Weight [mg]
Al	foil	^{27}Al (100)	13/14 Ø x 0.1/0.25	40/100
^{nat}Cr	foil	^{50}Cr (4.35), ^{52}Cr (83.79), ^{53}Cr (9.50), ^{54}Cr (2.36)	13 Ø x 1.0	1000
$^{52}Cr_2O_3$	sealed powder	^{50}Cr (0.01), ^{52}Cr (99.90), ^{53}Cr (0.09), ^{54}Cr (0.00)	10 x 10 x 0.15	50
$^{53}Cr_2O_3$	pressed pellet	^{50}Cr (0.03), ^{52}Cr (2.65), ^{53}Cr (97.2), ^{54}Cr (0.12)	11 x 0.2	50
$^{54}Cr_2O_3$	pressed pellet	^{50}Cr (0.13), ^{52}Cr (4.06), ^{53}Cr (2.01), ^{54}Cr (93.8)	11 Ø x 0.2	50
^{nat}Fe	foil	^{54}Fe (5.8), ^{56}Fe (91.7), ^{57}Fe (2.2), ^{58}Fe (0.3)	13 Ø x 0.25	250
^{nat}Fe	pressed pellet	^{54}Fe (5.8), ^{56}Fe (91.7), ^{57}Fe (2.2), ^{58}Fe (0.3)	14 Ø x 2.0	1500
$^{54}Fe_2O_3$	pressed pellet	^{54}Fe (97.6), ^{56}Fe (2.35), ^{57}Fe (0.04), ^{58}Fe (0.01)	10 Ø x 0.2	100
$^{54}Fe_2O_3$	sealed powder	^{54}Fe (97.2), ^{56}Fe (2.75), ^{57}Fe (0.05), ^{58}Fe (0.01)	10 x 10 x 0.15	45
^{nat}Ni	pressed pellet	^{58}Ni (68.27), ^{60}Ni (26.10), ^{61}Ni (1.13), ^{62}Ni (3.59), ^{64}Ni (0.91)	14 Ø x 5.0	5000
Nb	foil	^{93}Nb (100)	14 Ø x 0.20	250

Tab. 3.2 Irradiations performed for the investigated reactions.

Setup	Sample stack	Sample position [deg]	Reactions investigated	Neutron energy range [MeV]	Number of irradiations	Energy points	Irradiation time [min]
Jülich	Al-Fe-^{nat}Cr-Al-Fe	0	^{52}Cr(n,p)^{52}V, ^{53}Cr(n,p)^{53}V	9.3 - 12.3	24	4	10
Geel 1	Al-Fe-^{nat}Cr-Fe-Al	0, 60, 110	^{52}Cr(n,p)^{52}V, ^{53}Cr(n,p)^{53}V	13.7 - 21.1	21	7	10
	Al-^{nat}Fe-Al	0, 60	^{54}Fe(n,2n)$^{53m+g}$Fe	15.0 - 21.1	25	9	20
	7 x ^{nat}Fe	0	^{54}Fe(n,2n)^{53m,g}Fe (ICSR)	18.8 - 20.9	10	3	5
	7 x ^{nat}Fe	0	^{54}Fe(n,t)^{52g}Fe	16.0 - 20.4	5	5	600
	Nb-^{nat}Cr-Nb-^{nat}Cr-Nb-^{nat}Cr-Nb-^{nat}Ni-Nb Nb-^{nat}Ni-Nb	0, 30, 60, 105 130	^{50}Cr(n,np)^{49}V, ^{52}Cr(n,2n)^{51}Cr ^{58}Ni(n,α)^{55}Fe, ^{58}Ni(n,αp)^{54}Mn ^{62}Ni(n,α)^{59}Fe	13.0 - 19.7	1	5	6000
Geel 2	Al-^{nat}Cr-Al	0	^{52}Cr(n,p)^{52}V ^{53}Cr(n,p)^{53}V	16.0 - 20.2	10	5	5
	Al-$^{52}Cr_2O_3$-Al	0	^{52}Cr(n,p)^{52}V	16.0 - 20.2	10	5	8
	Al-$^{53}Cr_2O_3$-Al	0	^{53}Cr(n,p)^{53}V, ^{53}Cr(n,np)^{52}V	16.0 - 20.2	10	5	3
	Al-$^{54}Cr_2O_3$-Al	0	^{54}Cr(n,p)^{54}V,^{54}Cr(n,np)^{53}V ^{54}Cr(n,α)^{51}Ti	16.0 - 20.2	20	5	3 -10
	Al-$^{54}Fe_2O_3$-Al	0	^{54}Fe(n,2n)$^{53m+g}$Fe ^{54}Fe(n,2n)^{53m,g}Fe (ICSR) ^{54}Fe(n,t)^{52m}Fe	16.0 - 20.2. 19.1 - 20.2 16.0 - 20.2	10 4 3	5 2 3	10 5 60

3.2 Neutron Fields

3.2.1 DD-Neutron Source Reaction (*Jülich*)

- **Neutron Energy Spectra**

The average neutron energy effective at each sample was calculated with the Monte Carlo code NEUT_HAV [Bir 94]. The program is an improved version of the code NEUT [Bir 92]. It takes into account

- the energy loss and the straggling of the deuterons in the entrance window of the gas target,
- the energy loss in the D_2 gas according to the D_2 pressure,
- the angular distribution of the $^2H(d,n)^3He$ reaction [Lis 73],
- the production of the neutrons in the space of the gas cell,
- the dimensions of the sample and the distance between the sample and the beam stop,
- the break-up of the deuterons in the D_2 gas according to the results from Cabral et al. [Cab 90].

The program calculates the average neutron energy impinging on the sample and its uncertainty as well as the neutron spectrum in the sample in energy bins of 50 keV (monoenergetic part) and 200 keV (breakup part) width (normalized to unit area). The neutron spectra for the chosen four different incident deuteron energies are shown in **Fig. 3.6**. For comparison the spectra are all normalized to the same height of the monoenergetic peak. The breakup part in the spectrum increases with increasing deuteron energy. **Fig. 3.7** shows a similar spectrum for an identical gas target measured by a TOF method at PTB[10] [Cab 90].

- **Background Subtraction**

The contribution of background neutrons stemming from interactions of the deuterons with structural materials to the total reaction rate can be calculated from the gas-in / gas-out ratios (i. e. the ratios of the induced activities measured in the irradiations with filled and empty gas cell). The correction factor $\mathbf{c_{gas}}$ is

$$c_{gas} = 1 - \frac{A_{out} \cdot t_{out} \cdot q_{in} \cdot m_{in} \cdot \left(1 - e^{-\lambda t_{in}}\right)}{A_{in} \cdot t_{in} \cdot q_{out} \cdot m_{out} \cdot \left(1 - e^{-\lambda t_{out}}\right)} \qquad (3.1)$$

[10] Physikalisch - Technische Bundesanstalt, Braunschweig, Germany

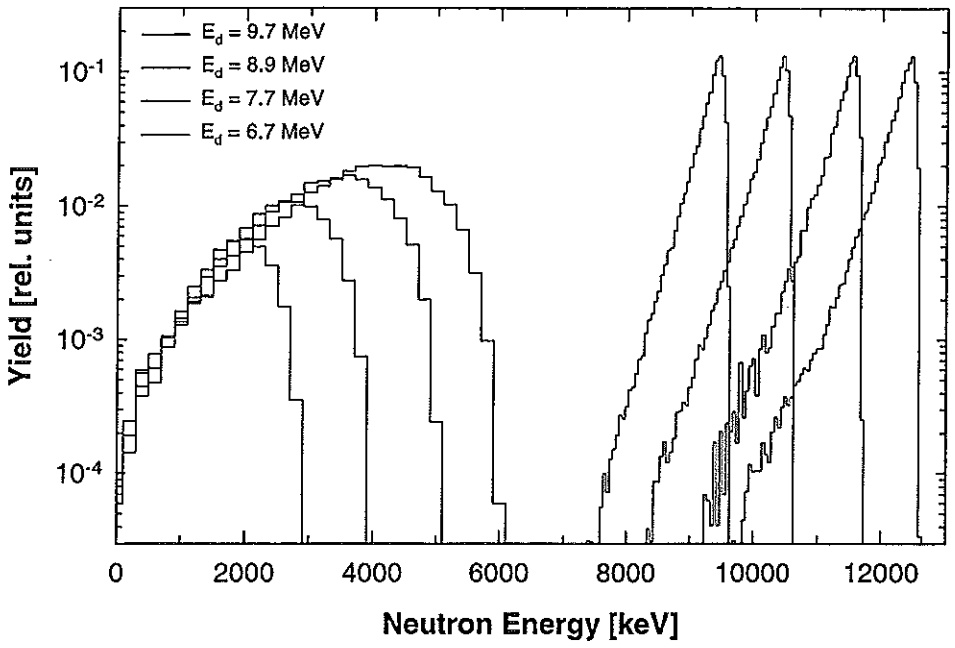

Fig. 3.6 Neutron spectra calculated with NEUT_HAV for deuteron energies of 6.7, 7.7, 8.9 and 9.7 MeV incident on the deuterium gas target at the Compact Cyclotron CV 28 at Jülich. The low energy neutrons are stemming from deuteron breakup D(d,np)D reactions.

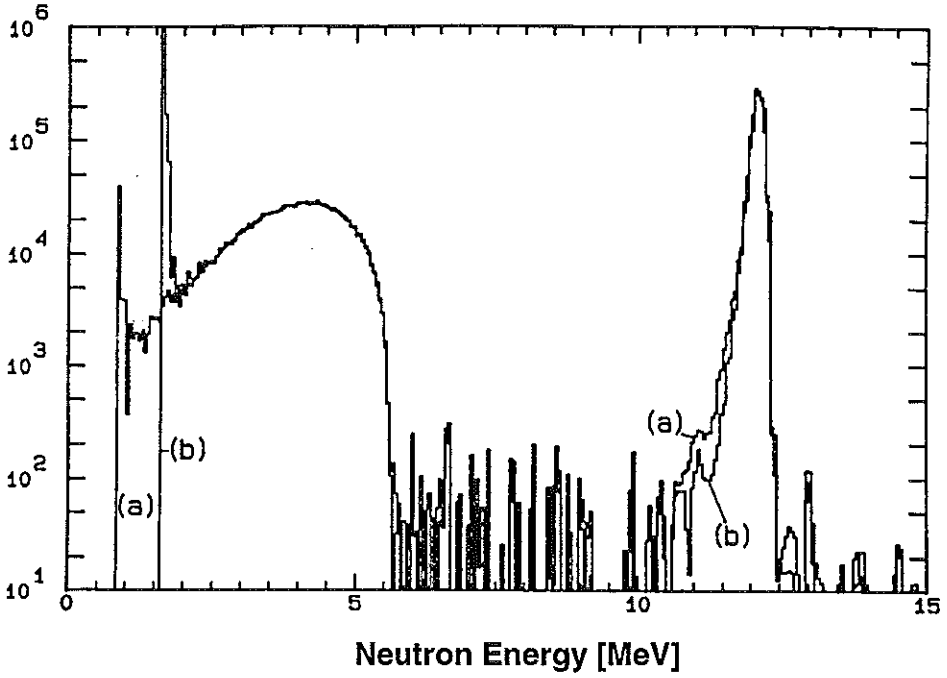

Fig. 3.7 Spectral neutron yield Y_E (at 0°) for a deuterium gas target and deuterium projectiles of 9.02 MeV, resulting from neutron TOF spectra after background subtraction and normalization for detector efficiency, taken from [Cab 90]. The spectra were recorded with (a) a hardware threshold corresponding to an equivalent electron energy E_e of 0.164 MeV and (b) a software threshold of 0.485 MeV.

where **A** is the measured activity, **t** the irradiation time, **q** the integrated beam current and **m** the sample mass. The indices refer to the gas -in or gas-out irradiations, respectively.

The corrections for the breakup neutrons were determined from the calculated neutron spectra. The spectra are split in a breakup part and a monoenergetic part and the fractional contribution of the breakup neutrons to the total reaction rate, c_{low}, was calculated.

$$c_{low} = 1 - \frac{A_{break}}{A_{total}} = 1 - \frac{\sum_{i=0}^{E_{break}^{max}} \sigma_i(E) \cdot f_i(E) \cdot dE}{\sum_{i=0}^{E^{max}} \sigma_i(E) \cdot f_i(E) \cdot dE} \qquad (3.2)$$

The cross sections $\sigma_i(E)$ are taken from evaluations or model calculations. $f_i(E)$ denotes the relative yield of neutrons with the energy **E**. The applied correction for these breakup neutrons was in the order of a few percent, depending on the reaction threshold and the excitation function of the investigated reaction.

3.2.2 DT-Neutron Source Reaction (*Geel 1* and *Geel 2*)

- **Neutron Energy Spectra**

The neutron energy spectra were determined in two independent ways. In the first approach the average neutron energy within the sample was determined in a similar way as done for the DD gas target. Therefore the program NEUT_HAV was slightly modified [Fes 97a]. The geometry of the Ti/T target was implemented as well as the angular distribution of the T(d,n)^{4}He reaction [Lis 73] was considered.

In the second approach the spectra were determined experimentally by TOF measurements in order to estimate the contribution of background neutrons. The principle involves the measurement of the time the neutron takes to traverse a flight path of length **L**. The velocity and therefore the kinetic energy of the neutron is deduced from the flight time **T**. If the neutrons, as a first approximation, are considered as non-relativistic, the relation between the neutron energy, the neutron mass, the flight time and the flight path is simply the expression for the kinematic energy

$$E_n = \frac{1}{2} m_n \left(\frac{L}{T}\right)^2 . \qquad (3.3)$$

By using the dimensions meter, nanoseconds and MeV for the flight path length, time of flight and neutron energy, respectively, the expression becomes in numerical form

$$E_n = \left(72.3 \cdot \frac{L}{T}\right)^2 . \qquad (3.4)$$

For the TOF measurements the Van de Graaff accelerator was operated in the pulsed mode. The neutrons were detected with a liquid scintillator (NE 213) with photomultiplier, placed 2.69 m behind the target at variable angles. The start signal of the time to amplitude converter (TAC) was a neutron signal in the photomultiplier, and the stop signal was deduced from a beam pick-up induction electrode in front of the target. The time calibration was done by the prompt gamma-rays from the target. In a second measurement the pulse shape was analysed for n/γ discrimination, allowing discrimination conditions dependent on the pulse height. A plastic scintillator (PILOT-U) under 120° and the long counter under 45° served for the neutron fluence normalization of the individual measurements. **Fig. 3.8** shows a raw TOF spectrum recorded at a deuteron energy of 3 MeV without n/γ discrimination. To convert the TOF spectra into neutron energy spectra the energy calibration was applied and the count rates for the individual energy bins were corrected for the detector efficiency. The efficiency was calculated by Meister [Mei 95] with the Monte-Carlo code NEFF7; an updated version of the NEFF4 code [Die 82] (cf. **Fig. 3.9**). Some processed neutron energy spectra for different incident deuteron energies are shown in **Fig. 3.10**. They are all normalised to the same height in the monoenergetic peak for comparison. The production of low energy neutrons strongly increases with the increasing incident deuteron energy. Some background peaks could be identified and are indicated in the figure.

- **Background Subtraction**

The correction for the background neutrons was done in a similar way as described for the breakup neutrons at the DD gas target. A cut-off energy for each investigated reaction (dependent on the reaction threshold) was defined below the monoenergetic neutron peak and the fractional contribution of the low energy neutrons to the total reaction rate was calculated according to (**3.2**). The correction factor at the highest incident deuteron energy was at the maximum 25 % for low threshold reactions (E_{thres} ~ 3 MeV). Since the final cross section determination relies on the ratio of two correction factors the correction in most cases is reduced to a few percent.

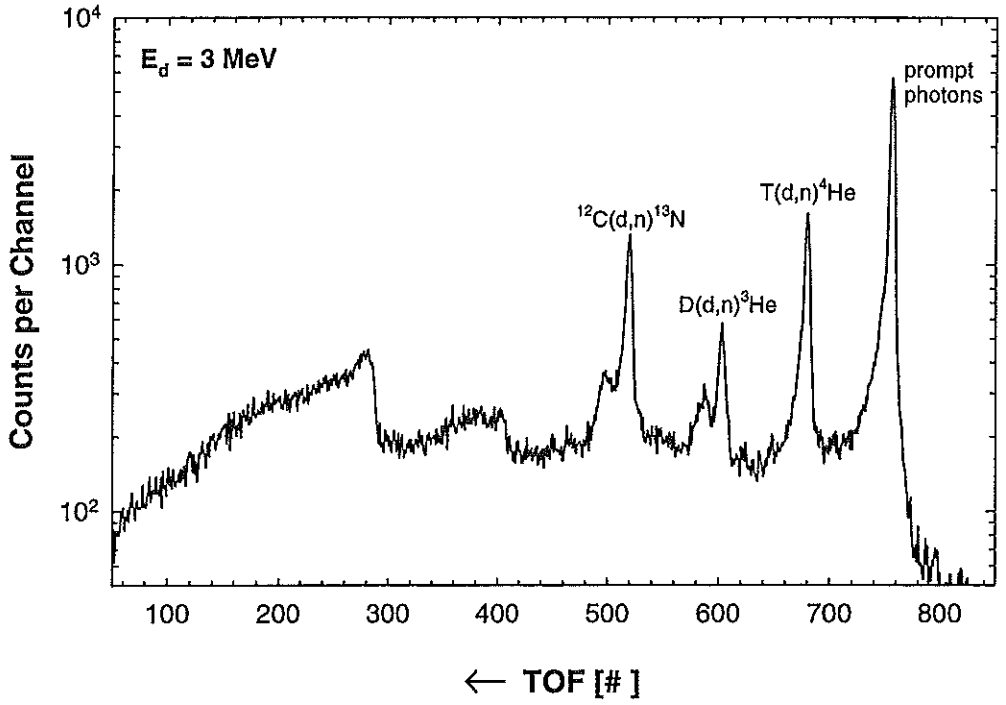

Fig. 3.8 Raw neutron time-of-flight spectrum (0.46 ns / #) from the Ti/T target (2.042 mg/cm^2) bombarded with 3 MeV deuterons.

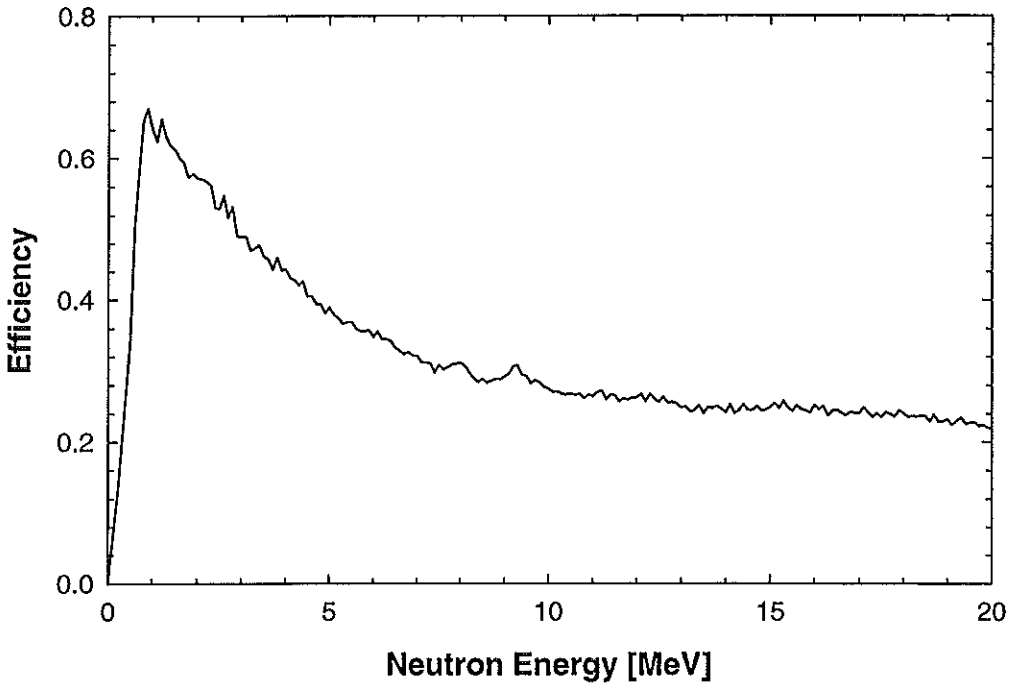

Fig. 3.9 Detector efficiency calculated for the NE 213 liquid scintillator with the code NEFF7 [Die 82] for a bias level of 50 keV.

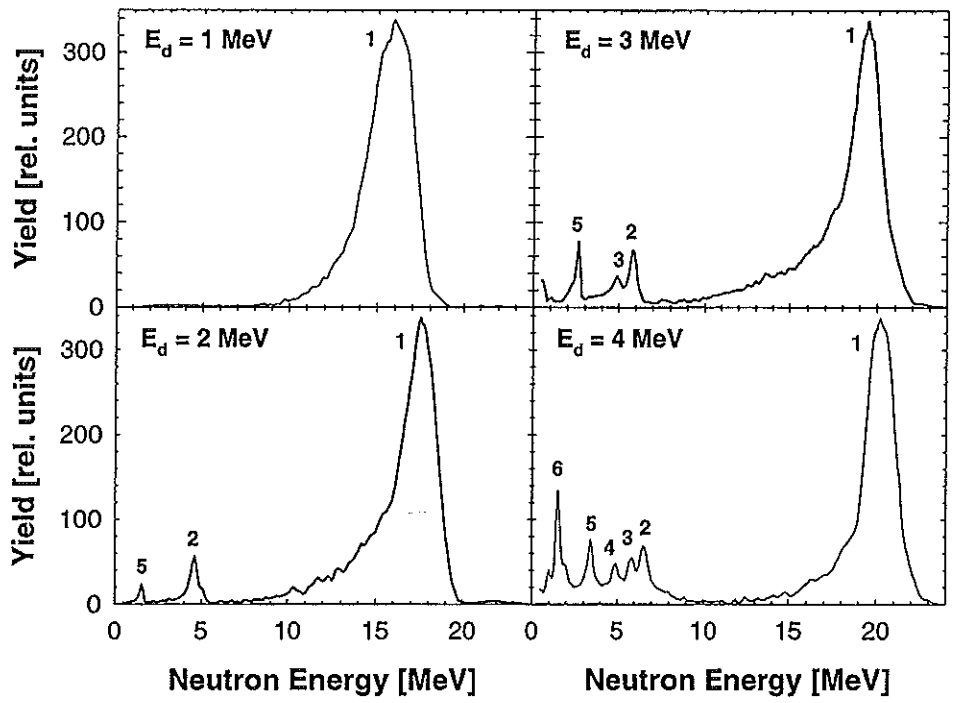

Fig. 3.10 Neutron energy spectra for the Ti/T target (2.042 mg/cm^2) bombarded with incident deuteron energies of 1, 2, 3 and 4 MeV. The indicated peaks belong to the following reactions: **1** T(d,n)^{4}He, **2** D(d,n)^{3}He, **3** and **4** not identified, **5** ^{12}C(d,n)^{13}N, **6** T(d,np)T.

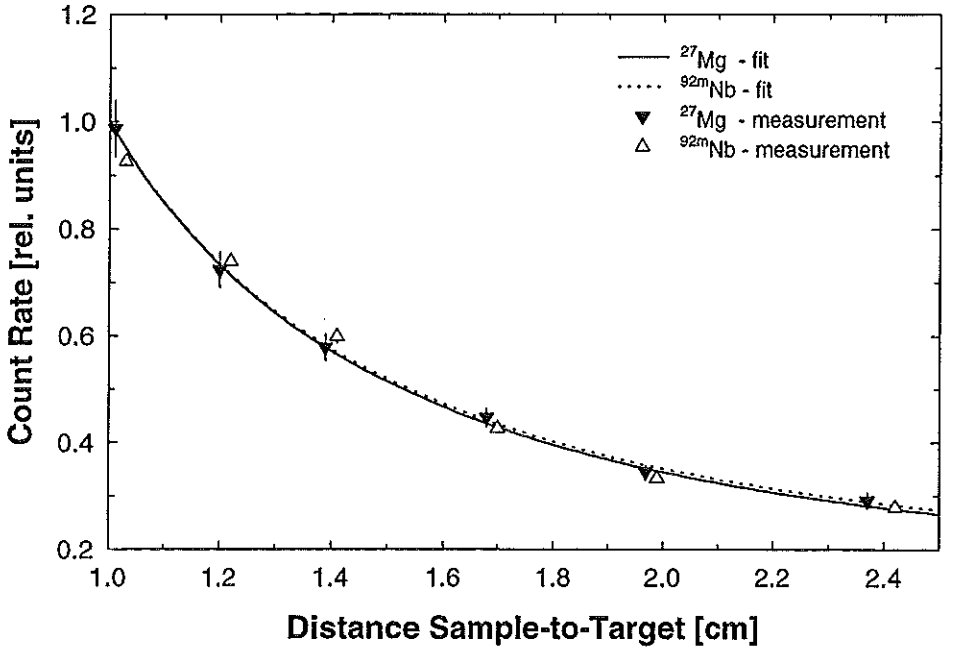

Fig. 3.11 Flux gradient in different sample material as a function of sample-to -target distance. The curves are calculated with equations of the type $y = a + b/x^2$.

3.2.3 Determination of Mean Flux Density within a Thick Sample

For thick samples the arithmetic mean of the measured activity in the monitor foils in front and at the back of the sample does not give the mean neutron flux. To determine the effective flux on the sample the flux gradient in the sandwich was measured with a simple method. In long stacks with many monitor foils at different distances (separated by 1.5 mm thick polyvinyl chloride (PVC) disks) the activity of each foil was determined. Taking into account the different neutron energies at the respective distances, the gradient is then given by the relation

$$c_{grad} = \frac{A_1 \cdot \sigma_1}{A_x \cdot \sigma x} \tag{3.5}$$

where A_1 is the activity at the foil closest to the target and σ_1 the cross section for the used reaction. A_x and σ_x are the activity and the cross section at the distance **x**. **Fig. 3.11** shows the flux gradient as a function of the sample-to-target distance for two different sample materials. The lines are least-squares fits of the determined ratios. A similar figure was obtained by Qaim et al. [Qai 92b]. They calculated the flux gradient inside a thick sample both by Monte Carlo and numerical integration methods.

3.2.4 Neutron Flux Fluctuations

Usually, the neutron flux varies during an irradiation due to the fluctuation of the deuteron beam intensity. The depletion of tritium is only of relevance for targets used at high flux neutron generators. When the flux variation is drastic, the assumption of a constant neutron flux is no longer valid. In this work the neutron production rate was always monitored by recording either the integrated deuteron beam charge (*Jülich*) or the neutron counts in a long counter (*Geel 1*) or Bonner sphere (*Geel 2*) using the MCS method throughout each irradiation. The dwell time (DT) was set according to the irradiation time, usually between 5 sec and 10 min. The correction factor c_{flux} for flux fluctuations is then calculated from the ratio

$$c_{flux} = \frac{\overline{\Phi} \cdot \left(1 - e^{-\lambda \cdot t_i}\right)}{\sum_{i=1}^{n} \Phi_i \cdot \left(1 - e^{-\lambda \cdot \Delta t}\right) \cdot e^{-\lambda \cdot (n-i) \cdot \Delta t}} \tag{3.6}$$

where $\overline{\Phi}$ is the mean flux of the irradiation, Φ_i the relative flux at the time bin **i**, **n** the total number of time bins (i=1, n), t_i the irradiation time and Δt the dwell time of the MCS.

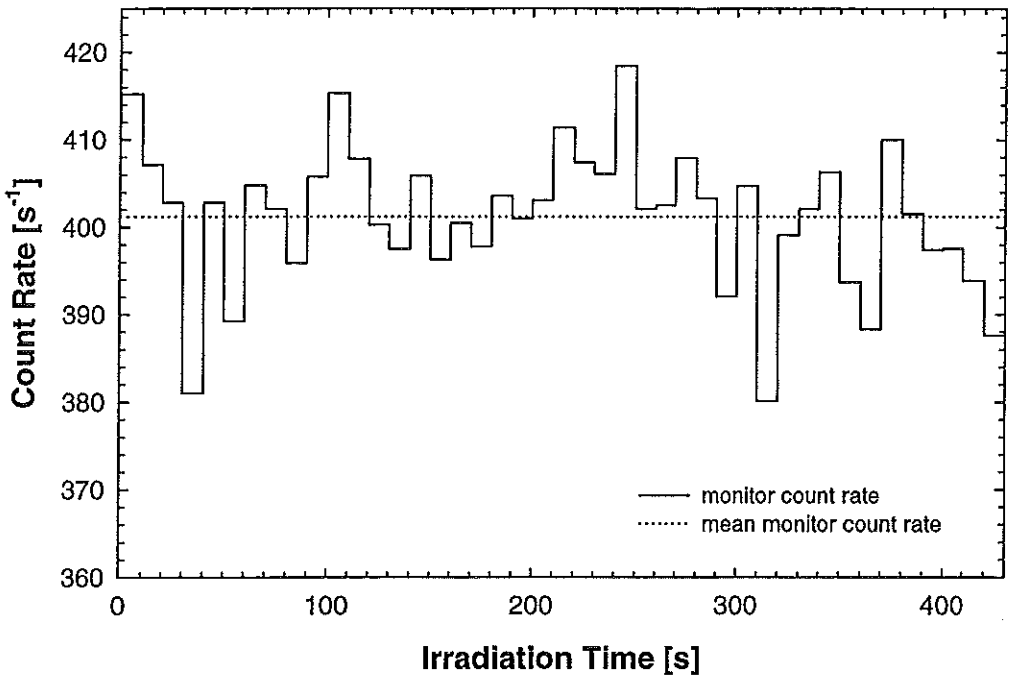

Fig. 3.12 Monitor count rate and mean monitor count rate in a 7 min irradiation with a MCS dwell time of 10 s. The deviations from the mean are very small (< 5 %).

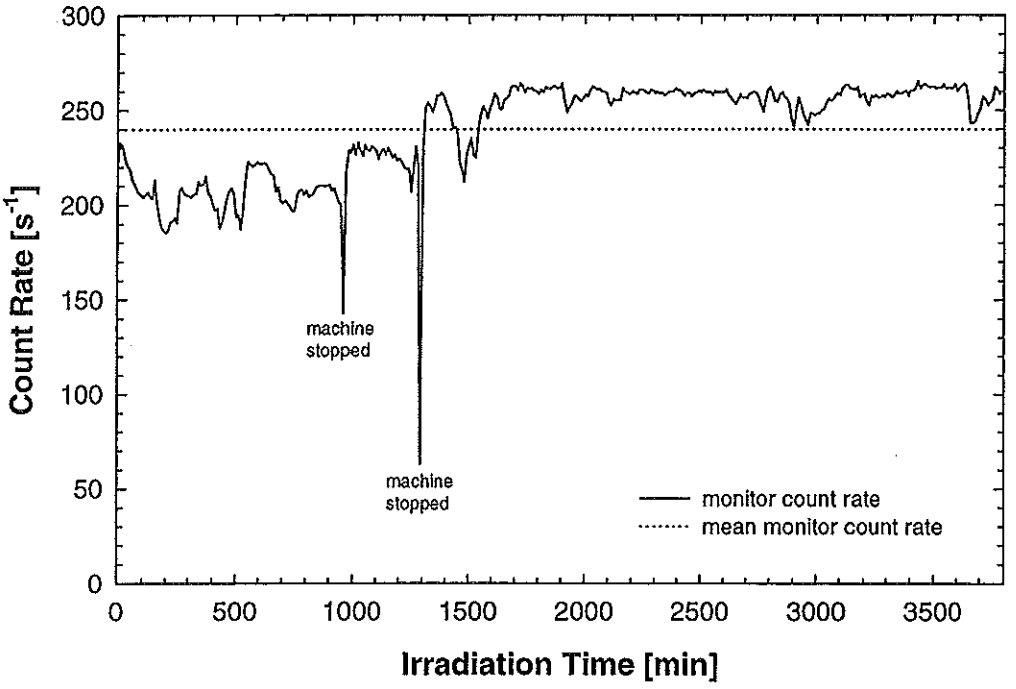

Fig. 3.13 Monitor count rate and mean monitor count rate in a 63 h irradiation with a MCS dwell time of 10 min. The deviations from the mean are up to 20 %.

A more detailed description of the correction procedure is given in [Ike 88]. In short irradiations c_{flux} was marginal (flux deviations from the mean less than 5 %, see **Fig. 3.12,** leading to $c_{flux} < 0.01$) whereas in longer irradiations, for reaction products which reach almost saturation, the correction is up to 20 % (see **Fig. 3.13**).

3.2.5 Neutron Multiple Scattering Corrections

Calculations for neutron multiple scattering corrections for the irradiations at *Geel 2* were done by Meadows [Mea 97] using the code CYSCT3 [Smi 77]. It is a rudimentary program for calculating the effects of neutron scattering on the measurement of (n,x) reaction cross sections in low mass systems. The calculation is restricted to a single scattering event before detection. It is carried out by Monte Carlo integration over the neutron source, scatterer and detector volumes. The quantity calculated is the ratio of the probability of a neutron being detected after scattering once to the probability that a neutron would be detected if no scatterer were present.

The complete system must be approximated by a collection of scattering cylinders plus the source and detector cylinders. The program handles only one scattering volume at the time, so if there are two or more scatterers, they require separate calculations and must be added together. The same is valid for different elements in one scatterer.

Neutron energies and the energy-angle relation are calculated by the subroutine KINAM. Information concerning the yield versus incident particle energy and neutron angle for specific source reactions are contained in subroutines as well.

The effects of inelastic scattering are calculated using the total inelastic cross section for reactions where the first emitted particle is a neutron (i. e. the (n,n') and (n,2n) reactions). The (n,np) and (n,nα) reactions are not considered since their cross sections are mostly not or only poorly known. The energy distribution of the inelastic neutrons is assumed to have the form E(exp(-E/T(M)), where **E** is the neutron energy and **T** is a "temperature" which is a function of the mass number.

The calculations were done using a more simplified sketch than given in **Fig. 3.4**. It became apparent that scattering from the aluminium target tube, the lucite and PVC tubes contributed very little to the total scatttering correction. The most important scatterer was found to be the lucite disk covering the samples at the frontside of the rabbit. Results of the performed calculations are given in **Tab. 3.3**. The correction factors c_{scat} to the cross section ratio (i. e. sample / monitor) never exceeded 5%. The highest values resulted for high threshold reactions compared to the lower threshold reference reaction $^{27}Al(n,p)^{27}Mg$. The overall uncertainty of the correction factor was estimated to be ~10 %.

Due to the resulting low correction factors with rather large errors, neutron scattering was considered to be negligible for the other set up's (*Geel 1* and *Jülich*). Here the samples were also not covered by any material that was found to be the most important scatterer at *Geel 2*.

Tab. 3.3 Scattering fractions calculated with CYSCT3 and deduced correction factors c_{scat} for the investigated reactions at Geel 2. In all cases the reference reaction was $^{27}Al(n,p)^{27}Mg$.

Sample reaction	Scattered Fraction [%] (S = Sample, R =Reference) correction factor, $c_{scat} = (100-S)/(100-R)$											
	E_d = 1 MeV			E_d = 2 MeV			E_d = 3 MeV			E_d = 4 MeV		
	S	R	c_{scat}	S	R	c_{scat}	S	R	c_{scat}	S	R	c_{scat}
$^{nat}Cr(n,p)^{52}V$	8.0	8.1	1.00	7.4	8.8	1.01	7.9	9.8	1.02	8.0	10.0	1.02
$^{nat}Cr(n,p)^{53}V$	7.2	8.1	1.01	7.0	8.8	1.02	6.6	9.8	1.03	7.1	10.0	1.03
$^{52}Cr(n,p)^{52}V$	4.0	4.9	1.01	4.4	4.9	1.01	4.7	5.9	1.01	4.8	6.0	1.01
$^{53}Cr(n,p)^{53}V$	3.4	5.4	1.02	3.6	5.1	1.02	3.9	5.5	1.02	3.8	6.2	1.03
$^{53}Cr(n,np)^{52}V$	0.9	5.4	1.05	1.2	5.1	1.04	1.5	5.5	1.04	1.9	6.2	1.05
$^{54}Cr(n,p)^{54}V$	2.2	4.8	1.00	1.8	5.3	1.01	2.2	5.7	1.02	2.0	6.2	1.02
$^{54}Cr(n,np)^{53}V$	0.4	4.8	1.05	0.8	5.3	1.05	1.3	5.7	1.05	1.3	6.2	1.05
$^{54}Cr(n,\alpha)^{51}Ti$	3.4	4.8	1.01	2.6	5.3	1.03	2.4	5.7	1.03	2.4	6.2	1.04
$^{54}Fe(n,2n)^{53}Fe$	1.0	5.1	1.04	1.4	5.5	1.04	1.7	5.7	1.04	1.9	6.0	1.04

3.3 Gamma-Ray Spectrometry

3.3.1 Data Acquisition

The induced radioactivity of the irradiated samples was measured off line with three lead-shielded (5 cm thick) HPGe detectors (*Jülich 7*, *Geel A* and *Geel B*). *Geel A* (active volume 120 cm^3, rel. efficiency 28 %) and *Geel B* (240 cm^3, 45 %) were connected via two ADC's to a PC Plug-in MCA card[1]. The data aquisition was controlled with the software TMCA[11]. *Jülich 7* (65 cm^3, 15 %) was connected to a 92X Spectrum Master[12] and controlled with the software GAMMAVISION[12]. A dead time correction was done by the saved real time (RT) and life time (LT) with each acquired spectra. All measurements were done non-destructively. Since the geometry of the detectors was different (see **Fig. 3.14**) the samples had to be mounted in different ways. In case of the detectors *Jülich 7* and *Geel A* the samples were placed directly on top of the detectors (centered) and fixed

[11] TARGET Systemelectronic GmbH, Kölner Str. 99, D-42651 Solingen, Germany
[12] EG&G Ortec, 100 Midland Road, Oak Ridge, TN 37831-0895, U.S.A.

with scotch tape. *Geel B* uses a movable lucite sample holder in which the samples are fixed in a cylindrical hole. Here the distance sample to detector was 0.5 cm. The 7 iron samples which were irradiated in a stack were placed as seven separate disks on the detector to avoid counting loss due to gamma-ray self absorbtion (see **Fig. 3.15**)

The counting was done in the following way. For the longer irradiations the samples and reference samples were measured separately whereas in the case of short half-lives both sample and reference had to be measured together. Generally the measuring time for the short-lived nuclides was 2 or 3 times the half-life. When the activity of the product was high enough a decay curve was recorded. The count rate at the end of the activation can then be calculated by a linear regression in a semi-log plot (see **Fig. 3.16**). The long-lived isotopes were counted as long as needed for accurate statistics (~1000 netto counts/peak). To take care of energy shifts in the spectra in very long measurements (days or weeks) the software TMCA contains a channel stabilisation, i. e. long term drifts in the preamplifier and main amplifier, etc. caused by thermal effects are compensated. A region of interest was set for the 1460.8 keV gamma-ray of ^{40}K (natural background). After each 500 counts in this peak the fine gain is checked and adjusted relativ to this peak (if needed).

The data of the decay modes, half-lives, gamma-ray energies and intensities were taken from the *Table of Isotopes* [Fir 96] (see **Tab. 3.4**). In one case, namely the nuclide ^{53}V, the half-life was taken from a recent evaluation [Smi 97].

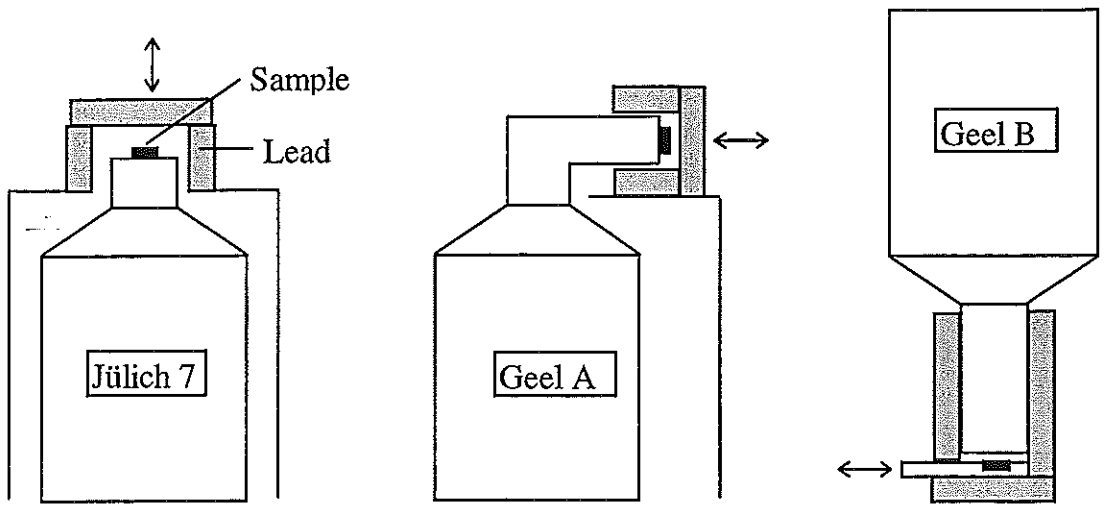

Fig. 3.14 Counting geometries for the different HPGe detectors

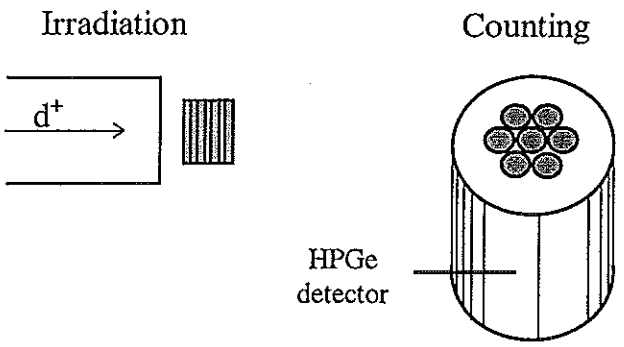

Fig. 3.15 Irradiation and counting geometry for the iron stack containing 7 individual samples (each 1.5 mm thick).

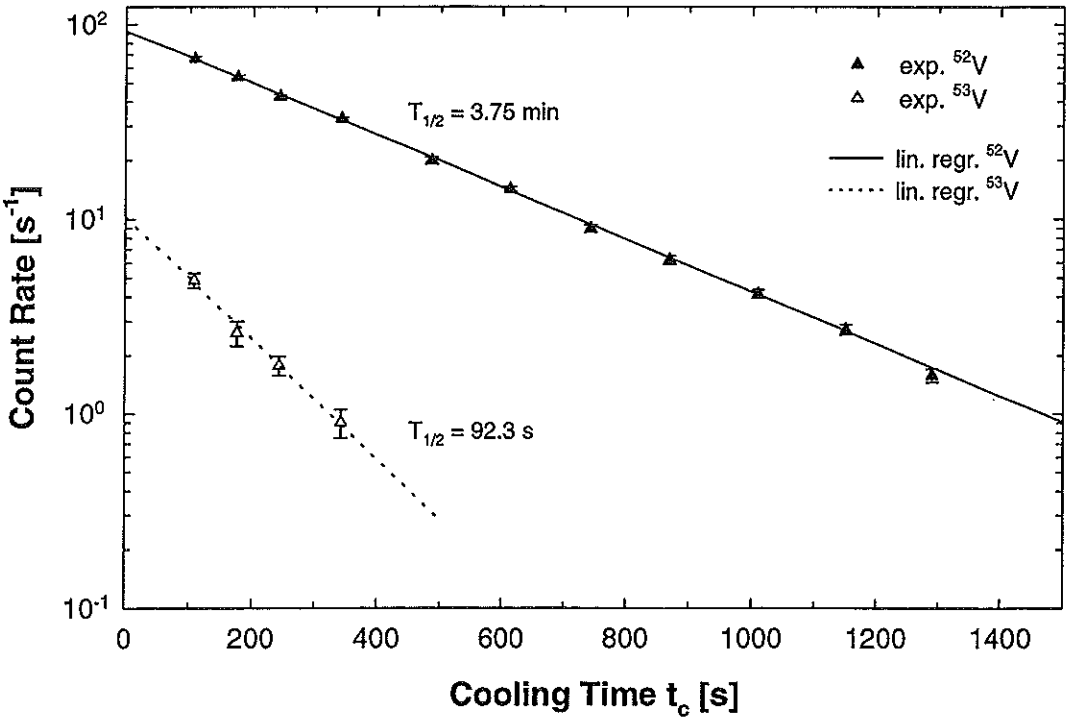

Fig. 3.16 Decay curves of the nuclides ^{52}V ($T_{1/2}$ = 3.75 min) and ^{53}V ($T_{1/2}$ = 92.3 s). The activities were produced in a 20 min irradiation of natural chromium samples.

Tab. 3.4 Properties of the studied activation products, taken from [Fir 96].

Nuclide	$T_{1/2}$	Decay mode (branching [%])	Gamma-ray energy [keV] (intensity [%])
^{51}Ti	5.76 min	β^- (100)	320.1 (93.4)
^{52}V	3.75 min	β^- (100)	1434.1 (100)
^{53}V	92.3 s†	β^- (100)	1006.0 (89.6)
^{54}V	49.8 s	β^- (100)	834.8 (97.1), 989.0 (80.1)
^{51}Cr	27.70 d	EC (100)	320.1 (9.86)
^{52m}Mn	21.1 min	EC + β^+ (98.25), IT (1.75)	1434.1 (98.3)
^{52g}Mn	5.59 d	EC (72.1), β^+ (27.9)	744.2 (90.6), 935.5 (94.9), 1434.1 (100)
^{54}Mn	312.3 d	EC (100)	834.9 (100)
^{53m}Fe	2.58 min	IT (100)	701.1 (100), 1011.5 (86) 1328.1 (87)
^{53g}Fe	8.51 min	β^+ (97.2), EC (2.8)	377.9 (42)
^{59}Fe	44.50 d	β^- (100)	1099.3 (56.5), 1291.6 (43.2)
references			
^{24}Na	14.96 h	β^- (100)	1368.6 (100)
^{27}Mg	9.46 min	β^- (100)	843.8 (71.8), 1014.4 (28)
^{56}Mn	2.58 h	β^- (100)	846.8 (98.9), 1810.7 (27.2)
^{92m}Nb	10.15 d	EC (>99), β^+ (<1)	934.4 (99.1)

† from [Smi 97]

3.3.2 Gamma-Ray Spectrum Analysis

The recorded gamma spectra were analysed in order to determine the positions and the areas of the gamma peaks of interest. The response of HPGe detectors allows the shape of the detected gamma peaks to be adequately fitted by a Gaussian function combined with some function describing the low-energy tail. Effects of pile-up and properties of the electronics may also cause a tail at the high-energy side, but this can often be avoided with careful experimental design. Tailing effects on the low-energy side arise from a variety of causes like imperfect charge collection in the detector due to radiation damage. Several mathematical forms of low- and high-energy tailing are given in refs. [Hel 80, Deb 88].

The peak area determination was done with the software program GAMMA-W[13] [Wes 90]. First the whole spectrum is subdivided into regions where the channels contain a

[13] Dr. Westmeier, Gesellschaft für Kernspektrometrie mbH, Ebersdorfergrund-Mölln, Germany

smoothly varying background distribution with some peaks on top. Then the background in each region is calculated with an algorithm [Wes 81, Wes 86] where the number of background counts in each channel is analytically determined from the experimental number of peak counts in all higher channels. The resulting background function is a smooth step function. Finally the peaks are fitted by a least-squares routine. The high-energy part is fitted by the basic analytical function

$$Y_G(x) = HGT / \exp\left((x - POS)^2 \cdot 4 \cdot \frac{\ln 2}{FWHM}\right) \qquad (3.7)$$

where **HGT** is the height of the Gaussian (in counts), **POS** is the peak position (in channels), **FWHM** is the full width at half maximum, and $\mathbf{Y_G(x)}$ the height of the Gaussian in channel **x**. The deviation from a pure Gaussian due to low-energy tailing is considered with a fifth order term. The empirical function

$$G(x) = Y_G(x)\left(1 - \kappa\ (x - POS)^5\right) \qquad (3.8)$$

where **G(x)** is the height of the peak function in channel **x** and κ is a free fit parameter, allows the generation of a long low-energy tail due to the high power of the (x-POS) term.

3.3.3 HPGe Detector Efficiency

- **Measurements**

Several standard single and multi gamma-ray point sources (energies from 59 to 1836 keV) were measured at several sample-to-detector distances (between 0.1 and 20.1 cm). The measuring time for each source was set in order to achieve a peak area of ≥ 10000 counts and the peak area evaluation was done as described in **section 3.3.2.** The sources were obtained from DAMRI[14] and PTB. For the double gamma-ray emitters ^{60}Co and ^{88}Y coincidence summing corrections had to be performed (see **section 3.3.5**). The properties of the used standard sources are given in **Tab. 3.5.**

- **Photopeak Efficiency Calculation**

The photopeak efficiency ε_{ph} was calculated by the equation

$$\varepsilon_{ph}\left(x, E_\gamma\right) = \frac{N_{ph}(x, E_\gamma)}{A \cdot p_\gamma \cdot e^{-\lambda \cdot t}} \qquad (3.9)$$

[14] Departement des Applications et de la Metrologie des Rayonnements Ionisants, 91193 Gif-Sur-Yvette Cedex France

where $N_{ph}(x, E_\gamma)$ is the count rate of the peak area corresponding to the energy E_γ at the source-to-detector distance **x**, **A** is the source activity at the time of standardization, p_γ is the absolute γ-ray emission probability, λ is the decay constant and **t** the elapsed time since standardization.

Tab. 3.5 Properties of the gamma-ray calibration sources, taken from [Fir 96].

Nuclide	$T_{1/2}$	Gamma-ray Energy [keV] (intensity [%])
^{241}Am	432.7 a	59.54 (35.9)
^{109}Cd	462.6 d	88.03 (3.65)
^{57}Co	271.79 d	122.06 (85.68), 136.47 (10.67)
^{139}Ce	137.640 d	165.86 (79.87)
^{51}Cr	27.706 d	320.08 (9.85)
^{113}Sn	115.09 d	391.70 (64.89)
^{85}Sr	64.849 d	514.01 (99.29)
^{137}Cs	30.15 a	661.66 (85.2)
^{54}Mn	312.3 d	834.84 (99.98)
^{65}Zn	244.26 d	1115.55 (50.75)
^{60}Co	5.271 a	1173.2 (99.89), 1332.5 (99.98)
^{88}Y	106.630 d	898.04 (94.1), 1836.06 (99.36)

- **Photopeak Efficiency as a Function of Energy**

A number of analytical functions describing the dependence of the photopeak efficiency versus the energy have been proposed by several authors [e. g. Wil 70, McN 73, Gmu 82, Gra 85, Sán 87, Deb 88]. The efficiency function used in this work has been proposed by Jäckel et al. [Jäc 87]. The high energy part (~200 up to ~2500 keV) is well described by a second order polynomial in a log-log display whereas the sharp decrease of the efficiency at low energies is characterized appropriately by an arctangent function. The function can be expressed as

$$\ln \varepsilon\ (E_\gamma) = \left(a_1 + a_2 \ln E_\gamma + a_3 \ln E_\gamma^2\right) \cdot \frac{2}{\pi} \cdot \arctan\left(\exp\left\{a_4 + a_5 \ln E_\gamma + a_6 \ln E_\gamma^2\right\}\right) - 25 \qquad \textbf{(3.10)}$$

where the constant $2/\pi$ serves for the normalization of the arctangent function and the constant **-25** shifts the $\ln \varepsilon(E_\gamma)$ values to positive numbers. This efficiency function was fitted to the experimental points as can be seen in **Fig. 3.17** for some selected source-to-detector distances.

- **Photopeak Efficiency as a Function of Energy and Distance**

The photopeak efficiency as a function of both energy and distance is useful for the determination of the mean efficiency of thicker samples. A method was chosen described in detail by Kawade et al. [Kaw 81]. The detector is considered as a point detector at large sample-to-detector distances whereas at short distances a correction has to be applied for the deviations from the point detector model. The proposed function is

$$\varepsilon_{ph}\left(x, E_\gamma\right) = \varepsilon_{ph}\left(20, E_\gamma\right) \cdot \left[\frac{20 + x_0\left(E_\gamma\right)}{x + x_0\left(E_\gamma\right)}\right]^2 \cdot \left[1 - B\left(x, E_\gamma\right)\right] \qquad \textbf{(3.11)}$$

where

$$x_0\left(E_\gamma\right) = a_1 - a_2 \cdot e^{-a_3 \cdot E_\gamma} - a_4 \cdot e^{-a_5 \cdot E_\gamma} \qquad \textbf{(3.12)}$$

and

$$B\left(x, E_\gamma\right) = a_6 \cdot E_\gamma^{-a_7} \cdot e^{-a_8 + a_9 \cdot E_\gamma \cdot x}. \qquad \textbf{(3.13)}$$

The so-called *effective interaction depth* $\mathbf{x_0}$ defines the distance below the surface of the outside detector mounting at which a gamma-ray of a particular energy appears to interact or gives up all its energy (x_0 decreases with decreasing gamma-ray energy) [Cri 71, Not 71]. **B (x, E_γ)** is the correction for the deviation of the gamma-ray beam from a parallel beam at short distances and nearly equal to zero in the range 7 - 20 cm. **Fig. 3.18** shows the fitted function to the experimental points.

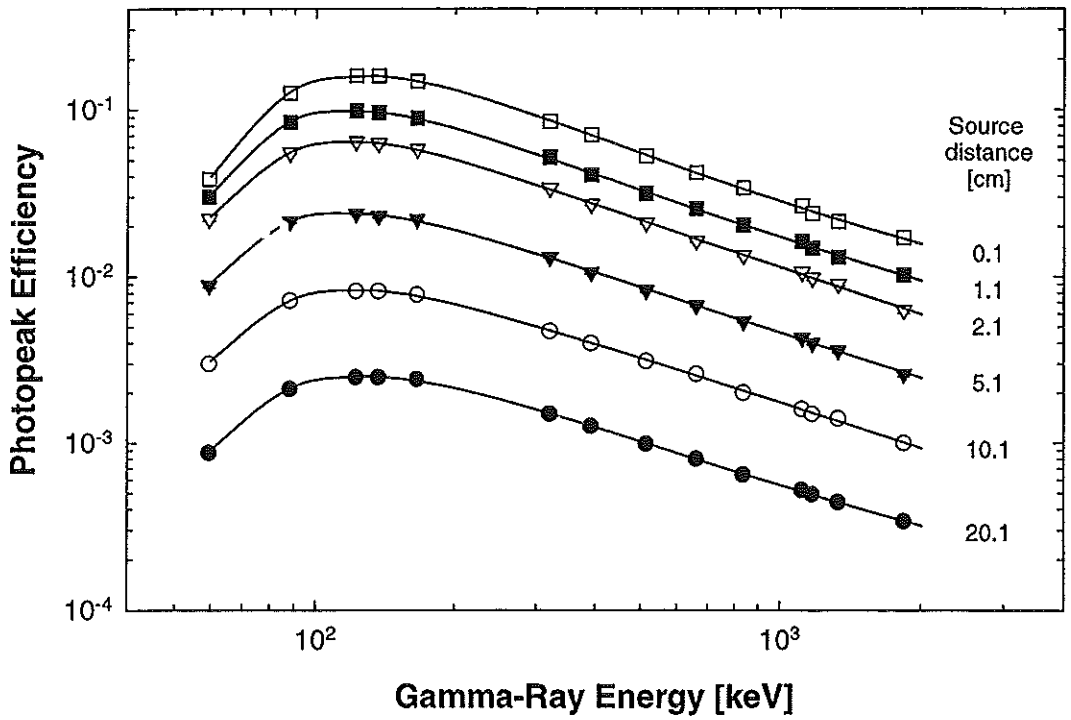

Fig. 3.17 Photopeak efficiency of the HPGe detector versus energy for various source-to-detector distances. The line fits are calculated with (3.10).

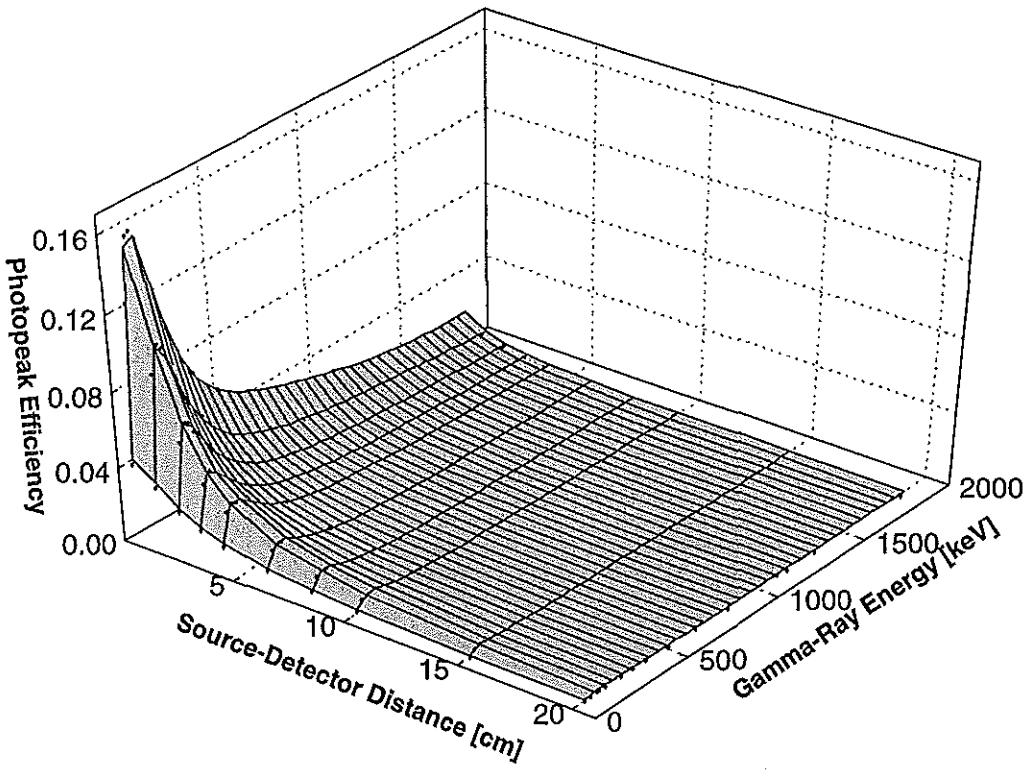

Fig. 3.18 Photopeak efficiency of the HPGe detector versus energy and distance. The fitted lines are calculated with (3.11).

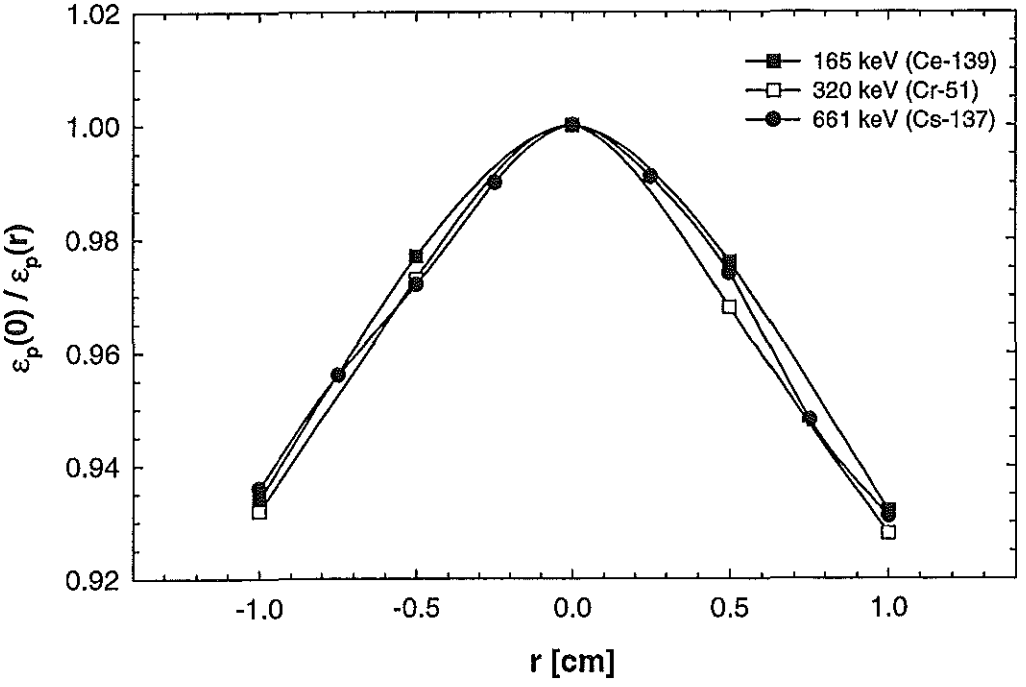

Fig. 3.19 Radial dependence of the efficiency of the HPGe detector for different gamma-ray energies at a source-to-detector distance of 0.1 cm (r = off-centre distance).

- **Corrections for Disk and Cylinder Type Sources**

In order to determine a correction factor for the efficiency of disk type sources, $\varepsilon_{ph}(\mathbf{R})$, the point sources were measured in several off-centre distances **r** and the efficiency $\varepsilon_{ph}(\mathbf{r})$ was calculated. According to Helmer [Hel 83] the correction factor $\mathbf{c_{disk}}$ for a disk source with radius **R** is given by

$$c_{disk} = \frac{\varepsilon_{ph}(R)}{\varepsilon_{ph}(0)} = \frac{\int_0^R \frac{\varepsilon_{ph}(r)}{\varepsilon_{ph}(0)} \cdot 2\pi r dr}{\int_0^R 2\pi r dr} = \frac{2}{R^2} \cdot \int_0^R r \cdot \frac{\varepsilon_{ph}(r)}{\varepsilon_{ph}(0)} dr \quad . \tag{3.14}$$

Fig. 3.19 shows the efficiency as a function of the off-centre distance for different point sources. In contradiction to Helmer, no dependence of $\mathbf{c_{disk}}$ from the gamma-ray energy could be determined due to the somewhat bigger experimental errors. In addition, measurements were done with two multi gamma-ray disc sources which were prepared in the IRMM Radionuclides Group. They were made of a mixed standard solution poured dropwise on two thin papers (13 and 14 mm in diameter). These were placed in stainless steel rings (34 mm outer diameter) and covered on both sides with self-adhesive plastic foil (0.01g/cm^2). The correction factors $\mathbf{c_{disk}}$ determined with these sources agreed with those determined with the point sources to within 5 % (the order of the uncertainty of the activity of the standard sources). Generally the correction factors were in the order of 2 to 8 %.

Cylindrical sources can be interpreted as multilayered disk sources where for each layer at the distance **x** from the detector equation **(3.14)** must be applied. If self absorption cannot be neglected and the activity in the sample is not homogeneously distributed, then the integrand has to be multiplied by a self-absorption correction term **T(x)** (s. below) and by the activity gradient $\mathbf{c_{grad}}$ in the sample (see **3.2.3**). The correction factor $\mathbf{c_{vol}}$ for the efficiency of a cylindrical sample of thickness **X** is given finally by the expression

$$c_{vol} = \frac{1}{X} \cdot \int_0^X c_{grad}(x) \cdot c_{disk}(x) \cdot T(x) \cdot dx \quad . \tag{3.15}$$

- **Total Detector Efficiency**

The total efficiency ε_t is defined as the ratio of the number of pulses recorded in the entire spectrum and the number of photons emitted from a source. The pulses need not to be due to photons originally emitted in the direction of the detector, but they may result from secondary photons produced by source photons in the surroundings.

ε_t is important in the calculation of coincidence-summing corrections (see following chapter), since the loss of events from the full-energy peak of one photon line is proportional to the total efficiencies for the coincident photons.It is

$$\varepsilon_t\left(x, E_\gamma\right) = \frac{N_t(x, E_\gamma)}{A \cdot p_\gamma \cdot e^{-\lambda \cdot t}} \qquad (3.16)$$

where N_t is the total count rate (extrapolated to zero keV). For the calibration the single gamma-ray emitters ^{139}Ce, ^{51}Cr, ^{85}Sr, ^{137}Cs, and ^{54}Mn were used. In the case of ^{57}Co and ^{60}Co, radionuclides emitting two photons of not too different energies, for p_γ the sum of the individual emission probabilities was inserted and ε_t assigned to the mean energy $\overline{E}$ (^{57}Co, $\overline{E}$ = 124 keV and ^{60}Co, $\overline{E}$ = 1253 keV). In the case of ^{113}Sn and ^{65}Zn , where the source emits two gamma-rays with well separated energies, the total efficiency $\varepsilon_t(E_1)$ for one energy was interpolated from other measured values. Then the corresponding number of total counts was subtracted and $\varepsilon_t(E_2)$ was obtained. The experimental data points were then fitted with a linear regression in a semi-log plot.

3.3.4 Photon Absorption Corrections

It was assumed that most of the samples can be considered as plane sources of thickness **x** with a homogeneous distribution of the attenuating material and the activity. The transmission **T** through a layer of thickness **x** (usually mass areal density in g/cm^2) is given by the expression

$$T = e^{-\mu\, x} \quad . \qquad (3.17)$$

where **μ** is the absorption coefficient (usually mass absorption in cm^2/g) The mean transmission $\overline{T}$ through a source is given by

$$\overline{T} = \frac{1}{x}\int_0^x e^{-\mu\, x} dx = \frac{1}{\mu\, x}\left(1 - e^{-\mu\, x}\right). \qquad (3.18)$$

$\overline{T}$ may be expressed in T:

$$\overline{T} = \frac{T-1}{\ln T} \qquad (3.19)$$

The values of μ were calculated with the program XCOM [Ber 87]. Additionally, transmission measurements were done to determine the self-absorption for the thick irradiated nickel cylinders (5 mm thick). The standard disk source was measured with increasing number (1 to 4) of thin nickel cylinders (1.5 mm thick) in between source and detector. The ratio of the count rates of measurements with absorber to the one without absorber gives the transmission **T(x)** as a function of absorber thickness.

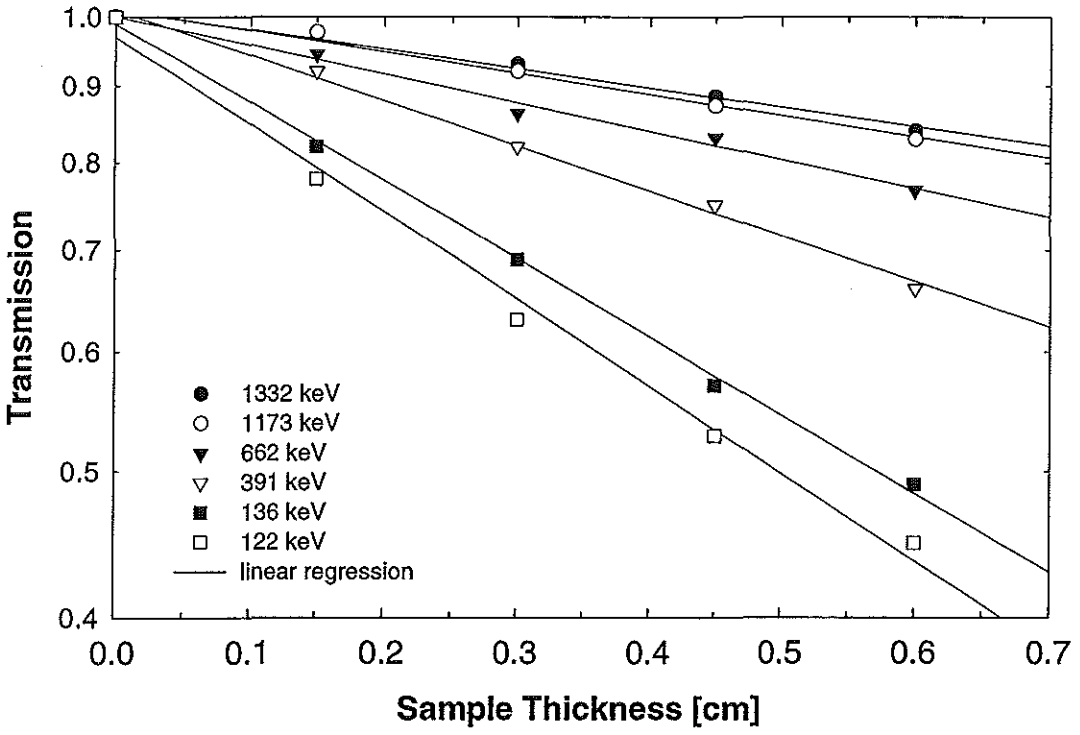

Fig. 3.20 Transmission through nickel for several gamma-ray energies as a function of sample thickness.

3.3.5 Coincidence Summing Corrections

Coincidence summing occurs in the case of radionuclides emitting two or more photons within the resolving time of the spectrometer. If, for example, the first photon spends its total energy in the germanium crystal and if the second photon is also detected, a sum pulse is recorded. The event is lost from the photopeak from the first photon. The probability for summing effects increases with increasing total efficiency, that is, with decreasing source-to-detector distance, but is independent of count rate. Correction factors can be determined experimentally or calculated for nuclides with arbitrary decay scheme [Deb 79]. Since the first method involves strong source activities (measurements at far source-to-detector distances) ,which was not possible for most of the measured nuclides in this work, the calculation method was used.

To illustrate the principle a simplified scheme of a gamma-ray cascade is shown in **Fig. 3.21**. Since each γ_1 is followed by a γ_2 in coincidence (internal conversion is neglected) it may happen that both gamma-rays are detected thus leading to a single pulse. If the energy of γ_1 is totally absorbed, this sum pulse is recorded at an energy between E_1 and $E_1 + E_2$ and the event is lost from the photopeak of γ_1 ("summing-out").

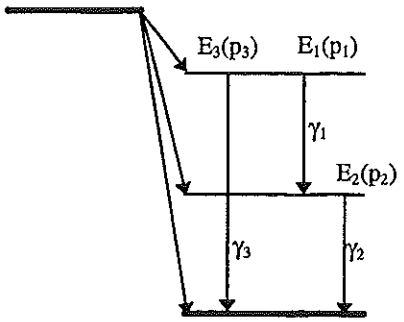

Fig. 3.21 Simplified decay scheme to illustrate the requirement for summing coincidence corrections

We get the relation

$$N_1^{'} = A \cdot p \cdot \varepsilon_{ph1} - A \cdot p \cdot \varepsilon_{ph2} \cdot \varepsilon_{t2} \qquad \textbf{(3.20)}$$

where $N_1^{'}$ is the observed photopeak count rate for γ_1 and ε_{T2} is the total efficiency for γ_2. From **(3.9)** and **(3.16)** we get the corretcion factor

$$c_{coin1} = \frac{N_1}{N_1^{'}} = \frac{1}{1-\varepsilon_{t2}}. \qquad \textbf{(3.21)}$$

For the photopeak 2 the situation is different since not each γ_2 is preceded by γ_1. Now we get

$$c_{coin2} = \frac{1}{1-\left(p_{\gamma 1} / p_{\gamma 2}\right)\varepsilon_{t1}}. \qquad \textbf{(3.22)}$$

For the photopeak γ_3 the summing of γ_1 and γ_2 leads to additional events in this peak ("summing-in"). Here we get the correction factor

$$c_{coin3} = \frac{1}{1+ p_{\gamma 1} \cdot \varepsilon_{ph1} \cdot \varepsilon_{ph2} / \left(p_{\gamma 3} \cdot \varepsilon_{ph3}\right)} \qquad \textbf{(3.23)}$$

The correction factors become more complicated when more than two photons are emitted in a cascade. The calculation of these factors, however, can be done in a similar way as explained for the example above [Deb 88]. In case of positron decay, in which the annihilation quanta are coincident with gamma-rays emitted in the deexcitation of the daughter nuclide, the decay scheme has to be suitably modified to allow for this situation. The positron branch is omitted but an electron capture branch is placed to a pseudo - level

511 keV above the level to which the positron decay occurs [McC 75]. Setting the conversion coefficient of the 511 keV pseudo-transition equal to $\alpha = -0.5$ ensures that the gamma-ray may coincide with either of the two annihilation quanta since $1/(1 + \alpha) = 2$. This simulates the fact that the two annihilation quanta are emitted in opposite directions (180°) so that only one quantum can be detected. Here the correction factor finally is

$$C_{ann} = \frac{1}{1 - 2 \cdot \varepsilon_{t511}}. \qquad (3.24)$$

Tab. 3.6 gives some calculated correction factors for samples placed directly on top of detector *Geel A*. For the other detectors similar values were obtained. The values decrease with increasing sample-to-detector distance (decreasing total efficiency).

Angular correlations between two photons usually can be neglected. The justification for this neglection can be explained by a simple consideration: Including the effect of angular correlations one has to replace ε_{t2} in **(3.21)** by $\varepsilon_{t2}\overline{W}_{12}$, where $\overline{W}_{12}$ is the directional correlation of γ_1 and γ_2 averaged over the solid angle Ω subtended by the detector. For most cascade transitions of practical interest $\overline{W}_{12}$ is in the range 1 to 1.2. For a given cascade the correlation term $\overline{W}_{12}$ is largest for small solid angles, but in that case ε_{t2} is small, so the correction factor C is commonly very near to unity. For large solid angles $\overline{W}_{12}$ could be of the order of 1.5, but the integration over the larger solid angle reduces $\overline{W}_{12}$ to near unity [Deb 88].

Tab. 3.6 Calculated coincidence summing correction factors c_{coin} for the investigated nuclides. They are given for samples placed directly on top of detector *Geel A*. For the other detectors similar values were obtained.

Nuclide	Gamma-ray energy [keV]	c_{coin}	Nuclide	Gamma-ray energy [keV]	c_{coin}
^{24}Na	1368	**1.15**	^{53}Fe	378	**1.67**
^{27}Mg	844	**1.00**	^{53m}Fe	701	**1.39**
	1014	**1.00**		1011	**1.30**
				1328	**1.19**
^{51}Ti	320	**1.00**	^{54}V	834	**1.38**
				988	**1.37**
^{51}Cr	320	**1.00**	^{54}Mn	835	**1.00**
^{52}V	1434	**1.00**	^{56}Mn	846	**1.06**
^{52}Mn	744	**1.23**	^{59}Fe	1099	**1.03**
	935	**1.25**		1292	**1.03**
	1434	**1.27**			
^{52m}Mn	1434	**1.00**	^{92m}Nb	935	**1.00**
^{53}V	1006	**1.00**			

3.4 Radiochemical Separation and Sample Preparation

Measurement of activity via X-Ray spectrometry, as applied in a few cases, demanded a special sample preparation using radiochemical methods. These methods can be divided in three parts. In the first step the radioactive product was separated from the bulk of the target material, then a thin sample was prepared for X-Ray counting, and finally the chemical yield of the first two steps was determined. The steps involved in the separation of ^{55}Fe from nickel and ^{49}V from Cr are described below. Furthermore, the preparation of a ^{48}V standard source for the Si(Li) detector calibration is outlined.

3.4.1 ^{55}Fe from Ni-Target

- **Separation**

The irradiated Ni-samples contained the long-lived radioisotopes ^{56}Co ($T_{1/2}$ = 78.8 d), ^{57}Co ($T_{1/2}$ = 271.3 d), ^{58}Co ($T_{1/2}$ = 70.8 d), ^{60}Co ($T_{1/2}$ = 5.272 a), ^{59}Fe ($T_{1/2}$ = 45.1 d) and ^{54}Mn ($T_{1/2}$ = 312.2 d). All of them could be measured via gamma-ray spectrometry. In addition some ^{55}Fe was also formed. To determine its activity via X-ray spectrometry, it was mandatory to separate the iron from the radiocobalt, radiomanganese and the thick Ni-target due to two reasons. Firstly, the soft X-rays MnK_α (5.89 keV) and MnK_β (6.49 keV) are almost completely stopped due to self-absorption. Secondly, ^{56,57,58}Co and ^{54}Mn decay with similar X-ray energies (FeK_α = 6.4 keV and CrK_β = 5.9 keV, respectively).

In order to obtain better counting statistics the pairs of samples which were irradiated under the same angle (0°, 30° and 330°, 60° and 300°, 105° and 255°, 130° and 230°, in total five samples) were dissolved in a hot solution of 50 ml conc. HCl and 20 ml 30% H_2O_2. After complete dissolution, 1.5 mg $FeCl_3$, 1 mg $MnCl_2$ and 1 mg $CoCl_2$ were added as carriers. This solution was then passed through an anion-exchange column (DOWEX 1X8, chloride form, 3 cm X 1 cm ∅) which was saturated with 8N HCl. The column was washed with 50 ml of 8N HCl (to remove nickel and manganese). Thereafter, 20 ml of 4N HCl were used to remove the cobalt from the column. The iron was finally eluted with 10 ml of 0.05N HCl. The flow chart of the whole separation is shown in **Fig. 3.22**. For further purification the eluted iron was evaporated to dryness, taken up in 8N HCl and the anion-exchange process was repeated. For quantification, the different eluents were checked via gamma-ray spectrometry of the lines 122 keV (^{57}Co), 835 keV (^{54}Mn) and 1099 keV (^{59}Fe). **Fig. 3.23** shows the gamma-ray spectrum of a Ni-target before the separation compared with the spectrum taken from the separated iron fraction. The iron was almost quantitatively (> 95 %) separated without any contamination from cobalt or manganese.

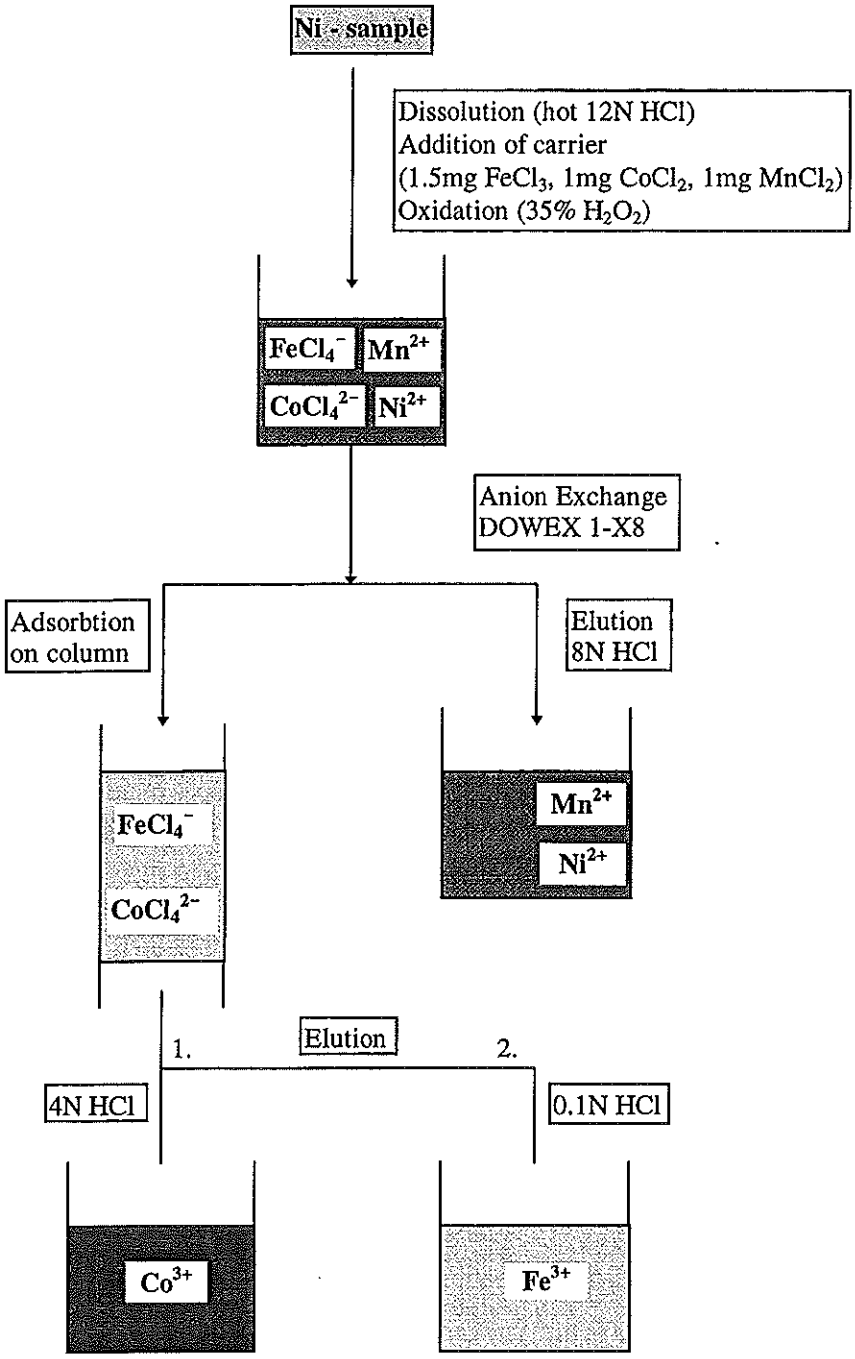

Fig. 3.22 Flow chart of the iron separation from the Ni-target by anion-exchange chromatography.

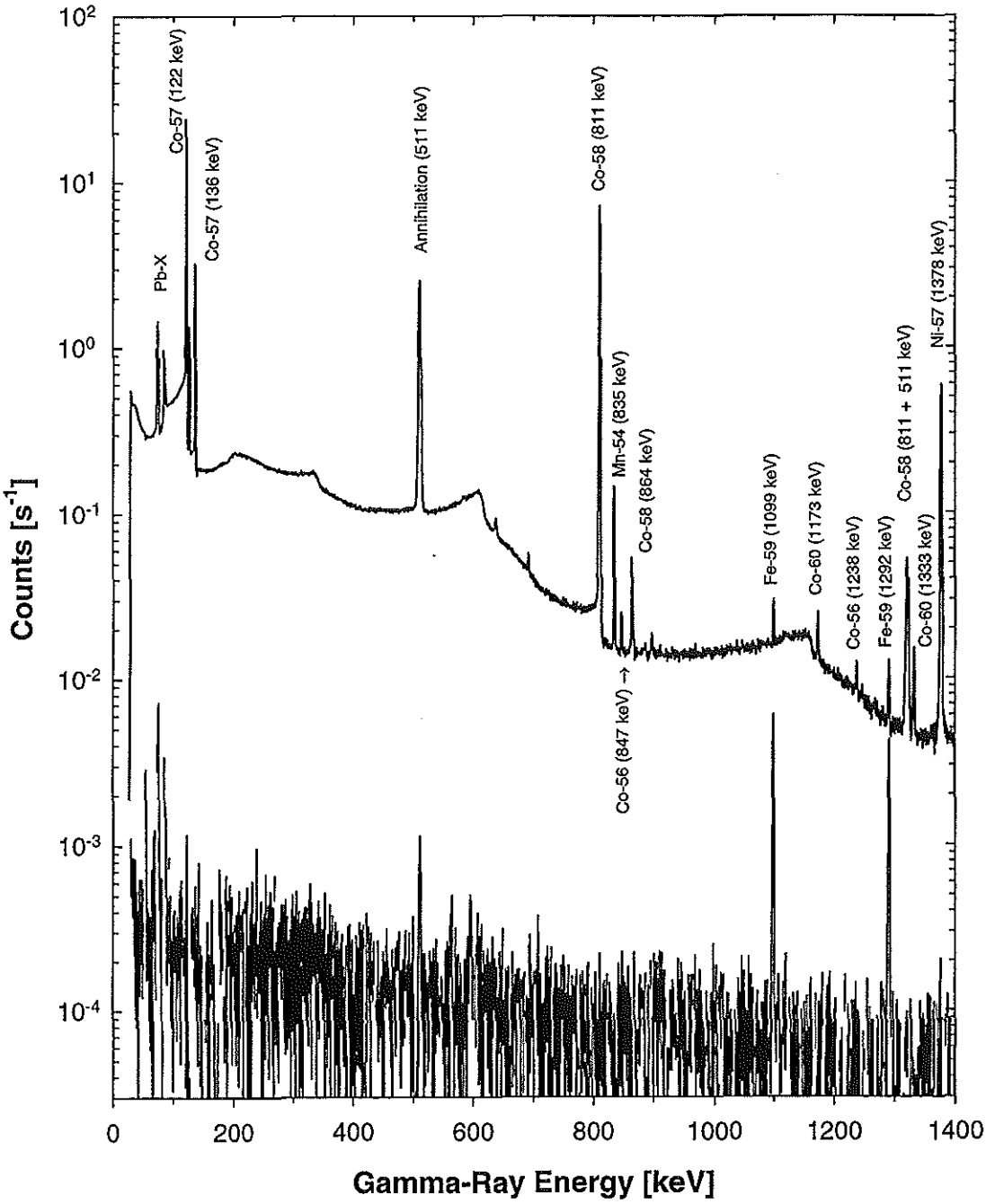

Fig. 3.23 Typical gamma-ray spectra before and after the separation of iron from nickel. The upper part shows the spectrum of the original Ni-target taken ~ 6 days after the end of irradiation (EOB). The lower part shows the spectrum of the separated iron fraction taken ~ 60 days after EOB. Both spectra are corrected for natural background.

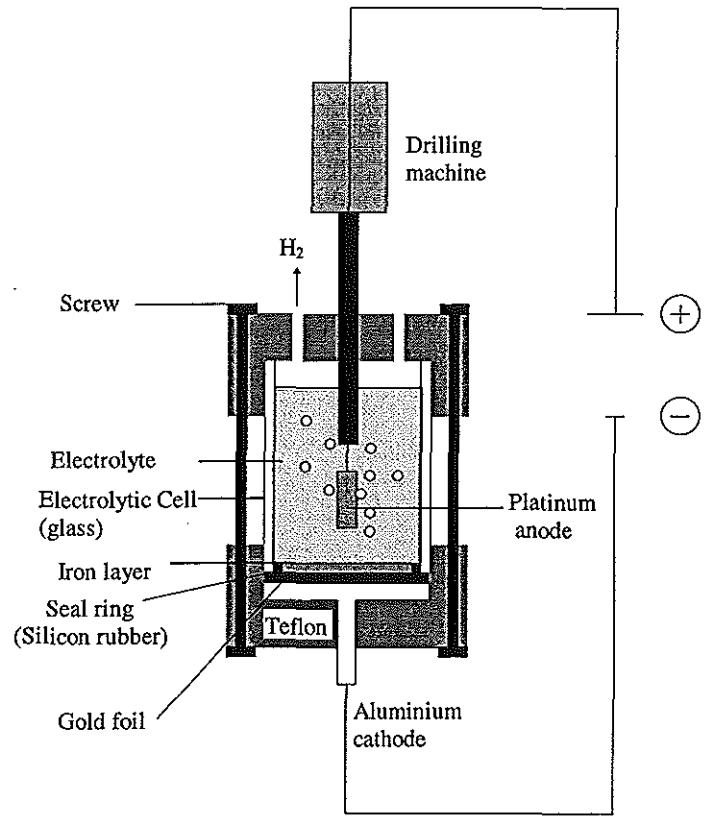

Fig. 3.24 Sketch of the electrolytic cell used for the electroplating of iron on a gold foil. The plating is carried out in an alkaline solution of Fe-citrate (pH 8.8).

- **Thin Sample Preparation**

This was carried out by an electroplating method [Hah 45]. First the iron containing eluent from the separation step was evaporated to dryness. The residue was taken up with 1 ml H_2O, 0.2 ml of a saturated Na-citrate solution and 5 mg of cevitamic acid. The pH was adjusted to 8.8 with some drops of ammonia. This solution was then transferred to a small electrolytic cell (see **Fig. 3.24** and [Qai 86, Mus 90.]). The iron is plated out on a circular gold foil (1.5 cm in diameter, 100 μm thick) at a potential of 6 V and a current of 250 mA. The diameter of the deposited iron layer was given by the diameter of the ectrolytic cell (1.0 cm). The complex formed by the mixture of these reagents is soluble and allows the plating to proceed in alkaline solution, resulting in a smooth, shiny plate. In the beginning the electrolyte has a brown colour, which gradually lightens until it is colourless when the electrolysis is complete (~1.5 - 2 hours).

- **Yield Determination**

Two independent methods were used to determine the chemical yield of the separation and electroplating steps. Firstly, the activity of ^{59}Fe was measured before and after the separation via gamma-ray spectrometry. Secondly, the electroplated iron was dissolved in 12N HCl and an UV-VIS absorption spectrum was recorded. The absorption maximum of the $[FeCl_4]^-$ complex at 362 nm was measured relative to a standard solution. This standard solution was diluted to different concentrations and for each concentration the absorption relative to a blank (H_2O) was measured (see **Fig. 3.25**). The resulting absorption values were fitted versus the Fe-concentration by a linear regression (see **Fig. 3.26**). The absorption is strongly dependent on the HCl concentration. The absorption maximum at 362.5 nm moves to lower wavelengths with decreasing acid concentration. **Fig. 3.27** shows the measured absorption spectra for different acid concentrations. For a precise Fe determination therefore a constant acid concentration has to be guaranteed. The average Fe-yield for all processed Ni targets was ~90 % after the electroplating step. The agreement between both methods was satisfactory (within 5%).

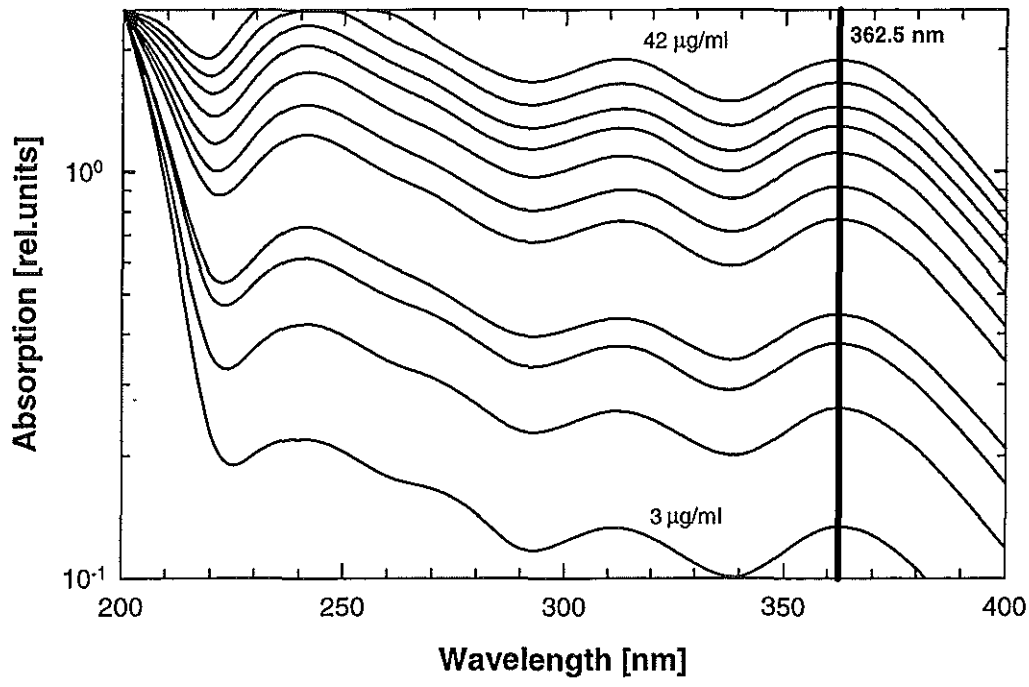

Fig. 3.25 UV-VIS absorption spectrum of the $[FeCl_4]^-$ complex in 12N HCl for different iron concentrations from 3 µg/ml to 42 µg/ml.

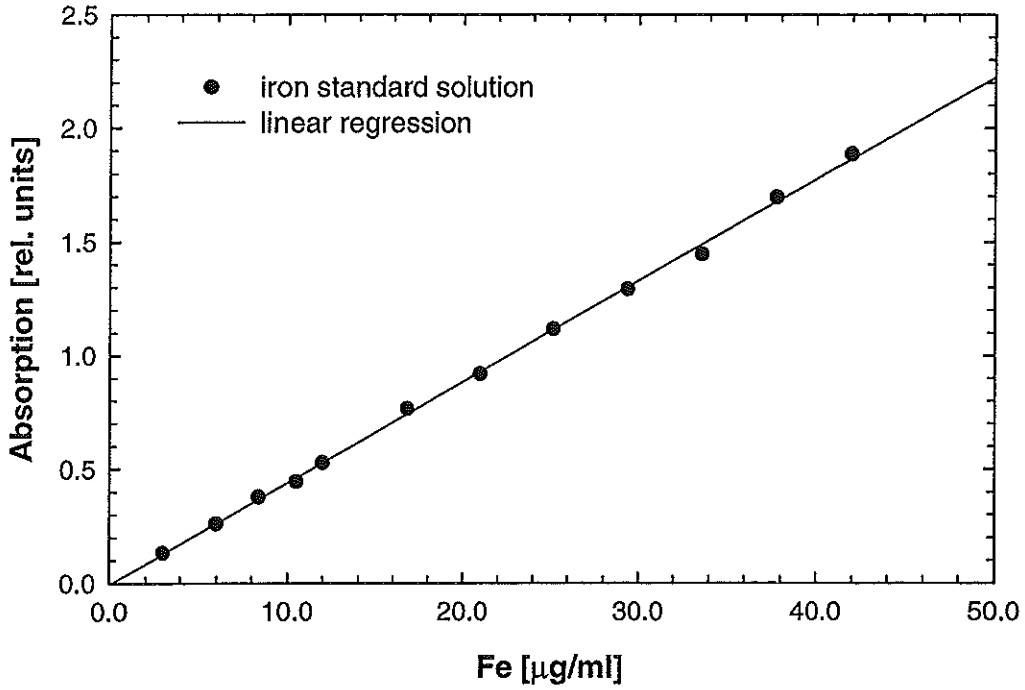

Fig. 3.26 Calibration curve for the determination of the chemical yield of iron separation via UV-VIS absorption spectroscopy.

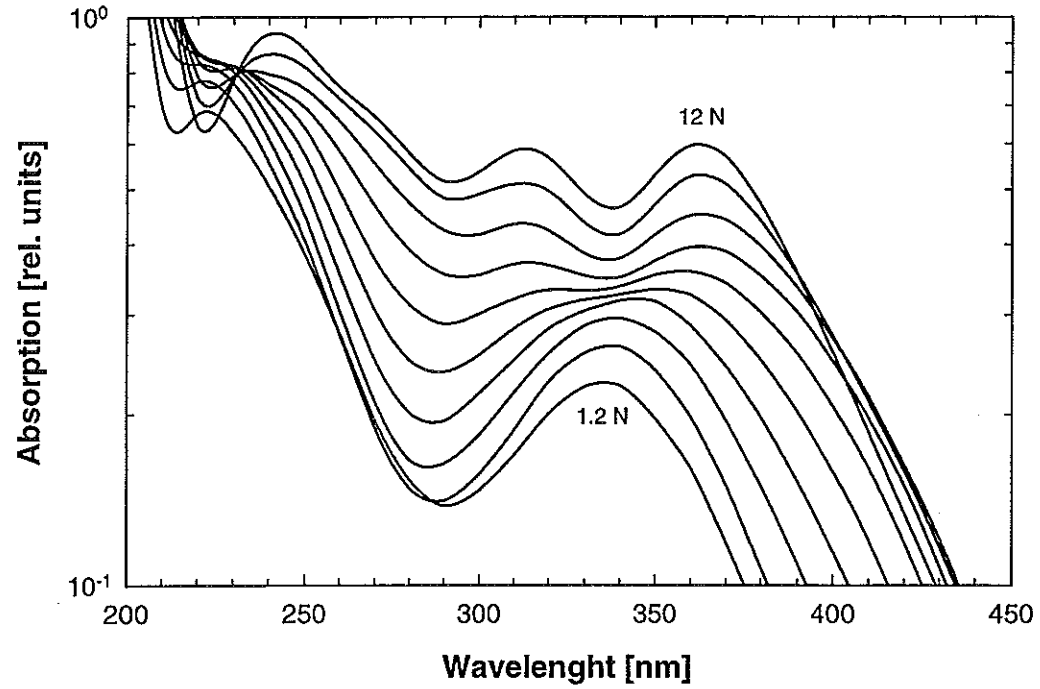

Fig. 3.27 Dependence of the absorption maximum on the HCl concentration. The Fe concentration was kept constant.

3.4.2 ^{49}V from Cr-Target

- **Separation**

As in the case of Ni-targets, the irradiated Cr-samples from the same irradiation angles were treated together (0°, 30° and 330°, 60° and 300°, 105° and 255°, in total 4 samples). The separation of vanadium from chromium was achieved by precipitating V(V) with "cupferron" (Nitro-phenyl-hydroxylamine ammonia, $C_6H_5N{\cdot}NO{\cdot}ONH_4$) [Kol 57, Pro 57] alongwith Fe(III) as collector from an acid solution (pH < 1) [Wil 53]. The iron was then separated from the vanadium by solvent extraction with di-iso-propyl ether (DIPE) [Nei 60]. The flow chart of the whole separation process is shown in **Fig. 3.28** and the procedure is described below.

The sample was dissolved in 100 ml hot 12N HCl. After complete dissolution the volume was reduced to 40 ml and 260 ml of H_2O were added. A few drops H_2O_2 were then added for complete oxidation of V(IV) to V(V). To the cold solution ~20 mg $FeCl_3$ and 1 ml of a V(V) solution (containing 2.25 mg V / ml) were added as carrier. Then, under stirring, 20 ml of a 6 % aqueous solution of cupferron were slowly thrown in at the edge of the beaker (20 % of excess cupferron is needed for complete precipitation of Fe). After one or two minutes the Fe and V got precipitated as a voluminous, red-brownish cupferron complex. An indication of the end of the Fe precipitation was the start of precipitation of the white, fine crystalline cupferron. After 20 min the precipitate was filtered through an ashless black ribbon filter, washed first with 2N HCl, then with water, dilute ammonia and again water. The filter with the precipitate was carefully ashed and finally glowed in an electric oven at 600°C ($\rightarrow Fe_2O_3$, V_2O_5). The residue was leached out with a few portions of 12N HCl, filtered (to remove traces of the ashed filter paper), evaporated to dryness and taken up in 10 ml 8N HCl. To this solution, 10 ml DIPE (saturated with 8N HCl) was added and the two phases were thoroughly mixed. The phases were allowed to separate and the DIPE phase (upper) containing Fe was withdrawn whereas the V was left in the aqueous phase. The process was repeated three more times to ensure complete separation.

- **Thin Sample Preparation**

The aqueous vanadium solution was evaporated to dryness and the residue was taken up in 1N H_2SO_4. From this solution V(IV) was recovered by precipitation as vanadate with NH_4OH. The precipitate was filtered through an ashless black ribbon filter, as done before, and the filter was ashed and glowed again at 600°C in the electric ofen. The final product, dark grey V_2O_5, was scratched from the porcelain crucible, mixed with toluol, sedimented on a thin aluminium foil (adding 1 % of organic binder, see also [Den 95]) and covered with a thin mylar foil (3 μm thick). The diameter of the vanadium layer was 0.5 cm.

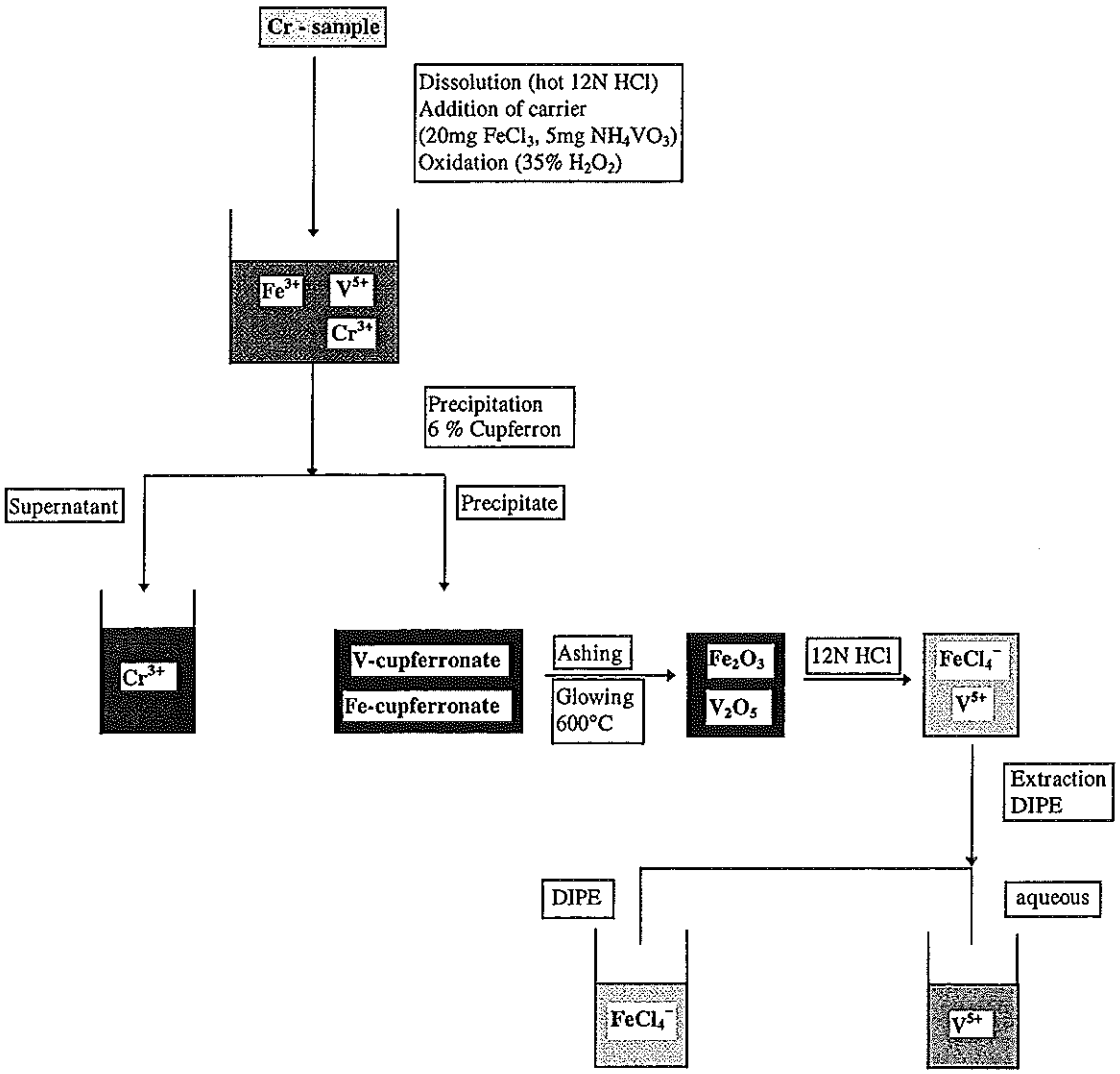

Fig. 3.28 Flow chart of the vanadium separation process from the Cr-target.

- **Yield Determination**

The yield determination was done via UV-VIS spectrometry. First the organic binder had to be removed from the aluminium backing by washing in toluol. The toluol solution, containing the V_2O_5, was filtered and the V_2O_5 was dissolved in 1N H_2SO_4. For each 10 ml of solution 0.25 ml of 3 % H_2O_2 was added and the absorption was measured at 450 nm. The red-brown colour of the acid solution of V(V) is primarily due to the formation of $VO(O_2)^+$. The amount of H_2O_2 has to be kept small otherwise the yellow $VO(O_2)_2^-$ is formed (absorption at 610 nm). The calibration was done in a similar way as for the iron determination. The absorption of different amounts of V(V) was measured and fitted versus the V(V) concentration by a linear regression. Some absorption spectra and the calibration curve are shown in **Fig. 3.29** and **Fig. 3.30**. The average vanadium yield for all processed Cr samples was ~ 50 % after the sedimentation process. The main problem occured in recovering all V_2O_5 from the porcelain crucible.

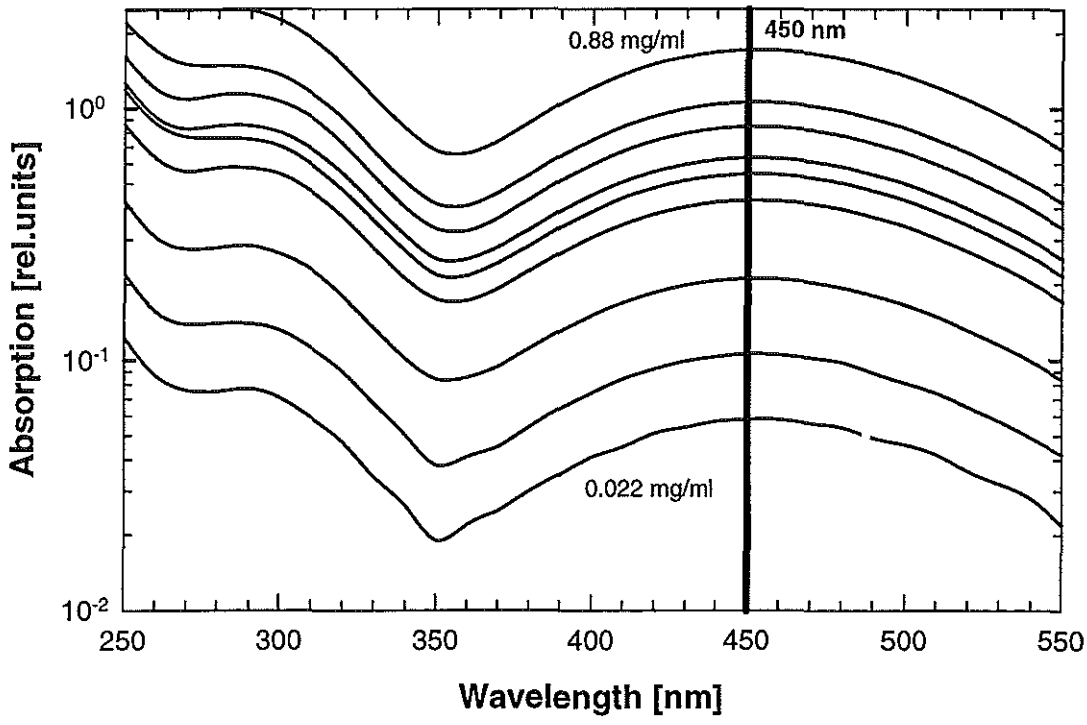

Fig. 3.29 UV-VIS absorption spectra of the $VO(O_2)^+$ complex in 1N H_2SO_4 for different vanadium concentrations from 0.022 mg/ml to 0.88 mg/ml.

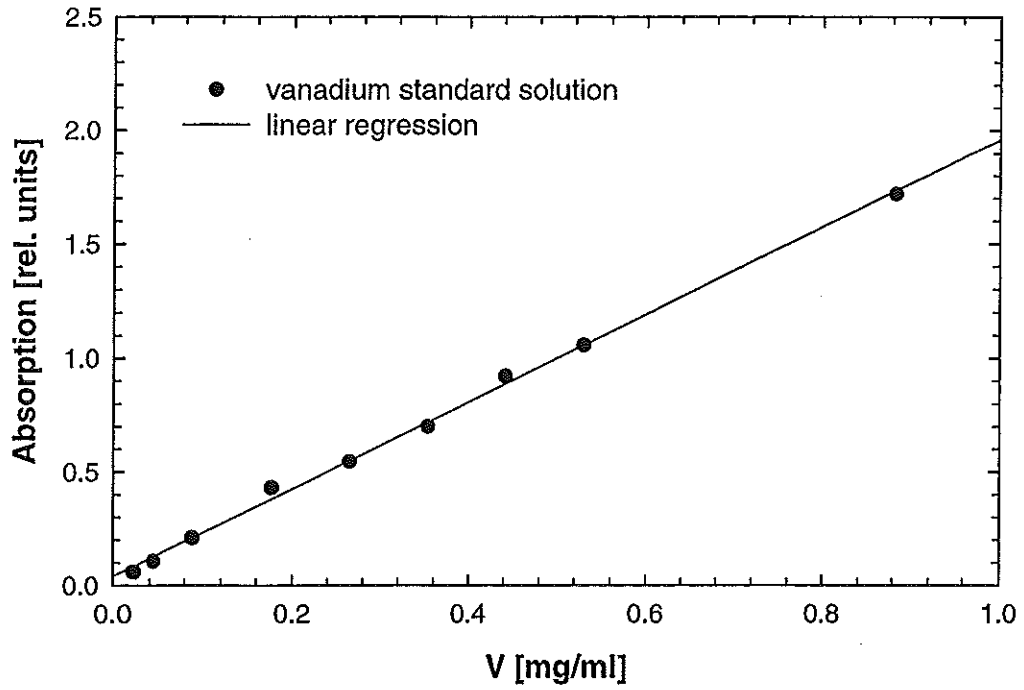

Fig. 3.30 Calibration curve for the determination of the chemical yield of vanadium separation via UV-VIS absorption spectroscopy.

3.4.3 ^{48}V Standard Source for Calibration of X-Ray Detector

Since a calibration source for the soft X-rays of ^{49}V (Ti K_α = 4.51 keV, Ti K_β = 4.93 keV) was commercially not available, a standard source had to be prepared using a different approach. One of the natural chromium foils used in this work for the cross section measurements was irradiated with 38 MeV protons at the injector cyclotron (JULIC) of the Cooler Synchroton (COSY) at the FZ Jülich. Details of the irradiation facility used for activation cross section measurements are given by Blessing et al. [Ble 95]. In the target, a large number of activation products were produced. One of those products was ^{48}V , formed via the ^{52}Cr(p,αn) and ^{50}Cr(p,^{3}He) reactions, respectively. Its decay is associated with the emission of the same X-rays as in the case of ^{49}V, but also with two strong gamma-rays (984 keV and 1312 keV with absolute emission probabilities of 100 % and 98 %, respectively) which can be used for calibration of the source via gamma-ray spectrometry. To separate the n. c. a. vanadium from the chromium target an anion-exchange method described by Kiriyama and Kuroda [Kir 83] was chosen.

- **Separation**

After the irradiation the sample was dissolved in 20 ml hot 12N HCl and the solution was evaporated to dryness. The residue was moisted with 1 ml of 12N HCl and 40 ml H_2O was then added for complete dissolution. Another 70 ml H_2O and 12 ml 30 % H_2O_2 were added and the solution passed through an anion-exchange column (DOWEX 1X8, chloride form, 3 cm x 1 cm ∅), previously conditioned with 0.1N HCl / 3 % H_2O_2 solution. Under these conditions the vanadium was strongly retained on the column whereas the chromium went into the effluent. The column was washed with several portions of 0.1N HCl / 3 % H_2O_2 solution and the vanadium was finally eluted with 20 ml of 1N HCl.

- **Thin Sample Preparation**

The eluted solution was evaporated to dryness and taken up in 10 ml of 0.01N HCl / 3 % H_2O_2 solution. A few crystals of the anion-exchange resin (DOWEX 1X8, chloride form) were added and the solution was stirred for 24 h. Thereafter the solution was filtered and the filtrate washed with 0.01 N HCl / 3 % H_2O_2. The dried resin was then placed in a small polyethylene ring (0.3 mm inner diameter, 0.1 mm thick) which was glued on a 3 µm thick mylar foil. The upper part was covered with a similar mylar foil, too.

3.5 X-Ray Spectrometry

3.5.1 Data Acquisition

The data acquisition was done in a similar way as described above for the gamma-ray spectrometry. A Si(Li) detector (4 mm in diameter, 4.59 mm thick, 0.0127 mm thick Be window) was connected to a 92X Spectrum Master and controlled with the software GAMMAVISION. The stability of the system was checked by measuring an ^{55}Fe standard source, supplied by Amersham[15], in a defined source-to-detector distance over several time intervals. The precise position of the silicon crystal was checked by axial and radial scanning of this source over the detector surface (see below). The measurement of each separated ^{55}Fe sample usually lasted one week, resulting in 1000 to 2000 counts under the photopeak. The ^{49}V samples were somewhat weaker and needed two weeks to obtain similar statistics. The spectrum analysis was done with a beta version of the program X-RAY [Wes 95] , a similar program as GAMMA-W which was used for the gamma-ray spectrum analysis. Corrections due to self-absorption were applied as explained in **section 3.3.4**. They were in the order of 5 to 8 % for the Fe and 20 to 25 % for the vanadium samples. The X-ray energies and emission probabilities for the measured nuclides are listed in **Tab. 3.7**.

[15] Amersham / Buchler GmbH & Co KG, Braunschweig, Germany

3.5.2 Si(Li) Detector Efficiency

The efficiency calibration was done in a different way than described in **section 3.3.3** for the HPGe detectors. Here no efficiency curve could be recorded due to the lack of a set of adequate calibrated sources. The only available calibrated source was the ^{55}Fe point source. Therefore, the ^{55}Fe samples were measured relative to this standard source. To apply corrections for disk type sources the standard was measured in various positions out of the centre, the same procedure as used for the HPGe detectors. **Fig. 3.31** shows the efficiency ratio for different out of centre distances to the efficiency at the centre versus the distance from the detector axis. The ratio slowly decreases with increasing distance, with a sharp drop to zero response at the edge of the crystal.

The efficiency calibration for the ^{49}V measurements was done with the self-prepared ^{48}V source (see **section 3.4.3**). Therefore, first the absolute activity of this source had to be determined by gamma-ray spectrometry. The source was measured several times at 20 cm distance to avoid any type of corrections (solid angle, coincidence summing etc.) and an absolute activity of 395 ± 15 Bq was determined via the 984 keV and 1312 keV gamma-ray lines. Then, 5 X-ray measurements were carried out over a time period of 5 months, in order to allow the complete decay of ^{48}V ($T_{1/2}$ = 15.97 d) and to be able to determine the ^{49}V activity ($T_{1/2}$ = 330 d), which was also present in the sample (produced via the ^{52}Cr(p,α)^{49}V reaction), by a least-squares fitting of the complex decay curve. The curve is plotted in **Fig. 3.32**. The activity of ^{49}V at EOB was 7 % of the total activity. The ^{48}V photopeak count rate was now used to determine the detector efficiency according to **(3.9)**. Thereafter, all ^{49}V samples were measured relative to this standard.

Tab. 3.7 X-ray energy and emission probability of the investigated nuclides. ^{48}V was needed for the Si(Li) calibration [Fir 96].

Nuclide	Transition	Energy [keV]	Probability
^{55}Fe	MnK$_\alpha$	5.89	0.249(9)
	MnK$_\beta$	6.49	0.034(1)
^{48}V	TiK$_\alpha$	4.51	0.0843(17)
	TiK$_\beta$	4.93	0.0094(5)
^{49}V	TiK$_\alpha$	4.51	0.171(9)
	TiK$_\beta$	4.93	0.0191(9)

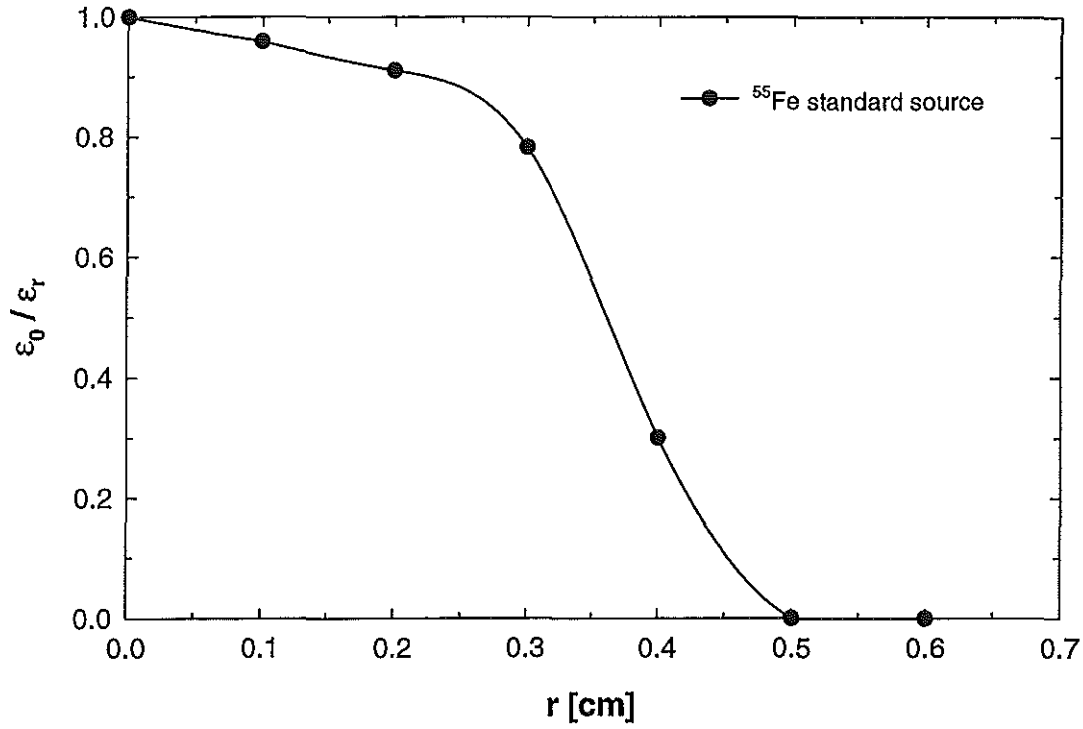

Fig. 3.31 Radial dependence of the efficiency of the Si(Li) detector (r = off-centre distance).

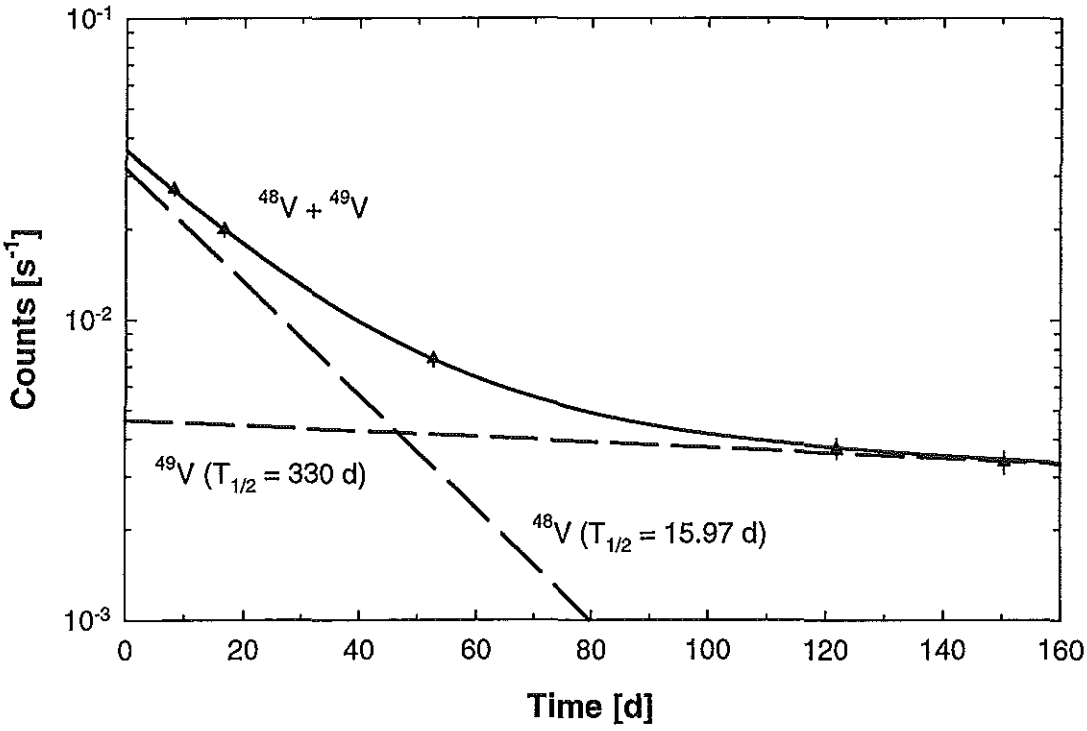

Fig. 3.32 Decay curve of the self-prepared ^{48,49}V standard source. The symbols represent the experimental data points, the dashed lines the individual count rates from ^{48}V and ^{49}V and the solid line the summed count rate.

3.6 Data Processing

3.6.1 Experimental Cross Sections

The activity of the reaction products was calculated from the net count rate under the photopeak determined by gamma- or X-ray spectrometry. Substituting the activity **A** and the number of target atoms **N** in **(1.7)** by

$$A = \frac{N_{ph}}{p_\gamma \varepsilon_{ph}\left(1-e^{-\lambda t_m}\right)} c_1 c_2 \ldots c_n \qquad (3.25)$$

and

$$N = \frac{m \cdot a \cdot N_A}{M} \qquad (3.26)$$

leads to an expression for the cross section

$$\sigma = \frac{\lambda \cdot N_{ph} \cdot \Phi_0 \cdot M}{p_\gamma \cdot \varepsilon_{ph} \cdot m \cdot a \cdot N_A} \cdot \frac{1}{\left(1-e^{-\lambda t_i}\right)} \cdot \frac{1}{\left(1-e^{-\lambda t_m}\right)} \cdot \frac{1}{e^{-\lambda t_c}} \cdot \frac{\prod_i c_i}{c_{vol}} \,, \qquad (3.27)$$

where **m** is the sample mass, **M** the molar mass, **a** the isotopic abundance of the target nuclide, N_A the Avogadro Number, t_m the measuring time and $c_i = c_{gas}, c_{low}, c_{flux}, c_{coin}, c_{scat}$). Corrections for the gamma-ray self-absorption **T(x)** and for the flux gradient in the sample c_{grad} are included in the term c_{vol} (see **section 3.3.3**). The term c_{gas} disappears in the case of a solid target.

To avoid the determination of the absolute neutron flux, finally all cross section values were obtained relative to the standard cross sections of the reactions $^{27}Al(n,p)^{27}Mg$, $^{27}Al(n,\alpha)^{24}Na$, $^{56}Fe(n,p)^{56}Mn$ and $^{93}Nb(n,2n)^{92m}Nb$ (all taken from [Koc 93], see **section 1.4.2**). Using **(3.26)** for the sample and the reference reaction and forming the ratio leads to the following expression for the cross section

$$\sigma = \sigma^r \frac{N_{ph}}{N_{ph}^r} \frac{p_\gamma^r \varepsilon_{ph}^r}{p_\gamma \varepsilon_{ph}} \frac{m^r a^r M}{m\, a\, M^r} \frac{\left(1-e^{-\lambda^r t_i}\right)}{\left(1-e^{-\lambda t_i}\right)} \frac{e^{-\lambda^r t_c}}{e^{-\lambda t_c}} \frac{\lambda\left(1-e^{-\lambda^r t_m}\right)}{\lambda^r\left(1-e^{-\lambda t_m}\right)} \cdot \frac{c_{vol}^r \prod_i c_i}{c_{vol} \prod_i c_i^r} \qquad (3.28)$$

where the index **r** denotes the variables for the reference reaction. In cases where two or more reference reactions were used the weighted mean $\mathbf{m^w}$ of the individual results $\mathbf{x_i}$ was calculated. It is given by

$$m^w = \frac{\sum_{i=1}^{n}\left(\frac{x_i}{s_i^2}\right)}{\sum_{i=1}^{n}\left(\frac{1}{s_i^2}\right)} \tag{3.29}$$

and

$$\frac{\Delta m^w}{m^w} = \left[\sum_{i=1}^{n}\left(\frac{1}{s_i^2}\right)\right]^{-1/2} \tag{3.30}$$

where $\mathbf{s_i}$ denotes the standard deviation of $\mathbf{x_i}$. **Tab. 3.8** gives the neutron fluence obtained via three different reference reactions for the irradiation of ^{nat}Cr foils at *Geel 1*. The agreement between the individual results is in the order of 5 %. If some cross section measurements at a given neutron energy were repeated several times the cross section is given as a weighted mean.

When two different reactions produce the same activity in one sample, e. g. the active product ^{52}V in the reactions ^{53}Cr(n,np) and ^{52}Cr(n,p) while using natural chromium samples, the cross sections for those reactions were deduced in the following way. Two irradiations were performed with samples of different target constituents. For the above mentioned reaction an irradiation had to be performed with a chromium sample enriched in ^{53}Cr. The mean production rates $\mathbf{PR_1}$ and $\mathbf{PR_2}$ of the activities in the two samples are

$$PR_1 = N_{11}\sigma_1 + N_{12}\sigma_2 \tag{3.31}$$

$$PR_2 = N_{21}\sigma_1 + N_{22}\sigma_2 \tag{3.32}$$

Solving these equations leads to the cross sections σ_1 and σ_2

$$\sigma_1 = \frac{N_{22}PR_1 - N_{12}PR_2}{N_{11}N_{22} - N_{21}N_{12}} \tag{3.33}$$

$$\sigma_2 = \frac{N_{11}PR_2 - N_{21}PR_1}{N_{11}N_{22} - N_{21}N_{12}} \tag{3.34}$$

where

N_{11} is the number of target nuclei for the reaction 1 in the sample 1,
N_{12} is the number of target nuclei for the reaction 1 in the sample 2,

N_{21} is the number of target nuclei for the reaction 2 in the sample 1,
N_{22} is the number of target nuclei for the reaction 2 in the sample 2.

Tab. 3.8 Neutron fluence determination via different reference materials and reactions.

Neutron energy	Neutron fluence [$cm^{-2} s^{-1}$] (uncertainty [%])				Neutron energy	Neutron fluence[$cm^{-2} s^{-1}$] (uncertainty [%])			
	$^{56}Fe(n,p)$ ϕ_1	$^{27}Al(n,p)$ ϕ_2	$^{27}Al(n,\alpha)$ ϕ_3	weighted mean ϕ_{mean}		$^{56}Fe(n,p)$ ϕ_1	$^{27}Al(n,p)$ ϕ_2	$^{27}Al(n,\alpha)$ ϕ_3	weighted mean ϕ_{mean}
13.71		2.12E6 (9.70)	2.10E6 (8.30)	2.11E6 (6.31)	17.8	2.38E6 (15.90)	2.01E6 (16.10)	2.05E6 (8.00)	2.10E6 (6.53)
13.71		1.61E6 (9.40)	1.54E6 (11.90)	1.58E6 (7.38)	17.8	1.20E7 (8.80)	1.04E7 (6.60)	1.15E7 (6.30)	1.12E7 (4.05)
15.01	8.27E6 (6.30)	8.59E6 (7.00)	8.60E6 (5.90)	8.49E6 (3.67)	18.73		9.20E6 (8.20)	8.88E6 (6.80)	9.01E6 (5.23)
15.01	5.34E6 (7.60)	5.02E6 (6.00)	5.27E6 (8.50)	5.17E6 (4.12)	18.73		8.85E6 (7.40)		8.85E6 (7.40)
15.95	3.70E7 (7.50)	3.38E7 (5.50)	3.66E7 (4.60)	3.57E7 (3.19)	19.7	9.09E6 (8.80)	8.82E6 (5.20)	8.76E6 (6.20)	8.85E6 (3.63)
15.95		4.01E7 (5.80)	4.21E7 (5.00)	4.12E7 (3.79)	19.7	1.28E7 (12.90)	1.29E7 (7.70)	1.08E7 (8.10)	1.20E7 (5.12)
17.54	4.24E6 (5.80)	4.02E6 (6.50)	4.10E6 (7.90)	4.13E6 (3.80)	21.7		2.29E7 (8.00)	1.93E7 (8.40)	2.12E7 (5.79)

3.6.2 Experimental Isomeric Cross Section Ratios

- **$^{54}Fe(n,t)^{52m,g}Mn$**

The level and decay schemes of the isomeric pair are shown in **Fig. 3.33**. The metastable ^{52m}Mn decays almost completely via positron emission to the 1434 keV level of the stable ^{52}Cr. Since the half-lives of the metastable ($T_{1/2}$ = 21 m) and the ground state ($T_{1/2}$ =5.59 d) are too different, the cross sections had to be determined in two independent measurements. The metastable state was measured via the 1434 keV gamma-ray whereas the 744 keV (from the level 3114 keV) and 936 keV (from the level 2370 keV) gamma-rays served for the measurement on the ground state. The ratio σ_m / σ_m + σ_g was then calculated from the individual cross sections.

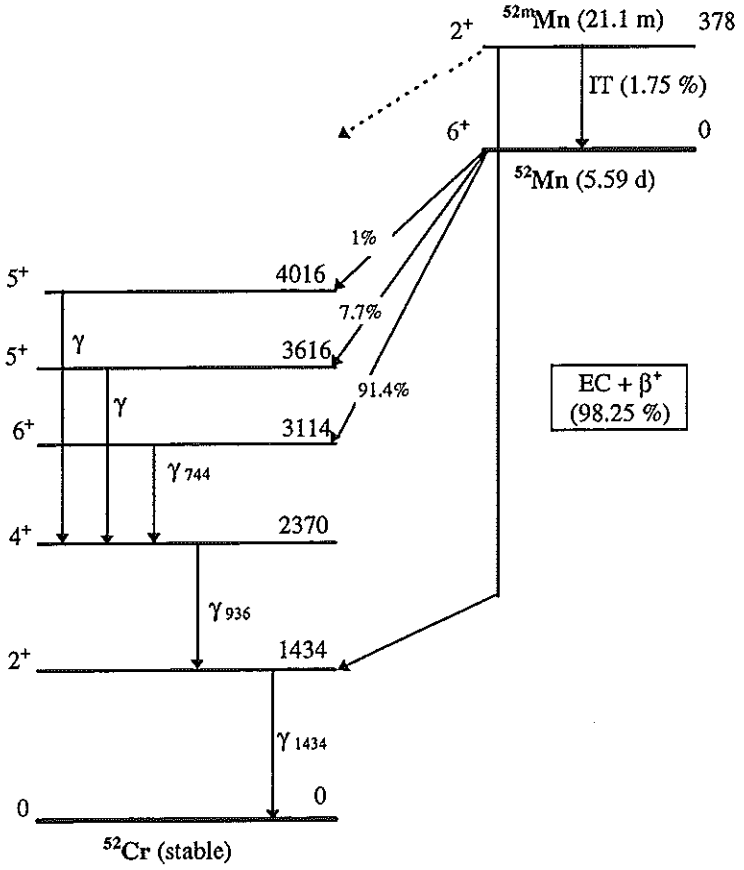

Fig. 3.33 Simplified level and decay scheme of the isomeric pair ^{52m,g}Mn.

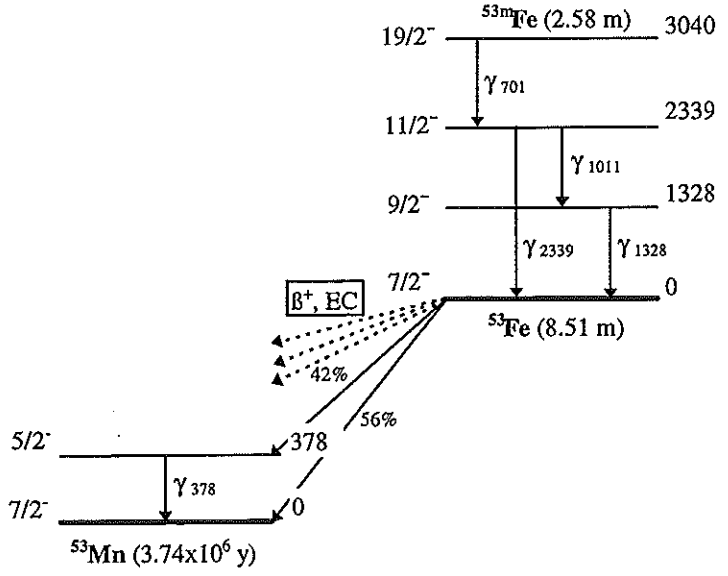

Fig. 3.34 Simplified level and decay scheme of the isomeric pair ^{53m,g}Fe.

- $^{54}Fe(n,2n)^{53m,g}Fe$

The metastable state decays 100% via IT. The level and decay scheme is illustrated in **Fig. 3.34**. Here the ICSR was determined according to (**1.14**). Substituting again the activity by (**3.25**) leads to

$$\frac{\sigma_m}{\sigma_g} = \left[\frac{\lambda_g \left(1-e^{-\lambda_m t_i}\right) e^{-\lambda_m t_c} \left(1-e^{-\lambda_m t_m}\right)}{\lambda_m \left(1-e^{-\lambda_g t_i}\right) e^{-\lambda_g t_c} \left(1-e^{-\lambda_g t_m}\right)} \cdot \left(\frac{\prod_i c_i^g}{\prod_i c_i^m} \frac{N_{ph}^g p_\gamma^m \varepsilon_{ph}^m}{N_{ph}^m p_\gamma^g \varepsilon_{ph}^g} - p \frac{\lambda_g}{\lambda_g - \lambda_m} \right) + p \frac{\lambda_m}{\lambda_g - \lambda_m} \right]^{-1} \tag{3.35}$$

The correction factors c_i are similar to those described in **section 3.6.1** . Factors like c_{grad} or c_{disk} do not have to be considered since they are the same for both states.

The activity of the ground state was measured via the 378 keV gamma-ray whereas for the metastable state the peak areas of the gamma-rays of 701, 1011 and 1328 keV were averaged (weighted with their emission probabilities). Several individual ICSR measurements at the same neutron energy were then weighted to obtain a mean value.

3.6.3 Uncertainties

The sources of uncertainties and their estimated magnitudes are given in **Tab. 3.9**. The total uncertainties s_σ of the measured cross sections σ were obtained by quadratically summing up all the individual uncertainties s_i according to the law of error propagation. Correlations were not taken into account. It is

$$s_\sigma = \left[\sum_{i=1}^{n} \left(\frac{\partial \sigma}{\partial x_i} \right)^2 s_{x_i}^{\ 2} \right]^{1/2} \tag{3.36}$$

where s_σ is the standard deviation in σ.

Tab. 3.9 Principal sources of uncertainty and their estimated magnitudes in %.

Source of uncertainty	Symbol	Resulting uncertainty [%]
net peak count rate (counting statistics and peak area determination)	s_{net}	1.0 - 20.0
detector efficiency a) HPGE detector (gamma-rays) b) Si(Li) detector (X-rays)	s_{ε}	 1.5 - 3.0 5.0 - 8.0
gamma-ray emission probability	$s_{p\gamma}$	0.1 - 2.0
half-life of activity	s_{λ}	0.1 - 4.0
irradiation time	s_{ti}	0.1 - 3.0
cooling time	s_{tc}	0.1 - 1.0
counting geometry	s_{geo}	1.0 - 5.0
coincidence summing correction	s_{coin}	0.0 - 3.0
gamma-ray absorption (transmission)	s_{T}	0.1 - 3.0
sample mass (weight and homogeneity)	s_{m}	0.1- 5.0
activity induced by background neutrons a) gas-in / gas-out b) breakup c) low energy	s_{low}	 0.5 - 2.0 0.0 - 2.0 0.0 - 10.0
neutron flux fluctuation	s_{flux}	0.1 - 0.5
neutron multiple scattering	s_{scat}	0.0 - 10.0
reference cross section	s_{ref}	0.5 - 4.0
total uncertainty	s_{σ}	5.0 - 25.0

4. Nuclear Model Calculations

4.1 Introduction

Neutron cross section calculations started to play an important role in the data evaluation process from the beginning of the eighties, a progress which was favoured by achievements in the seventies regarding the use of nuclear models and related computer codes. Since neutron, charged-particle and gamma-ray emission cross sections (as a function of energy and angle) are important for many applications, extensive efforts have been devoted to reproduce the rather scarce experimental data and to use realistic models to provide reliable interpolation and extrapolation to other energy and angular regions where no data are available. The main improvements in the calculational methods consisted of

- a unified description of the pre-equilibrium (PE) and equilibrium processes or, at least, a unitary use of the common parameters for both reaction mechanisms,
- the use of consistent input parameters, determined or validated by means of various independent experimental data, and
- a unitary account of a whole body of related data for an isotope chain or neighbouring elements (e. g. [Avr 87b, Avr 88a, Avr 90].

Examples of model codes of this type, i. e. Hauser-Feshbach (HF) codes with precompound option, are GNASH [You 77], GRAPE [Gru 85], MAURINA [Uhl, unpublished], SINCROS-II [Yam 90], STAPRE [Uhl 76], STAPRE-H [Avr 87b] and TNG [Fu 80, SH 86].

In the present work, the STAPRE-H code was used to perform a comprehensive set of nuclear model calculations for neutron activation reactions on Cr, Fe and Ni, guided by the determined experimental data. The aim was to achieve a better understanding of nuclear models for this particular mass range (A ~ 50) and type of reactions and therefore to improve the reliability of extrapolations based on these models. As an example, excitation curves will be given for two reactions on an unstable nucleus, namely the $^{51}Cr(n,p)^{51}V$ and $^{51}Cr(n,np)^{50}V$ reactions, calculated with parameters established by the good reproduction of 8 reactions on different stable Cr-isotopes. This is a so-called "blind" calculation since no experimental data of any type can be measured and thus a parameter adjustment is not possible.

4.2 The Code STAPRE-H

4.2.1 General Remarks

STAPRE-H [Avr 87a] is an extension of the computer code STAPRE [Uhl 76] which is designed to calculate energy-averaged cross sections for particle-induced nuclear reactions with several emitted particles and gamma-rays under the assumption of sequential evaporation. Both codes are written in FORTRAN and are available from the NEA Data Bank[16]. The original STAPRE code takes into account

- ◊ equilibration of the compound system formed in the first stage of a reaction by means of the particle precompound emission exciton model (EM) [Gri 66, Cli 71, Bra 72, Kal 75],
- ◊ statistical de-excitation in the frame of the Hauser-Feshbach-Moldauer (HFM) model with consideration of angular momentum and parity conservation [Hau 52, Mol 64],
- ◊ intermediary gamma-ray cascades,
- ◊ fission mechanism.

The extensions in STAPRE-H are mainly

- ◊ calculation of particle transmission coefficients by means of the spherical optical model code SCAT 2 [Ber 81] as a subroutine,
- ◊ inclusion of the pre-equilibrium emission geometry-dependent hybrid (GDH) model code HYBRID [Bla 73] as a subroutine with a version including the angular momentum, parity conservation and alpha-particle emission,
- ◊ computation of the nuclear level densities taking into account the analytical formulas of Ignatyuk et al. [Ign 75] and Schmidt et al. [Sch 82b] for higher excitation energies with an interpolation range between them and the back-shifted Fermi-gas (BSFG) model [Lan 66, Von 69, Dil 73] which is used at medium excitation energies,
- ◊ inclusion of the energy-dependent Breit-Wigner model (EDBW) [Gar 79, Gar 81] for the electric dipole gamma-ray strength function evaluation.

For a specified sequence of emitted particles the following quantities can be obtained for all nuclei involved in the cascade

- ◊ activation cross sections,
- ◊ population of isomeric states,
- ◊ production cross sections for gamma-rays from low excited levels,
- ◊ energy spectra for all emitted particles,
- ◊ gamma-ray production spectra.

[16] Nuclear Energy Agency, Issy-les Moulineaux, France

In the following the main steps of the nuclear model calculations done by STAPRE / STAPRE-H are briefly described (for a complete description of STAPRE see [Uhl 76, Uhl 81] and STAPRE-H see [Avr 87a, Avr 88b, Avr 88c, Avr 95a]). Thereafter some aspects of the treatment of PE emission and the calculation of level densities by different approaches are outlined.

4.2.2 Formalism and Program Flow

The different ways of populating a particular state of a final nucleus in a particle-induced nuclear reaction are illustrated in **Fig. 4.1**. In the first step of a nuclear reaction the incident particle π_0, and the target nucleus **T** are assumed to form a composite system, formally called first compound nucleus (1st CN) even if not yet in the equilibrium stage. Emission of the (i - 1) particle of a specified sequence (π_1, π_2, π_3, ...) is regarded as leading to the population of the **i**th CN (i ≥ 2). The de-excitation of each CN can proceed through emission of particles (n, p, α, d) and gamma-rays or by fission.

In the first step of the evaporation cascade pre-equilibrium particle emission is taken into account in the frame of either the EM, the GDH model or the modified GDH model including angular momentum and parity conservation. The results of this calculation are

- the PE emission differential cross sections which finally contribute to the particle production spectra calculation
- the PE contribution to the initial population of the 2nd CN (if the modified GDH model including angular momentum and parity conservation is used)
- the fraction of the 1st CN initial population surviving PE emission.

For that fraction of the population of the composite system that survives PE decay the well-known Hauser Feshbach-Moldauer (HFM) formula is applied.

$$\sigma_{cc'}^{(HFM)}(E,J,\Pi)=\frac{\pi}{k^2}\cdot g(J)\cdot\frac{T_c\,T_{c'}}{N_1(E,J,\Pi)}\cdot S_{cc'}(E,J,\Pi)\cdot\rho_{c'}(E,J,\Pi) \qquad (4.1)$$

where **k** is the wave number of the relative motion, **g(J)** is a statistical factor, $\mathbf{T_c}$ and $\mathbf{T_{c'}}$ the transmission coefficients for the entrance and outgoing particle channels, $\mathbf{S_{cc'}}$ is the width fluctuation correction and $\rho_{c'}$ the level density of the residual nucleus. The HF denominator $\mathbf{N_1}$ consists of the sums of the transmission coefficients for all open channels consistent with angular momentum and parity selection rules

$$N_1(E,J,\Pi)=\sum_c T_c = N_1^{part}(E,J,\Pi)+N_1^{\gamma}(E,J,\Pi)+N_1^{f}(E,J,\Pi) \qquad (4.2)$$

In case that a particle is evaporated before reaching the equilibrium, the corresponding PE contribution is added to the Hauser-Feshbach cross section. From the HF formula the following quantities are derived

- ◊ the equilibrium first chance particle emission differential cross sections
- ◊ the HF contribution to the initial population of the 2nd CN
- ◊ the first chance photon emission
- ◊ the first chance fission cross sections

All further evaporations are treated within the conventional evaporation model, giving the primary populations combined with a gamma-ray cascade model [Uhl 70, Uhl 76, Str 80]. From this quantity the activation cross section, population of isomeric states and related results for the i^{th} CN are obtained.

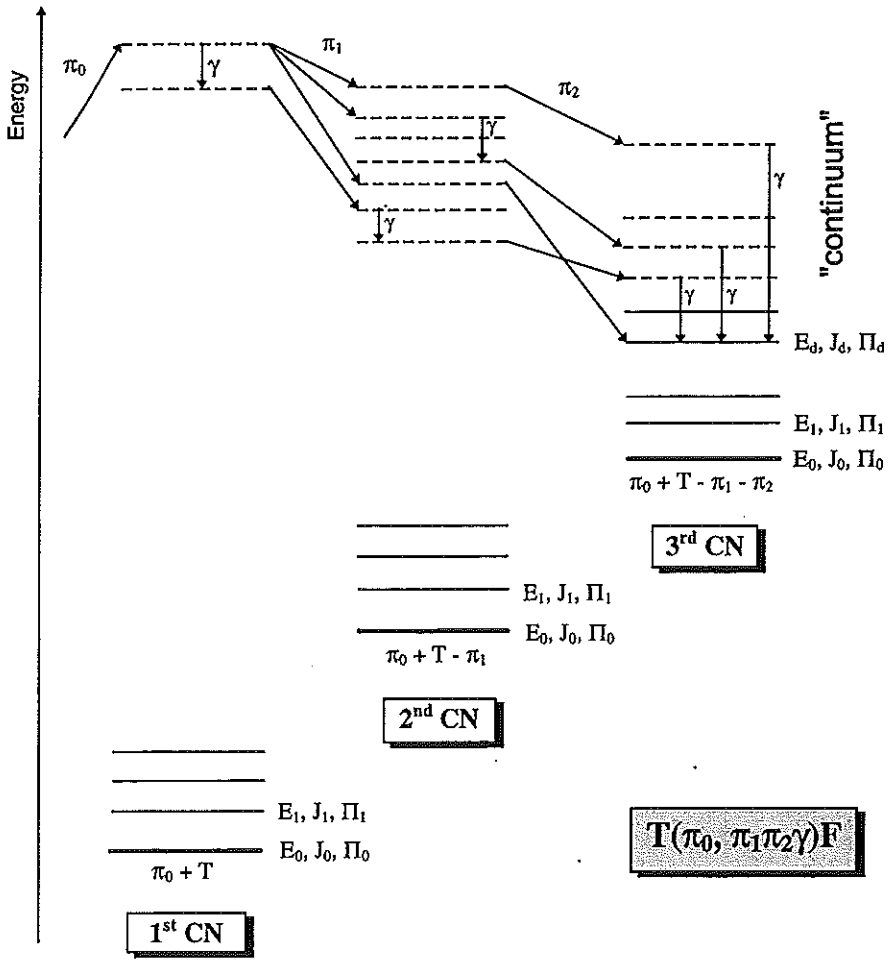

Fig. 4.1 Schematic representation of the different ways of populating final levels (E_D, J_D, Π_D) in a reaction $T(\pi_0, \pi_1\pi_2\gamma)F$ (taken from [Uhl 76]). In the continuum region transitions between energy bins rather than individual levels are illustrated.

4.2.3 Pre-Equilibrium Emission (PE)

Since the basic work of Griffin [Gri 66] a variety of pre-equilibrium models have been developed (see reviews [Bla 75, Gad 76, Dun 78]. The most widely used models are the intranuclear cascade (INC) model, the Harp-Miller-Berne (HMB) model [Har 68], the exciton model (EM) and the geometry-dependent hybrid (GDH) model. These are all semi-classical models which provide a simple means of calculating the energy distributions of the emerging particles, using parametrized expressions for the interaction matrix. In more recent years fully quantum-mechanical theories have been developed that provide, at least in principle, a parameter free method of calculating the required cross section [Tam 77, Tam 82, Fes 80, Fes 85]. The semi-classical models are conceptually simpler, more flexible and the corresponding computer codes are generally much faster. Therefore, they have become the most popular PE models for applications in nuclear data evaluation [Hod 88].

In the following the basic features of the EM and GDH model, which are optionally used in the STAPRE-H calculations, are briefly described.

- **Exciton model (EM)**

The EM assumes that, after the initial interaction between the incident particle and the target nucleus, the excited system can pass through a series of states of increasing complexity before equilibrium is reached, and emission of particles may occur from all intermediate states. The different states of the system are classified according to the number of particles **p** and holes **h** excited, called excitons **n = p + h**. The application of a two-body interaction to states of a (p,h) configuration leads to states with (p+1, h+1), (p,h) or (p-1, h-1) excited particle. For all these processes transition rates averaged over all states of a configuration are employed. Let b^k (n) = b^k (p,h) be the population probability of the states of a (p,h) configuration resulting from **k** internal transitions. The corresponding quantity b^{k+1}(n) for **k+1** internal transitions is obtained from

$$b^{k+1}(n) = b^k(n+2)\frac{\lambda^-(n+2)}{\lambda(n+2)} + b^k(n)\frac{\lambda^0(n)}{\lambda(n)} + b^k(n-2)\frac{\lambda^+(n-2)}{\lambda(n-2)} \qquad \textbf{(4.3)}$$

where

$$\lambda(n) = \lambda^-(n) + \lambda^+(n) + \lambda^0(n) + \lambda^e(n) \qquad \textbf{(4.4)}$$

and

$$\lambda^e(n) = \sum_\nu \int d\varepsilon_\nu \lambda^e_\nu(n, \varepsilon_\nu) \qquad \textbf{(4.5)}$$

λ^+**(n)**, λ^0**(n)** and λ^-**(n)** are the internal average transition rates for **n** → **n + 2** , **n** → **n** and **n** → **n - 2**, respectively, and λ^e**(n)** represents the total rate for emission of particles. The initial condition for solution of these equations is

$$b^0(p,h) = \delta(p,p_0)\delta(h,h_0) \tag{4.6}$$

where the initial particle number is $\mathbf{p_0 = 2}$ and the initial hole number is $\mathbf{h_0 = 1}$. The PE contribution to the differential cross section is given by

$$\frac{\partial\sigma^{pre}_{\pi_0\pi_1}}{\partial\varepsilon_1}d\varepsilon_1 = \sigma^{non}_{\pi_0}\sum_{k=0}^{k}\sum_{n} b^{(k)}(n)\frac{\lambda^e_{\pi_1}(n,\varepsilon_1)}{\lambda(n)}d\varepsilon_1 \tag{4.7}$$

where $\sigma^{non}_{\pi_0}$ represents the optical model absorption cross section for the projectile π_0 and $\lambda^e_{\pi_1}(n,\varepsilon_1)$ is the average rate for emission of a particle π_1 with energy of relative motion ε_1.

The internal transition rates are calculated using Fermi's "Golden Rule":

$$\lambda = \frac{2\pi}{\hbar}|M|^2 Y \tag{4.8}$$

where $|\mathbf{M}|^2$ is the averaged squared matrix element for two-body interactions between specific initial and final states (parametrized according to the Kalbach systematics [Kal 85]) and Y is an expression for the accessible phase-space for the transition. $|\mathbf{M}|^2$ is dependent on the mass number **A** and the excitation energy **E** through the expression

$$|M|^2 = C\cdot A^{-3}\cdot E^{-1} \tag{4.9}$$

proposed by Kalbach-Cline [Kal 73]. A way to calculate values for the parameter **C** will be given later in **section 4.3** (page 88, eq. **4.23**). To calculate the accessible phase-space, the equidistant single-particle state density expression of Williams [Wil 71] is used as follows:

$$\omega_n(p,h,E) = \frac{g^n\left(E - A_{p,h}\right)^{n-1}}{p!h!(n-1)!} \tag{4.10}$$

where $\mathbf{A_{p,h}}$ is a factor which restricts the number of allowed states due to the Pauli exclusion principle and **g** is obtained from the level density parameter **a** by the relation $\mathbf{g = 6a/\pi^2}$.

- **Geometry-dependent hybrid (GDH) model**

The hybrid model PE cross section is calculated from the expression

$$\frac{\partial\sigma_x^{pre}(\varepsilon)}{\partial\varepsilon}d\varepsilon = \sigma_x^{non}P_x(\varepsilon)\ d\varepsilon = \sigma_x^{non}\sum_{\substack{n=n_0\\ \Delta n=+2}}^{\bar{n}}\left[X_{n,x}\frac{\omega_n(p,h,U,\varepsilon)}{\omega_n(p,h,E)}\right]d\varepsilon\left[\frac{\lambda_c(\varepsilon)}{\lambda_c(\varepsilon)+\lambda_+(\varepsilon)}\right]D_n \tag{4.11}$$

$\mathbf{P_x(\varepsilon)d\varepsilon}$ describes the number of particles of the type **x** emitted into the unbound continuum with channel energy between ε and $\varepsilon+d\varepsilon$, $\mathbf{n_0}$ is the initial exciton number and $\bar{\mathbf{n}}$ the equilibrium exciton number. The quantity in the first set of brackets describes the fraction of the **n** exciton state population such that one of the excitons is in an unbound level with the energy within $d\varepsilon$ around ε, while the remaining **p-1** particles and **h** holes share the residual energy **U**.

$$U = E - B_x - \varepsilon \tag{4.12}$$

where **E** is the *composite excitation energy* and $\mathbf{B_x}$ the *particle binding energy*. $\mathbf{X_{n,x}}$ denotes the number of all particles of type **x** in an **n** exciton state. The second set of brackets represents the fraction of the **x** type particles at energy ε which should undergo emission into the continuum rather than making an intranuclear transition. $\mathbf{D_n}$ represents the fraction of the initial population which has survived to an **n** exciton state (also called *depletion factor*). The main quantity entering **(4.11)** is the *single-particle state density* $\omega_n(\mathbf{p,h,E})$ which is calculated according to **(4.10)**. The quantity $\omega_n(\mathbf{p,h,U,\varepsilon})$ is calculated in a similar way (replacing **n** by **n+1** and **E** by **U** in **(4.10)**). The *continuum transition rates* $\lambda_c(\varepsilon)$ are calculated with the expression

$$\lambda_c(\varepsilon) = \frac{(s_x+1)\ \mu\varepsilon}{\pi^2\hbar^3 g_x}\sigma_x^{inv}(\varepsilon) \tag{4.13}$$

where $\mathbf{s_x}$ is the spin of the nucleon of type **x**, $\boldsymbol{\mu}$ is the reduced mass in the emergent channel, σ_x^{inv} is the inverse reaction cross section and $\mathbf{g_x}$ the single-particle level density. The *intranuclear transition rates* $\lambda_+(\varepsilon)$ can be derived by the equation

$$\lambda_+(\varepsilon) = \rho\cdot\langle\sigma(E)\rangle\cdot\sqrt{\frac{2\left(\varepsilon+V^{real}\right)}{m_x}} \tag{4.14}$$

where $\mathbf{V^{real}}$ is the real potential , ρ the nuclear matter density, $\langle\sigma\ (\mathbf{E})\rangle$ the average effective nucleon-nucleon scattering cross section and $\mathbf{m_x}$ the nucleon mass. In **(4.14)** lies one of the important differences between hybrid model and EM since the transition rate $\lambda_+(\varepsilon)$ is a

function of ε referring to the individual particle rather than to the nuclear system as a whole as in the EM.

Comparisons between experimental results, EM and INC calculations [Har 71] showed that the EM model gave too few PE particles and that these were too soft in spectral distribution for the expected initial exciton configurations. The INC results indicated that the exciton model deficiency resulted from a failure in reproducing properly the enhanced emission from the nuclear surface. The GDH model considers the diffuse surface properties. Here the emission cross section is calculated by the function

$$\frac{\partial \sigma_x^{pre}(\varepsilon)}{\partial \varepsilon} d\varepsilon = \pi \lambda\!\!\!^{-2} \sum_{l=0}^{\infty} (2l+1) T_l P_x(l,\varepsilon)\ d\varepsilon \qquad \textbf{(4.15)}$$

where $\lambda\!\!\!^{-}$ is the reduced de Broglie wavelength, l is the orbital angular momentum in units of $\hbar$ and T_l is the transmission coefficient for the l^{th} partial wave.

4.2.4 Level Densities

The excited states of all nuclei relevant for a particular reaction are described by means of a level density formula. At low excitation energy, where the experimental information on the quantum numbers E_i, J_i and Π_i (i = 1, ..., d) of the "discrete levels" is complete, the level density reads

$$\rho\ (E,J,\Pi) = \sum_i \delta\ (E - E_i)\ \delta_{JJ_i} \delta_{\Pi\Pi_i} \qquad \textbf{(4.16)}$$

where **E** represents the excitation energy, **J** the angular momentum and **Π** the parity. At medium excitation energy (E ≤ 10 MeV), where the information on discrete levels is not complete ("continuum region"), the level density is calculated by means of the empirical back-shifted-Fermi gas (BSFG) model. The energy and spin-dependent level density at an excitation energy **E** is thus given by

$$\rho\ (E,J) = \frac{2J+1}{\sqrt{8\pi\sigma^3}} \sigma\ (E)\ \exp\left[-\frac{(J+0.5)^2}{2\sigma^2}\right] \qquad \textbf{(4.17)}$$

and the total state density ω(**E**) has the form

$$\omega\ (E) = \frac{\sqrt{\pi}}{12} \frac{\exp\left[2\sqrt{a\ (E-\Delta)}\right]}{a^{0.25}(E-\Delta)^{1.25}} \qquad \textbf{(4.18)}$$

and the spin cut-off parameter σ is given by

$$\sigma^2 = \frac{1}{\hbar^2}\Theta_{eff}\left(\frac{E-\Delta}{a}\right)^{0.5} \tag{4.19}$$

The parameters in the relations **(4.18)** and **(4.19)** are the so-called *level density parameter* **a** which determines the energy dependence, the *back-shift* Δ which determines the zero point of the effective excitation energy, and the *effective moment of inertia* Θ_{eff} which determines the spin dependence of the nuclear level density. Usually Θ_{eff} is expressed as the *rigid body moment of inertia* $\Theta_{rigid} = 2/5\ MR^2$, with the *nuclear radius* $\mathbf{R} = 1.25\ A^{1/3}$. The level density parameter **a** and the back-shift Δ can be determined by least-squares fitting of discrete levels and s-wave neutron resonance spacings **D** obtained in the neutron energy range Δ**E** above the *neutron binding energy* $\mathbf{S_n}$. Compilations of level density parameters and back-shifts are given by Dilg et al. [Dil 73], Ivascu et al. [Iva 87] or Avrigeanu et al. [Avr 95b].

At higher excitation energies ($\geq$ 10 MeV) the strong shell effects observed for the **a**-values in the E< 10 MeV region gradually disappear. Therefore energy-dependent level density parameters are needed to describe the vanishing shell effects with increasing energy. Ignatyuk et al. [Ign 75] use the parametrization

$$a = a_{LDM}\left[1+\frac{\delta W}{E}\left(1-e^{-0.054E}\right)\right] \tag{4.20}$$

where the high energy asymptotic value $\mathbf{a_{LDM}}$ has the form

$$a_{LDM} = A\left(0.154 - 6.3\cdot 10^{-5}A\right) \tag{4.21}$$

and δ**W** is an experimental shell correction. Microscopic calculations by Schmidt et al. [Sch 82b], including realistic single-particle levels, have confirmed the results obtained with the Ignatyuk formula. They used for the level density parameter an expression for a Fermi gas with a diffuse surface

$$a = \frac{A}{14.61}\left(1+4A^{-1/3}F_2\right) \tag{4.22}$$

proposed by Töke and Swiatecki [Tök 81], where $\mathbf{F_2}$ is an expression for the surface area of the nucleus.

4.3 Input Parameters

For calculations with STAPRE-H several parameters have to be supplied in an input file. These are

- ◊ Optical model potential (OMP) parameters
- ◊ PE parameter,
- ◊ Reduction factor related to non-CN and non-PE reaction mechanisms
- ◊ Separation energies,
- ◊ Discrete levels (energy, spin, parity, gamma-ray branching),
- ◊ Level density parameter.

The parameters used in the present calculations are given below.

- **OMP's**

Both the HF theory and the EM require optical potentials to calculate transmission coefficients and inverse reaction cross sections. Before using an optical potential to generate transmission coefficients and reaction cross sections, the potentials were checked by comparing their predictions of nonelastic and total cross sections with experimental data, where available. The calculation of the transmission coefficients is done with the code SCAT2 which is implemented as subroutine. The optical model parameters used are given in **Tab. 4.1 - Tab 4.4**. They are selected from a huge list included in the subroutine SYSPOT. Proton and alpha transmission coefficents for all investigated reactions were calculated with the optical model potential of Arthur and Young [Art 80] and Avrigeanu et al. [Avr 94a], respectively. The neutron transmission coefficients were calculated with different OMP's in order to reproduce the experimental data. For Cr the OMP of Ferrer et al. [Fer 77], modified by Uhl et al. [Uhl 92] gave best results whereas for Fe and Ni the OMP's of Arthur and Young [Art 80] and Ferrer et al. [Fer 77] were preferred.

- **PE parameter**

The only free parameter in the exciton model is the parameter C in **(4.9)**, in the following called *FM*. It was calculated according to Strohmaier [Str 82]:

$$FM = \frac{\lambda^{+} \cdot \hbar \cdot A^{1/3} \cdot E \cdot 4}{2\pi g\left[g\left(E - \Delta ph\right) - C_{3,2}\right]^2} \qquad (4.23)$$

where the single-particle state density was derived by $\mathbf{g=6a/\pi^2}$, λ^{+} is approximately $5 \cdot 10^{21}$ s^{-1} (with n = 3 , E ~ 21 MeV), found by extensive data analysis by Braga et al. [Brag 72] and Gadioli et al. [Gad 75], $\hbar$ is $6.58 \cdot 10^{-22}$ MeVs and $C_{3,2}$ is 6.5. The parameter values for **a** and Δ are given in **Tab. 4.5**. The dependence of the *FM* parameter on the cross section was tested by modifying its value by ± 20 to ± 30 %.

In the GDH model the only parameter to choose is g. As suggested by Avrigeanu and Avrigeanu [Avr 94b], a so-called composite single-particle state density, based on the Fermi-gas model (FGM), has been used. More details and comparisons with other single-particle state density descriptions are extensively discussed in [Avr 94b].

- **Separation energies**

The separation energies were calculated with masses from the atomic mass evaluation done by Audi and Wapstra [Aud 95].

- **Non-CN and non-PE fractions**

The code offers the possibility to account for the fraction of the total reaction cross section related to non-compound and non-precompound reaction mechanisms, mainly direct reactions. Values of 3 to 8 % were used as determined from Avrigeanu et al. [Avr. 90] and Uhl et al. [Uhl 92] with DWBA calculations. In one case, namely the $^{50}Cr(n,np)^{49}V$ reaction, a slightly increased value of 15 % was chosen according to Klochkova et al. [Klo 94].

Tab. 4.1 Proton OMP's (V^{real} Woods-Saxon real well depth, V^{surf} Woods-saxon derivative imaginary well depth, V^{vol} Woods-Saxon imaginary well depth (volume), $V^{S\text{-}O}$ spin-orbit potential depth, **r** reduced radius, $\mathbf{r_c}$ coulomb radius and **a** diffuseness)

Optical potential [MeV]	r [fm]	r_c [fm]	a [fm]	Ref.
$V^{real} = 58.384 - 0.550\,E$	1.2500	1.25	0.65	[Art 80]
$V^{surf} = 13.500 - 0.150\,E$	1.2500		0.47	
$V^{vol} = 0$	0.0000		0.00	
$V^{S\text{-}O} = 7.5$	1.0800		0.47	

Tab. 4.2 Alpha OMP's (symbols as defined in **Tab 4.1**).

Optical potential [MeV]	r [fm]	r_c [fm]	a [fm]	Ref.
$V^{real} = 101.1 + 6.051\,Z/A^{1/3} - 0.248\,E$	1.245	1.30	$0.817\text{-}0.0085\,A^{1/3}$	[Avr 94a]
$V^{surf} = 0$	0.000		0.00	
$V^{vol} = 12.64 - 1.706\,A^{1/3} + 0.20\,E$	1.570		$0.692\text{-}0.02\,A^{1/3}$	
$V^{S\text{-}O} = 0$	0.000		0.00	

Tab. 4.3 Neutron OMP's (symbols as defined in **Tab 4.1**,).

Element	Optical potential [MeV]	r [fm]	a [fm]	Ref.
Cr	$V^{real} = 52.444 - 0.3155\,E$	1.1980	0.63	[Uhl 92]
	$V^{surf} = 7.295$ $(E < 5.0$ MeV)	1.3910	0.33	
	$V^{surf} = 7.295$ $(E \geq 5.0$ MeV)	1.2950	0.53	
	$V^{surf} = 7.295 + 0.400\,E$ $(E \geq 10.0$ MeV)	1.2950	0.53	
	$V^{surf} = 13.20 - 0.390\,E$ $(E \geq 15.0$ MeV)	1.2950	0.53	
	$V^{vol} = 0$ $(E < 15.0$ MeV)	0.0000	0.00	
	$V^{vol} = -4.30 + 0.380\,E$ $(E \geq 15.0$ MeV)	1.295	0.53	
	$V^{S\text{-}O} = 6.2$	1.1200	0.47	
Fe	$V^{real} = 49.747 - 0.4295\,E - 0.003\,E^2$	1.2870	0.56	[Art 80]
	$V^{surf} = 6.053 - 0.074\,E$ $(E < 6.25$ MeV)	1.3448	0.47	
	$V^{surf} = 8.477 - 0.325\,E$ $(E \geq 6.25$ MeV)	1.3448	0.47	
	$V^{vol} = -2.070 + 0.253$	1.3450	0.47	
	$V^{S\text{-}O} = 6.2$	1.1200	0.47	
Ni	$V^{real} = 46.364$	1.2700	0.71	[Fer 77]
	$V^{surf} = 12.090$	1.2700	0.434	
	$V^{vol} = 0$	0.0000	0.00	
	$V^{S\text{-}O} = 4.55$	1.2700	0.71	

Tab. 4.4 Deuteron OMP's (symbols as defined in **Tab 4.1**).

Optical potential [MeV]	r [fm]	r_c [fm]	a [fm]	Ref.
$V^{real} = 93.324 - 0.220\,E$	1.150	1.15	0.81	[Per 63]
$V^{surf} = 14.400 + 0.240\,E$	1.340		0.68	
$V^{vol} = 0$	0.000		0.00	
$V^{S\text{-}O} = 0$	0.000		0.00	

- **Discrete levels and level density parameter**

The discrete levels including information about energy, spin, parity and gamma-ray branching were taken from the most recent issue of the *Table of Isotopes* [Fir 96]. Levels up to energies of ~ 4MeV were taken where the level information seemed to be complete. In cases where spin and parity were not known these were estimated from the adjacent levels. Missing gamma-ray branching ratios were calculated by the program BRANCH [Sud 97].

The level density above the discrete levels was calculated by the BSFG model. The level density parameter and the back-shift Δ were taken from the compilations of Ivascu et al. [Iva 87] and Avrigeanu et al. [Avr 95b]. In some cases they were sligthly modified in order to fit better the experimentally determined excitation functions. These adjustments never exceeded 5 % so that they did not exceed the error limit predicted by the compilations. **Tab. 4.5** lists the parameters used for the level density, back-shift and the number of used discrete levels together with the energy of the highest level.

At higher energies the level density formula of Schmidt et al. [Sch 82b] was tested for different transition regions between the latter one and the BSFG model. A fast transition (12 to 15 MeV) was compared with a large transition (12 to 50 MeV) and an intermediate transition region (12 to 30 MeV).

Tab. 4.5 Level density parameter **a**, back-shift Δ and number of discrete levels N_d up to excitation energy E_d used in STAPRE-H calculations.

Nuclide	a [MeV^{-1}]	Δ [MeV]	N_d	E_d [MeV]	Nuclide	a [MeV^{-1}]	Δ [MeV]	N_d	E_d [MeV]
^{47}Ca	5.55	0.25	17	4.103	^{51}Cr	5.70	0.60	34	3.207
^{45}Sc	5.45	-2.24	14	1.662	^{52}Cr	5.67	-0.90	24	4.837
^{46}Sc	5.74	-2.80	16	1.141	^{53}Cr	5.60	-1.07	17	2.827
^{47}Sc	5.10	-1.90	18	2.002	^{54}Cr	5.60	-0.12	25	4.254
^{48}Sc	6.00	-1.20	30	2.891	^{55}Cr	6.10	-1.20	16	2.390
^{49}Sc	5.60	0.48	18	4.493	^{52}Mn	6.30	-1.98	20	2.337
^{50}Sc	6.20	0.10	9	2.614	^{53}Mn	5.80	-1.24	24	3.097
^{48}Ti	5.55	-0.25	21	3.852	^{54}Mn	5.70	-2.20	24	1.925
^{49}Ti	6.25	-0.50	15	2.720	^{52}Fe	5.60	1.15	12	5.140
^{50}Ti	5.40	-0.77	11	2.084	^{53}Fe	5.54	-1.00	21	3.040
^{51}Ti	5.55	-0.52	15	3.237	^{54}Fe	5.50	0.52	18	4.103
^{52}Ti	5.60	0.30	6	3.024	^{55}Fe	5.60	-1.30	16	2.600
^{53}Ti	5.70	0.00	1	0.000	^{57}Fe	6.15	-1.55	26	2.599
^{48}V	6.00	-2.50	10	0.776	^{58}Fe	6.20	0.03	36	4.323
^{49}V	5.60	-1.81	23	2.408	^{59}Fe	6.40	-1.08	12	1.517
^{50}V	6.00	-2.16	21	1.811	^{57}Co	6.00	-1.08	16	2.611
^{51}V	5.78	-0.88	25	3.454	^{58}Co	6.60	-2.37	24	1.435
^{52}V	6.10	-1.58	24	2.428	^{62}Co	6.45	-2.05	9	0.707
^{53}V	5.80	-1.42	11	2.084	^{58}Ni	6.00	0.28	32	4.578
^{54}V	6.35	-2.05	15	1.215	^{59}Ni	6.25	-1.20	13	1.948
^{48}Cr	5.50	1.10	9	4.280	^{62}Ni	6.76	0.21	14	3.370
^{49}Cr	5.60	-0.90	12	2.612	^{63}Ni	6.85	-1.47	10	1.454
^{50}Cr	5.40	-0.15	19	3.895					

5. Results and Discussion

5.1 Data for Reactions on Chromium

5.1.1 Experimental Data

The cross sections determined using ^{nat}Cr samples are listed in **Tab. 5.1** and those obtained using enriched isotopes ^{52}Cr, ^{53}Cr and ^{54}Cr in **Tab. 5.2.**

Tab. 5.1 Experimental cross sections for reactions on Cr-isotopes determined with ^{nat}Cr samples. The (n,pn) reaction includes contributions also from the (n,np) and (n,d) reactions.

Neutron Energy [MeV]	Cross section [mb]			
	$^{50}Cr(n,pn)^{49}V$	$^{52}Cr(n,2n)^{51}Cr$	$^{52}Cr(n,p)^{52}V$	$^{53}Cr(n,p)^{53}V$
at Jülich				
9.31 ± 0.20			50.8 ± 3.5	
10.33 ± 0.22			55.1 ± 3.6	
11.57 ± 0.24			65.3 ± 3.9	28.3 ± 6.0
12.27 ± 0.26			70.7 ± 4.4	36.4 ± 5.7
at Geel 1				
13.71 ± 0.25			88.2 ± 5.6	48.9 ± 6.0
14.25 ± 0.20	350.5 ± 62.1	330.3 ± 17.0		
15.01 ± 0.25			82.9 ± 4.1	46.4 ± 4.3
15.95 ± 0.25			74.7 ± 3.6	42.3 ± 3.5
17.20 ± 0.25	626.1 ± 78.9	591.0 ± 29.1		
17.54 ± 0.30			59.3 ± 3.7	
17.80 ± 0.30			58.9 ± 3.2	40.5 ± 5.2
18.73 ± 0.35			45.5 ± 2.7	30.5 ± 2.8
18.80 ± 0.30	699.2 ± 77.0	621.9 ± 31.3		
19.40 ± 0.32	680.0 ± 92.1	637.4 ± 33.2		
19.70 ± 0.40			34.2 ± 1.7	19.7 ± 2.2
21.07 ± 0.50			27.1 ± 2.6	15.4 ± 2.3
at Geel 2				
16.02 ± 0.25			79.6 ± 3.9	48.4 ± 2.9
16.99 ± 0.20			65.8 ± 4.3	45.8 ± 4.3
17.73 ± 0.25			58.3 ± 4.1	45.7 ± 3.4
19.04 ± 0.25			46.6 ± 3.1	35.2 ± 2.8
20.24 ± 0.25			28.8 ± 2.1	16.8 ± 1.3

Tab. 5.2 Experimental cross sections for reactions on Cr-isotopes determined using enriched Cr samples. The (n,pn) reaction includes contributions also from the (n,np) and (n,d) reactions.

Neutron Energy [MeV]	Cross section [mb]		
	$^{52}Cr(n,p)^{52}V$	$^{53}Cr(n,p)^{53}V$	$^{53}Cr(n,pn)^{52}V$
at Geel 2			
16.02 ± 0.25	76.0 ± 3.8	49.2 ± 3.6	26.1 ± 2.1
16.99 ± 0.20	61.7 ± 4.1	43.9 ± 5.6	55.3 ± 4.2
17.73 ± 0.25	57.4 ± 3.2	41.2 ± 5.0	70.9 ± 5.0
19.04 ± 0.25	40.5 ± 2.7	28.0 ± 3.1	77.7 ± 5.5
20.24 ± 0.25	28.3 ± 2.6	20.0 ± 2.1	78.1 ± 5.8
	$^{54}Cr(n,p)^{54}V$	$^{54}Cr(n,pn)^{53}V$	$^{54}Cr(n,\alpha)^{51}Ti$
at Geel 2			
16.02 ± 0.25	22.4 ± 1.7	6.5 ± 0.6	14.1 ± 1.2
16.99 ± 0.20	26.3 ± 2.0	15.0 ± 1.6	14.3 ± 1.4
17.73 ± 0.25	27.1 ± 2.1	22.5 ± 2.3	14.3 ± 1.3
19.04 ± 0.25	21.1 ± 1.8	35.3 ± 2.5	10.3 ± 0.9
20.24 ± 0.25	14.3 ± 1.5	32.5 ± 3.0	6.1 ± 0.7

5.1.2 Comparison with Literature Data, Evaluations and STAPRE-H Calculation

The cross sections determined in this work are plotted together with the data available in the literature as a function of neutron energy in **Fig. 5.1** - **Fig. 5.6**. The results of some evaluations as well as STAPRE-H calculations are also shown. Some remarks on the individual reactions are given below. The new data obtained in this work are referred to in the following as *Jülich* and *Geel*. The (n,pn) reaction is always the sum of (n,pn+np+d). The STAPRE-H plots describe the calculation with the exciton model and adjusted FM parameter (see **section 5.1.3**)

- **$^{50}Cr(n,pn+np+d)^{49}V$**

Cross sections of this process could be measured for the first time above 14 MeV and are given in **Fig 5.1**. The technique developed, i. e. chemical separation of the product ^{49}V, thin sample preparation and X-ray counting, allowed the cross section determination with an uncertainty between 12 and 20 %. The values are consistent with ENDF/B-VI whereas JENDL-3.2 and JEF-2.2 are much higher and lower, respectively. Among the literature data points available at 14.7 MeV, that of Qaim [Qai 82] was determined via a similar technique and is in good agreement with *Geel 1*. The two other points [All 61, Klo 94] lie somewhat lower. Both of them were deduced from the total proton emission spectrum via

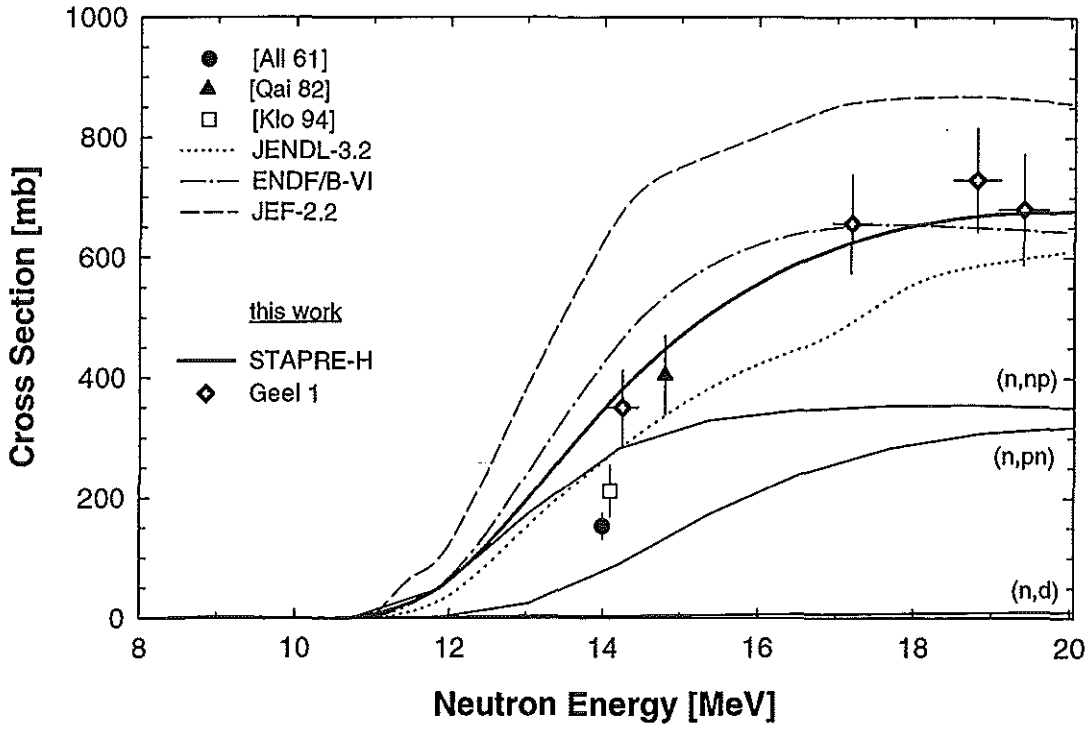

Fig. 5.1 Excitation function of the $^{50}Cr(n,pn+np+d)^{49}V$ reaction.

an analysis of the contributions of the (n,p) and (n,np) reactions. Klochkova et al. [Klo 94] achieved this goal by fitting a theoretical spectrum to the experimental one using the non-linear least-squares method. The former was constructed on the basis of existing models of the nuclear structure and nuclear models, i. e. relying on the fact that the emission of a proton in the reaction (n,np) is an almost entirely evaporative process and small contributions from the PE and direct processes may be neglected. For the first chance emission they found a contribution of non-equilibrium processes of 15 %. Allan [All 61] had not only to divide the proton emission spectrum in the contributions of the (n,p) and (n,np) reactions but also to subtract a substantial part of protons stemming from the $^{16}O(n,p)^{16}N$ reaction since he used chromium oxide as the sample material. In conclusion, it is difficult to compare the activation data with the proton emission data since different quantities are measured.

The STAPRE-H calculation, giving the individual results for the (n,pn), (n,np) and (n,d) reactions as well as the sum of all the processes, is in good agreement with the *Geel 1* data (within ~ 10 %). In order to test the quality of the model calculation, also the (n,p), (n,α) and (n,2n) reactions were calculated and compared with the scanty literature data. **Fig. 5.8** shows the excitation functions of all the 4 reactions. A good agreement between calculation and experiment is obtained in all cases. The calculations are given for different

PE parameters. A discussion of the influence of these parameter changes on the cross section will follow in **section 5.1.3**. It should be mentioned here that the experimental (n,2n) data above 16 MeV seem to be consistently lower than the STAPRE-H calculation by ~ 20 % (cf. **Fig. 5.8**, at the right hand side, down). Later, we will see that the data of this experiment [Gho 87] are 20 to 30 % lower also for the ^{52}Cr(n,p)^{51}V and ^{52}Cr(n,2n)^{51}Cr reaction, i. e. they are not very certain. The present calculation is thus reliable.

- **^{52}Cr(n,p)^{52}V and ^{52}Cr(n,2n)^{51}Cr**

The excitation function of the ^{52}Cr(n,p)^{52}V reaction is shown in **Fig. 5.2**. The *Jülich* data provide the first cross sections for the "gap-region" between 9 and 13 MeV. They agree very well with JENDL-3.2 whereas JEF-2.2 and ENDF/B-VI are slightly higher. The low energy part fits well with the data of Smith and Meadows [Smi 80]. A recent experiment reported by Mannhart et al. [Man 97] is consistent with the two lowest points of this work (9.3 and 10.3 MeV), whereas at higher energies the Mannhart data are ~ 10 % higher (consistent with JEF-2.2). The new data above 13 MeV (*Geel*) agree very well with the data of Viennot et al. [Vie 91], Mannhart et al. [Man 97] and ENDF/B-VI. The data of Kern et al. [Ker 59] are much higher and those of Ghorai et al. [Gho 87] ~ 20 % lower (see above). Nevertheless, the latter two data sets give a similar shape of the excitation function. It seems that all evaluators were somehow averaging these two data sets to describe the decrease in the excitation function above 14 MeV. This approach led to a reasonable result as could be proved now with the *Geel* data. Some comments should be given also on the 14 MeV data. Many single data points have not been included in the figure for reasons of simplicity and clarity (for references see caption of **Fig. 1.6**). They all lie between 75 and 100 mb. The data of Ikeda et al. [Ike 88] and Kawade et al. [Kaw 90] around 14 MeV (both plotted in the figure) are 10 % lower than the Viennot, Mannhart and *Geel* data. A similar trend can be seen in **Fig. 5.3** for the (n,2n) reaction. All the other data around 14 MeV are 10 % higher than the Ikeda data. Above 16 MeV the measurements split into two groups; the data of Liskien et al. [Lis 89b] represent a higher trend while those of Ghorai et al. [Gho 87] and Bormann et al. [Bor 68] show a lower trend in the excitation function. The evaluations also split in these two goups, ENDF/B-VI relying on Liskien and JENDL-3.2 on Ghorai / Bormann. The new *Geel* data agree very well with the Liskien data and the new Mannhart data at 14 MeV. Keeping in mind that the Ghorai data also for the (n,p) reaction are systematically lower by 20 to 30 % the higher trend in the excitation function above 16 MeV is clearly validated.

For both the (n,p) and (n,2n) reactions the new STAPRE-H calculation is in very good agreement over the whole energy range. The small overestimation of the (n,2n) cross section (~ 8%) could not be solved by a parameter adjustment since each variation which decreased this cross section simultaneously increased the (n,p) value.

Summing up, it is evident that both the reactions are now very well investigated. The (n,2n) reaction is well described by ENDF/B-VI whereas for the (n,p) reaction a new evaluation should be undertaken including the data of Mannhart, *Jülich* and *Geel*.

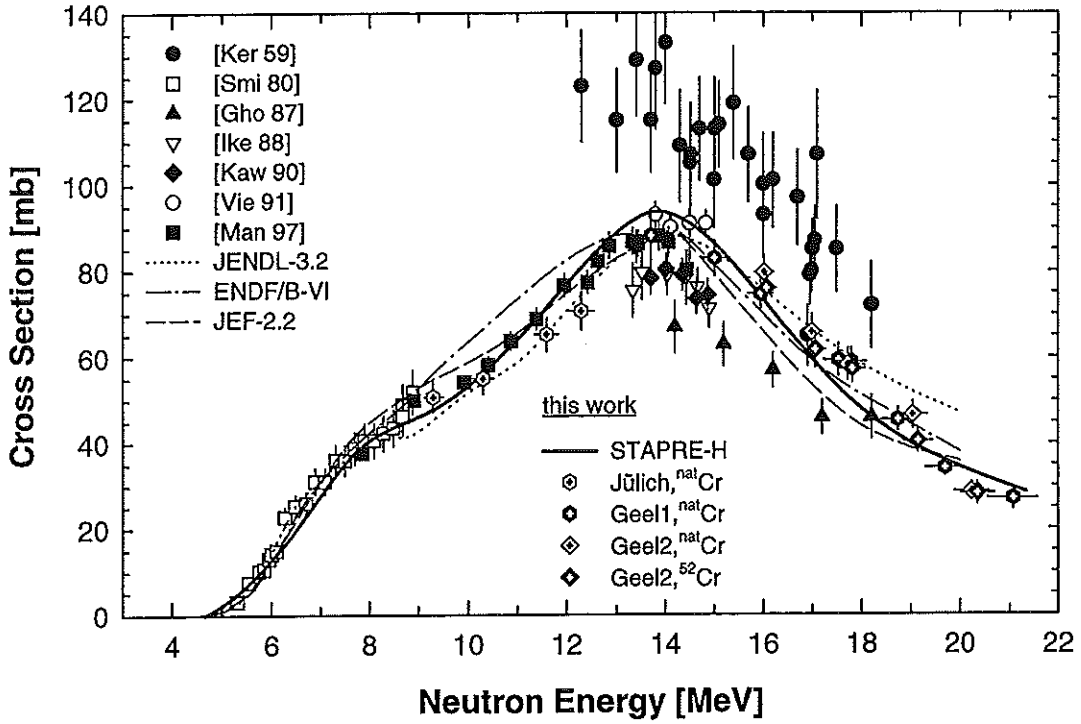

Fig. 5.2 Excitation function of the $^{52}Cr(n,p)^{52}V$ reaction.

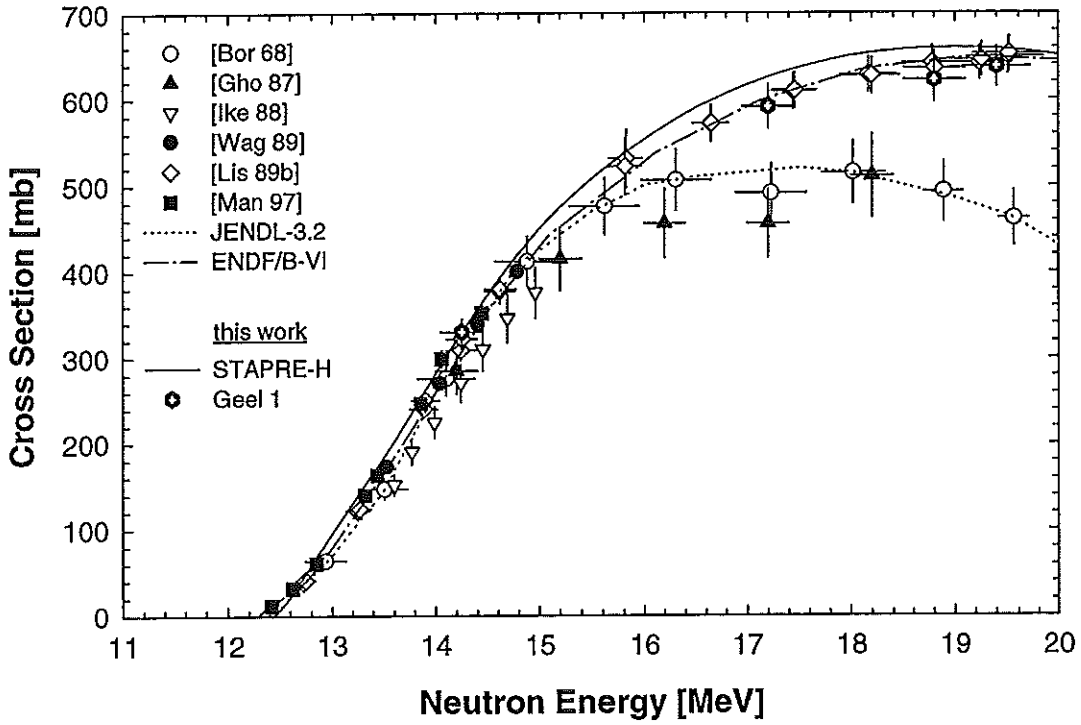

Fig. 5.3 Excitation function of the $^{52}Cr(n,2n)^{51}Cr$ reaction.

- **$^{53}Cr(n,p)^{53}V$ and $^{53}Cr(n,pn)^{52}V$**

The updated status of the available data for the (n,p) reaction is illustrated in **Fig. 5.4.** Again the *Jülich* data provide the first cross sections in the "gap-region", consistent with JENDL-3.2 and ENDF/B-VI. The *Geel* data around 14 MeV are consistent with the average value of the literature data. Above 14 MeV the *Geel* data represent the first experimental study, favouring the ENDF/B-VI evaluation up to 19 MeV. At higher energies the experimental data are much lower. Comparing the three evaluations over the whole energy range, large discrepancies are observed above 10 MeV. At 20 MeV the recommended cross sections are 5 mb (JEF-2.2), 35 mb (ENDF/B-VI) and 53 mb (JENDL-3.2), respectively. Thus, this reaction is a good example to demonstrate the need of new experimental data to solve discrepancies between different evaluations. The STAPRE-H calculation follows the trend of the new experimental data quite well up to 19 MeV; at higher energies it is ~20 % higher than the experimental data.

The situation regarding the (n,pn) reaction is less satisfying (see **Fig. 5.5**). The *Geel* data are again the first reported values. They agree fairly well with the evaluations and the model calculation above 16 MeV (± 20 %). The 16 MeV value is in perfect agreement with the calculation and JENDL-3.2. The calculation reproduces very well also the few 14 MeV data. The calculated individual contributions of the (n,pn), (n,np) and (n,d) reactions to the formation of ^{52}V are also given in the figure.

In summary, the data base for these two reactions could be substantially improved with the new data. The inconsistency in the evaluations for the (n,p) reaction could be solved by clearly supporting ENDF/B-VI through the new data.

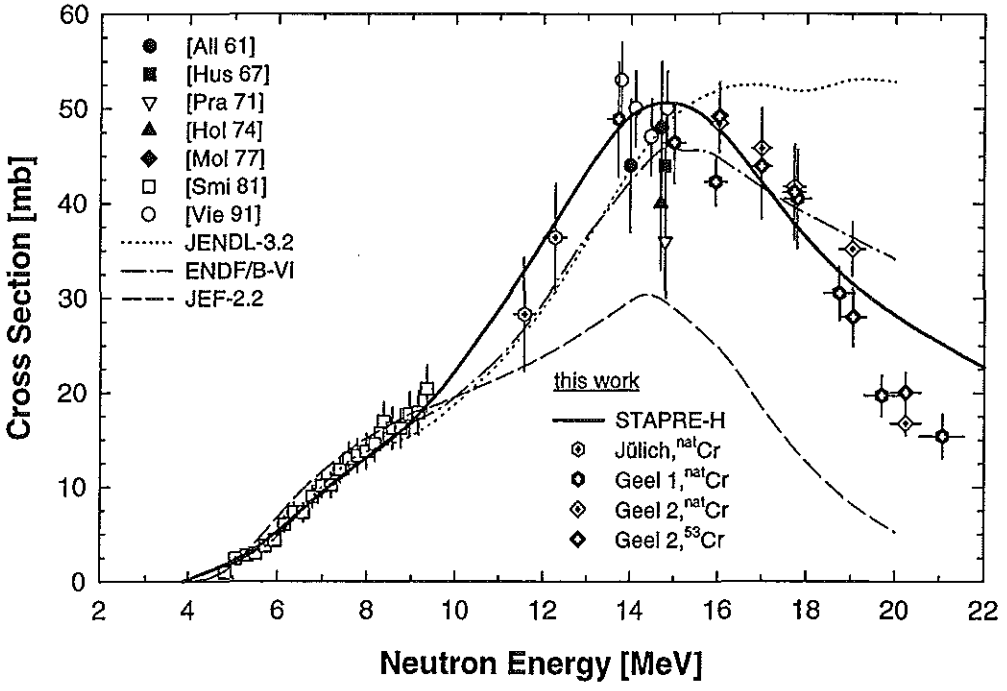

Fig. 5.4 Excitation function of the $^{53}Cr(n,p)^{53}V$ reaction.

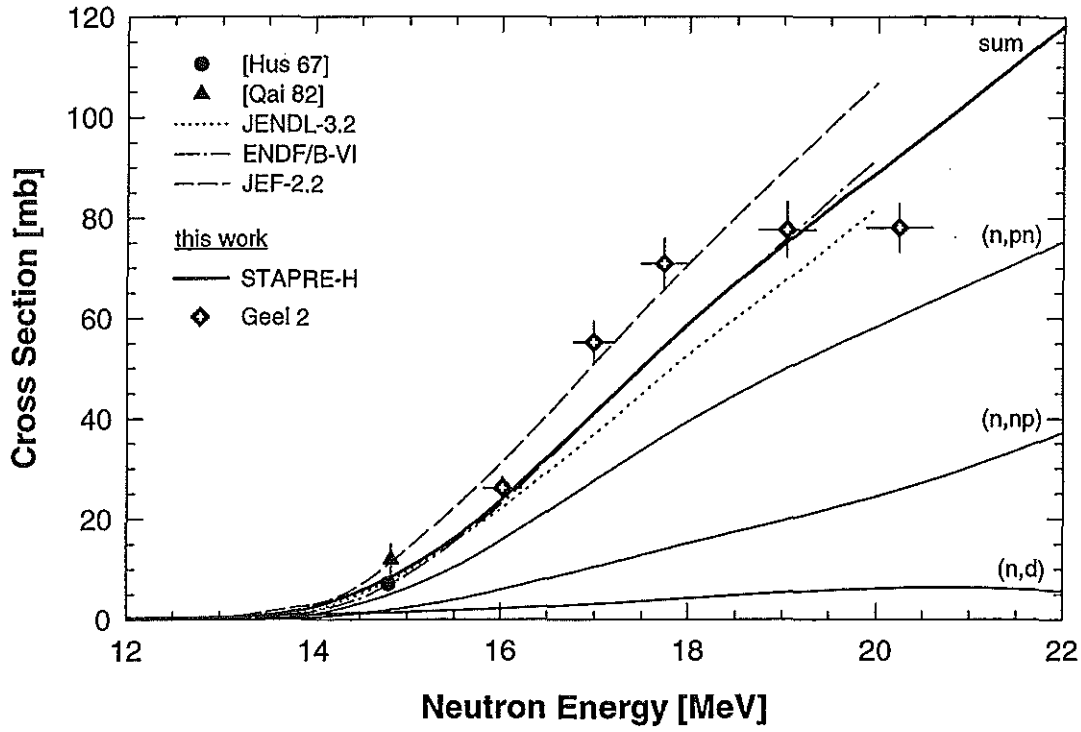

Fig. 5.5 Excitation function of the $^{53}Cr(n,pn+np+d)^{52}V$ reaction.

- **$^{54}Cr(n,p)^{54}V$, $^{54}Cr(n,pn)^{53}V$ and $^{54}Cr(n,\alpha)^{51}Ti$**

The excitation functions of these three reactions are shown in **Fig. 5.6**. All of them have been hitherto poorly investigated due to the low abundance of ^{54}Cr. The new *Geel* data represent the first values above 14 MeV and agree fairly well with the STAPRE-H calculation in all three reactions (± 10 to 20 %). For the (n,p) and (n,α) reactions the best evaluation seems to be JENDL-3.2 which agrees with *Geel* up to 18 MeV but above 18 MeV JENDL-3.2 is systematically higher. JEF-2.2 is much too low whereas ENDF/B-VI is much too high (factor of 3 to 5 at 20 MeV) and even not consistent in the shape. The *Geel* data for the (n,pn) reaction are best reproduced by the JEF-2.2 evaluation up to 19 MeV. The decrease of the excitation function above this value is neither described by any evaluation nor the STAPRE-H calculation which below 19 MeV lies systematically 10 % lower than the experimental data.

Summing up, the improvement in the data base through the new experimental data is substantial, also for the reactions on ^{54}Cr. Of particular interest is also the fact that all the three reactions, involving emission of different types of particles, are described well by the calculation, without adjusting any parameter.

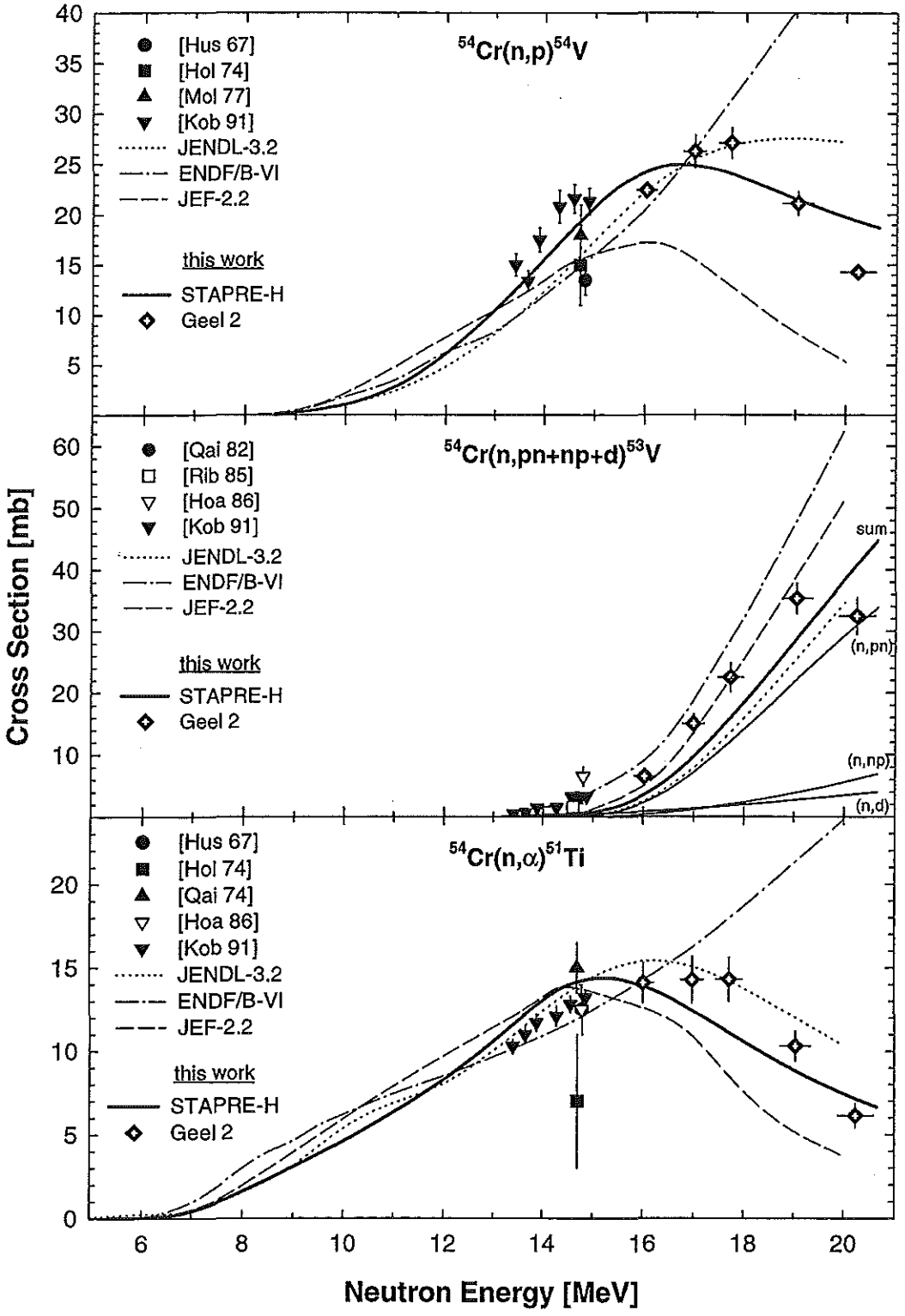

Fig. 5.6 Excitation functions of the ^{54}Cr(n,p)^{54}V, ^{54}Cr(n,pn+np+d)^{53}V and ^{54}Cr(n,α)^{51}Ti reactions.

5.1.3 Influence of Model Parameters

- **PE Emission Fraction**

As outlined in the previous chapter the code STAPRE-H offers the possibility to use two models for the calculation of the preequilibrium part of the reaction cross section. The results for the different models are illustrated in the **Fig. 5.8** to **Fig. 5.10**. Calculations were done either with the GDH model or with different FM values in the EM. The general conclusion can be drawn as follows:

The decrease of FM increases the PE fraction and makes the first chance emission spectrum harder (see **Fig. 5.7**). This reduces the second chance emission. **Fig. 5.9** clearly demonstrates this effect. The reduction of FM increases the $^{52}Cr(n,n')^{52}Cr$ cross section at the cost of the $^{52}Cr(n,2n)^{51}Cr$ cross section and the $^{52}Cr(n,p)^{52}V$ cross section increases at the cost of the $^{52}Cr(n,pn)^{51}V$ cross section. The (n,p) reaction is best reproduced with a slightly increased FM value (as calculated with **(4.3)**) whereas the (n,2n) reaction fits better the experimental data with a decreased FM value. Similar results for the (n,p) and (n,pn+np+d) reactions on $^{53,54}Cr$ are shown in **Fig. 5.10**. Here the influence of FM on the (n,p) reaction is much stronger than in the case of the $^{52}Cr(n,p)$ reaction whereas the (n,pn+np+d) reactions are almost independent of FM. It seems that opposite effects on the (n,pn) and (n,np) reactions are compensating each other. The reactions on ^{50}Cr, shown in **Fig. 5.8**, are less sensitive to variations in FM.

Summing up, one can state that the GDH model (bold lines in the figures) and the EM with standard FM parameter (dotted lines) lead almost to similar results. Variations in the FM parameter affect more the (n,p) cross section with increasing mass number. An increased FM value gives somehow better reproduction of the experimental (n,p) reaction data but at the cost of a worsened description of the (n,2n) reaction.

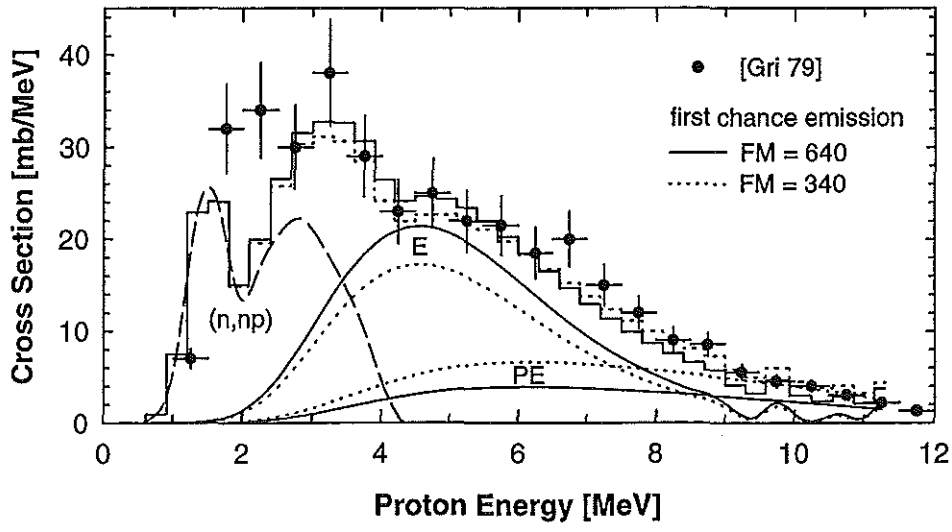

Fig. 5.7 Comparison of calculated and experimental proton emission spectra in the interaction of 14.8 MeV neutrons with ^{52}Cr. The calculations were done with different FM parameters in the EM.

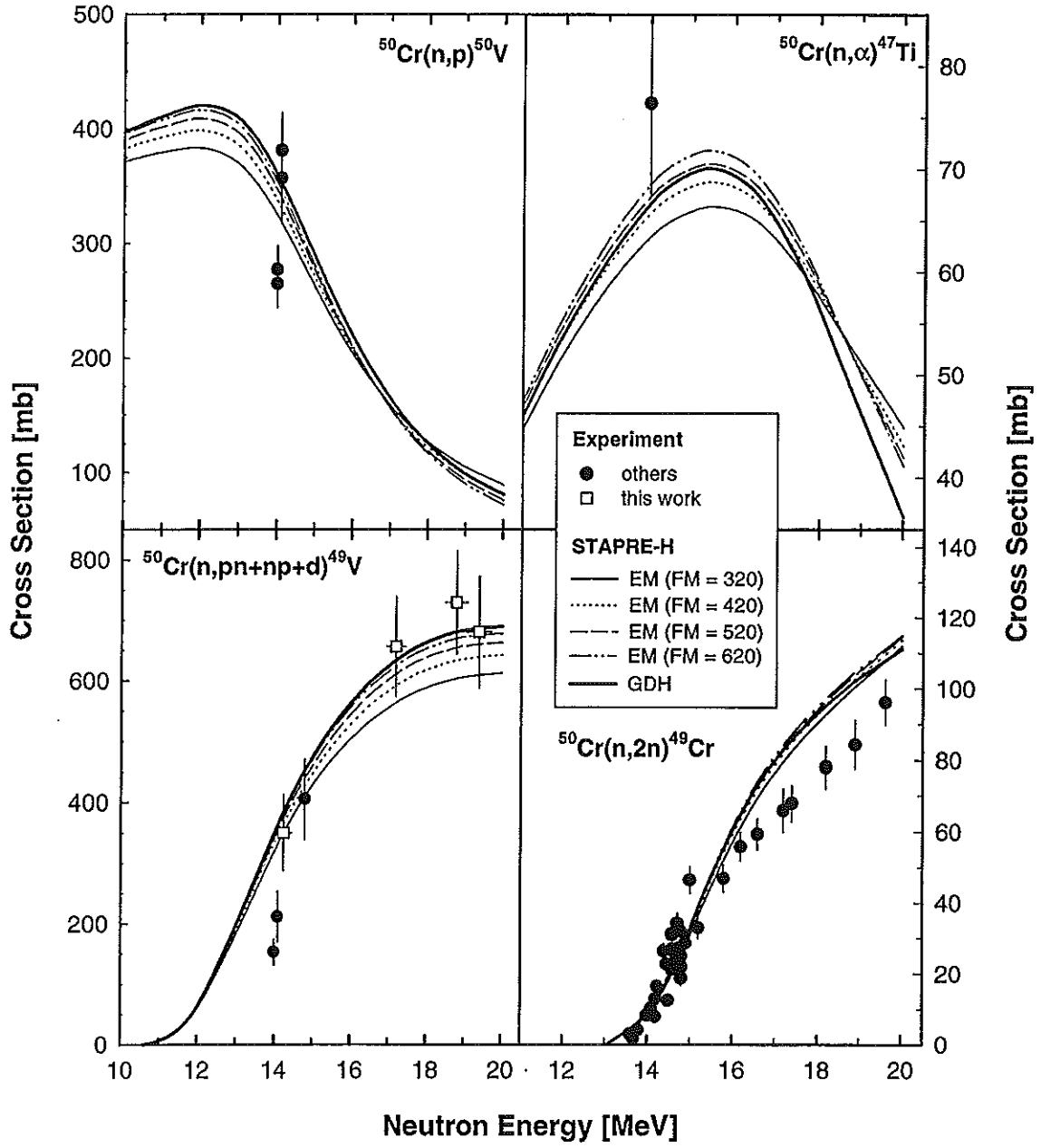

Fig. 5.8 Influence of FM parameter in EM and comparison with GDH model studied in different reactions on ^{50}Cr.

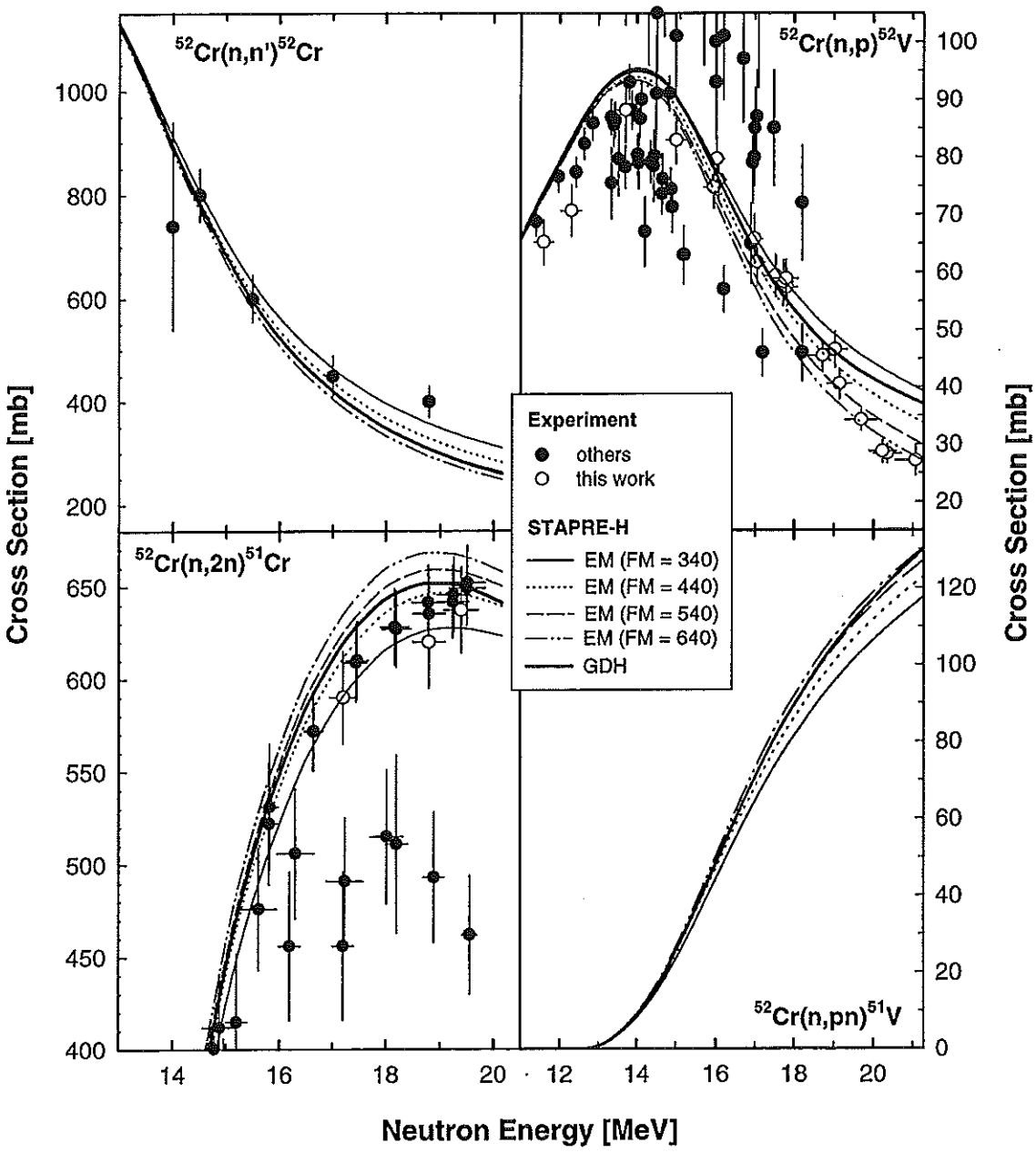

Fig. 5.9 Influence of FM parameter in EM and comparison with GDH model studied in different reactions on ^{52}Cr.

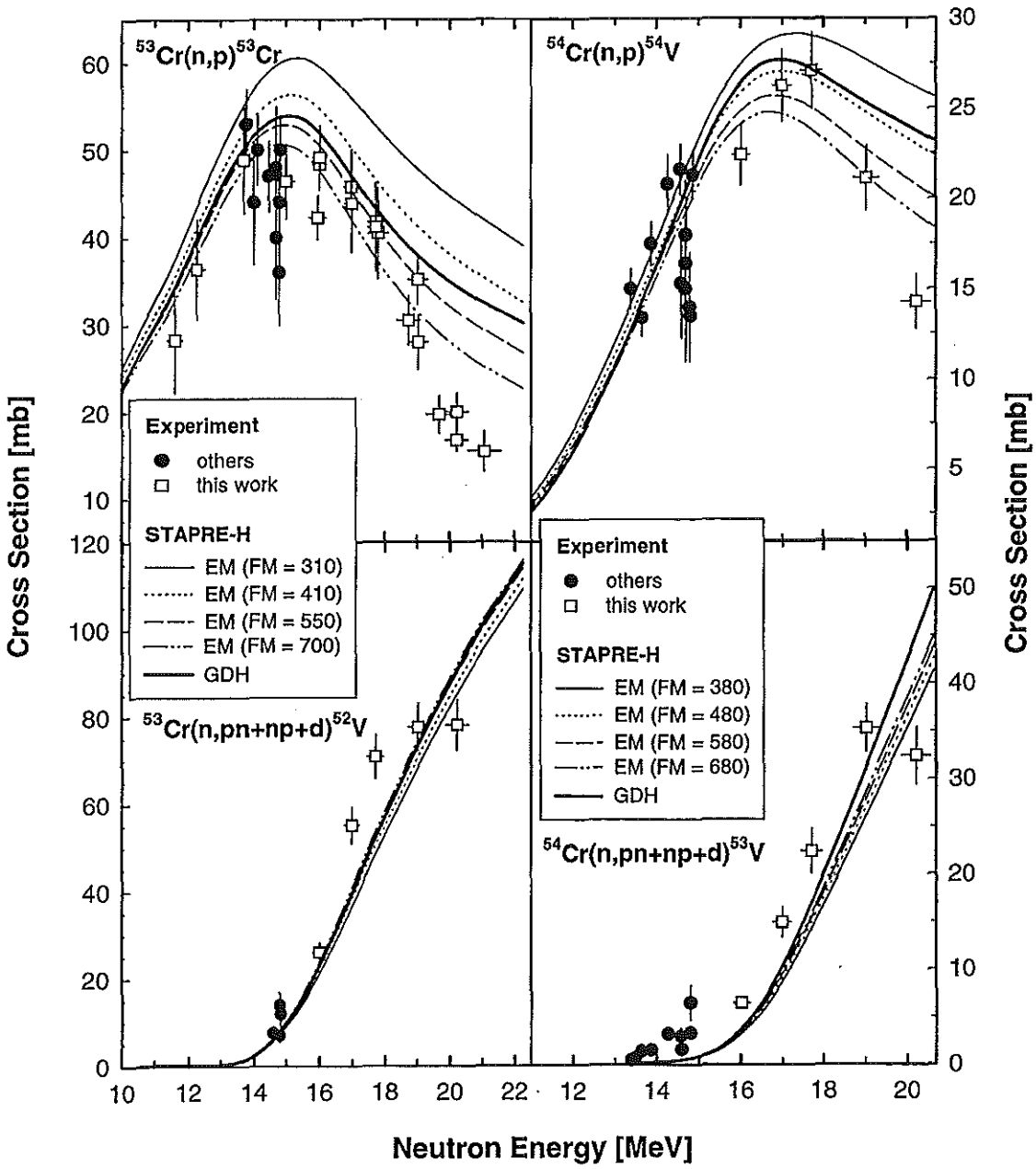

Fig. 5.10 Influence of FM parameter in EM and comparison with GDH model studied in different reactions on ^{53}Cr and ^{54}Cr.

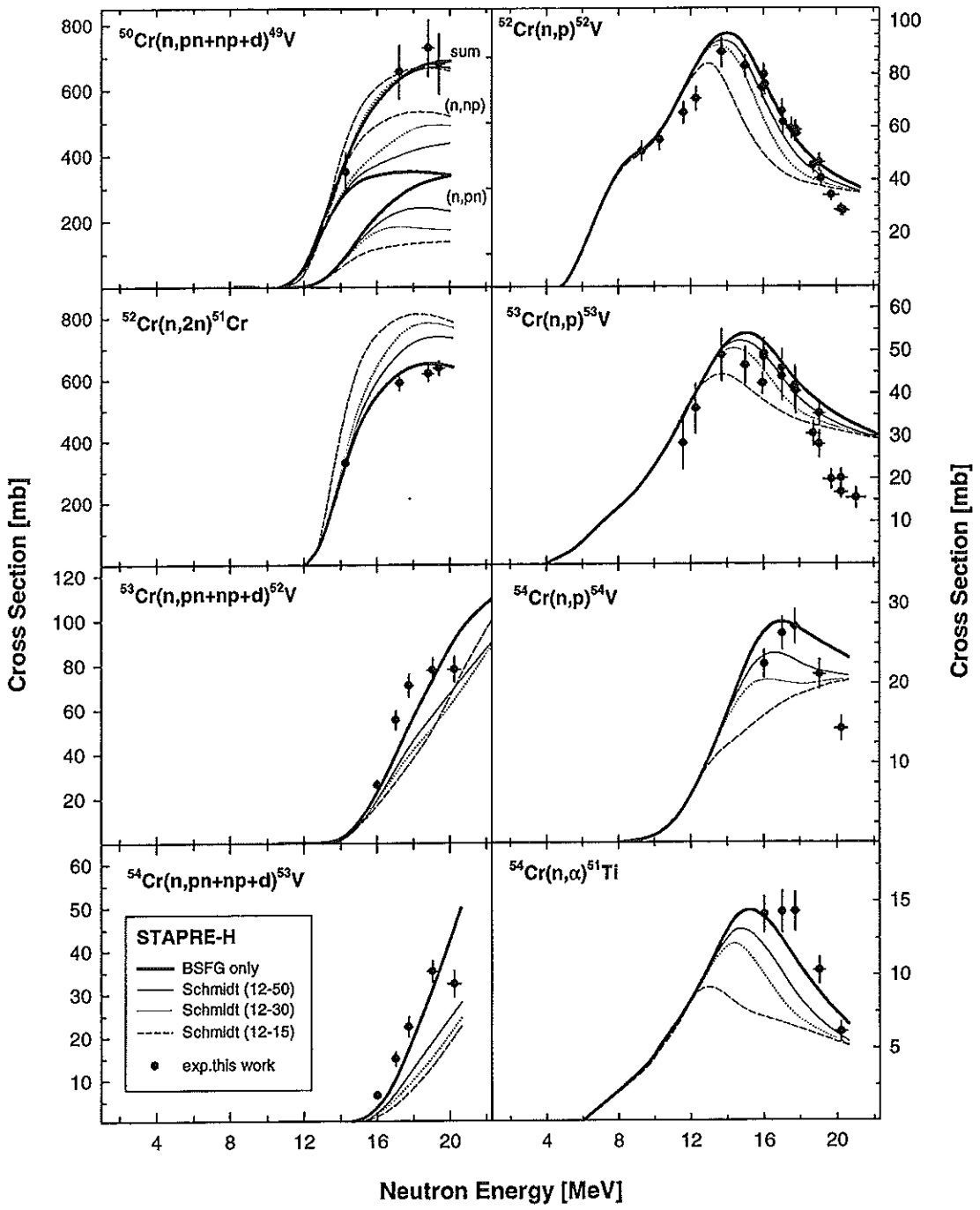

Fig. 5.11 Effect of level density on the excitation functions of neutron induced reactions on several isotopes of Cr. The level density calculation at high excitation energies was done with the BSFG model alone as well as with different transition ranges between BSFG and the Schmidt et al. [Smi 82b] formula.

- **Level Density**

The influence of the level density at higher excitation energies was tested by varying the transition range between the BSFG model and the Schmidt et al. formula. The calculations shown in **Fig. 5.11** are all done with the GDH model. The best reproduction of the experimental data is given by the use of the BSFG model alone. With the shortening of the transition range (from 12-50 to 12-15 MeV) the calculated cross sections decrease for the (n,p) and increase for the (n,2n) reaction. The two-step linear transition factor introduced by Avrigeanu et al. [Avr 90] appears to be unjustified in the present form. Probably a less strong decrease in the first quarter of the transition range would improve the calculations. Anyway, it is difficult to set a proper transition region since there are no experimental data available between 20 and 50 MeV to validate the parameter for the transition factor.

5.1.4 Isotope Effect in (n,p) and (n,pn+np+d) Reactions

The isotope effect stated by Molla and Qaim [Mol 77], Molla et al. [Mol 92] and Dóczi et al. [Dóc 97a] could be clearly demonstrated. **Fig. 5.13** shows the results of the present experiment together with the STAPRE-H calculation for the (n,p) reactions on ^{50}Cr, ^{52}Cr, ^{53}Cr and ^{54}Cr. With increasing target mass number the maximum cross section for the (n,p) reaction on adjacing isotopes decreases by about a factor of two. The maximum position is shifted from 12.5 MeV for ^{50}Cr to 16.5 MeV for ^{54}Cr. The threshold of the reaction increases with the increasing mass number, the odd-even isotopes having a somewhat smaller threshold than the even-even ones, an effect attributable to the pairing energy. The isotope effect decreases with the increasing neutron energy since the Q-value becomes less important. The same trend can be stated for the (n,pn+np+d) reactions (see **Fig. 5.13**). In no previous study has such a trend been explicitely reported.

The overall good reproduction of the the experimental data with the STAPRE-H calculation gives confidence to the chosen consistent parameter set. This confidence lead to the attempt to calculate the excitation functions for the ^{51}Cr(n,p)^{51}V and ^{51}Cr(n,pn+np+d)^{50}V reactions to see if they fit in the systematics. Both reactions are not measurable at all, since ^{51}Cr is radioactive. Thus the calculations are "blind" calculations without any possibility of a parameter adjustment on the basis of experimental data. The (n,pn+np+d) excitation function fits quite well in the systematic trend whereas the (n,p) reaction shows a behaviour which is somewhat doubtful: the excitation function has a first maximum around 3 MeV, decreases again, and above 4 MeV fits well in the established trend with the stable isotopes. A probable reason for this "dip" was thought to be a bad fitting of the level density between the discrete levels and the BSFG calculation. But any adjustment of the level density parameters of the nuclei ^{51}Cr and ^{51}V, the products of the strongest reaction channels, or any variation of the number of used discrete levels, could not remove this "dip".

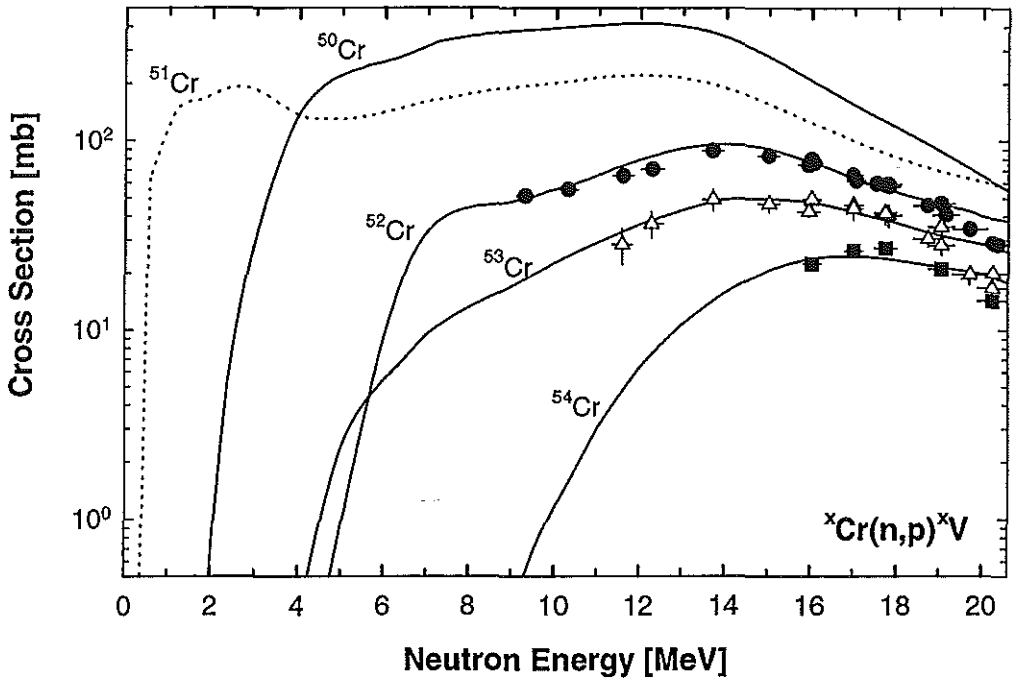

Fig. 5.12 Isotope effect in (n,p) reactions on Cr-isotopes. The symbols represent the experimental data points of this work, the solid lines the STAPRE-H calculations, and the dotted line a "blind" STAPRE-H calculation for the unstable ^{51}Cr.

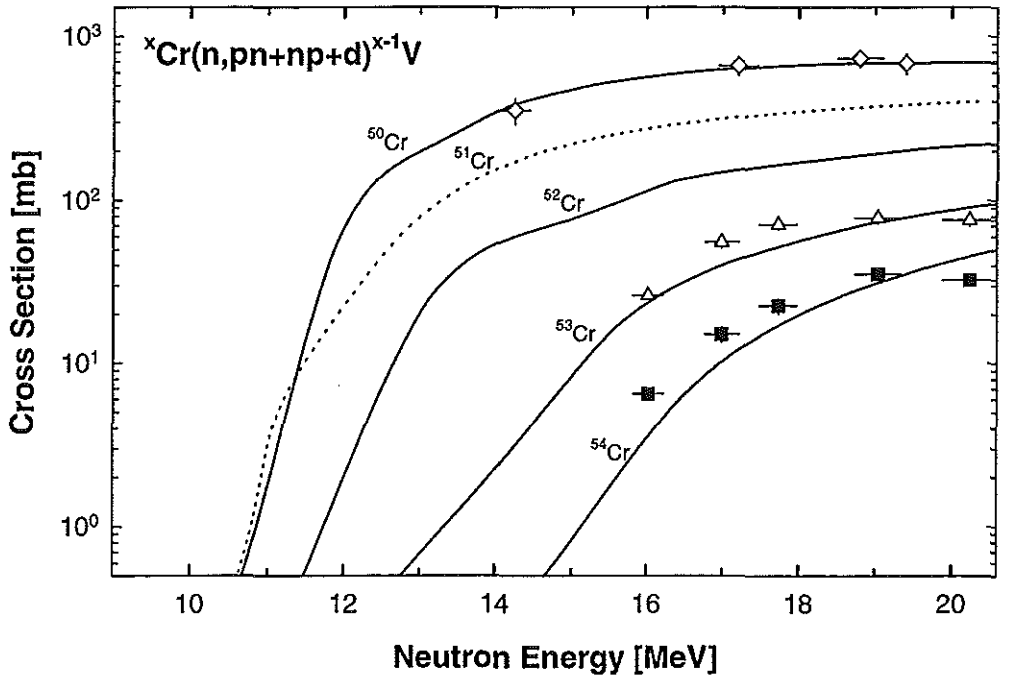

Fig. 5.13 Isotope effect in (n,pn+np+d) reactions on Cr-isotopes. The symbols represent the experimental data of this work, the solid lines the STAPPRE-H calculations, and the dotted line a "blind" STAPRE-H calculation for the unstable ^{51}Cr.

5.2 Data for Reactions on Iron

5.2.1 Experimental Data

The cross sections for the $^{54}Fe(n,2n)^{53m+g}Fe$ and $^{54}Fe(n,t+dn)^{52g}Mn$ reactions are listed in **Tab. 5.3**. The *Geel 1* cross sections were determined with ^{nat}Fe and the *Geel 2* data with enriched ^{54}Fe. The (n,2n) values are given as cumulative cross sections since the metastable state ($T_{1/2}$ = 2.58 min) decays 100 % via IT to the ground state.

Tab. 5.3 Measured cross sections for the $^{54}Fe(n,2n)^{53m+g}Fe$ and $^{54}Fe(n,t+dn)^{52g}Mn$ reactions.

$^{54}Fe(n,2n)^{53m+g}Fe$		$^{54}Fe(n,t+dn)^{52g}Mn$	
E_n [MeV]	σ [mb]	E_n [MeV]	σ [mb]
Geel 1		*Geel 1*	
15.22 ± 0.22	22.6 ± 2.0	16.05 ± 0.25	0.02 ± 0.01
15.64 ± 0.27	26.6 ± 2.0	16.89 ± 0.30	0.05 ± 0.01
16.51 ± 0.30	48.2 ± 3.7	17.82 ± 0.30	0.19 ± 0.02
17.54 ± 0.29	63.1 ± 5.2	19.14 ± 0.35	0.26 ± 0.03
17.91 ± 0.30	69.4 ± 6.9	20.35 ± 0.40	0.34 ± 0.03
18.21 ± 0.40	72.6 ± 4.8		
18.30 ± 0.32	75.6 ± 4.9		
Geel 2			
16.07 ± 0.20	39.1 ± 3.0		
17.06 ± 0.22	61.1 ± 4.6		
17.82 ± 0.25	71.4 ± 6.2		
19.15 ± 0.30	81.4 ± 7.7		
20.36 ± 0.35	88.2 ± 7.2		

5.2.2 Comparison with Literature Data, Evaluations and STAPRE-H Calculation

- **$^{54}Fe(n,2n)^{53m+g}Fe$**

The excitation function for the $^{54}Fe(n,2n)^{53m+g}Fe$ reaction is shown in **Fig. 5.14.** The new data obtained with ^{nat}Fe and ^{54}Fe as target materials are consistent. The older experimental data scatter very much. The data of Andreev and Serov [And 68] seem to be much too high and the values of Bormann et al. [Bor 76] above 15 MeV are rather low. The best agreement is given with the data of Ryves et al. [Ryv 78a] obtained with ^{nat}Fe; their data with enriched ^{54}Fe are somewhat higher [Ryv 78b]. Compared with the three given evaluations, our measurements are in good agreement up to 18 MeV with the ENDF/B-VI

values whereas beyond 18 MeV they are somewhat lower. The JEF-2.2 curve is consistently higher and the JENDL-3.2 curve consistently lower.

Two different STAPRE-H calculations are given in the plot. The curve **(a)** was obtained with the suggested level density parameter of Avrigeanu et al. [Avr 95b]. The values are much higher than the experimental ones. In order to solve this discrepancy the level density parameter for the residual nucleus ^{53}Fe was slightly decreased (- 2.8 %) and for the nucleus ^{53}Mn slightly increased (+ 3.5 %). Now the calculation fits very well with the experiment (curve **(b)**). In order to validate the chosen level density parameters the excitation function for the strong (n,p) channel is shown in **Fig. 5.15**. The parameter adjustment has almost no influence on the cross section, the calculations **(a)** and **(b)** giving identical results (therefore only one plot is given in the figure). The experimental data from the CSISRS data library [CSI 97] as well as the ENDF/B-VI values are in good agreement with the calculation.

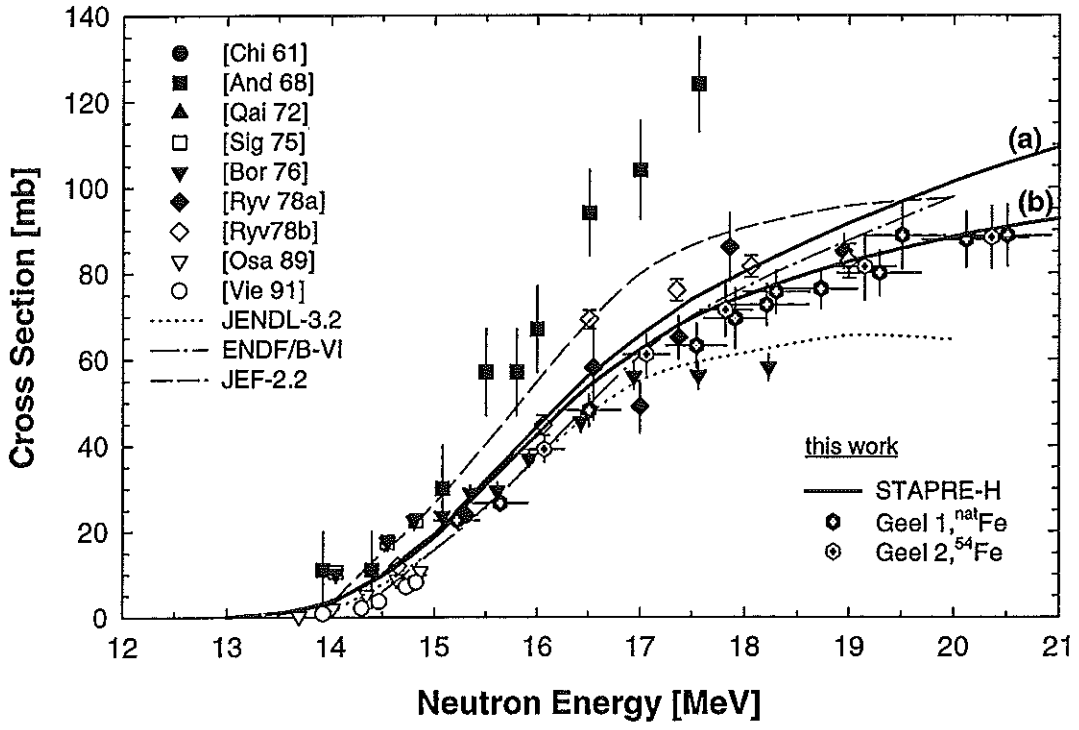

Fig. 5.14 Excitation function of the ^{54}Fe(n,2n)$^{53m+g}$Fe reaction. The bold lines are the STAPRE-H calculations for different level density parameters, **(a)** a(^{53}Fe) = 5.60, a(^{53}Mn) = 5.60, **(b)** a(^{53}Fe) = 5.45, a(^{53}Mn) = 5.80.

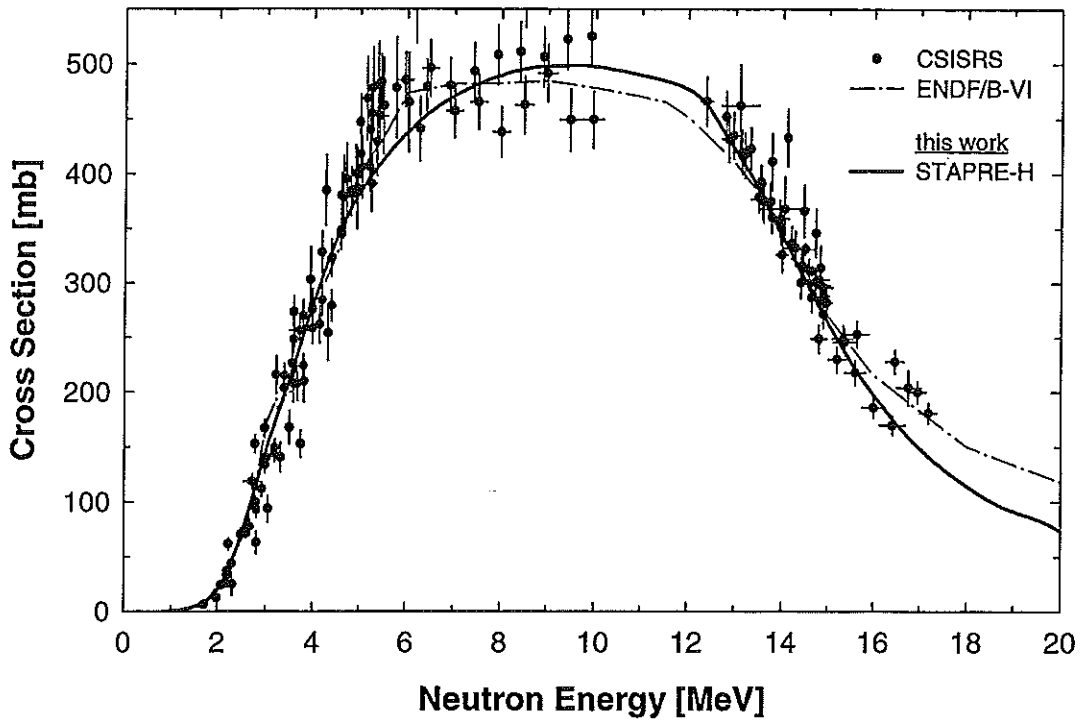

Fig. 5.15 Excitation function of the $^{54}Fe(n,p)^{54}Mn$ reaction.

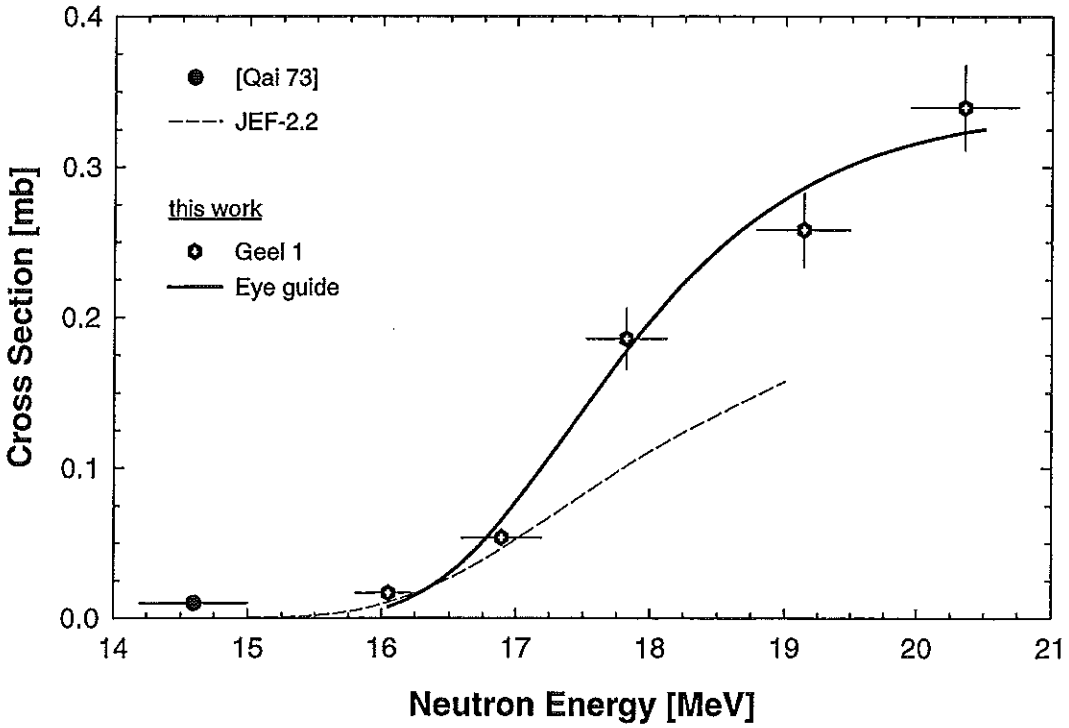

Fig. 5.16 Excitation function of the $^{54}Fe(n,t+dn)^{52g}Mn$ reaction.

- $^{54}Fe(n,t+dn)^{52g}Mn$

The excitation function of this reaction was measured from threshold to 20 MeV has been investigated for the first time in this work (see **Fig. 5.16**). So far only one data point had been reported by Qaim and Stöcklin [Qai 73] at 14.6 MeV. The cross sections are very low. They increase from the threshold of the (n,t) reaction at 12.66 MeV steadily to a value of 0.34 mb at 20.4 MeV. Above 19.03 MeV also the (n,dn) reaction contributes to the production cross section. The $^{54}Fe(n,p2n)^{52g}Mn$ reaction has a too high threshold (E_{thres} = 21.30 MeV) to contribute to the production cross section. The only available evaluation (JEF 2.2) agrees with our data up to 17 MeV; and beyond this energy the evaluated curve is much lower. A systematic study of excitation functions of (n,t) reactions by Wölfle et al. [Wöl 90] reported much higher cross section values. However, since they studied only reactions on odd-mass targets, which have generally higher cross sections than reactions on even-mass targets (see section 1.2.1 and [Qai 76]), the present study is not in contradiction to the systematics.

5.3 Data for Reactions on Nickel

5.3.1 Experimental data

Cross sections of three reactions were measured (see **Tab. 5.4**). They all were determined with ^{nat}Ni but represent cross sections on the individual isotopes since no competing reactions leading to the same activation product were energetically possible. The values for the $^{58}Ni(n,\alpha p)^{54}Mn$ process include also contributions of the (n,pα) reaction.

Tab. 5.4 Measured cross sections of some reactions on Ni.

Neutron Energy [MeV]	Cross section [mb] $^{58}Ni(n,\alpha)^{55}Fe$	$^{58}Ni(n,\alpha p)^{54}Mn$	$^{62}Ni(n,\alpha)^{59}Fe$
12.97 ± 0.20	98.5 ± 8.0		13.0 ± 1.2
14.25 ± 0.20	101.6 ± 8.9	0.3 ± 0.1	19.7 ± 1.5
17.19 ± 0.25	66.2 ± 5.8	12.4 ± 1.1	16.0 ± 1.4
18.79 ± 0.30	55.7 ± 5.0	22.2 ± 1.9	15.8 ± 1.4
19.40 ± 0.32	50.4 ± 4.5	26.8 ± 2.3	15.1 ± 1.5

5.3.2 Comparison with Literature Data, Evaluations and STAPRE-H Calculation

- **^{58}Ni(n,α)^{55}Fe and ^{58}(n,αp)^{54}Mn**

The available data on the (n,α) reaction are illustrated in **Fig. 5.17**. As mentioned earlier, most of the literature data were obtained by measuring the total helium emission, i. e. they represent the sum of the ^{58}Ni(n,α), ^{58}Ni(n,nα), ^{58}Ni(n,αn), ^{58}Ni(n,αp) and ^{58}Ni(n,pα) reactions. They are comparable with activation data up to a neutron energy of about 10 MeV, the threshold of the (n,nα) reaction. The present experimental data (*Geel 1*) are the first (n,α) cross sections above 10 MeV apart from the single data point of Qaim and Molla [Qai 77] at 14.8 MeV. This cross section is ~ 20 % higher than the *Geel 1* value at 14.3 MeV. None of the three given evaluations confirms all the *Geel 1* data; at 13 MeV JENDL-3.2 and JEF-2.2 are in agreement, at 14.3 and 17.2 MeV ENDF/B-VI is matching, and the two highest points between 18 and 20 MeV are best reproduced by JEF-2.2. Considering also the low energy part of the excitation function the evaluations show significant disagreement. They were all done over a decade ago and had only the experimental results near 14 MeV and the activation data of Qaim et al. [Qai 84]. The JEF-2.2 evaluator (M. Uhl) did not even know of the Qaim data. The problem of big differences in the evaluations between 6 and 12 MeV was attributed to the level densities used in the different calculations [Fu 96]. The JEF-2.2 evaluation was done using much larger level densities in all binary channels. In a calculation near 8 MeV, secondary neutrons and protons can sense the large differences in level densities, but outgoing alpha-particles are emitted predominantly to the discrete levels, so the (n,α) cross section becomes smaller. As incident energies go higher, the outgoing alpha-particles can reach the larger level densities and the calculated cross sections increase again. This explains the rise-flatten-rise shape of the JEF-2.2 evaluation.

Since 1987 many spectral measurements have been reported below 10 MeV but none of them could confirm the higher activation values. It seems that they lie ~ 20 to 40 % too high. A recent measurement of Haight et al. [Hai 97b] with neutrons from the pulsed, fast neutron spallation source at the Los Alamos Neutron Science Centre confirms the lower trend up to 10 MeV as well as the 14 MeV data.

The STAPRE-H calculation is in excellent agreement with the *Geel 1* data. Summing up the cross sections of the (n,α), (n,nα+αn) and (n,pα+αp) reactions leads to the (n,xα) cross section, which reproduces the Haight values very well. It seems that the parameter set for the calculation is well chosen. The only discrepancy lies in the threshold region where the calculation is systematically higher. This seems to be a problem of the optical model parameters but could not be solved by using another potential.

The ^{58}Ni(n,αp)^{54}Mn reaction was first observed by Iwasaki et al [Iwa 93]. The excitation function is shown in **Fig. 5.18**. It was natural to assume that such a two charged particle emission process would be hindered. Nevertheless, it was found that the cross section at 20 MeV is appreciable high (~ 20 mb). A later experiment reported almost the double of this value [Iwa 94]. The new *Geel 1* data confirm the older data of Iwasaki et al.

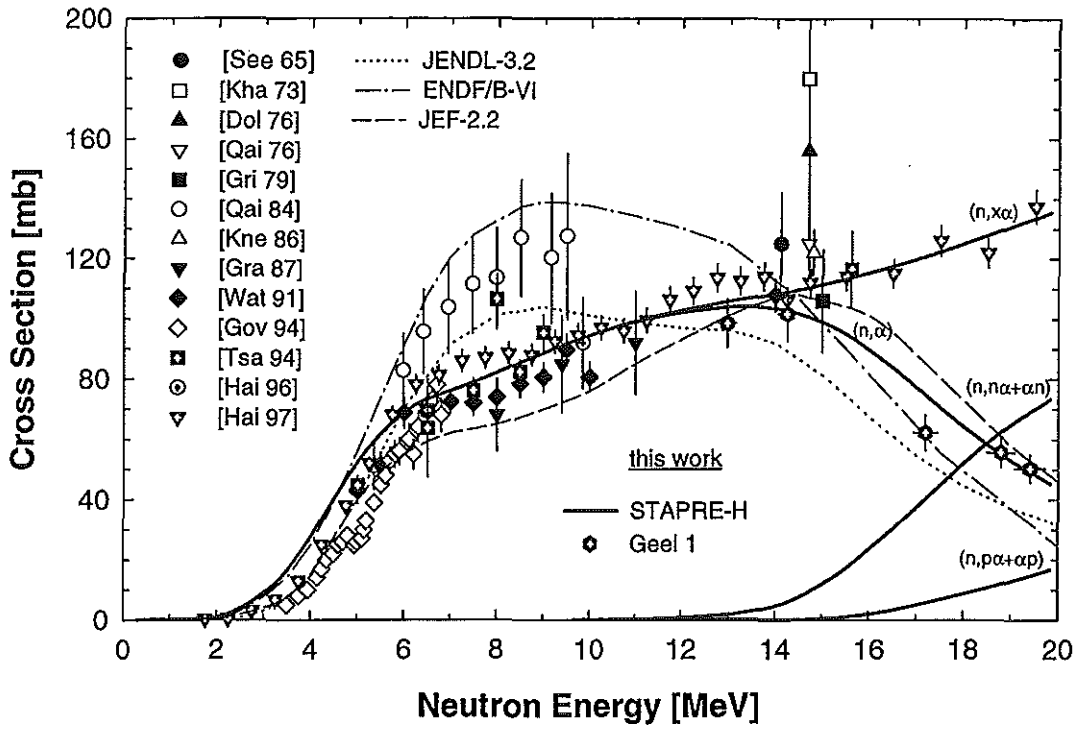

Fig. 5.17 Excitation function of the $^{58}Ni(n,\alpha)^{55}Fe$ and $^{58}Ni(n,x\alpha)$ reactions.

The STAPRE-H calculation is systematically ~ 50 % lower than the experimental values but is in agreement with the SINCROS-II calculation of Yamamuro [Yam 90], which is also based mainly on the statistical model.

In summary, the data base for the (n,α) reaction could be extended to 20 MeV and the appreciable cross section of the (n,αp) reaction, which contributes ~ 20 % to the total helium emission at 20 MeV, could be confirmed. The model calculation describes the (n,α) reaction well but fails to reproduce the complex (n,αp) process.

- **$^{62}Ni(n,\alpha)^{59}Fe$**

This reaction has hitherto been only poorly studied (see **Fig. 5.19**). The *Geel 1* data agree with the value of Qaim and Molla [Qai 77] around 14 MeV whereas the other scattered 14 MeV data are slightly higher. They were all measured with different techniques (activation method [Yu 67, Wei 75, Qai 77], alpha-particle detection [Dol 76], mass spectrometry [Kne 86]). One measurement was done from threshold to 10 MeV [Qai 84]. The points beyond 17 MeV are lying higher than the predicted values from the evaluations whereas the point at 13 MeV is in excellent agreement with them. The STAPRE-H calculation reproduces the low energy data of Qaim et al. [Qai 84], the lower trend in the 14 MeV data and the evaluations up to 15 MeV. Beyond this energy it suggests a higher value than the evaluations but is consistent with the new experimental data measured in this work.

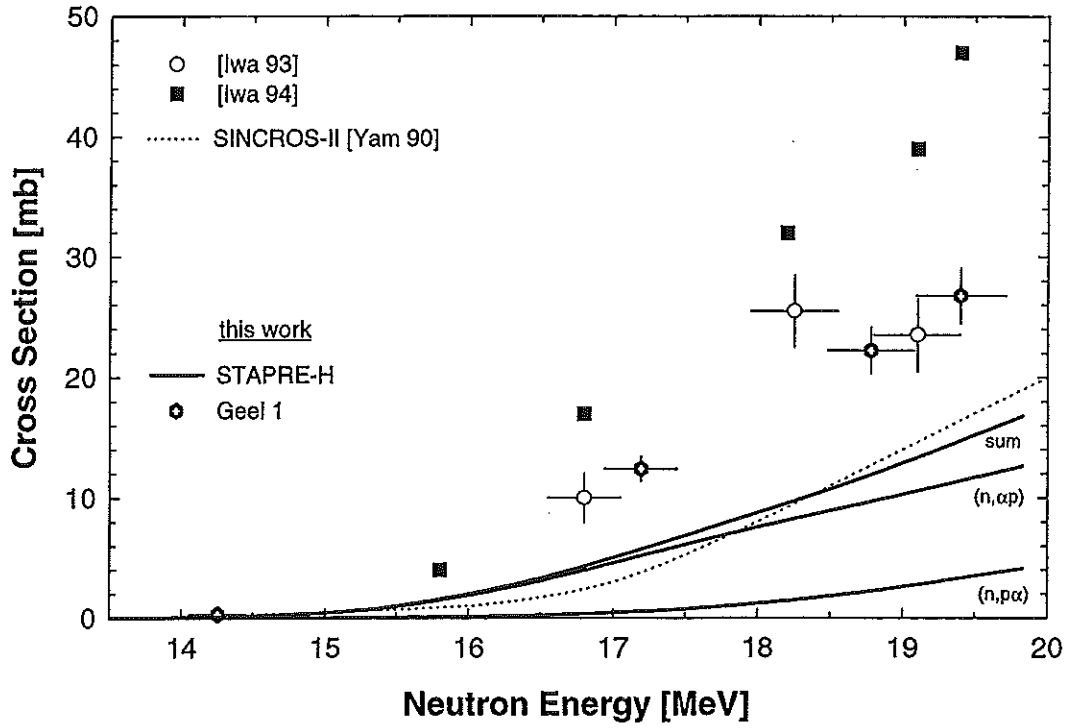

Fig. 5.18 Excitation function of the ^{58}Ni(n,αp+pα)^{54}Mn reaction.

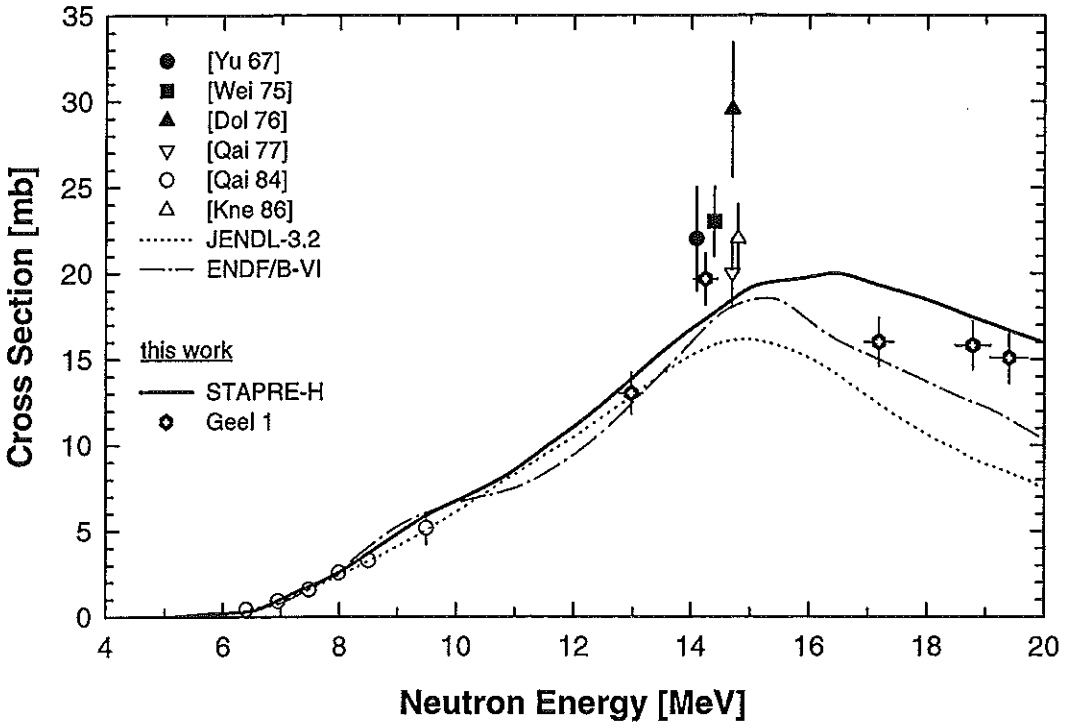

Fig. 5.19 Excitation function of the ^{62}Ni(n,α)^{59}Fe reaction.

5.4 Isomeric Cross Section Ratios

5.4.1 Experimental Data

The measurement of the ICSR's in the two investigated reactions, viz. $^{54}Fe(n,2n)^{53m,g}Fe$ and $^{54}Fe(n,t)^{52m,g}Mn$, appeared to be very difficult. In the first case the ICSR is very low and the threshold of the reaction very high. Therefore, only 5 points between 18.9 and 20. 9 MeV, the upper limit of the available neutron energy range, could be measured. In the other case, the ICSR is much higher but the cross sections for the individual states are very low (10 - 300 μb). In addition only a limited amount of enriched ^{54}Fe sample material was available due to economic reasons. The enriched material was mandatory for the measurement of the metastable state ($T_{1/2}$ = 21 min) since by using a natural sample a too high matrix activity was obtained. The main isotope of iron, ^{56}Fe, leads to ^{56}Mn ($T_{1/2}$ = 2.58 h) via the strong (n,p) reaction. ^{56}Mn has a strong gamma-ray at 1810 keV which gives a high Compton background and covers the weak 1434 keV gamma-ray of ^{52m}Mn. The determination of the cross section of the ground state could be done with a natural sample since here due to the long half-life all short-lived activities completely decayed before starting the activity counting of ^{52g}Mn. Another problem occurred at the time of the measurements: the experimental conditions were not satisfying, mainly the available deuteron current of the accelerator was too low. For this experiment a current of only 5 μA was available what was a factor of 4 less than it was generally during the cross section measurements. A repetition was not possible due to limitation of time. Nevertheless, two data points could be measured and an upper limit for a third could be given. The ICSR for both reactions are listed in **Tab. 5.5.**

Tab. 5.5 Isomeric cross section ratios of the investigated reactions. The *Geel 1* data are determined with ^{nat}Fe and the *Geel 2* data with ^{54}Fe (* σ_g, ** σ_m).

$^{54}Fe(n,2n)^{53m,g}Fe$		$^{54}Fe(n,t+dn)^{52m,g}Mn$	
E_n [MeV]	$\sigma_m / \sigma_m + \sigma_g$	E_n [MeV]	$\sigma_m / \sigma_m + \sigma_g$
Geel 1			
18.87 ± 0.37	0.004 ± 0.001		
20.08 ± 0.40	0.013 ± 0.003		
20.90 ± 0.50	0.016 ± 0.004		
Geel 2		*Geel 1**, *Geel 2***	
		16.05 ± 0.30	0.00 ± 0.65
19.15 ± 0.40	0.006 ± 0.002	19.15 ± 0.40	0.43 ± 0.16
20.36 ± 0.50	0.011 ± 0.003	20.36 ± 0.50	0.46 ± 0.11

5.4.2 Isomeric Cross Section Ratios of ^{53m,g}Fe and ^{52m,g}Mn in various Nuclear Reactions

- **^{53m,g}Fe**

The ICSR of the ^{54}Fe(n,2n)^{53m,g}Fe reaction as a function of incident projectile energy is illustrated in **Fig. 5.20**. For comparison, the only known ICSR in a charged particle reaction, namely the ^{52}Cr(^{3}He,2n)^{53m,g}Fe reaction, is also given in the figure. The ICSR for both reactions increases with increasing incident projectile energy, that means the ground state with the lower spin (J_g = 7/2$^-$) is preferentially populated than the higher spin metastable state (J_m = 19/2$^-$). However, with increasing projectile energy this effect becomes less severe. Both ICSR's are very small. The (^{3}He,2n) reaction seems to have its maximum at a value of ~ 0.12 whereas for the (n,2n) reaction the maximum could not be deduced since in the present work only some data in the threshold region could be measured. The STAPRE-H calculation (for details see below), which is in excellent agreement with both the experimental data sets on the (n,2n) reaction studied in this work, suggests a maximum at an incident neutron energy value of about 0.045 to 0.05 above 30 MeV. The maximum value of the ratio is by a factor of more than two less than in the case of the (^{3}He,2n) reaction. A value of 0.10 reported by Qaim [Qai 72] at 14.8 MeVseems to be erronous since the reaction threshold is much higher (16.5 MeV).

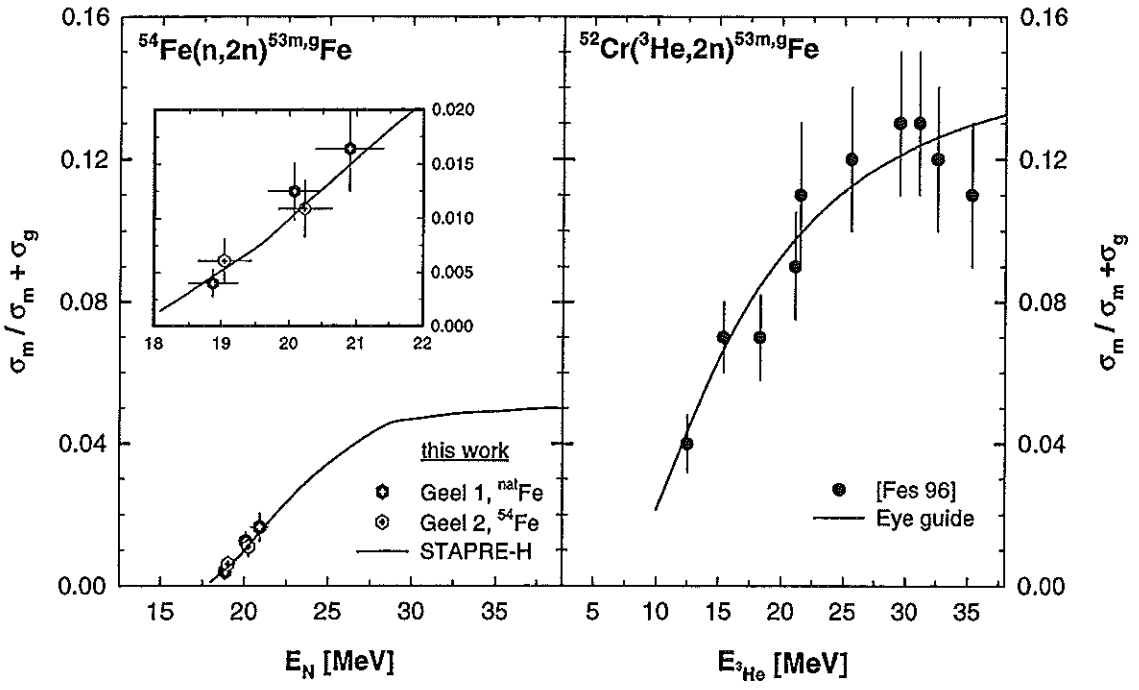

Fig. 5.20 Isomeric cross section ratio of the isomeric pair ^{53m,g}Fe in two different reactions. The small figure in the insert gives a magnification of the threshold region.

Generally, the isomeric ratio is expected to depend on factors like spin of the target nucleus, type of the emitted particle, spins of the isomeric states concerned and the type and energy of the projectile used [Qai 94, Sud 96]. Here, only the latter point is of interest since both the target nuclei have the same spin and parity ($J = 0^+$), the emitted particles are in both cases two neutrons and the same isomeric pair is formed. The differences in the ICSR could arise from the different angular momentum distributions of the produced compound nucleus ^{55}Fe. The higher kinetic energy of the ^{3}He particle involved may allow the absorption of the particle with higher angular momentum. This was suggested by Sudár and Qaim [Sud 96] in a similar study involving (α,n), (p,pn) and (n,2n) reactions. The present work furnishes a more clear proof of that postulate.

- **^{52m,g}Mn**

The present data on the ^{54}Fe(n,t)^{52m,g}Mn reaction are compared with the results of three charged particle induced reactions in **Fig. 5.21**. From the three data points (one of them is only given as an upper limit) it is difficult to conclude a systematic behaviour of the ICSR as a function of energy. Two eye guides are given in the figure: curve (**a**), taking into account the two data points from Qaim et al., one at 14 MeV measured at a neutron generator [Qai 73] and the other at 22.5 MeV average neutron energy, measured in a broad neutron spectrum produced via break-up of 53 MeV deuterons on a Be target [Qai 78], and curve (**b**), using only the present data with the point at 16 MeV as zero. A comparison with the ICSR's of the two reactions in the left part of the figure, namely the ^{52}Cr(p,n)^{52m,g}Mn and ^{52}Cr(^{3}He,t)^{52m,g}Mn reactions, makes curve (**a**) more reliable since their shape is similar. Starting from low energies the ICSR rapidly decreases with increasing energy, reaching a constant value at higher energies. This behaviour is expected since the metastable state has lower spin ($J_m = 2^+$) compared to the ground state ($J_g = 6^+$) and should therefore be preferentially populated at lower energies. A more quantitative interpretation seems to be difficult since apart from the ^{52}Cr(p,n)^{52m,g}Mn reaction with the highest ICSR (~ 0.55 to 0.9) all other reactions are more complex. The ^{54}Fe(^{3}He,αp)^{52m,g}Mn reaction proceeds via two intermediate excited (compound) nuclei, emitting two particles of which the alpha-particle is even a light complex particle (ICSR ~ 0.4) whereas both the ^{52}Cr(^{3}He,t)^{52m,g}Mn (ICSR ~ 0.3 to 0.6) and ^{54}Fe(n,t)^{52m,g}Mn (ICSR ~ 0.4 to 0.9) reactions contain contribution from ^{52}Cr(^{3}He,t+nd+p2n)^{52m,g}Mn and ^{54}Fe(n,t+nd)^{52m,g}Mn processes, respectively.

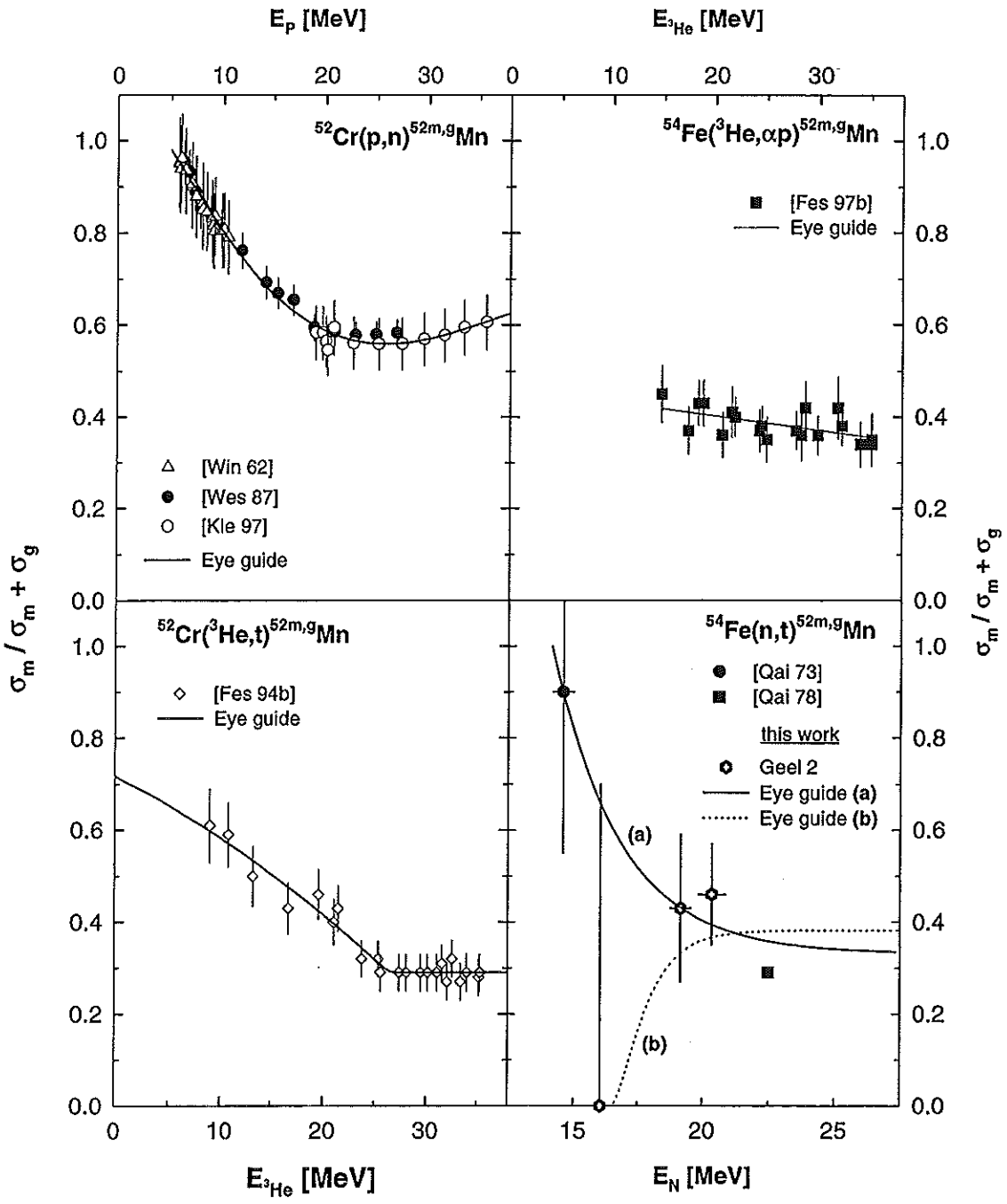

Fig. 5.21 Isomeric cross section ratio of the isomeric pair ^{52m,g}Mn in four different reactions.

5.4.3 Model Calculation

Since calculations of ICSR are strongly dependent on the input level scheme of the product nucleus [Qai 88], the parameters have to be chosen very carefully. In this work the isomer ratio was calculated only for the pair ^{53m,g}Fe, formed in a relatively simple (n,2n) reaction. The energies , spins, parities and branching ratios of the levels were selected from the *Table of Isotopes* [Fir 96] and are given in **Tab. 5.6**. The level density in the continuum region was calculated with the BSFG model as explained earlier. The spin distribution of the level density was characterized by the ratio of the effective moment of inertia Θ_{eff} to the rigid-body moment of inertia Θ_{rig}.($\eta = \Theta_{eff} / \Theta_{rig}$). The calculations were performed for $\eta = 1.0$ (see also **section 4.2.4**).

Since the calculation is in good agreement with the experimental data (cf. **Fig. 5.20**, at the left hand side) it seems that the input parameters are well chosen. Nevertheless, to validate the input values of the discrete levels (energy, spin, parity, branching ratio), calculations should be done for other reactions leading to the same isomeric pair.

Tab. 5.6 Energy levels of ^{53}Fe used in the STAPRE-H calculation.

E [keV]	J^{π}	Level (branching ratio [%])
0	$7/2^-$	β^+
741	$3/2^-$	0 (100)
774	$1/2^-$	741 (100)
1328	$9/2^-$	0 (100)
1423	$5/2^-$	741 (79), 774 (21)
1696	$7/2^-$	0 (5), 741 (95)
1896	$1/2^-$	741 (52), 774 (48)
2043	$3/2^-$	0 (100)
2315	$1/2^-$	741 (52), 774 (48)
2339	$11/2^-$	0 (13), 1328 (87)
2405	$5/2^-$	0 (70), 741 (23), 1423 (5), 1696 (3)
2479	$5/2^-$	741 (100)
2680	$3/2^-$	741 (46), 774 (43), 1423 (8), 1896 (1), 2043 (1) 2315 (1)
2829	$3/2^-$	0 (100)
2845	$7/2^-$	0 (100)
2892	$1/2^-$	741 (47), 774 (45), 1328 (5), 1423 (3)
2915	$7/2^-$	0 (73), 1328 (12), 1423 (10), 1696 (5)
2926	$1/2^+$	741 (48), 774 (45), 1896 (2), 2043 (1), 2315 (3)
2944	$3/2^-$	741 (40), 774 (380), 1423 (13), 1896 (4), 2043 (3), 2405 (1)
2967	$1/2^+$	741 (100)
3040	$19/2^-$	2339 (99), 1328 (1)

6. Summary and Conclusions

The knowledge of cross sections of neutron induced reactions on the structural materials Cr, Fe and Ni is important for practical applications in fusion reactor technology as well as for testing nuclear models. The present study was performed using the activation method where the induced activity of a reaction product is measured off-line. In this work high-resolution gamma-ray spectrometry and X-ray spectrometry were used, the latter in combination with radiochemical separation and preparation of thin samples. Excitation functions of a total of 13 reactions were measured in the energy range between 9 and 21 MeV. These included (n,p), (n,np), (n,2n), (n,α) and (n,t) reactions on the above mentioned elements. In the neutron energy range of 9.3 to 12.3 MeV irradiations were performed at the variable energy Compact Cyclotron CV28 at the Forschungszentrum Jülich using the D(d,n)^{3}He reaction on a deuterium gas target, whereas in the energy range of 13.0 to 21.0 MeV irradiations were done at the 7 MV Van de Graaff accelerator at the CEC-JRC, IRMM at Geel using the ^{3}H(d,n)^{4}He reaction on a solid Ti/T target. All cross sections were determined relative to the IRDF-90.2 standard cross sections of the ^{27}Al(n,p)^{27}Mg, ^{27}Al(n,α)^{24}Na, ^{56}Fe(n,p)^{56}Mn and ^{93}Nb(n,2n)^{92m}Nb reactions.

A pneumatic sample transport system was installed at Geel to enable measurements of short-lived reaction products. Compressed air was used to transport a sample container to the target area through a plastic tube, and a vacuum pump was used to retrieve it to the remote counting room after the irradiation. This system was successfully applied to the determination of reaction products with half-lives $\geq$ 10 seconds.

For the (n,p) and (n,np) reactions on the four stable Cr-isotopes, viz. ^{50}Cr, ^{52}Cr, ^{53}Cr and ^{54}Cr, a systematic trend in the excitation functions could be observed. With the increasing mass of the target nucleus, the threshold increases, the maximum of the excitation function is shifted to higher energies and the cross section at the maximum tends to decrease for adjacent isotopes by about a factor of two. The effect is ascribed to the Q-values of the reactions. The odd-even isotopes have a somewhat smaller threshold than the even-even ones, an effect attributed to pairing energy. Data were measured for the first time for the ^{52}Cr(n,p)^{52}V and ^{53}Cr(n,p)^{53}V reactions in the "gap-region" between 10 and 14 MeV. Beyond 14 MeV, substantial new information was obtained. In the case of the ^{52}Cr(n,2n)^{51}Cr and ^{54}Cr(n,α)^{51}Ti reactions the data base was strengthend. Thus, for all studied reactions on the Cr-isotopes, especially for the ^{53}Cr(n,p)^{53}V, ^{54}Cr(n,p)^{54}V and ^{54}Cr(n,α)^{51}Ti reactions, where large discrepancies exist in the major evaluations, the present data should contribute appreciably to solving those discrepancies.

The cross sections of the ^{50}Cr(n,pn+np+p)^{49}V reaction were measured for the first time beyond 14 MeV using a special technique. The product ^{49}V was separated from the Cr-target by precipitation with cupferron alongwith Fe(III) as collector from an acid solution. Iron was then separated from the vanadium by solvent extraction with diisopropyl ether

(DIPE) and a thin sample was prepared by precipitating the vanadium as vanadate. The activity measurement was then done by X-ray spectrometry.

A standard source for the efficiency calibration of the Si(Li) detector for the soft X-rays of ^{49}V (4 and 4.5 keV) was prepared using ^{48}V which emits X-rays of the same energies but also has some strong gamma-ray lines which can be used for standardization purposes. The ^{48}V was produced in a proton irradiation on ^{nat}Cr, separated from the target by anion-exchange, and a thin sample was made by adsorption of the "no carrier added" (n. c. a.) ^{48}V on a few crystals of DOWEX-1X8 and covering the sample with a thin mylar foil. The absolute activity of the sample was then determined via gamma-ray spectrometry.

Excitation functions were determined for two reactions on iron, namely $^{54}Fe(n,2n)^{53m+g}Fe$ and $^{54}Fe(n,t+dn)^{52g}Mn$. The latter reaction was investigated for the first time; as expected the cross section was small (340 μb at 20.4 MeV). In the case of the (n,2n) reaction, the present measurement provided more consistent data.

As far as the reactions on Ni are concerned, the main interest was on $^{58}Ni(n,\alpha)^{55}Fe$, $^{58}Ni(n,\alpha p)^{54}Mn$ and $^{62}Ni(n,\alpha)^{59}Fe$. The activation method allowed the measurement of the cross sections of these individual reactions whereas most of the literature data report total helium emission cross sections, i. e. the sum of (n,α), (n,nα) and (n,pα) reactions. In this work the three above mentioned reactions could be studied using ^{nat}Ni as target material. Whereas the $^{58}Ni(n,\alpha p)^{54}Mn$ and $^{62}Ni(n,\alpha)^{59}Fe$ reactions could be studied non-destructively using gamma-ray spectrometry, the (n,α) reaction on ^{58}Ni was measured via the soft X-rays MnK_α and MnK_β emitted from the reaction product ^{55}Fe. Therefore the ^{55}Fe was separated from the bulk of Ni using an anion-exchange column, and a thin sample was prepared by a electrodeposition. The plating of iron was carried out in a small electrolytic cell from an alkaline solution of Fe-citrate in an almost quantitative way.

In addition to excitation functions, isomeric cross section ratios were also measured for the isomeric pairs formed in $^{54}Fe(n,2n)^{53m,g}Fe$ and $^{54}Fe(n,t+dn)^{52m,g}Mn$ processes. Five data points between 18.9 and 20.5 MeV could be measured for the former reaction and three data points (one of them as upper limit) for the latter. In the first case the ratio increases with increasing neutron energy but is generally very small. In the second case the ratio decreases with increasing neutron energy. This effect is explained in terms of the higher spin of the isomeric state as compared to that of the ground state in the first case, and the lower spin of the isomeric state in the second case. A comparison of the isomer ratios in reactions induced by charged particles (p or ^3He) leading to the same isomeric pairs showed the same trend. The somewhat smaller isomeric cross section ratio of the $^{54}Fe(n,2n)^{53m,g}Fe$ reaction compared to the $^{52}Cr(^3He,2n)^{53m,g}Fe$ reaction seems to be associated with the different angular momentum distribution of the produced compound nucleus. The higher kinetic energy of the ^3He particle involved may allow the absorption of the incident particle with higher angular momentum, resulting in somewhat enhanced population of the high spin isomer.

On the basis of the experimentally determined cross sections and isomeric cross section ratios nuclear model calculations were carried out with the code STAPRE-H in order to test the underlying models. STAPRE-H uses the Hauser-Feshbach formula for the

equilibrium and the Exciton or Geometry Dependent Hybrid (GDH) Model for the pre-equilibrium (PE) contribution. Starting from input parameters from the literature, a consistent parameter set for all reactions was developed by small adjustments of the level density parameters in order to obtain a better reproduction with the experimental values. The influence of the PE contribution to the cross section was investigated with the two PE models and by varying the FM parameter in the Exciton Model. GDH and Exciton Model gave almost similar results. It was found that the decrease of FM increases the PE fraction and makes the first chance emission spectrum harder, which reduces the second chance emission. The influence of the level density was tested by using different level density formulas. The best results were obtained by using the semi-empirical Back Shifted Fermi Gas (BSFG) Model up to 20 MeV. Attempts to use a more realistic level density formula at higher energies gave unsatisfactory results.

Most of the reactions could be described by the model calculation with deviations of $\pm$ 10 % to the experiment. This shows that the underlying models can reproduce the excitation functions satisfactorily, provided the input parameters are well chosen.

The author of this dissertation is convinced that the cross sections of the neutron induced reactions on Cr, Fe and Ni, determined in this work, substantially improved the existing data base. The present data were successfully used to determine a unique parameter set for testing nuclear model predictions in one particular mass range. In the future, the data should be useful for practical applications, like fusion reactor technology, since all these isotopes are important components of structural materials. The merits and problems of the various alloys of these elements can be addressed more reliably by nuclear engineers.

7. Zusammenfassung

Die Kenntnis von Wirkungsquerschnitten von neutroneninduzierten Kernreaktionen an den Strukturmaterialien Chrom, Eisen und Nickel ist wichtig für die Entwicklung und das Design von Fusionsreaktoren sowie zum Test von Kernreaktionsmodellen. In dieser Arbeit wurden Wirkungsquerschnitte und isomere Wirkungsquerschnittsverhältnisse mit der Aktivierungstechnik bestimmt, eine Methode bei der die induzierte Aktivität eines Reaktionsprodukts "off-line" gemessen wird, d. h. die Bestrahlung der Aktivierungsprobe und ihre Messung erfolgen zeitlich und räumlich getrennt. Die Aktivitätsmessung erfolgte entweder mit hochauflösender Gammaspektrometrie oder Röntgenspektrometrie. Im letzteren Fall wurden die Reaktionsprodukte radiochemisch von den bestrahlten Proben abgetrennt und dünne Messproben hergestellt. So wurden Anregungsfunktionen von (n,p)-, (n,np)-, (n,2n)-, (n,α)- und (n,t)-Kernreaktionen, insgesamt 13 verschiedene Reaktionen, an den oben bezeichneten Elementen im Neutronenenergiebereich zwischen 9 und 21 MeV bestimmt. Zwischen 9.3 und 12.3 MeV wurden die Bestrahlungen am Kompaktzyklotron CV 28 des Forschungszentrums Jülich durchgeführt. Die Neutronen wurden über die $D(d,n)^3He$ Reaktion an einem Deuterium Gas-Target erzeugt. Im Energiebereich zwischen 13.0 und 21.0 MeV erfolgten die Bestrahlungen am 7 MV Van de Graaff Beschleuniger des CEC-JRC, IRMM in Geel, Belgien. Hier wurden die Neutronen über die $T(d,n)^4He$ Reaktion an einem Ti/T Target erzeugt. Alle Wirkungsquerschnitte wurden relativ zu den IRDF-90.2 Referenzwirkungsquerschnitten der Kernreaktionen $^{27}Al(n,p)^{27}Mg$, $^{27}Al(n,\alpha)^{24}Na$, $^{56}Fe(n,p)^{56}Mn$ und $^{93}Nb(n,2n)^{92m}Nb$ gemessen.

Für die Messung von kurzlebigen Reaktionsprodukten wurde in Geel eine Rohrpostanlage installiert. Ein kleiner Probencontainer wurde in einer Plastikröhre mit Pressluft zum Neutronentarget transportiert und nach der Bestrahlung mit einer Vakuumpumpe zurück zum Messraum gebracht. Dieses System wurde erfolgreich für die Bestimmung von Reaktionsprodukten mit Halbwertszeiten $\geq$ 10 s angewendet.

Eine Systematik wurde für die Anregungsfunktionen der (n,p) und (n,np) Reaktionen an den vier stabilen Chrom-Isotopen (^{50}Cr, ^{52}Cr, ^{53}Cr und ^{54}Cr) beobachtet. Mit zunehmender Masse des Targetnuklids nimmt die Schwellenenergie zu, das Maximum der Anregungsenergie verschiebt sich nach höheren Neutronenenergien und der Wirkungsquerschnitt am Maximum reduziert sich zwischen benachbarten Isotopen ungefähr um den Faktor zwei; ein Effekt, der den unterschiedlichen Q-Werten der Reaktionen zugeschrieben wird. Die Isotope mit ungerader Massenzahl haben eine etwas niedrigere Reaktionsschwelle als die Isotope mit gerader Massenzahl aufgrund der freiwerdenden Paarungsenergie.

Zum ersten Mal wurden in dieser Arbeit Wirkungsquerschnitte in der sogenannten "Gap-Region" zwischen 10 und 14 MeV für die Reaktionen $^{52}Cr(n,p)^{52}V$ und $^{53}Cr(n,p)^{53}V$

gemessen. Oberhalb 14 MeV wurden wertvolle neue Informationen für den Verlauf der Anregungsfunktionen erhalten. Im Falle der $^{52}Cr(n,2n)^{51}Cr$ und $^{54}Cr(n,\alpha)^{51}Ti$ Reaktionen wurde die Datenbasis erweitert und bekannte Daten erhärtet. Mit den neuen Daten wurden für alle untersuchten Kernreaktionen an Cr-Isotopen wichtige Kenntnisse erzielt, um bestehende Diskrepanzen in den bedeutendsten Evaluierungen (ENDF/B-VI, JENDL-3.2 und JEF-2.2), besonders für die Reaktionen $^{53}Cr(n,p)^{53}V$, $^{54}Cr(n,p)^{54}V$ und $^{54}Cr(n,\alpha)^{51}Ti$, aufzuklären.

Die Wirkungsquerschnitte der Kernreaktion $^{50}Cr(n,pn+np+d)^{49}V$ konnten mittels einer speziel entwickelten Technik erstmals oberhalb 14 MeV bestimmt werden. Das Reaktionsprodukt ^{49}V wurde vom Cr-Target durch Ausfällen mit Kupferron (zusammen mit Fe(III) als nichtisotopem Träger) aus einer sauren Lösung radiochemisch abgetrennt. Anschließend wurde das Eisen durch Extraktion mit Diisopropylether (DIPE) von Vanadium abgetrennt, das Vanadium als Vanadat ausgefällt, zum V_2O_5 geglüht und eine dünne Messprobe durch Sedimentation des V_2O_5 aus einer Toluollösung hergestellt. Die Aktivität des ^{49}V wurde dann röntgenspektrometrisch bestimmt.

Für die Bestimmung der Ansprechwahrscheinlichkeit des für die Röntgenspektrometrie verwendeten Si(Li) Detektors wurde eine ^{48}V-Standardprobe hergestellt. ^{48}V emittiert dieselben Röntgenstrahlen wie ^{49}V, besitzt aber darüberhinaus auch einige intensive Gammastrahlen die für die Standardisierung der Probe geeignet sind. Das ^{48}V wurde durch die Bestrahlung von ^{nat}Cr mit Protonen produziert (Kernreaktion $^{52}Cr(p,\alpha n)^{48}V$) und über eine Anionenaustauschersäule abgetrennt. Anschließend wurde eine trägerfreie Probe durch Fixierung des ^{48}V an einigen Kristallen DOWEX-1X8 hergestellt und zum Schutz mit einer dünnen Mylarfolie abgedeckt. Die absolute Aktivität der Probe wurde dann gammaspektrometrisch bestimmt.

Für zwei Reaktionen an Eisen, $^{54}Fe(n,2n)^{53m+g}Fe$ und $^{54}Fe(n,t)^{52g}Mn$, wurden Anregungsfunktionen bestimmt. Die letztere wurde zum ersten Mal untersucht. Wie erwartet war der Wirkungsquerschnitt von 340 μb (bei 20.4 MeV) sehr klein. Im Falle der (n,2n)-Reaktion lieferten die Datenpunkte dieser Arbeit konsistentere Werte gegenüber den etwas streuenden Literaturdaten.

Im Falle von Nickel als Targetelement lag das Hauptinteresse der Untersuchung in den Reaktionen $^{58}Ni(n,\alpha)^{55}Fe$, $^{58}Ni(n,\alpha p)^{54}Mn$ und $^{62}Ni(n,\alpha)^{59}Fe$. Die Aktivierungstechnik ermöglichte die Messung von Wirkungsquerschnitten der einzelnen Reaktionen wogegen die meisten Literaturdaten sich auf die totale Heliumemission beziehen, d. h. die Summe der (n,α)-, (n,nα)- und (n,pα)- Reaktionen. In dieser Arbeit wurden die drei erwähnten Reaktionen mit ^{nat}Ni als Targetmaterial untersucht. Im Falle der $^{58}Ni(n,\alpha p)^{54}Mn$ und $^{62}Ni(n,\alpha)^{59}Fe$ Reaktionen konnte die Aktivität der Reaktionsprodukte gamma-spektrometrisch gemessen werden, wogegen die durch die (n,α)-Reaktion an ^{58}Ni induzierte ^{55}Fe Aktivität über die niederenergetischen Röntgenstrahlen (MnK_α und MnK_β) bestimmt wurde. Hierzu wurde unter Zugabe von etwas inaktivem Fe-Träger das ^{55}Fe vom Ni-Target über eine Anionenaustauschersäule abgetrennt und elektrolytisch auf einer Goldfolie abgeschieden. Die Abscheidung erfolgte aus einer alkalischen Fe-Citratlösung in einer kleinen Elektrolysezelle und war nahezu quantitativ.

Zusätzlich zu den Anregungsfunktionen wurden für die über die Kernreaktionen $^{54}Fe(n,2n)^{53m,g}Fe$ und $^{54}Fe(n,t)^{52m,g}Mn$ gebildeten Isomerenpaare die isomeren Wirkungsquerschnittsverhältnisse bestimmt. Fünf Datenpunkte zwischen 18.9 und 20.5 MeV konnten für die (n,2n)- und drei Datenpunkte (einer davon als obere Grenze) zwischen 16 und 20 MeV für die (n,t)-Reaktion bestimmt werden. Im ersteren Fall nimmt das Verhältnis mit zunehmender Neutronenenergie zu, ist aber generell sehr klein. Im zweiten Fall nimmt das Verhältnis mit zunehmender Neutronenenergie ab. Dieser Trend kann mit den unterschiedlichen Spins der isomeren Zustände und Grundzustände erklärt werden; im ersten Fall hat der isomere Zustand den höheren Spin wogegen im zweiten Fall der Grundzustand den höheren Spin besitzt. Ein Vergleich der isomeren Wirkungsquerschnittsverhältnisse mit Kernreaktionen mit geladenen Teilchen als Projektil zeigte den gleichen Trend. Das etwas geringere isomere Wirkungsquerschnittsverhältnis der $^{54}Fe(n,2n)^{53m,g}Fe$ Reaktion gegenüber der $^{52}Cr(^{3}He,2n)^{53m,g}Fe$ Reaktion scheint mit dem erzeugten Drehmoment des Compoundkerns zusammenzuhängen. Die etwas höhere kinetische Energie des ^{3}He-Teilchens könnte die Aufnahme des Projektils mit einem etwas höheren Drehmoment ermöglichen, was zu einer etwas größeren Bevölkerung des Isomers mit dem höheren Spin führen könnte.

Auf der Grundlage der experimentell bestimmten Wirkungsquerschnitte und isomeren Wirkungsquerschnittsverhältnisse wurden Kernmodellrechnungen mit dem Programm STAPRE-H durchgeführt, um die zugrundeliegenden Kernmodelle zu testen. STAPRE-H verwendet die Hauser-Feshbach Formel für die Berechnung des Gleichgewichtsanteils und das Excitonenmodell oder das "Geometry Dependent Hybrid Model" (GDH) für die Bestimmung des Vorgleichgewichtsanteils. Ausgehend von aus Literaturwerken ausgewählten Eingabeparametern wurde ein einheitlicher Parametersatz entwickelt mit dem alle Kernreaktionen berechnet wurden. Hierzu wurden einige Niveaudichteparameter geringfügig abgeändert, um eine bessere Übereinstimmung der experimentellen Daten mit den Rechnungen zu erzielen. Der Einfluß des Vorgleichgewichtsanteils wurde mit den beiden Vorgleichgewichtsmodellen untersucht, wobei der FM Parameter im Excitonenmodell variiert wurde. Die erzielten Ergebnisse mit beiden Modellen sind nahezu identisch. Bei Abnahme des FM Parameters nimmt die Vorgleichgewichtsemission zu; die "first chance" Emission verschiebt sich zu höheren Energien während die "second chance" Emission verringert wird. Der Einfluß der Niveaudichte wurde durch die Wahl unterschiedlicher Niveaudichteformeln untersucht. Die besten Ergebnisse wurden mit dem halbempirischen "Back-Shifted Fermi Gas Model" (BSFG) erzielt. Rechnungen mit einer realistischeren Niveaudichteformel bei höheren Energien gaben keine zufriedenstellenden Ergebnisse.

Die Mehrzahl der Reaktionen konnte mit den Modellrechnungen gut beschrieben werden. Die Abweichungen zwischen Experiment und Modellrechnung lagen meist bei ± 10 %. Dies zeigt daß die zugrundeliegenden Modelle die Anregungsfunktionen gut reproduzieren können, vorausgesetzt die Eingabeparameter sind sorgfältig ausgewählt.

Der Verfasser dieser Dissertation ist davon überzeugt, daß die in dieser Arbeit bestimmten Wirkungsquerschnitte der neutroneninduzierten Kernreaktionen an den

Strukturmaterialien Chrom, Eisen und Nickel die bestehende Datenbasis entscheidend verbessert haben. Die bestimmten Daten wurden erfolgreich für die Entwicklung eines konsistenten Parametersatzes zum Testen von Kernreaktionsmodellen in einem definierten Kernmassenbereich (A ~50) eingesetzt. In der Zukunft sollten die Daten für technische Anwendungen nützlich sein, wie z. B. für die Entwicklung von Fusionsreaktoren, da alle untersuchten Isotope wichtige Komponenten von Strukturmaterialien sind. Die Vorzüge und Probleme der verschiedenen Legierungen dieser Elemente können von Ingenieuren und Reaktortechnikern besser eingeschätzt werden, wodurch die Wahl geigneter Materialien erleichtert wird.

References

[Ait 87] S. Ait-Tahar, Nucl. Phys. **13**, 121 (1987).

[All 61] D. Allan, Nucl. Phys. **24**, 274 (1961).

[Alv 72] K. R. Alvar, Nucl. Phys. **A195**, 289 (1972).

[And 68] M. F. Andreev and V. I. Serov, Sov. J. Nucl. Phys. **7**, 454 (1968).

[Ara 73] J. Araminowicz and J. Dresler, Progress Report INR 1464, Inst. Badan Jadrowych, Warsaw, Poland, 14 (1973).

[Art 80] E. D. Arthur and P. G. Young, Report LA-8626-MS (ENDF-304), Los Alamos National Laboratory, U.S.A. (1980).

[Arn 92] R. Arndt and L. Workman, *"The H(n,n)H Cross Section from 20 to 350 MeV"*, in [Con 92], 10 (1992).

[Aud 95] G. Audi and A. H. Wapstra, Nucl. Phys. **A595**, 409(1995).

[Avr 87a] M. Avrigeanu, M. Ivascu and V. Avrigeanu, *"STAPRE-H - A Computer Code for Particle Induced Activation Cross Sections and Related Quantities"*, Report NP-63-1987, IPNE Bucharest, P. O. Box MG-6, Romania (1987).

[Avr 87b] M. Avrigeanu, M. Ivascu and V. Avrigeanu, Atomkernenergie - Kerntechnik, **49**, 133 (1987).

[Avr 88a] M. Avrigeanu, M. Ivascu and V. Avrigeanu, Z. Phys. **A329**, 177 (1988).

[Avr 88b] M. Avrigeanu, M. Ivascu and V. Avrigeanu, *STAPRE-H,* as computer file, ID IAEA 0971, NEA Data Bank, Paris, France (1988).

[Avr 88c] M. Avrigeanu, M. Ivascu and V. Avrigeanu, *"Fast Neutron Reaction Data Calculation with the Computer Code STAPRE-H"*, in [Met 88], 762 (1988).

[Avr 90] M. Avrigeanu, M. Ivascu and V. Avrigeanu, Z. Phys. **A335**, 299 (1990).

[Avr 94a] V. Avrigeanu, P. E. Hodgson and M. Avrigeanu, Phys. Rev. **C49**, 2136 (1994).

[Avr 94b] M. Avrigeanu and V. Avrigeanu, J. Phys. G: Nucl. Part. Phys. **20**, 613 (1994).

[Avr 95a] M. Avrigeanu and V. Avrigeanu, *"Recent Improvements of the STAPRE-H Preequilibrium and Statistical Model Code"*, Report NP-86-1995, IPNE Bucharest, P. O. Box MG-6, Romania (1995).

[Avr 95b] M. Avrigeanu, A. Harangozo and V. Avrigeanu, *"Surface effects in Feshbach-Kerman-Koonin analysis of (n,n') and (n,p) reactions at 7 to 26 MeV"*, Report NP-85-1995, IPNE Bucharest, P. O. Box MG-6, Romania (1995).

[Bab 94a] M. Baba, N. Ito, I. Matsuyama, S. Matsuyama, N. Hirakawa, S. Chiba, T. Fukahori, M. Mizumoto, K. Hasegawa and S. Meigo, *"Measurement of Double-Differential (n,α) Cross Sections of Fe, Ni, Cu and ^{50}Cr for 4.5 - 14.1 MeV Neutrons"*, in [Dic 94], 941 (1994).

[Bab 94b] M. Baba, N. Ito, I. Matsuyama, S. Matsuyama, N. Hirakawa, S. Chiba, T. Fukahori, M. Mizumoto, K. Hasegawa and S. Meigo, J. Nucl. Sci Tec. **31**, 745 (1994).

[Bad 91] S. A. Badikov and A. B. Pashenko, *"Comparative Analysis of (n,p) Reaction Cross Section Systematics for 14 - 15 meV Neutrons"*, Report INDC(CCP)-325, IAEA, Vienna, Austria (1991).

[Bah 84] B. M. Bahal and R. Pepelnik, Report GKSS 84/E, Forschungszentrum Geesthacht GmbH (1984).

[Bah 85] B. M. Bahal and R. Pepelnik, Report GKSS 85/E/11, Forschungszentrum Geesthacht GmbH (1984).

[Bar 52] H. H. Barschall, L. Rosen, R. F. Taschek, Rev. Mod. Phys. **24**, 1 (1952).

[Ber 81] O. Bersillon, Report CEA-N-2227, CE Bruyeres-le-Chatel, France (1981).

[Ber 87] M. J. Berger and J. H. Hubbel, *"XCOM: Photon Cross Sections on a Personal Computer"*, Internal Report National Bureau of Standards, NBSIR 87-3597, Gaithersburg, U.S.A. (1987).

[Bir 75] T. Biró, S. Sudár, Z. Miligy, Z. Dezsö and J. Csikai, J. Inorg. Nucl. Chem. **37**, 1583 (1975).

[Bir 92] I. G. Birn, *"NEUT - Ein Programm zur Berechnung von Neutronenspektren erzeugt durch die D(d,n)^{3}He-Reaktion in einem Gastarget am Zyklotron"*, Internal Report KFA-INC-IB-1/92, Forschungszentrum Jülich GmbH (1992).

[Bir 94a] I.-G. Birn, *"Calculation of the Mean Energy and the Energy Spread of Neutrons produced by the D(d,n)^{3}He reaction in a Gas Target"*, Internal Report GE/R/VG/85/94, CEC-JRC IRMM Geel (1994).

[Bir 94b] I.-G. Birn and S. M. Qaim, Nucl. Sci. Eng. **116**, 125 (1994).

[Bir 95] I.-G. Birn, B. Strohmaier, H. Freiesleben and S. M. Qaim, Phys. Rev. **C52**, 2546 (1995).

[Bla 73] M. Blann, Report COO-3494-10, Rochester University, (1973).

[Bla 75] M. Blann, Ann. Rev. Nucl. Sci. **25**, 123 (1975).

[Ble 95] G. Blessing, W. Bräutigam, H. G. Böge, N. Gad, B. Scholten and S. M. Qaim, Appl. Radiat. Isot. **46**, 955 (1995).

[Böc 83] K. H. Böckhoff (Editor), *"Nuclear Data for Science and Technology"*, Proccedings of an International Conference, held in Antwerp, Belgium, 6 - 10 Sep. 1982, D. Reidel Publishing Company, Dordrecht, Holland (1983).

[Böd 87] Z. Bödy (Editor), *"Handbook on Nuclear Activation Data"*, Technical Report Series No. 273, IAEA, Vienna, 29 (1987).

[Bor 68] M. Bormann, A. Behrend, I. Riehle and O. Vogel, Nucl. Phys. **A115**, 309 (1968).

[Bor 76] M. Bormann, H.-K. Feddersen, H.-H. Hölscher ,W. Scobel and H. Wagener, Z. Phys. **A277**, 203 (1976).

[Bos 94] M. Bostan and S. M. Qaim, Phys. Rev. **C49**, 266 (1994).

[Bra 72] G. M. Braga-Marcazzan, E. Gadioli-Erba, L. Millazzo-Colli and P. G. Sona, Phys. Rev. **C6**, 1398 (1972).

[Bre 70] M. Brendle, M. Mörike, G. Staudt and G. Steidle, Nucl. Instr. Meth. **81**, 141 (1970).

[Bre 72] H. J. Brede, Z. Physik **254**, 364 (1972).

[Byc 80] V. M. Bychkov, V. N. Manokhin, A. B. Pashenko and V. I. Plyashin, *"Cross Sections for the (n,p), (n,α) and (n,2n) Threshold Reactions"*, Report INDC(CCP)-146, IAEA, Vienna, Austria (1980).

[Cab 90] S. Cabral, G. Börker, H. Klein and W. Mannhart, Nucl. Sci. Eng. **106**, 308 (1990).

[Cha 32a] J. Chadwick, Nature **129**, 312 (1932).

[Cha 32b] J. Chadwick, Proc. Roy. Soc. (London) **A136**, 692 (1932).

[Chi 62] D. M. Chittenden, II., D. G. Gardner and R. W. Fink, Phys. Rev. **122**, 860 (1962).

[Chi 89] S. Chiba, M. Mizumoto, K. Hasegawa, Y. Yamanouti, M. Sugimoto, Y. Watanabe and M. Drosg, Nucl. Instr. Meth. **A281**, 581 (1989).

[Cie 83] S. Cierjacks (Editor), *"Neutron Sources for Basic Physics and Applications"*, an OECD/NEA Report, Pergamon Press (1983).

[Cie 94] S. Cierjacks and K. Shibata, *"Blind Intercomparison of Nuclear Models for Predicting Charged Particle Emission"*, Report NEA/NSC/DOC(93)4, OECD (1994).

[Cli 71] C. K. Cline and M. Blann, Nucl. Phys. **A172**, 225 (1971).

[Con 92] H. Condé (Editor), *"Nuclear Data Standards for Nuclear Measurements"*, Report NEANDC-311, INDC(SEC)-101, NEA, France (1992).

[Cor 78] V. Coralciuc, B. Holmquist, B. Marcinkowski and A. Prokopets, Nucl. Phys. **A307**, 445 (1978).

[Cri 71] D. F. Crisler, J. J. Jarmer and H. B. Eldridge, Nucl. Instr. Meth. **94**, 285 (1971).

[Cse 94] F. Cserpák, S. Sudár, J. Csikai and S. M. Qaim, Phys. Rev. **C49**, 1525 (1994).

[Csi 87] J. Csikai, *"Handbook of Fast Neutron Generators"*, Vol. I, CRC Press, Inc., Boca Raton, Florida (1987).

[CSI 97] CSISRS, Experimental Nuclear Data from the Data Base at BNL, as computer file from http://t2.lanl.gov/data/data.html, (1997).

[De 67] A. K. De,, S. M. Khopkar and R. A. Chalmers, *"Solvent Extraction of Metals"*, Van Nostrand Reinhold Company, London (1967).

[Deb 79] K. Debertin and U. Schötzig, Nucl. Instr. Meth. **158**, 471 (1979).

[Deb 88] K. Debertin and R. G. Helmer, *"Gamma and X-Ray Spectrometry with Semiconductor Detectors"*, North-Holland, Amsterdam, Oxford, New York, Tokyo (1988).

[Den 95] F. - O. Denzler, F. Rösch and S. M. Qaim, Radiochimica Acta **68**, 13 (1995).

[Dic 94] J. K. Dickens (Editor), Proc. Int. Conf. Nucl. Data Sci. Tec., 9 - 13 May 1994, Gatlinburg, U.S.A. (1994).

[Die 82] G. Dietze, H. Klein, *"NRESP4 and NEFF4 - Monte Carlo codes for the calculation of neutron response functions and detection efficiencies for NE 213 scintillation detectors"*, Report PTB-ND-22, PTB Braunschweig, Germany (1982).

[Dil 73] W. Dilg, W. Schantl, H. Vonach and M. Uhl, Nucl. Phys. **A217**, 269 (1973).

[Dit 90] B. Dittrich, *"Radiochemische Untersuchung protonen- und α-induzierter Spallations- und Fragmentationsreaktionen mit Hilfe der γ- und Beschleunigermassen-Spektrometrie"*, Dissertation Universität zu Köln (1990).

[Dóc 97a] R. Dóczi, V. Semkova, A. D. Majdeddin, Cs. M. Buczko and J. Csikai, *"Investigations on (n,p) Cross Sections in the 14 MeV Region"*, Report INDC(HUN), IAEA, Vienna, Austria, in press.

[Dóc 97b] R. Dóczi, A. D. Majdeddin, M. Várnagy, Cs. M. Buczko and J. Csikai, *"Status of Systematics in (n,p) and (n,α) Cross Sections at around 14 MeV"*, in [Ref 97], to be published.

[Dol 76] G. P. Dolya, A. P. Klyuscharev, V. Bozhko, V. Y. Golovnya, A. S. Kachan and A. I. Tutubalin, Proc 3rd All-Union Conf. Neutron Physics, Kiev, 173 (1976).

[Dra 77] D. M. Drake, G. F. Auchampaugh, E. D. Arthur, C. E. Ragan and P. G. Young, Nucl. Sci. Eng. **63**, 401 (1977).

[Dra 89] L. Drapchinsky, Nucl. Instr. Meth **A282**, 308 (1989).

[Dro 90] M. Drosg, Nucl. Sci. Eng. **106**, 279 (1990).

[Dun 80] V. E. Dunakov, Proc. Trieste Course on Nuclear Theory for Applications - 1978, IAEA-SMR-43, 255 (1980).

[Ede 72] G. Eder, G. Winkler and P. Phille, Z. Physik **253**, 355 (1972).

[Elm 87] D. Elmore, and F. M. Philips, Science **236**, 543 (1987).

[Fas 94] M. Faßbender, A. F. Novgorod, F. Rösch and S. M. Qaim, Radiochim. Acta **65**, 215 (1994).

[Fas 96] M.Faßbender, *"Aktivierungsquerschnitte von (p,x)-Prozessen an biologisch relevanten Elementen im Energiebereich von 50 bis 350 MeV für medizinisch-therapeutische Anwendungen"*, Dissertation Universität zu Köln (1996).

[Fer 77] J. C. Ferrer, J. D. Carlson and J. Rapaport, Nucl. Phys. **A275**, 325 (1977).

[Fes 80] H. Feshbach, A. Kerman and S. Koonin, Ann. Phys. **125**, 429 (1980).

[Fes 85] H. Feshbach, Ann. Phys. **159**, 150 (1985).

[Fes 94a] A. Fessler, Z. B. Alfassi and S. M. Qaim, Radiochimica Acta **65**, 207 (1994).

[Fes 94b] A. Fessler, Diploma Thesis, Universität zu Köln (1994).

[Fes 96] A. Fessler and S. M. Qaim, Radiochimica Acta **72**, 121 (1996).

[Fes 97a] A. Fessler, unpublished.

[Fes 97b] A. Fessler et al. , to be published.

[Few 68] T. R. Fewell, Nucl. Instr. Meth. **61**, 61 (1968).

[Fir 96] R. B. Firestone, *"Table of Isotopes"*, Vol. 1 and 2, V. S. Shirley (Editor), Wiley & Sons, Inc., New York, U.S.A. (1996).

[Fis 72] A. Fischer and L. Turi, *"The RFSP Program for Unfolding Neutron Spectra from Activation Data"*, Report INDC(HUN)-8/u, IAEA, Vienna (1972).

[For 86] R. A. Forrest, *"Systematics of Neutron -Induced Threshold Reactions with Charged Products at about 14.5 MeV"*, Report AERE-R12419, UKAEA Atomic Energy Research Establishment, Harwell (1986).

[Fre 59] H. Freiser and G. H. Morrison, Ann. Rev. Nucl. Sci. **9**, 221 (1959).

[Fre 80] W. Frehaut, A. Bertin, R. Bois and J. Jary, *"Neutron Cross Sections at 10 to 50 MeV"*, BNL, Brookhaven, 399 (1980).

[Fow 80] J. L. Fowler, J. A. Cookson, M. Hussain, R. B. Schwartz, M. T. Swinhoe, C. Wise and C. A. Uttley, Nucl. Instr. Meth. **175**, 449 (1980).

[Fu 80] C. Y. Fu, *"TNG: A two Step Hauser-Feshbach Code with Precompound Decays and Gamma-Ray Cascades"*, Technical Memorandum, Oak Ridge National Laboratory, (1980).

[Fu 96] C. Y. Fu and D. C. Larson (Eds.), *"Comparison of Evaluated Data for Chromium-52, Iron-56 and Nickel-58"*, Report NEA/WPEC-1, NEA/OECD, Paris, France (1996).

[Gad 76] E. Gadioli, E. Gadioli-Erba, L. Sajo-Bohus and G. Tagliaferri, Rev. Nouvo Cim. **6**, 1 (1976).

[Gar 62] D. G. Gardner, Nucl. Phys. **29**, 373 (1962).

[Gar 64] D. G. Gardner and Yu-Wen Yu, Nucl. Phys. **60**, 49 (1964).

[Gar 79] D. G. Gardner and F. S. Dietrich, Report UCRL-82998, LLNL, Livermore, U.S.A. (1979).

[Gar 81] M. A. Gardner and D. G. Gardner, Report UCRL-86265, LLNL, Livermore, U.S.A. (1979).

[Gho 87] S. K. Ghorai, J. R. Williams and W. L. Aford, J. Phys. G: Nucl. Phys. **13**, 405 (1987).

[Gmu 82] S. Gmuca and I. Ribanský, Nucl. Instr. Meth. **20**, 435 (1982).

[God 95] C. Goddio, E. Wattecamps and I.-G. Birn, *"Comparison of two independent background determinations for flueence measurements by the Bonner sphere technique applied at 2.5 and 16.0 MeV"*, Internal Report GE/VG/87/95, CEC-JRC, IRMM Geel (1995).

[Gov 94] A. A. Goverdovski, V. A. Khryachkov, V. V. Ketlerov, V. F. Mitrofanov, H. Vonach and R. C. Haight, *"(n,α) Reaction Studies Using a Gridded Ionisation Chamber"*, in [Dic 94] 117 (1994).

[Gra 85] P. W. Gray and A. Ahmad, Nucl. Insr. Meth. **A237**, 577 (1985).

[Gra 87] S. L. Graham, M. Ahmad, S. M. Grimes, H. Satyanarayana and S. K. Saraf, Nucl. Sci. Eng. **95**, 60 (1987).

[Gra 93] Á. Grallert, J. Csikai, S. M. Qaim and J. Knieper, Nucl. Instr. Meth. **A334**, 154 (1993).

[Gra 94] Á. Grallert, J. Csikai and S. M. Qaim, Nucl. Instr. Meth. (Letters) **A337**, 615 (1994).

[Gri 66] J. J. Griffin, Phys. Lett. **17**, 478 (1966).

[Gri 77] S. M. Grimes, R. C. Haight and J. D. Anderson, Nucl. Sci. Eng. **62**, 187 (1977).

[Gri 78] S. M. Grimes, R. C. Haight and J. D. Anderson, Phys. Rev. **C17**, 508 (1978).

[Gri 79] S. M. Grimes, R. C. Haight, K. R. Alvar, H. H. Barschall and R. R. Borchers, Phys. Rev. **C19**, 2127 (1979).

[Gri 96] S. M. Grimes, C. E. Brient, F. C. Goecker, F. B. Bateman, M. B. Chadwick, R. C. Haight, T. M. Lee, S. M. Sterbentz, P. G. Young, D. A. Wasson and H. Vonach, Nucl. Sci. Eng. **124**, 271 (1996).

[Gru 85] H. Gruppelar and J. M. Akkermans, *"The GRAPE Code System for the Calculation of Precompound and Compound Nuclear Reactions - GRYPHON Code Description and Manual"*, Report ECN-164 (1985).

[Gru 88] H. Gruppelar et al. *"The REAC-ECN-3 Data Library with Neutron Activation and Transmutation Cross Sections for Use in Fusion Reactor Technology"*, Report ECN-207, Petten, Netherlands (1988).

[Gul 95] K. Gul, *"Systematics of (n,p) and (n,a) Cross Sections for 14 MeV Neutrons on the Basis of Statistical Model"*, Report INDC(PAK)-009, IAEA, Vienna (1995).

[Hah 21] O. Hahn, Chem. Berichte **54**, 1131 (1921).

[Hah 45] P. F. Hahn, Ind. Eng. Chem. **17**, 45 (1945).

[Hai 81] R. C. Haight, S. M. Grimes, R. G. Johnson and H. H. Barschall, Phys. Rev. **C23**, 700 (1981).

[Hai 89] R. C. Haight, *"Activation with an Intense Source of Monoenergetic Neutrons in the Range 8 - 14 MeV"*, Proc. NEANDC Specialists' Meeting for Neutron Activation Cross Sections for Fission and Fusion Applications, Argonne National Laboratory, 13. -15. Sept. 1989, Report NEANDC-259U, 95 (1989).

[Hai 90] R. C. Haight and J. Garibaldi, Nucl. Sci. Eng. **106**, 296 (1990).

[Hai 96] R. C. Haight, D. W. Kneff, B. M. Oliver, L. R. Greenwood and H. Vonach, Nucl. Sci. Eng. **124**, 219 (1996).

[Hai 97a] R. C. Haight, *"Charged Particles Produced in Neutron Reactions on Nuclei from Beryllium to Gold"*, in [Ref 97], to be published.

[Hai 97b] R. C. Haight, F. B. Bateman, S. M. Sterbenz, M. B. Chadwick, P. G. Young, S. M. Grimes, O. A. Wasson, P. Maier-Komor and H. Vonach, *"The ^{58,60}Ni(n,a) Reactions from Threshold to 50 MeV"*, in [Ref 97], to be published.

[Hal 92] G. M. Hale and P. G. Young, *"The H(n,n)H Cross Section below 20 MeV"*, in [Con 92], 10 (1992).

[Han 73] L. F. Hansen, J. D. Anderson, P. S. Browne, R. J. Howerton, J. L. Kammerdiener, C. M. Logan E. F. Plechaty and C. Wong, Nucl. Sci. Eng. **51**, 278 (1973).

[Har 68] G. D. Harp, J. M. Miller and B. J. Berne, Phys. Rev. **165**, 1166 (1968).

[Har 71] G. D. Harp and J. M. Miller, Phys. Rev. **C3**, 1847 (1971).

[Här 71] M. Häring, H. Vonach and E. J. Feicht, Z. Physik **244**, 352 (1971).

[Hau 52] W. Hauser and H. Feshbach, Phys. Rev. **87**, 336 (1952).

[Hay 51] H. R. Haymond, W. M. Garrison, J. G. Hamilton, J. Chem. Phys. **17**, 382 (1951).

[Hel 80] R. G. Helmer and M. A. Lee, Nucl. Instr. Meth **178**, 499 (1980).

[Hel 83] R. G. Helmer, Int. J. Appl. Radiat. Isot. **34**, 1105 (1983).

[Her 82] G. Herrmann and N. Trautmann, Ann. Rev. Nucl. Part. Sci. **32**, 117 (1982).

[Hoa 86] Hoang Dac Luc, Inst. of Physics, Acad. of Science, Hanoi, in [McL 88], (1986).

[Hod 88] P. E. Hodgson, *"Pre-Equilibrium Processes in Nuclear Reactions; Intercomparison of Theories and Codes"*, in [Iga 88], 655 (1988).

[Hol 74] P. Holmberg, R. Rieppo, J. K. Keinänen and M. Valkonen, J. Inorg. Nucl. Chem. **36**, 715 (1974).

[Hua 97] X. Huang and D. Cai, Nucl. Sci. Eng. **125**, 371 (1997).

[Hus 67] L. Husain and P. K. Kuroda, J. Inorg. Nucl. Chem. **29**, 2665 (1967).

[Hus 68] L. Husain, A. Bari and P. K. Kuroda, J. Inorg. Nucl. Chem. **30**, 3145 (1968).

[IAE 86] "Nuclear Data for Fusion Reactor Technology", Proceedings of an Advisory Group Meeting organized by the IAEA and held in Gaussig, GDR, 1.-5. Dec. 1986, IAEA-TECDOC-457, WIEN (1988].

[Iga 88] S. Igarasi (Editor), *"Nuclear Data for Science and Technology"*, Proccedings of an International Conference, held at Mito, Japan, 30 May - 3 June 1988, Saikon, Tokio (1988).

[Ign 75] A. V. Ignatyuk, G. N. Smirenkin and A. S. Tiskin, Sov. J. Nucl. Phys. **21**, 255 (1975).

[Ike 88] Y. Ikeda, C. Konno, K. Oishi, T. Nakamura, H. Miyade, K. Kawade, H. Yamamoto and T. Katoh, Report JAERI 1312, (Editor T. Fuketa), JAERI Tokai-mura, Japan (1988).

[Ike 92] Y. Ikeda, C. Konno, M. Mizumoto, H. Hasegawa, C. Chiba, Y. Yamanouchi and M. Sugimoto, in [Qai 92a], 294 (1992).

[Ito 94] N. Ito, M. Baba, S. Matsuyama, I. Matsuyama and N. Hirakawa, Nucl. Instr. Meth. **A337**, 474 (1994).

[Iva 87] M. Ivascu, V. Avrigeanu and M. Avrigeanu, Rev. Roum. Phys. **32/7**, 697 (1987).

[Iwa 93] S. Iwasaki, M. Sakuma, K. Sugiyama and N. Odano, Report JAERI-M 93-046, 257 (1993).

[Iwa 94] S. Iwasaki, S. Matsuyama, T. Ohkubo, H. Fukuda, M. Sakuma and M. Kitamura, *"Measurement of Activation Cross-Sections for Several Elements between 12 and 20 MeV"*, in [Dic 94], 305 (1994).

[Jäc 87] B. Jäckel, W. Westmaier and P. Patzelt, Nucl. Instr. Meth. **A261**, 543 (1987).

[Kal 73] C. Kalbach-Cline, Nucl. Phys. **A210**, 590 (1973).

[Kal 75] C. Kalbach, Acta Phys. Slov. **25**, 100 (1975).

[Kal 90] H. Kalka, M. Torjman, H. N. Lien, R. Lopez and D. Seliger, Z. Phys. **A335**, 163 (1990).

[Kal 91] H. Kalka, *"EXIFON-A Statistical Multistep Reaction Code"*, NEA Data Bank, Saclay, France (1991).

[Kam 74] F. B. K. Kam, F. W. Stallmann, *"A Computer Program Automated for Determining Neutron Spectra from Activation Measurements"*, Report ORNL-TM-4601, Oak Ridge National Laboratory (1974).

[Kan 92] Y. Kanda and Y. Nakajima, *"The ^{238}U Fission Cross Section"*, in [Con 92], 70 (1992).

[Kas 96] Y. Kasugai, Y. Ikeda, Y. Yamamoto and K. Kawade, Ann. Nucl. Energy **23**, 1429 (1996).

[Kaw 81] K. Kawade, M. Ezuka, H. Yamamoto, K. Sugioka and T. Katoh, Nucl. Instr. Meth. **190**, 101 (1981).

[Kaw 90] K. Kawade, H. Yamamoto, T. Yamada, T. Katoh, T. Iida and A. Takahashi, *"Measurement of Formation Cross Sections of Short-Lived Nuclei by 14 MeV Neutrons"*, Report JAERI-M 90-171, NEANDC(J)-154/U, INDC (JPN)-140/L, JAERI, Japan (1990).

[Ker 59] B. D. Kern, W. E. Thompson and J. Ferguson, Nucl. Phys. **10**, 226 (1959).

[Kha 73] N. A. Khan, S. Mubarakmand and M. Ahmad, Nucl. Phys. **A202**, 123 (1973).

[Kir 83] T. Kiriyama and R. Kuroda, Talanta **30**, No.4, 261 (1983).

[Kle 97] A. Klein et al., to be published.

[Klo 94] L. I. Klochkova, B. S. Kovrigin and V. N. Kuritsin, *"Investigation of the Reactions (n,p) and (n,np) on ^{27}Al, ^{28}Si, ^{50}Cr, ^{54}Fe, ^{56}Fe, ^{58}Ni and Ni at 14.1 MeV Neutron Energy"*, Report INDC(CCP)-376, IAEA, Vienna (1994).

[Klo 97] R. M. Klopries, R. Dóczi, S. Sudár, J. Csikai and S. M. Qaim, Radiochimica Acta **76**, 3 (1997).

[Kne 86] D. W. Kneff, B. M. Oliver,H. Farrar IV and L. R. Greenwood, Nucl. Sci. Eng. **92**, 491 (1986).

[Kob 91] T. Kobayashi, A. Taniguchi, T. Ikuta, K. Kawade, H. Yamamoto, T. Katoh, T. Iida and A. Takahashi, *"Measurement of Formation Cross Sections of Short-Lived Nuclei Production by 14 MeV Neutrons (IV)"*, in Proc. of the 1990 Symposium on Nucl. Data, M. Igashira and T. Nakagawa (Eds.), Report JAERI-M 91-032, NEANDC(J)-160/U, INDC(JPN)-148/L, JAERI, Japan (1991).

[Koc 93] N. P. Kocherova and P. K. McLaughlin , *"The International Reactor Dosimetry File"*, Report IAEA-NDS-141, IAEA, Vienna (1993); as computer file from http://iaeand.iaea.or.at/ndspub/libraries/irdf/IRDF90V2.TXT.

[Kol 57] G. J. Kolmeschate, *"Elemente der fünften Nebengruppe"*, in W. Fresenius und G. Jander, *"Handbuch der Analytischen Chemie"*, Vol. **5b**, 24 (1957).

[Kop 87] J. Kopecky and H. Gruppelar, *"Systematics of Neutron-Induced Isomeric Cross Section Ratios at 14.5 MeV"*, Report ECN-200, Petten, Netherlands (1987).

[Kor 89] J. Korkisch, *"Handbook of Ion Exchange Resins"*, CRC Press, Inc., Boca Raton, Florida (1989).

[Kor 93] Z. Kormány, Nucl. Instr. Meth. **A337**, 258 (1993).

[Koz 78] I. E. Kozyr, V. A. Pljuiko and G. A. Prokopets, Proc of the 4th All Union Conf. on Neutron Physics, Kiev, 256 (1978).

[Kra 57] K. A. Kraus and F. Nelson, Ann. Rev. Nucl. Sci. **7**, 31 (1957).

[Lan 63] D. W. Lang, Nucl. Phys. **77**, 545 (1966).

[Ler 70] J. L. Leroy, J. L. Huet and J. Gentil, Nucl. Instr. Meth. **88**, 1 (1970).

[Lev 69] V. N. Levkovskii, g. e, Kovel'skaya, G. P. Vinitskaya, V. M. Stepanov and V. V. Sokol'skii, Sov. J. Nucl. Phys. **8**, 4 (1969).

[Lev 73] V. N. Levkovskii, Yad. Phys. **18**, 705 (1973).

[Lis 69] H. Liskien and A. Paulsen, Nucl. Instr. Meth. **69**, 70 (1969).

[Lis 73] H. Liskien, A. Paulsen, Nucl. Data Tables **11**, 569 (1973).

[Lis 75] H. Liskien, *"Techniques for the Determination of Neutron Induced Charged Particle Reactions"*, in [Sch 75], 156 (1975).

[Lis 88] H. Liskien, R. Widera, R. Wölfle and S. M. Qaim, Nucl. Sci. Eng. **98**, 266 (1988).

[Lis 89a] H. Liskien, *"Improved Neutron Fluence Accuracies in Activation Experiments"*, NEANDC Specialists Meeting on Neutron Activation Cross Sections for Fission and Fusion, 13 - 15 Sept. 1989, Argonne, U.S.A. (1989).

[Lis 89b] H. Liskien, M. Uhl, M. Wagner and G. Winkler, Ann. Nucl. Energy **16**, 563 (1989).

[Lis 90a] H. Liskien, R. Wölfle, R. Widera and S. M. Qaim, Appl. Radiat. Isot. **41**, 83 (1990).

[Lis 90b] P. W. Lisowski, C. D. Bowman, G. J. Russell and S. A. Wender, Nucl. Sci. Eng. **104**, 208 (1990).

[Lu 89] Lu Hanlin, Yu Weixiang, Zhao Wenrong and Zhao Yiwi, Report INDC(CPR)-16/L, IAEA, Vienna (1989).

[Maj 84] M. Ibn Majah and H. A. Ait, Report INDC(MOR)-003/GI, (1984).

[Maj 90] M. Ibn Majah and S. M. Qaim, Nucl. Sci. Eng. **104**, 271 (1990).

[Maj 97] A. D. Majdeddin, V. Semkova, R. Dóczi, Cs. M. Buczko and J. Csikai, *"Investigations on (n,α) Cross Sections in the 14 MeV Region"*, Report INDC(HUN)-031/L, IAEA, Vienna, Austria, (1997).

[Man 88] A. Mannan and S. M. Qaim, Phys. Rev. **C38**, 630 (1988).

[Man 94] W. Mannhart, D. Schmidt and X. Haihong, *"Measurement of the $^{59}Co(n,\alpha)^{56}Mn$, $^{59}Co(n,p)^{59}Fe$ and $^{59}Co(n,2n)^{58m+g}Co$ Cross Sections between 8 and 14 MeV"*, in [Dic 94], 285 (1994).

[Man 97] W. Mannhart, D. Schmidt and D. L. Smith, *"Measurement of the $^{52}Cr(n,p)^{52}V$, $^{52}Cr(n,2n)^{51}Cr$, $^{51}V(n,p)^{51}Ti$ and $^{51}V(n,\alpha)^{48}Sc$ Cross Sections between 7.9 and 14.4 MeV"*, in [Ref 97], to be published.

[Mas 72] G. N. Maslov, F. Nasyrov and N. F. Pashkin, Report YK-9, Obninsk Reports, U.S.S.R. (1972).

[Mat 94] I. Matsuyama, M. Baba, S. Matsuyama, T. Kiyosumi, T. Sanami, N. Hirakawa, N. Ito, S. Chiba, T. Fukahori, M. Mizumoto, K. Hasegawa and S. Meigo, Report JAERI-M 94-019, 191 (1994).

[McC 75] G. J. McCallum and G. E. Coote, Nucl. Instr. Meth. **130**, 189 (1975).

[McL 88] V. McLane, C. L. Dunford and P. F. Rose, *"Neutron Cross Sections. Volume 2 - Neutron Cross Section Curves"*, Academic Press (1988).

[McN 73] L. A. McNelles and J. L. Campbell, Nucl. Instr. Meth. **109**, 241 (1973).

[Mea 80] J. W. Meadows, D. L. Smith and G. Winkler, Nucl. Instr. Meth. **176**, 439 (1980).

[Mea 97] J. W. Meadows, private communication.

[Mei 95] A. Meister, *"Counting efficiency calculated for a neutron detector with a 4 cm * 5 cm NE 213 scintillator"*, Internal Report GE/R/ND/03/95, CEC-JRC IRMM Geel (1995).

[Met 88] M. K. Metha and J. J. Schmidt (Editors), Workshop on *"Applied Nuclear Theory and Nuclear Model Calculations for Nuclear Technology Applications"*, held at Trieste, Italy, 15 Feb - 19 Mar 1988, World Scientific (1988).

[Mia 94] M. M. H. Miah, H. Voach, W. Mannhart and D. Schmidt, *"Measurement of the Cross Section for 103Rh(n,n')103mRh in the Energy Range 6 - 12 MeV"*, in [Dic 94], 278 (1994).

[Mil 70] D. Miljanic, V. Valkovic, D. Rendic and M. Furic, Nucl. Phys. **A156**, 193 (1970).

[Mit 66] B. Mitra and A. M. Ghose, Nucl. Phys. **83**, 157 (1966).

[Mol 64] P. A. Moldauer, Revs. Mod. Phys. **36**, 1079 (1964).

[Mol 77] N. I. Molla and S. M. Qaim, Nucl. Phys. **A283**, 269 (1977).

[Mol 83] N. I. Molla, I. M. Mizanul, R. M. Mizanur and S. Khatun, Progress Report INDC(BAN)-002, IAEA, 2 (1983).

[Mol 91] N. I. Molla, S. M. Qaim, H. Liskien and R. Widera, Appl. Radiat. Isot. **42**, 337 (1991).

[Mol 92] N. I. Molla, S. M. Qaim and H. Kalka, Phys. Rev. **C45**, 3002 (1992).

[Mul 77] R. A. Muller, Science **196**, 439 (1977).

[Mus 90] A. Mushtaq and S. M. Qaim, Radiochimica Acta **50**, 27 (1990).

[Nei 60] J. M. Neilson, *"The radiochemistry of iron"*, Nuclear Science Series, NAS-NS3017, 14 (1960).

[Nel 64] F. Nelson, T. Murase and K. A. Kraus, J. Chromatography **13**, 503 (1964).

[Neu 94] B. Neumaier, F. Rösch, S. M. Qaim and G. Stöcklin, Radiochimica Acta **65**, 1 (1994).

[Not 71] A. Notea, Nucl. Instr. Meth. **91**, 513 (1971).

[Oka 80] K. Okamoto (Editor), Proccedings of the IAEA Consultants' Meeting on Neutron Source Properties, Debrecen, Hungary, 17 - 21 March 1980, Report INDC(NDS)-114/GT, Wien (1980).

[Oka 87] K. Okamoto (Editor), *"Properties of Neutron Sources"*, Proccedings of an Advisory Group Meeting on Properties of Neutron Sources organized by the IAEA and held in Leningrad, USSR, 9.-13. June 1986, Report IAEA TECDOC-410 (1987).

[Oki 92] Y. Oki, M. Numajiri, T. Suzuki, T.Miura and K. Kondo, Appl. Radiat. Isot. **43**, 1355 (1992).

[Osa 89] A. Osa, H. Yoshida, M. Miyachi, K. Kato, A. Hosoya, M. Shibata, H. Yamamoto, K .Kawade, T. Katoh, T. Iida and A. Takahashi, *"Measurement of*

Formation Cross Sections of Short-Lived Nuclei Produced by 14 MeV Neutron (II)", Proc. of the 1988 Seminar on Nuclear Data (eds. T. Nakagawa and A . Zukerau), Report JAERI-M89-026, NEANDC(J)-133"U", INDC(JPN)-120/L, JAERI, Japan, 293 (1989).

[Pau 71] A. Paulsen, R. Widera, A. Berlin and A. Trapani, Nucl. Instr. Meth. **91**, 589 (1971).

[Pau 81] A. Paulsen, H. Liskien, F. Arnotte and R. Widera, Nucl. Sci. Eng. **78**, 377 (1981).

[Pav 82] A. Pavlik, G. Winkler, H. Vonach, A. Paulsen and H. Liskien, J. Phys. G: Nucl. Phys. **8**, 1283 (1982).

[Per 63] C. M. Perey and F. G. Perey, Phys. Rev. **132**, 755 (1963).

[Per 74] J. P. Perroud, C. Sellem and J. F. Loude, Nucl. Instr. Meth. **115**, 357 (1974).

[Pra 71] R. Prasad and D. C. Sarkar, Il Nuovo Cimento **3**, 467 (1971).

[Pro 57] W. Prodinger, *"Organische Fällungsmittel in der quantitativen Analyse"*, in G. Jander, *"Die chemische Analyse"*, Vol. **37**, 60 (1957).

[Qai 72] S. M. Qaim, Nucl. Phys. **A185**, 614 (1972).

[Qai 73] S. M. Qaim and G. Stöcklin, J. Inorg. Nucl. Chem. **35**, 19 (1973).

[Qai 74a] S. M. Qaim, R. Wölfle and G. Stöcklin, J. Radioanalyt. Chem. **21**, 395 (1974).

[Qai 74b] S. M. Qaim, J. Inorg. Nucl. Chem. **36**, 239 (1974).

[Qai 74c] S. M. Qaim, R. Wölfle and G. Stöcklin, J. Inorg. Nucl. Chem. **36**, 3639 (1974).

[Qai 76] S. M. Qaim and G. Stöcklin, Nucl. Phys. **A257**, 233 (1976).

[Qai 77] S. M. Qaim and N. I. Molla, Proc. of the 9th Symp. On Fusion Techn., Garmisch-Partenkirchen, June 14-18, 1976, EUR-5602, Pergamon Press, Oxford, 589 (1977).

[Qai 78] S. M. Qaim and R. Wölfle, Nucl. Phys. **A295**, 150 (1978).

[Qai 79] S. M. Qaim, H. Ollig and G. Blessing, Radiochimica Acta **26**, 59 (1979).

[Qai 81] S. M. Qaim (Editor), *"14 MeV Activation Cross Sections"*, Handbook of Spectroscopy, Vol. III, 141 (1981).

[Qai 82] S. M. Qaim, Nucl. Phys. **A382**, 255 (1982).

[Qai 84] S. M. Qaim, R. Wölfle, M. M. Rahman and H. Ollig, Nucl. Sci. Eng. **88**, 143 (1984).

[Qai 85] S. M. Qaim, Nucl. Phys. **A438**, 384 (1985).

[Qai 86a] S. M. Qaim, G. Blessing and H. Ollig, Rad. Acta **39**, 57 (1986).

[Qai 86b] S. M. Qaim, *"Systematics of 14 MeV Neutron Induced Reaction Cross-Sections"*, in [IAE 86], 89 (1986).

[Qai 88] S. M. Qaim , A. Mushtaq and M. Uhl, Phys. Rev. **C38**, 645 (1988).

[Qai 90] S. M. Qaim, M. Ibn Majah, R. Wölfle and B. Strohmaier, Phys. Rev. **C42**, 363 (1990).

[Qai 92a] S. M. Qaim (Editor), *"Nuclear Data for Science and Technology"*, Proccedings of an International Conference, held at the Forschungszentrum Jülich GmbH, Germany, 13 - 17 May 1991, Springer Verlag Heidelberg (1992).

[Qai 92b] S. M. Qaim, F. Cserpák and J. Csikai, Appl. Radiat. Isot. **43**, 1065 (1992).

[Qai 94] S. M. Qaim, *"Recent Developments in the Study of Isomeric Cross Setions"*, in [Dic 94], 186 (1994).

[Qai 96] S. M. Qaim, S. Spellerberg, F. Csérpak and J. Csikai, Radiochimica Acta **73**, 111 (1996).

[Ref 97] G. Reffo (Editor), Proccedings of the International Conference on Nuclear Data for Science and Technology, held at the ICTP, Trieste, Italy, 19 - 23 May 1997, to be published.

[Rib 85] I. Ribansky, T. Pantaleev and L. Stoeva, Ann. Nucl. Energy **12**, 577 (1985).

[Ric 81] N. M. Rice, Hydrometallurgy **7**, 177 (1981).

[Ryv 78a] T. B. Ryves, P. Kolkowski and K. J. Zieba, Metrologia **14**, 127 (1978).

[Ryv 78b] T. B. Ryves, P. Kolkowski and K. J. Zieba, J. Phys. G: Nucl. Phys. **4**, 1783 (1978).

[Sai 77] K. Sailer, S. Daroczi, P. Raics and S. Nagy, Proc. Conf. On Neutron Physics, Kiev, U.S.S.R., Report INDC(CCP)-118/G, 246 (1977).

[Sal 71] O. A. Salnikov, G. N. Lovchikova, G. V. Kotelnikova, V. S. Nesterenko, N. I. Fetisov and A. M. Trufanov, Sov. J. Nucl. Phys. **12**, 620 (1971).

[San 87] A. F. Sánchez-Reyes, M. I. Febrián, J. Baró and J. Tejada, Nucl. Instr. Meth. **B28**, 123 (1987).

[Sch 75] R. A. Schrack and C. D. Bowman (Editors), Proc. Conf. Nuclear Cross Sections and Technology, Washington D. C., 3 - 7 March, 1975, NBS SP 425 (1975).

[Sch 82a] G. Schwedt, *"Chromatographische Praxis in der anorganischen Analyse"*, Georg Thieme Verlag, Stuttgart, New York (1982).

[Sch 82b] K. H. Schmidt, H. Delagrange, J. P. Dufour, N. Cârjan and A. Fleury, Z. Phys. **A308**, 215 (1982).

[Sch 93] B. Scholten, S. M. Qaim and G. Stöcklin, Radiochimica Acta **62**, 107 (1993).

[Sch 95] T. Schiekel, *"Radiochemische Untersuchungen zur Produktion kosmogener Radionuklide: Wirkungsquerschnitte, Modelle und Modellrechnungen"*, Dissertation Universität zu Köln (1995).

[See 65] U. Seebeck and M. Bormann, Nucl. Phys. **68**, 387 (1965).

[Sig 75] R. A. Sigg and P. K. Kuroda, J. Inorg. Nucl. Chem. **37**, 631 (1975).

[Smi 77] D. L. Smith and J. W. Meadows, Report ANL/NDM-37, Argonne National Laboratory, U.S.A. (1977).

[Smi 80] D. L. Smith and J. W. Meadows, Nucl. Sci. Eng. **76**, 43 (1980).

[Smi 81] D. L. Smith, J. W. Meadows and F. F. Porta, Nucl. Sci. Eng. **78**, 420 (1981).

[Smi 97] D. L. Smith and A. Fessler, Radiochimica Acta, in press.

[Str 80] B. Strohmaier and M. Uhl, STAPRE - A Statistical Model code with Consideration of Pre-Equilibrium Decay", Proc. Trieste Course on Nuclear Theory for Applications - 1978, IAEA-SMR-43, 313 (1980).

[Str 82] B. Strohmaier, *"Report on a Training Course on Nuclear Data Evaluation and Processing Techniques"*, Report INDC(AUS)-7/G, IAEA, Vienna, Austria (1982).

[Sud 79] S. Sudár and J. Csikai, Nucl. Phys. **A319**, 157 (1979).

[Sud 89] S. Sudár, *"A Solution for the Neutron Spectrum Unfolding Problem without using Input Spectrum"*, Report INDC(HUN)-26/L, IAEA, Vienna, Austria (1989).

[Sud 93] S. Sudár, F. Szelecsenyi and S. M. Qaim, Phys. Rev. **C48**, 3115 (1993).

[Sud 96] S. Sudár and S. M. Qaim, Phys. Rev. **C53**, 2885 (1996).

[Sud 97] S. Sudár, private communication.

[Suh 88a] A. Suhaimi, *"Studies of (n,t) Reactions on Light Nuclei"*, Report Jül-2196, KFA Jülich, Germany (1988).

[Suh 88b] A. Suhaimi, R. Wölfle, S. M. Qaim, P. Warwick and G. Stöcklin, Radiochimica Acta **43**, 133 (1988).

[Sut 90] M. Suter, Nucl. Instr. Meth. Phys. Res. **B52**, 146 (1990).

[Tak 96] M. Takada, T. Nakamura, M. Baba, T. Iwasaki, T. Kiyosumi, Nucl. Instr,. Meth. **A372**, 253 (1996).

[Tam 77] T. Tamamura, T. Udagawa, D. Feng and K. Kan, Phys. Lett. **66B**, 109 (1977).

[Tam 82] T. Tamamura, T. Udagawa and H. Lenske, Phys. Rev. **C26**, 379 (1982).

[Tök 81] J. Töke, J. Swiatecki, Nucl. Phys. **A372**, 141 (1981).

[Tsa 94] C. Tsabaris, E. Wattecamps and G. Rollin, *"Double Differential (n,xp) and (n,xα) Cross Section Measurements of ^{27}Al, ^{58}Ni and ^{63}Cu in the Neutron Energy Range from 2.0 to 15.5 MeV"*, in [Dic 94], 282 (1994).

[Tsa 97] C. Tsabaris, E. Wattecamps, G. Rollin and C. T. Papadopoulos, Nucl. Sci. Eng., submitted.

[Uhl 70] M. Uhl, Acta Phys. Austriaca **31**, 245 (1970).

[Uhl 76] M. Uhl and B. Strohmaier, Report IRK-76/01, IRK Vienna, Austria (1976).

[Uhl 81] M. Uhl and B. Strohmaier, Program Manual for STAPRE Code, NEA Data Bank, Paris, France (1981).

[Uhl 92] M. Uhl, H. Gruppelaar, H. A. J. van der Kamp, J. Kopecki and D. Nierob, *"The EFF-2 Evaluation for the Reaction Systems n + ^{52}Cr, ^{56}Fe, ^{58}Ni and ^{60}Ni"*, in [Qai 92a], 924 (1992).

[Uno 96] Y. Uno, Y. Uwamino, T. S. Soewarsono and T. Nakamura, Nucl. Sci. Eng. **122**, 247 (1996).

[Ura 78] I. Uray, I. Török, P. Bornemisza-Pauspertl and L. Végh, Z. Phys. **A287**, 51 (1978).

[Uwa 88] Y. Uwamino, T. Ohkubo, A. Torii and T. Nakamura, Nucl. Instr. Meth. **A271**, 546 (1988).

[Uwa 92] Y. Uwamino, H. Sugita, Y. Kondo and T. Nakamura, Nucl. Sci. Eng. **111**, 391 (1992).

[Uwa 94] Y. Uwamino, H. Sugita, Y. Kondo and T. Nakamura, J. Nucl. Sci. Tec. **31**, 1 (1994).

[Uwa 97] Y. Uwamino, T. S. Soewarsono and T. Nakamura, Nucl. Instr. Meth. **A389**, 463 (1997).
[Vän 81] R. Vänskä and R. Rippo, Nucl. Instr. Meth. **179**, 525 (1981).
[Vie 91] M. Viennot, M. Berrada, G. Paic and S. Joly, Nucl. Sci. Eng. **108**, 289 (1991).
[Von 69] H. Vonach and M. Hille, Nucl. Phys. **A127**, 289 (1969).
[Wag 88a] M. Wagner, G. Winkler, H. Vonach and H. Liskien, *"Measurement of the $^{93}Nb(n,n')^{93m}Nb$ Cross Section at 7.9 MeV"*, in [Iga 88], 1049 (1988).
[Wag 88b] M. Wagner, G. Winkler, H. Vonach, and G. Petö, Ann. Nucl. Energy **15**, 363 (1988).
[Wag 89] M. Wagner, G. Winkler, H. Vonach, Cs. M. Buczko and J. Csikai, Ann. Nucl. Energy **16**, 623 (1989).
[Wat 83] E. Wattecamps, H. Liskien and F. Arnotte, *"Measurement for (n,α) Cross Sections for Cr, Fe and Ni at 14 MeV Neutron Energy"*, in [Böc 83], 156 (1983).
[Wat 91] E. Wattecamps, *"Measurement of Double Differential (n,xα) Cross Sections of ^{nat}Ni, ^{58}Ni, ^{60}Ni, ^{nat}Cu, ^{63}Cu,and ^{65}Cu in the 5 to 14 MeV Neutron Energy Range"*, in [Qai 92a], 310 (1992).
[Wei 36] C. F. von Weizsäcker, Naturwissenschaften **24**, 813 (1936).
[Wei 75] H. Weigel, R. Michel and W. Herr, Radiochimica Acta **22**, 11 (1975).
[Wei 91] J. Weiß, *"Ionenchromatographie"*, Verlag Chemie, Weinheim (1991).
[Wen 62] R. Wenusch and H. Vonach, Anz. Öst. Akad. Wiss. **99**, 1 (1962).
[Wes 81] W. Westmaier, Nucl. Instr. Meth. **180**, 205 (1981).
[Wes 86] W. Westmaier, Nucl. Instr. Meth. **A242**, 437 (1986).
[Wes 87] H. I. West, Jr., R. G. Lanier and M. G. Mustafa, Phys. Rev. **C35**, 2067 (1987).
[Wes 90] W. Westmaier and J. van Arle, Nucl. Instr. Meth. **A286**, 439 (1990).
[Wes 95] W. Westmaier, *"X-Ray"*, Program Manual, Dr. Westmaier GmbH, Ebersdorfergrund - Mölln, Germany, (1995).
[Wil 53] H. H. Willard, E. L. Martin and R. Feltham, Z. Anal. Chem. **25**, 1963 (1953).
[Wil 70] J. B. Willet, Nucl. Instr. Meth. **84**, 157 (1970).
[Wil 71] F. C. Williams, Nucl. Phys. **A166**, 231 (1971).
[Win 62] J. Wing and J. R. Huizenga, Phys. Rev. **128**, 280 (1962).
[Win 80] G. Winkler, D. L. Smith and J. M. Meadows, Nucl. Sci. Eng. **76**, 30 (1980).
[Win 89] G. Winkler, Nucl. Instr. Meth. **A282**, 317 (1989).
[Win 91] G. Winkler, V. E. Lewis, T. B. Ryves and M. Wagner, *"The $^{238}U(n,f)$ Cross Section and its Ratio to the $^{27}Al(n,\alpha)^{24}Na$ and $^{56}Fe(n,p)^{56}Mn$ Cross Section in the 14 MeV Region"*, in [Qai 92a], 401 (1991).
[Wöl 84] R. Wölfle, S. Khatun and S. M. Qaim, Nucl. Phys. **A423**, 130 (1984).
[Wöl 85] R. Wölfle, S. Sudár and S. M. Qaim, Nucl. Sci. Eng. **91**, 162 (1985).
[Wöl 88] R. Wölfle, A. Mannan, S. M. Qaim, H. Liskien and R. Widera, Appl. Radiat. Isot. **39**, 407 (1988).
[Wöl 90] R. Wölfle, S. M. Qaim, H. Liskien and R. Widera, Rad. Acta **50**, 5 (1990).
[Wöl 93] R. Wölfle, A. Suhaimi and S. M. Qaim, Nucl. Sci. Eng. **115**, 71 (1993).

[Yaf 62] L. Yaffe, Ann. Rev. Nucl. Sci. **12**, 153 (1962).

[Yam 90] N. Yamamuro, Report JAERI-M 90-006, JAERI, Japan (1990).

[You 77] P. G. Young and E. D. Arthur, "*GNASH: A Pre-equilibrium Statistical Nuclear Model Code for Calculation of Cross Sections and Emission Spectra*", LA-6947, Los Alamos Scientific Lab. Report (1977).

[Yu 67] Y. W. Yu and D. Gardner, Nucl. Phys. **A98**. 451 (1967).

[Zha 86a] Z. Zhao and D. Zhou, *"Systematics of (n,charged particle) Reactions"*, in [IAE 86], 151 (1988).

[Zha 86b] J. Zhang, D. Zhou and D. Cai, *"Systematics of (n,2n) and (n,3n) Cross Sections"*, in [IAE 86], 159 (1988).

[Zwe 88] J. Zweit, S. Downey and H. Sharma, Appl. Radiat. Isot. **39**, 1197 (1988).

Acknowledgements

I had the privilege to work with Prof. Dr. S. M. Qaim who suggested the problem and was my supervisor for the last three years. He was a real "Doktorvater", giving me not only scientific advice but also established the contacts to Geel and helped me in receiving a fellowship. The work with him was based on trust, a prior condition for an independent effort.

I would like to thank the directors of the Institute in Jülich , Prof. Dr. G. Stöcklin and Prof. Dr. H. H. Coenen, and in Geel, Prof. Dr. W. Müller, Prof. Dr. A. J. Deruytter and Prof. Dr. M. Grasserbauer, for supporting this work.

I stayed with pleasure at the Van de Graaff lab at Geel where most of this work was done. I would like to thank Dr. H. Weigmann as leader of the Nuclear Data Group, Dr. E. Wattecamps for his help with the experiments, and Dr. A. J. M. Plompen who joined the group towards the end of the work but directly showed interest and gave several useful advices. I am also grateful for the help of Dr. F. J. Hambsch, H. Bax, W. Schubert and Dr. G. Giorginis, who placed a HPGe detector at my disposal.

The help of Stefan Spellerberg with the irradiations at Jülich is gratefully acknowledged. Dipl. Chem. Andreas Klein is thanked for his advice on the chemical separations and the introduction to the UV-VIS spectrometry.

I am very grateful to Dr. Donald L. Smith from Argonne National Laboratory (ANL) who had the idea of the pneumatic transport system and helped to make the "rabbits" run. The experiment together with him in September 1996 was one of the most pleasant moments during this thesis work. His large experience in activation measurements and many discussions stimulated me a lot. Also I would like to show my gratitude to Dr. J. W. Meadows for the calculation of the multiple scattering corrections.

One other person I am specially obliged to is Dr. Immo Birn. He was part of the Nuclear Data group at the Van de Graaff on my arrival and guided me along through the "activation business" during the first year. It has been nice to work with him and I am grateful for all the help, valuable suggestions and discussions.

I am grateful to Prof. Dr. J. Csikai and Dr. S. Sudár from the Institute of Experimental Physics of the Kossuth University at Debrecen, Hungary, for the hospitality I received during my stay at their Institute in April 1997. Dr. S. Sudár gave me many useful advices on the nuclear model calculations with the STAPRE code.

I would like to thank also Dr. A. Crametz in his function as Head of the Van de Graaff accelerator. He always took care to give me the best "beam", even in cases where the general conditions were not so good due to lack of manpower or antiquitated machine parts.

Of the many persons who helped to realize this thesis project I would like to thank the operators of the Compact Cyclotron at Jülich and the Van de Graaff at Geel, the staff of

the drawing office, the sample preparation and the workshop at Geel. Especially I want to thank M. Conti, P. Falque, J. Leonard and Dr. C. Ingelbrecht.

The support from the European Community through the award of a three years' fellowship is gratefully acknowledged.

Forschungszentrum Jülich

Jül-3502
January 1998
ISSN 0944-2952